NASA Technical Memorandum 113128

Hot Corrosion of Single-Crystal NiAl-X Alloys

James A. Nesbitt
Lewis Research Center, Cleveland, Ohio

National Aeronautics and
Space Administration

Lewis Research Center

May 1998

Available from

NASA Center for Aerospace Information
800 Elkridge Landing Road
Linthicum Heights, MD 21090-2934
Price Code: A08

National Technical Information Service
5287 Port Royal Road
Springfield, VA 22100
Price Code: A08

Hot Corrosion of Single-Crystal NiAl-X Alloys

James A. Nesbitt
NASA Lewis Research Center
Cleveland, OH

Abstract

Several single-crystal NiAl-X alloys (X=Hf, Ti, Cr, Ga) underwent hot corrosion testing in a Mach 0.3 burner rig at 900°C for 300 1-hr cycles. The surface morphology after testing consisted of either mounds or an inward, uniform-type of attack which preserved surface features. It was observed that the surface morphology was affected by the surface preparation treatments. Microstructurally, the hot corrosion attack initiated as pits but evolved to a rampant attack consisting of the rapid inward growth of Al_2O_3. Electropolishing and chemical milling produced many pits and grooves on the surface. However, the presence of pits and grooves did not appear to strongly influence the hot corrosion response. Attack on many samples was strongly localized which was attributed to compositional inhomogeneity within the samples. It was found that increasing the Ti content from 1% to 5% degraded the hot corrosion response of these alloys. In contrast, the addition of 1-2% Cr reduced the susceptibility of these alloys to hot corrosion attack and negated the deleterious effect of the 4-5%Ti addition.

Executive Summary

Ten single-crystal NiAl-X alloys (X=Hf, Ti, Cr, Ga), supplied by GEAE, underwent hot corrosion testing in a Mach 0.3 burner rig at the NASA Lewis Research Center. Samples were tested for up to 300 1-hr cycles at a temperature of 900°C. It was found that increasing the Ti content from 1% (Alloy D218) to 5% (Alloys D219, AFN20) degraded the hot corrosion response. In contrast, the addition of 1-2% Cr to alloys containing 4-5% Ti additions (Alloys AFN19, AFN21-26) reduced the susceptibility of these alloys to hot corrosion attack and negated the deleterious effect of the Ti addition.

The sample surface was prepared by either electropolishing, chemically milling, or mechanical polishing. The electropolishing produced a shiny surface finish on all the alloys, whereas the chemical milling treatment resulted in a flat matte finish on all alloys except D218, which remained shiny. In addition, the electropolishing and chemical milling treatments produced many pits and grooves on the surface, especially in the alloys containing 4-5% Ti. However, the presence of these pits and grooves did not appear to strongly influence the hot corrosion response and little difference was observed in the corrosion morphology on the outer surface between the electropolished and chemically milled samples. In contrast, mechanically polishing the surface did effect a change in the corrosion morphology and improved the hot corrosion response over that of the chemically milled surface treatment.

The surface morphology after testing consisted of either mounds or an inward, uniform-type of attack which preserved surface features. The mounds initiated early and grew and coalesced through the 300 hours of testing, however, few new corrosion mounds were observed after 50-100 hrs. Microstructurally, the hot corrosion attack initiated as pits but evolved to a rampant attack consisting of the rapid inward growth of Al_2O_3. Within these pits and the larger, rampant internal oxide structures, Ca and Mg were commonly detected while Na was observed only at trace levels. Sulfides were not observed, and S was only detected at or near the surface. Attack on many samples was strongly localized on one end of the sample or certain regions on the curved surface. Since the sample orientation was changed every 10 cycles, this localized attack was attributed to compositional inhomogeneity within the samples.

Introduction

Single-crystal nickel aluminide* has been under considerable investigation this decade as a potential structural material in aero gas turbine engines. The attractive features of NiAl in comparison to Ni-base superalloys include a higher melting point, lower density, higher thermal conductivity and excellent oxidation resistance.[1,2] However, NiAl suffers from a lack of ductility and fracture toughness at low temperatures, and low creep strength at high temperatures. These physical and mechanical properties have recently been reviewed in detail elsewhere.[3,4] Alloying additions of Hf, Ga, Ti and Cr have each shown some benefit to the mechanical properties over that of the binary alloy.[5] However, the collective effect of these alloying additions on the environmental resistance of NiAl-X was unclear. Hence, the purpose of the present study was to examine the hot corrosion behavior of these alloys. A companion study was undertaken to examine the cyclic oxidation resistance of these alloys.[6]

Hot corrosion of Ni- and Co-based alloys was studied extensively in the 1970's and early 1980's. These studies showed that the hot corrosion problem is complex, being strongly dependent on numerous parameters, including the alloy composition, salt composition and deposition, environment (e.g., O_2 and SO_3 pressures), and temperature. Experimental studies at many laboratories have also shown that widely varying results can occur with different tests techniques used to examine hot corrosion (e.g., burner rigs, thermogravimetric analysis (TGA), crucible tests, furnace tests, etc.), many of which do not reproduce the hot corrosion morphologies observed on field components. Many mechanisms have been proposed to explain the various observations for a specific test. As an illustration of the complexity of the hot corrosion process, one detailed study of a Ni-based superalloy[7] proposed that two seemingly contrary mechanisms, basic fluxing and acidic fluxing, were occurring during a single test but at different stages of the attack. Numerous review papers have been written to summarize various aspects and mechanisms of hot corrosion with some of the more recent reviews given in references 8-12.

Previous Hot Corrosion Studies of NiAl

One of the earlier studies of NiAl alloys was that of Kaufman[13] who examined additions of Cr and Ti to β NiAl alloys. Kaufman reported that additions of either 10% Cr or 10%Ti to NiAl improved the hot corrosion resistance. Lower Cr contents (2%) with additions of other elements (i.e., 5%Ti or 5%Mo) were also reported as beneficial. Kaufman stated that β NiAl was relatively resistant to Na_2SO_4 attack but the lower-Al, γ' Ni_3Al phase was much more susceptible to attack. It was concluded that "major attack on NiAl is preceded by transformation of a surface layer to Ni_3Al due to Al loss to the otherwise protective Al_2O_3 scale."[13] Romeo and McKee[14] examined the hot corrosion behavior of a series of γ, γ' and Ni-Cr and Ni-Al alloys in a variety of laboratory tests (e.g., TGA and crucible tests). In agreement with the earlier work of Kaufman, Romeo and McKee found that, in general, the β NiAl phase exhibited excellent resistance to attack while the γ' phase appeared to be the most susceptible to "accelerated salt-induced hot corrosion."[14] In a later study of various Ni-Al alloys, McCarron, et al.,[15] also found that β

---

[*] All references to nickel aluminide, or NiAl, will refer to the β phase unless otherwise stated.

NiAl was more corrosion resistant than γ' Ni_3Al and that Cr significantly improved the hot corrosion resistance of NiAl. However, for γ' Ni_3Al, although Cr also improved the short-term hot corrosion resistance of this alloy, Ti additions definitely degraded the corrosion resistance.[15]

One of the more recent studies was that of Ellis[16] who examined the effect of 2, 5 and 15 wt.% Cr additions to β NiAl. In this study, the hot corrosion behavior was examined by TGA in a vertical furnace with salt-coated specimens. Ellis identified several stages in the hot corrosion attack of NiAl with the initial stage (Stage I) being protective Al_2O_3 scale formation and growth similar to that during oxidative attack. Surprisingly, preoxidation of the sample to form an initial Al_2O_3 film had only a small effect on the duration of the Stage I behavior. However, decreasing the Al content from 50 to 45% resulted in the elimination of Stage I and the immediate start of the accelerated attack identified as Stage II. In contrast, the addition of as little as 2% Cr to Ni-46Al and 5% Cr to Ni-45Al resulted in only Stage I behavior throughout the test duration of 555 and 400 hrs, respectively. Ellis proposed a mechanism for the transition from Stage I to Stage II behavior which involved Al depletion resulting in the formation of γ' Ni_3Al and basic fluxing (dissolution) of the protective Al_2O_3 scale. Subsequent oxidation in Stage III caused rapid internal oxidation within the Ni_3Al phase. Continued basic conditions on the surface prevented reformation of any protective oxide scales.

Experimental Procedure

Ten single-crystal NiAl alloys were tested in a Mach 0.3 burner rig at 900°C (1652°F). Samples were examined using optical microscopy, scanning electron microscopy (SEM) and electron microprobe (EMP). Qualitative chemical analysis was accomplished on the SEM by energy dispersive spectroscopy (EDS) whereas quantitative chemical analysis and x-ray dot maps were performed by wavelength dispersive spectroscopy (WDS) with the EMP. Water soluble reaction products were identified by ICP emission spectroscopy. Surface oxide phases were determined by x-ray diffraction (XRD). For optical microscopy of mounted sample cross sections, samples were etched with a molybdic acid etch (50-75 ml HF, 150 ml H_2O, and 100 gm molybdic acid).

Material Tested

All material was supplied by GEAE in a heat treated, hot isostatic pressed (HIP'ed) and aged condition. The heat treatment, performed by GEAE, consisted of a homogenization treatment, HIP'ing, and an aging treatment according to the following schedule:

Homogenization: 32 hrs at 1371°C (2500°F)
HIP Cycle: 6 hrs at 1371°C (2500°F) and 138 Mpa (20 Ksi)
Aging: 30 min at) 1371°C (2500°F), cool to 982°C (1800F) at 55°C/min (100°F/min), 6 hrs at 982°C (1800°F), cool to room temperature

The alloy designations and compositions supplied by GEAE, are given in Table I. Alloy compositions, including Si, were also determined from a random piece of material at the NASA Lewis Research Center (LeRC) for each of the NiAl-Hf-X alloys and are also shown in Table I. As shown, most of the alloy compositions measured at LeRC are in relatively good agreement with those supplied by GEAE. Si levels ranged from less than 0.2% to as high as 0.6%. Initially, seven alloys were received (AFN19, AFN21-26) and tested in the burner rig (Series I). Following this test, three additional alloys, AFN20, D218 and D219, were received and tested (Series II and III). D218 was considered a baseline alloy with no Cr and only 1%Ti.

Initial Alloy Microstructures

Each of the alloy microstructures contained small oxide, carbide and intermetallic precipitates as previously described.[6] The carbides were identified as either HfC or (Hf,Ti)C and the oxide was identified as HfO_2. The oxides and carbides were often agglomerated. The baseline alloy, D218, contained relatively large (~1 micron) precipitates which were most likely either NiHfSi or Heusler $Ni_2Al(Hf,Ti)$ phase. In contrast, the high-Ti alloys (AFN19-26 and D219) contained fine Heusler precipitates. Morphologies of the oxides, carbides and fine precipitates are shown and discussed elsewhere in greater detail.[6,17-19]

The high-Ti alloys (AFN19-26 and D219) also contained large Hf-rich, multiphase regions consisting of primary Heusler, NiAl and NiHfSi.[6,18,19] Porosity was occasionally associated with these three-phase regions, in agreement with earlier studies.[18] These regions are remnants of Hf-rich interdendritic regions observed in as-cast microstructures.[18] A typical three-phase region with quantitative chemical analyses by EMP is shown in Fig 1. A small Zr content is often detected in regions with high Hf levels. This Zr impurity was previously traced to the starting Hf material.[19]

Sample Geometry and Machining

Samples were machined into hollow right circular cylinders with approximate dimensions of 1.27cm (0.5 in) outer diameter, 0.635cm (0.25 in) inner diameter by 1.27cm (0.5 in) height (Fig 2). All machining was accomplished by wire EDM. Samples were cut from single-crystal bars from which mechanical test pieces had previously been cut. As a consequence, samples were cut randomly from the remaining material without regard to crystal orientation. Due to the limited material, only two samples of some compositions could be machined. In addition, full sized samples could not always be cut from the remaining material such that some of the samples contained small flat or curved sections on the circumference or ends of the sample where mechanical test samples had previously been removed or from the edge of the ingot.

Surface Preparation and Morphology Prior to Testing

Electropolishing Treatment

The results in this study showed a distinct effect of the hot corrosion response on the surface preparation. As a consequence, the initial surface morphology of the samples will be reviewed in some detail below. The wire EDM procedure to remove samples from the ingot pieces produced a thin, uniform recast layer on the surface of the samples. In addition, cracks formed at the sample edges and surfaces. Samples were initially electropolished to remove the EDM recast layer. The electropolishing conditions are given in Table II. The electropolishing treatment produced a shiny, metallic finish on the surface of the samples, often with a small "tarnished" region on the curved surface near where the electrode clip was attached. EDS analysis of the thin tarnished region detected Cl in addition to the matrix elements. However, after 10 hrs of testing, the tarnished region was not observed and did not appear to have any effect on the corrosion on the sample surface. Occasionally the elctropolishing treatment left small regions on the surface of the sample with a different morphology (Fig 3a). A closer view of one of these areas showed that it contained numerous etch pits (Fig 3b). (Several of the pits shown in this figure contain epoxy from previously mounting and polishing one end of this sample.) On the remainder of the surface, pits were occasionally observed, but much less frequently than in this region, and they tended to have more rounded edges as though they were being dissolved. Sufficient material was removed from the surface to occasionally reveal oxide and carbide particles (Fig 3c). The electropolish did not seem to preferentially attack the multiphase regions consisting of primarily Heusler, β NiAl and Ni(Hf,Ti)Si, as shown in Fig 3d. As previously mentioned, porosity, such as that shown in Fig 3d, was commonly associated with these multiphase regions.[6,18] The smooth surface typical of the electropolishing treatment is also apparent in Fig 3c,d.

Due to the limited number of samples, only one sample (AFN26) was mounted and polished in order to examine the surface in cross section after electropolishing. Although most regions appeared smooth (Fig 4a), many regions still contained small cracks penetrating less than 10 microns into the sample (Fig 4b). However, some cracks were observed which extended hundreds of microns into the sample (Fig 5) while some cracks appeared widened and tips blunted by the electropolishing treatment (Fig 6). Following all surface treatments, the samples were ultrasonically cleaned with acetone and ethanol prior to testing. During the first series of burner rig testing (Series I), all of the electropolished samples underwent some form of fracture before 150 cycles. Upon examination, it was apparent that there was considerably greater attack and corrosion product formation on the ID surface of the samples than on the OD surface. This accelerated attack was likely the result of incomplete removal of the EDM recast layer and the remaining cracks. The volume expansion associated with the significant corrosion product formation on the ID was presumably the cause for the fracture of the samples. In summary, electropolishing generally resulted in a shiny, relatively smooth metallic finish although some distinct regions showed significant pit formation. Fine cracks were not all removed by electropolishing and although some cracks were widened and the tips blunted, many deep cracks remained after the electropolishing treatment.

Chemical Milling Treatment

Macrostructural Features. All electropolished samples (AFN19 and AFN21-26), as well as three new alloys received from GEAE (D218, D219 and AFN20), underwent a chemical milling treatment in order to better remove the EDM recast layer, particularly on the ID surface. The chemical milling treatment was performed for 30 minutes at General Electric, Evandale. Chemically milling the D218 alloy resulted in a shiny, polished, metallic-appearing surface similar to that produced by electropolishing (Fig 7). Chemical milling of all other alloys resulted in a dark gray, matte surface finish, often revealing features of the cast microstructure. Since the samples were cut at random orientations, the features of the cast microstructure varied between samples and were strongly influenced by lighting conditions. The dendritic structure was evident on the end and sides of some samples (Fig 8a,f) while different orientations gave other regular patterns (Fig 8b-e). There was no obvious difference in the surface finish between alloys which were chemically milled only (AFN20 and D219) and those which were electropolished prior to chemical milling (AFN19 and AFN21-26). Cracks at the edges, widened either by the electropolish or chemical milling treatments, were found on almost all samples and were more prevalent on the ID (Fig 9a) than on the OD (Fig 9b).

Most of the top, bottom and outer curved surfaces appeared similar apart from the different dendritic patterns discussed above. One exception, however, was the top and bottom surfaces of the AFN24 sample. One end of this sample exhibited a shiny and pitted metallic surface (Fig 10a), whereas most of the other end of the sample, as well as the curved surface showed the typical dark matte finish (Fig 10b,c). One small localized region on the dark matte end also showed this rough, metallic structure (see arrow in Fig 10b). Since none of the other samples showed this extreme variation in structure, it is possibly due to the response of a compositional inhomogeneity to the electropolishing or chemical milling treatment. As mentioned above, full circular samples could not always be cut from the ingots due to the limited material. The AFN25 sample had four such regions as indicated by the arrows in Fig 11. Following electropolishing and chemical milling, the typical dark matte finish was produced on three of these regions, including the large region on the top of Fig 11a (double arrows on top), while the remaining flat region had a shiny, metallic, pitted finish (Fig 11b) similar to that of the shiny, pitted end of the AFN24 sample (Fig 10a). However, as will be shown in a later section, these two shiny, pitted regions on AFN24 and AFN25 behaved differently during hot corrosion testing.

Microstructural Features. At an intermediate magnification, the surface of D218, which had only received the chemical milling treatment, appeared polycrystalline (Fig 12a). However, at higher magnifications, large, shallow, oval-shaped etch pits were apparent (Fig 12b) as well as surface-connected porosity (Fig 12c). This morphology was typical on the curved surfaces, flat ends, as well as what could be seen on the ID surface. Cracks near the edges appeared widened and crack tips blunted (Fig 12d). The chemical milling treatment also revealed small HfO_2 particles highlighting subgrain boundaries (Fig 13a,b), oxide/carbide particles at the surface (Fig 13c), as well as other unidentified microstructural features (Fig 14).

In comparison, the surface of the other alloys which were only chemically milled (AFN20 and D219) contained more distinct and deeper etch pits than those on D218. What appeared to be subgrain boundaries were also deeply etched by the chemical milling treatment. In addition, the morphology of the etched surface varied considerably over the surface, possibly due to crystal orientation. Some of this variety in the morphology on the same D219 sample is shown in Figs 15-18. Pits and subgrain boundaries (dark arrows) are shown in Fig 15. Although the chemical milling treatment appeared to strongly etch most of the surface, small localized regions appeared to resist the treatment. These regions, which appear dark in the SEM micrographs, are indicated by white arrows in Figs 15,16. A small oxygen peak was detected by EDS at these dark regions in addition to the Ni, Al, Ti and Cr peaks associated with the matrix, indicating that a thin oxide film may have existed on these regions, consistent with their darker image in the SEM. The oxide film appears to have resisted the chemical milling in comparison the metal. The fine microstructure of the Heusler precipitates along certain crystallographic orientations is apparent in Figs 15c, 16b and 17b,c. The attack of the chemical milling on subgrain boundaries, as well as some elongated "trench-like" pits is shown in Fig 18. Some of the subgrain crevices appeared to be near 10 microns deep. Different etching patterns on different sides of a crack or deeply etched subgrain boundary in AFN20 is evident in Fig 19. In addition to pits and crevices produced by the chemical milling, pre-existing porosity was also observed on the surface of samples as shown in Fig 20. The chemical milling treatment did appear to widen and blunt cracks at the edges of the samples, as shown in Fig 21. As with the electropolishing treatment, chemical milling revealed oxides and carbides at the surface (Fig 22).

The surface morphology of samples chemically milled after electropolishing (AFN19, AFN21-26) was very similar to that for the samples chemically milled only. Following the electropolishing and chemical milling treatments, the surfaces contained etch pits revealing Heusler precipitates along crystallographic planes as well as preferentially etched subgrain boundaries (Fig 23). Again, some dark regions which were likely oxidized were not attacked by the etch as was the surrounding material (Fig 24). Some of the pitting appeared related to the porosity in some locations (Fig 25). There were also differences in the features on the curved surface, as shown by the light and dark regions in Fig 26. Other regions showed additional fine crack networks on both ends and curved surfaces (Fig 27). Again, some cracks were obviously widened and the tips blunted by either the electropolish or chemical milling (Fig 28). On each sample, there was usually some different surface feature resulting from either the electropolish or chemical milling treatments such as that for AFN23 shown in Fig 29.

Several replicate samples were polished by hand through 600 grit SiC paper to remove or reduce the wide spectrum of surface features resulting from the chemical milling treatment. This surface polishing resulted in fine polishing marks remaining on the surface (Fig 30). Some regions of the sample, particularly near the edges, contained larger scratch marks from coarser sanding papers which were not removed with the finer grit papers (Fig 31). Even with polishing, all surface features were not eliminated, such as the fine pores shown in Fig 32 and the larger pores and cracks shown in Figs 33,34. The ID of each sample was also polished through 600 grit SiC paper.

Burner Rig Testing

The samples were tested in a Mach 0.3 burner rig at the Lewis Research Center. A synthetic sea salt solution was injected into the burner to yield a concentration of 2 ppmw in the hot combustor exhaust. Each sample was positioned on an individual holder designed for the sample to operate at a nearly constant temperature with rapid heat-up and cool-down of the sample. In addition, the holders were designed to have a minimum of contact between the sample and small alumina rods in order to reduce the trapping of condensed salts. The samples and holders were fixtured on a twelve position carousel which rotated in the flame of the burner. Further details of the carousel and individual sample holders are given in Appendix A. The carousel was rotated at 250-300 RPM in the burner flame for 1 hr. After 1 hr, the burner was shifted away exposing the samples to a high velocity, ambient temperature air stream to cool the samples for a minimum of 6 minutes. An average sample temperature was continuously monitored using a two-color and laser pyrometer aimed at the rotating samples. A feedback loop was used to make fine adjustments in the fuel to air ratio in the combustor to maintain an average sample temperature of 900°C (1652°F). The accuracy of the pyrometer temperatures was checked with a short test run of a thermocoupled dummy sample prior to testing the NiAl samples.

Over the test duration of 300 hrs, differences in the pyrometer readings suggest an uncertainty in temperature of 15°C. The samples were removed following either five or ten cycles after cooling to be weighed. Occasionally the samples were submitted for x-ray analysis to determine surface scales and reaction products prior to additional testing. Further details of the burner rig operation including a schematic of the burner rig and the measured heating and cooling cycle are given in Appendix A.

Testing was performed in three series. The first series (Series I) was run with electropolished samples (AFN19, AFN21-26) for 180 cycles, although most samples fractured and were removed between 75 and 150 cycles. Whenever a NiAl sample fractured and was removed from the test, a dummy sample was substituted in that position to maintain the full carousel configuration. Series II included samples which were chemically milled only (AFN20, D218, D219) as well as samples which were electropolished and chemically milled (AFN19, AFN21-26) and was run for 300 1-hr cycles. Series III contained replicates of several alloys (AFN20, 23, 26, D218 and D219) as well as D218 and D219 samples with mechanically polished surfaces. Samples in Series III were run for either 150 or 300 cycles.

Results

Results for the electropolished samples (AFN19, AFN21-26) which were tested in Series I will not be discussed in the main body of this report since samples fractured at various times before 150 hrs. In addition, the weight change measured during Series I is not comparable to that for Series II and III due to the significant attack on the ID surface. However, in general, the corrosion morphology which developed during testing in Series I was similar to that of samples which were also chemically milled and tested in Series II. For comparison, the weight change and macrographs of select samples from Series I are shown in Appendix B. The following results will focus on results from testing in Series II and III which contained samples with the three surface conditions: electropolished followed by chemical milling (AFN19, AFN21-26), chemically milled only (AFN20, D218, D219), and mechanically polished following chemical milling (D218, D219).

Weight Change

The weight change measured at various intervals through 300 hrs for Series II is shown in Fig 35. AFN20 and D219, alloys with 5% Ti but no Cr, exhibited the highest weight gains. Alloys with high Ti levels but containing 1-2% Cr (AFN19, AFN21-26) resulted in consistently lower weight gains. D218 with low Ti (1%) and no Cr also exhibited a small weight change representative of good hot corrosion behavior. The sharp weight loss between 60 and 70 hrs for this sample was due to the loss of a chip from the edge of the sample (shown below in Fig 54c). The rapid weight gain of AFN25 after 150 hrs appears as an exception to the alloys containing both high Ti and Cr. However, as will be shown and discussed below, this high weight gain was due to very significant localized attack on one region of the curved surface and is likely the result of a compositional inhomogeneity on this sample. Using the behavior of D218 as a baseline, the weight change data indicate that increasing the Ti from 1% to 5% (i.e., going from D218 to AFN20 or D219) increases the susceptibility of these alloys to hot corrosion attack. However, the addition of 1-2% Cr to the high-Ti alloys (i.e., AFN19, AFN21-26) reduces the susceptibility of the alloys to hot corrosion attack. Stated otherwise, the addition of 1-2% Cr appears to negate the deleterious effect of the addition of 4-5%Ti on the hot corrosion resistance of these alloys.

Series II versus III

The weight change for most replicate samples during Series III were unexplainably greater than that for Series II (Figs 36,37). Only AFN23 showed a lower weight gain during Series III than that during Series II (Fig 36). However, the ranking of the alloys based on Ti and Cr content discussed above for Series II was consistent for Series III. Since three alloys and several replicate samples showed higher weight gains in Series III, it does not appear likely that the higher weight gains could be due to sample inhomogeneity although that appears to be the only reasonable explanation for the anomalous behavior of AFN23. Hence, the higher weight gains during Series III suggest a more severe test, although all measurable test parameters were identical. Consequently, comparisons between alloys will generally only be made within the same test series. Comparisons between test series will only be made to show that the increased weight gains can be directly correlated with the scale morphology. In these comparisons, the test series is clearly noted. It is noteworthy that if Series III was indeed a more severe test, D218, AFN23 and AFN26, which showed good resistance to hot corrosion attack, were not significantly affected.

Chemical Milling versus Mechanical Polishing

Mechanically polishing the surface of D219 through 600 grit SiC paper increased the time before the onset of rapid weight gain (Fig 38). Mechanically polishing the baseline alloy D218, which already exhibited good resistance to hot corrosion attack, had little effect on the weight change. Hence, mechanically polishing the surface appears to improve the hot corrosion behavior, at least for the alloys with poorer hot corrosion resistance.

X-ray Diffractometry of Surface Scales

X-ray diffraction of the ends and curved surfaces of many of the samples was performed after various exposures. No attempt was made to use the relative peak heights to quantitatively indicate the proportions of the various reaction products because of the curved surfaces and varying substrate crystal orientations. However, for some phases, the results are described qualitatively (i.e., strong, weak, trace) when possible. Oxide phases present on the samples tested in Series II for 300 hrs are shown in Table III. The main oxide phases present on surfaces were α-Al_2O_3, NiO, a spinel phase (a_o=8.05 to 8.30A), $Ca_3Al_2O_6$ (Al_2O_3•CaO) and HfO_2. At times, a single small peak indicating the presence of TiO_2 was detected. An unidentified peak was typically observed on the sample ends with d=3.73-3.82A and an intensity that ranged from 1-24% of the highest observed peak. Substrate peaks were often observed with some sample orientation but not others because of the random orientation of the single crystal samples. Typically, both ends of a sample gave similar results although the relative proportions of the phases were sometimes different. Also, in general, the rougher, more-attacked regions of a sample exhibited a higher NiO/spinel ratio in contrast to that in smoother regions which appeared less-attacked. At shorter times (e.g., 50 hrs), less NiO was observed in the scale and the spinel appeared to have a smaller lattice parameter of a_o=8.05-8.10A, typical of $NiAl_2O_4$. Similar oxides were present on most of the alloys, although one conspicuous difference was the absence of $Ca_3Al_2O_6$ on D218.

Surface and Scale Morphology During Testing

Two general types of corrosion morphology were produced on the surface, distinct mounds, and a uniform type of attack. Typically, the mound morphology appeared as small bumps, growing with time into larger mounds. These mounds often coalesced so that an entire region became raised. The uniform attack grew rapidly inward such that some of the cast dendritic features initially on the surface were evident even after 300 hrs of testing. On many samples, the degree of attack on one end of the sample differed significantly from the other end. In addition, the hot corrosion attack on the curved surface of many of the samples was nonuniform such that the degree of attack at different locations on the curved surface also varied strongly. Since the samples were inverted every 10 hrs and allowed to rotate by vibration on their individual holder, no specific orientation relationship between the sample and burner flame was maintained. Consequently, the differences within a particular sample are not likely related to the burner rig test procedure.

AFN19

The AFN19 alloy exhibited a minimal amount of hot corrosion attack on the surface consistent with the low weight gain during testing. A small number of corrosion "mounds" are shown on the ends and curved surface of the AFN19 sample in Fig 39. SEM micrographs of the end shown in Fig 39a reveal significant porosity and fine cracks in the outer (Fig 40b) and inner region (Fig 40c) which resulted from the electropolishing and chemical milling treatments. The radial location of the mounds on the ends (Fig 39a,b) do not suggest any increased tendency for formation in the inner region with the higher pore density or the outer region with the larger number of fine cracks. Moreover, it is noteworthy that this sample exhibited good hot corrosion behavior while containing significant pores and cracks. EDS spectra of the three regions numbered (1), (2) and (3) in Fig 40b are shown in Fig 41. The porous inner region (1) and the darker smooth scale (2) contain significant levels of Ca and Mg, and smaller levels of Ni, Si, O, Al and S. Fe, Cr, Si and sometimes Mn were also commonly detected on the surface. These elements are deposited onto the samples during hot corrosion testing by the deterioration of Fe-based alloys used in the burner and nozzle (Appendix A). Since many of the alloys contain 1-2% Cr, and all of the alloys contain small levels of Si, it is difficult to determine the source of the Cr and Si detected on the surface, whether from within the alloy or deposited from the burner. However, Cr and Fe were detected on the surface of D218, which contains no Cr. Hence, at least some Cr and Si deposition from the burner is likely when Fe is also detected. Surprisingly, no Na was detected on the surface of any of the samples. The EDS spectra taken from the top of the mound in Fig 40b (location 3) shows high levels of Al, Ni and Ca. The ratio of these elements was common for the top of mounds on many of the samples.

The angled view of the end of AFN19 shown in Fig 39b clearly shows that the corrosion mounds, indicated by black arrows, are not in regions of the highest porosity (Fig 42a). EDS spectra of smooth regions between the mounds again showed high Ca and

Mg peaks, but different from those in Fig 41 in that the Ni peak was significantly higher (Fig 42b,c). In most spectra, the Ca peak was substantially higher than that for Mg, however the ratio varied as shown in the EDS spectra in Fig 42b,c. The spectra in Fig 42d indicates an Al-rich oxide which, with the presence of Ni and Ca, is likely a mix of Al_2O_3, $NiAl_2O_4$ or $Ca_3Al_2O_6$. SEM micrographs of other regions on this end of the sample also show some porosity and elongated pores (Fig 43). EDS analysis of both the smooth regions and the "bumpy, nodular" morphology in Fig 43c exhibited almost identical spectra with high Ca and Mg concentrations similar to that for the porous region shown in Fig 41b. This bumpy, nodular morphology was very common on the surface of many of the samples. Magnified views of pores and cracks near the sample ID show that neither the pores or cracks display any tendency for enhanced corrosion attack (Fig 44).

The curved surface exhibited many of the same features as that on the ends. Porosity near both ends is shown in Fig 45a,c. EDS analysis of the scale in these porous regions again showed a high Ca level along with Al, Si and Ni peaks (Fig 46a). The spectra also indicates a higher Fe level in this region than that observed on the ends. The three large particles in Fig 45d are Fe and Ca-rich (Fig 46b) and have likely been deposited from the burner. A corrosion mound on the curved surface is shown in Fig 47. The two pores on the top of the mound (Fig 47b) indicate that the mound is growing inward with little disturbance to the outer surface apart from the outward displacement. The magnified view of the top of the mound (Fig 47c) shows oxide structures with very different compositions. The darker, continuous oxide (1) is Al and Ca-rich (Fig 48a), possibly $Ca_3Al_2O_6$. The light, round bumps (2) appear to be NiO (Fig 48b) while the light crystals near the bottom of the figure (3) are primarily Ni but with significant concentrations of Ca and Mg (Fig 48c).

AFN23

The AFN23 alloy also exhibited a low weight gain during testing similar to that for AFN19. However, the surface contained distinct regions which showed a different response to the hot corrosion attack. Optical macrographs of the end and curved surface of AFN23 after 300 hrs of testing are shown in Fig 49. The end shows more corrosion mounds on one half than the other (Fig 49a) while the two regions can also be discerned on the curved surface (Fig 49b). EDS analysis of the "smoother" region (1) in Fig 49c showed significant concentrations of Ca, Ni, Fe and Al, similar to the spectra shown in Fig 42c but with the height of the Fe peak between that of the Ni and Al peaks. The smooth mounds in the magnified view of the "rougher" region (see arrows in Fig 49d) are NiO.

AFN24

As previously mentioned, the two ends of the AFN24 sample were significantly different after electropolishing and chemical milling (Fig 10a,b). One surface appeared rough and shiny while the other exhibited the flat matte finish. Not surprisingly, the two ends responded very differently during hot corrosion testing with the originally rough but shiny end undergoing accelerated attack. Optical macrographs of the ends and curved surface are shown in Fig 50. Magnified SEM views of the rough end are shown in Fig 51. EDS spectra for the small bumpy nodules in Fig 51c are similar to those previously shown for scales with a similar morphology (see Figs 43 and 41b). The composition of the darker scale atop the mounds was also similar to that measured on the mounds in AFN19 (Figs 40c and 41c).

AFN25

The high weight gain of this alloy after 150 hrs can be attributed to a significant but localized attack on one region of the curved surface. This particular sample had several flat and beveled regions on the surface from the edge of the ingot or where mechanical samples had been cut from the ingot at GEAE (Fig 11). One of these flat regions appeared shiny in contrast to the flat matte finish on most of the sample (see arrow in Fig 11b). Macrographs of this sample after 200 hrs of testing are shown in Fig 52. Accelerated localized attack on one of the flat surfaces is apparent (Fig 52d) although other flat or beveled regions on the surface showed essentially no unusual or accelerated attack (Fig 52c). The ends of the sample showed only a small amount of attack (Fig 52a,b). The nonuniformity of the attack on the curved surface continued through 300 cycles, as shown in Fig 53. Again, it is significant to note that the flat region which had the shiny, metallic appearance prior to testing (Fig 11b) showed no indication of the accelerated localized attack (see arrow in Figs 52c and 53a). Furthermore, not all flat regions on the curved surfaces of other samples underwent accelerated attack. Hence, although the surface is obviously important, the appearance of the surface, whether shiny and metallic or flat matte, does not necessarily indicate the hot corrosion response. It is likely that some compositional inhomogeneity, produced during casting, resulted in the different surface appearances on AFN24 and AFN25 after chemical milling. It is also likely that compositional inhomogeneities resulted in the nonuniform accelerated attack on the bottom of AFN24 and the curved surface of AFN25. However, experience with AFN25 has also shown that an unusual response of the surface to the chemical milling treatment does not necessarily indicate an unusual response of that surface to hot corrosion testing.

D218

The D218 alloy exhibited a minimal amount of hot corrosion attack on the surface and a low weight gain similar to that of AFN19. The limited number of corrosion mounds on the ends and curved surface are shown in Fig 54. The chip missing from the edge of the sample in Fig 54c is the cause of the weight decrease between 60 and 70 hrs shown in Fig 35. The only peculiar surface morphology change with this sample was the disproportionate attack at the ID and OD edges which resulted in the formation of a corrosion product "lip" (Fig 54a,b). A magnified view of the end of the sample and the "smooth" oxide in the center of the end is shown in Fig 55. The EDS spectra of this scale is nearly identical to that shown in Fig 46a only with a slightly higher Al peak suggesting this smooth scale is $Ca_3Al_2O_6$. The corrosion mound and part of the lip shown in the box in Fig 55a is shown at higher magnifications in Fig 56. The backscattered electron (BSE) image in Fig 56c clearly shows the cracks near the edge resulting from the growth of the lip as well as bright regions associated with oxides formed with high atomic number elements. The smooth, darker oxides in Fig 56b (point 1 in Fig 56c) are Al-rich with smaller concentrations of Ca and Ni, such as that shown in Fig 42d, and likely contain Al_2O_3, possibly mixed with some $NiAl_2O_4$ and $Ca_3Al_2O_6$. The bright oxides in Fig 56c (point 2) are Ni-rich, most likely NiO, with some locations containing small concentrations of Al, Cr and Ca. The top of the mound (point 3) again contains comparable amounts of Al and Ni, similar to the EDS spectra shown in Fig 41c suggesting the oxide is primarily $NiAl_2O_4$. The bumpy nodules (point 4) in the figure are again Ca and Al-rich, with nearly equal peak heights.

AFN20

The chemical milling treatment resulted in one end of the AFN20 sample being rougher than the other. Like AFN24, the corrosion morphology on each end was also different, apparent after only 50 hrs. The different corrosion morphology on the two ends after 100 hrs is shown in Fig 57. This morphology coarsened with time as shown after 200 and 300 hrs in Figs 58 and 59. It is interesting to note that although the mounds have grown slightly larger, there was no significant increase in the number of the mounds from 100 through 300 hrs. This behavior, that mounds which formed after short exposures only coarsened and coalesced with time without new mound formation, was typical on all the alloys. Nonuniform attack on the curved surface is shown after 200 hrs in Fig 58c,d. Although there is a noticeable increase in the size of the mounds and raised corrosion region after 300 hrs, again, there is no significant increase in the number of mounds or spread of the raised region on the curved surface between 200 and 300 hrs (compare Figs 58c,d and 59c,d). The somewhat parallel, raised lines in Fig 58c appear related to some dendritic structure. The lines are still visible after an additional 100 hrs (Fig 59c) indicating that, as stated earlier, the corrosion attack is by growth inward. Magnified views of the rough end of the sample (Fig 59a) are shown in Fig 60. The EDS spectra of the bumpy oxide in Fig 60c is Ca-rich, similar to that previously shown in Fig 46a. The smooth oxide in this figure is Al-rich with significant Ni and Ca similar to that in Fig 41c suggesting $NiAl_2O_4$ and/or mixtures with $Ca_3Al_2O_6$. The magnified view of the top of a corrosion mound in Fig 61a and the various contrasts in the BSE image of the same view given in (b) indicate the variety of oxides at the top and surrounding the mound. EDS analysis shows that the bright region (point 1) in Fig 61b is HF-rich, presumably HfO_2. EDS analysis of the light gray oxide near the top of the figure (point 2) shows only the presence of Ni and O, indicating NiO. The EDS spectra of the area indicated as point 3 also indicates NiO, but with the presence of Mg and Ca. The EDS spectra of the darker oxide on top of the mound (point 4) is shown as Fig 61c and indicates a high level of Al but also substantial quantities of Ca, Ni and Ti. A lower magnification SEM view of the smoother end of the AFN20 sample (Fig 59b) is shown in Fig 62. The appearance of the scale morphology is similar to that previously observed on other alloys with much better hot corrosion behavior (Figs 49a, 52a). EDS analysis of the oxides and mounds were similar to that already described.

Magnified views of the corrosion morphology on the curved surface of the AFN20 sample are shown in Figs 63 and 64. Fig 63 shows the rough, heavily attacked, left end of the sample shown in Fig 59c. EDS analysis of the scale shown in Fig 63c shows the typical Ca-rich oxides with a significant level of Al and lesser amounts of Fe, Ti, Ni Si and S, closely resembling that shown in Fig 46a. Fig 64 shows the surface near the center of the sample shown in Fig 59c at the edge of the heavily attacked "rough" and less-attacked "smooth" region. The "ledge" type structure shown in Fig 64b (area 1) shows a fine structure similar to the etched and chemically milled surface, such as that shown in Figs 17a,c and 24a. The EDS spectra for this ledge is high in Al and Ca similar to that in Fig 42d, only with the addition of substantial Fe and Si. An unidentified oxide appears to be growing out of cracks in the plates (see arrows). The brightness of the oxide suggests NiO which is an outward growing oxide. Dotted across the side of the corrosion mound are dark plates, as shown in Fig 64c,d. EDS analysis of the plates showed that they were high in Ca and Ti with smaller amounts of Al and Ni and a trace of Hf (Fig 65). This is the only alloy in which these Ti-rich plates were observed. Figure 66 shows the scale in the less attacked, "smooth" area of the sample (right end of Fig 59c,d). The EDS spectra (Fig 67a) of the large nodule/particle shown in (c) indicates a high Ca content, as well as significant S, Fe and Ti. The presence of Ca, S and Fe suggest that the particle may have been deposited on the surface rather than grown as a result of corrosion although the significant Ti level suggests a reaction with the alloy. The two smaller mounds in (b) and (d) suggest an inward growth process is occurring causing the outward projection of the mound. Since all indications are that the corrosion reaction proceeds inward, it is not surprising that the EDS spectra of the surface of the small mound shown in (d) (Fig 67b) appears similar to that of the nodule/particle shown in (c) (Fig 67a). Chemical inhomogeneity appears the only reasonable explanation for the rampant attack on only a portion of this sample.

D219

The corrosion morphology on one of the D219 samples (D219A) was very similar to that on AFN20, including the nonuniform attack on half the sample (Fig 68). However, both ends of the second D219 sample (D219B) appeared similar and the attack on the curved surface was also more uniform and not as swollen as the raised region on D219A (Fig 69). Magnified views of the scale morphology were also similar to those previously shown. Fig 70a shows a magnified view of the top of a corrosion mound (dark) on the rough end (Fig 68a) of D219A. The contrast in brightness in the BSE images (Fig 70b,c) shows that the top of the mound consists of a variety of oxides. The EDS spectra of the darkest oxides (e.g. Point 2) show that these oxides are Al-rich, presumably being primarily Al_2O_3. The EDS spectra of the somewhat less-dark oxide in Fig 70c (point 3) contains primarily Al and a Ca peak half as high as that for Al suggesting $Ca_3Al_2O_6$. The light gray scale (point 4) contains Al and a Ni peak half the height of the Al peak, a ratio indicative of $NiAl_2O_4$. EDS analysis of the bright oxide (point 1) to the right of the mound in Fig 70b shows that this oxide is Ni-rich, presumably NiO. In general, for SEM micrographs taken of the surface scales and with polished cross sections, HfO_2, which was infrequently observed in large amounts, was very bright, Al_2O_3 was the darkest oxide, NiO was much lighter, and $NiAl_2O_4$ had a brightness between that of NiO and Al_2O_3.

Chemical Milled Versus 600 grit SiC Polished Surfaces

There were significant differences in the hot corrosion response between samples which were chemically milled and those mechanically polished through 600 grit SiC paper. The lower weight gain of the mechanically polished samples (Fig 38) is reflected in the corrosion morphology after 50 hrs, as shown in Figs 71 and 72. Small distinct mounds are apparent on the surface and ends although one of the samples (D219F) exhibited a localized, scaly reaction product on one portion of the curved surface (Fig 71c) The growth of the corrosion mounds after 300 hrs on D219E is shown in Fig 73. In contrast to the mechanically polished samples, most of the surface of the chemical milled samples showed a relatively uniform and continuous attack (Figs 74, 75) although one end of D219D exhibited the distinct mound formation (Fig 74a). The uniform attack on the curved surface of the chemically milled samples shows the cast dendritic structure in relief (Fig 75c), again indicating that the growth of the hot corrosion attack is inward. Although the uniform attack gives an appearance as being less severe than the large, distinct mound formation, the depth of the attack was sufficient that after only 100 hrs, large, relatively thick corroded layers began to spall from the curved surface (Fig 76). Some of the cast dendritic structure is still apparent in the intact surface (Fig 76d).

Series II versus Series III

The weight change data showed that most alloys gained more weight during testing in Series III than that in Series II. AFN23 was the single exception to this observation while D218 showed no significant difference between Series II and Series III, exhibiting low weight changes during both. Although the difference in weight change was difficult to relate to the surface morphology on the D219 and AFN20 alloys which underwent significant attack during both series of tests, the difference could be observed in other alloys. Greater attack is evident on the AFN26 alloy after 300 hrs in Series III than Series II (Fig 77). The cause of the higher weight gain for AFN23 during Series II is less obvious. During Series II, this alloy had many small mounds on the end but also a localized region of heavier attack on the curved surface. During Series III, large, more distinct mounds were formed on the sample ends, however no accelerated attack was evident on the surface (Fig 78).

Evolution of the Corrosion Mounds

The corrosion mounds appeared at short times and grew with additional testing although few new mounds were initiated after 50-100 hrs. Most of the mounds on the end of D218B can be discerned after only 50 hrs, as shown in Fig 79. A single mound growing at a crack is apparent at 200 hrs but not at 100 (see arrow in Fig 79b,c). Most mounds are not apparent after 50 hrs in D218D which had been mechanically polished (Fig 80). However, all of the mounds visible after 300 hrs are visible after 100 hrs. These observations for D218B and D218D suggest that the surface finish may be affecting the initiation of the corrosion mounds. In D219, with a poorer corrosion behavior than that of D218, the mounds are clearly apparent after 50 hrs and grow through 300 hrs, however without any observable increase in the number of mounds (Fig 81). Both the growth of distinct mounds and the more uniform attack is evident for AFN20 in Fig 82. Even after 150 hrs, the uniform attack (Fig 82d-e) has grown but has not spread to the edges of the sample. Hence, it appears that the corrosion attack on most samples is initiated at very distinct locations and at short times with little additional attack initiated with further testing.

Soluble Reaction Products

Water soluble reaction products on several samples tested in Series II were examined by ICP emission spectroscopy. The samples were boiled in deionized water for two hrs to dissolve the water soluble reaction products. The results for elements detected in excess of 0.1 μg/ml are shown in Table IV. Only relative comparisons between samples and elements have been considered. Somewhat surprising, the Ca concentration is significantly higher than that of either Na or Mg, consistent with the EDS data. It is also interesting that Si is at a much higher level than that of either Al or Cr, and that Ni, Hf and Fe, although detected on the surface by EDS, were not in the soluble reaction product. In addition, Cr was detected on D219, D218 and AFN20, all alloys not containing Cr. Hence, some or all of the soluble Cr may have been deposited from the burner or nozzle. The Sr is a common impurity in Ca, although a separate ICP analysis of the sea salt did not detect this element. The source of the B is unknown. Although the concentration of all elements shown in Table IV was greatest for D219, which showed the highest weight gain during testing, AFN20, which showed the second highest weight gain and behaved similar to D219, does not show the second or even the third highest concentration for any element. Hence, there is no apparent correlation between the weight change or hot corrosion behavior, and the concentration of soluble reaction products.

Microstructures

Attack Initiation

There were regions on each of the samples where localized attack (i.e., pits) had not initiated. In these regions, the scale microstructures showed many common features between the various alloys. SEM micrographs of this "pre-initiation" scale on D218 and D219, which exhibited good and poor corrosion behavior, respectively, are shown in Fig 83. EDS spectra at various locations indicate that these scales are rich in Al with smaller concentrations of Ti, Ca and sometimes Hf (Fig 84). On alloys containing large amounts of this "pre-initiation" scale (e.g., AFN19), the diffractometry results, taken together with the EDS results, suggest that the "pre-initiation" scale is primarily Al_2O_3 with smaller amounts of $Ca_3Al_2O_6$. However, no $Ca_3Al_2O_6$ was detected on the surface of D218 suggesting that any CaO present in the scale was at a level too low to be detected. Although Ti was commonly detected by EDS in the "pre-initiation" scales on the alloys containing higher Ti levels (e.g., Fig 84d,e), TiO_2 was only detected by x-ray diffraction at trace levels on about half of the samples. The concentration of Ca was typically higher in the outer half of the scale (compare Fig 84d,e). A small Mg peak was often associated with a high Ca peak. Foreign deposits containing Fe, Ni, Cr, Si and Mn from the burner and nozzle were often observed on the surface of the scales (point 3, Figs 83d and 84c). Even where no surface deposits were observed, it was common to detect some of these elements in the outer portion of the scale (Fig 84a). Sulfur was occasionally detected very near the gas surface in the scale generally when significant Ca levels were observed (Fig 84a,d).

The bright oxide particles within the Al_2O_3 are Hf-rich and presumably HfO_2. This oxide was detected on the surface of most of the samples by x-ray diffraction. The Hf in these alloys is preferentially oxidized before the Al and Ti but is in insufficient concentration to form a continuous scale. The oxide fingers reaching into the substrate are also HfO_2 (bright) which are often encased in Al_2O_3 (dark). The formation of oxide stringers is common in high-temperature alloys containing small quantities of a reactive element, such as Hf, Zr or Y. Larger and more developed stringers were observed during the cyclic oxidation of these alloys at 1100°C.[6] The development of the stringer morphology in these alloys was previously discussed,[6] however, it is important to note that oxygen readily travels down the porous and fine-grained HfO_2 cores of the stringers.

Although samples were not metallographically examined after various exposures, certain oxide morphologies on each of the samples suggest the microstructural evolution leading to attack initiation. Figure 85a shows a location where the inner portion of the scale (containing the HfO_2 particles) has grown thicker resulting in the start of a small mound. The scale has also cracked on both sides of this mound. It is not known whether the scale fractured first causing the inner scale to thicken, or whether the outward growth of the mound caused the scale to fracture. Figure 85b and c show two other possible initiation morphologies, the former with a "bulb" type pit and the latter with a much broader, shallow pit. The external scale appears intact over both initiation sites. The EDS spectra taken within the "bulb" pit (Fig 85d) indicates the same elements as in the "pre-initiation" scale, including Ca (Fig 84b and e). Bright Hf-rich precipitates are present just below the pit, with a broader band nearly depleted of precipitates below these bright precipitates (Fig 85c). The precipitates characteristic of the unaffected alloy are visible in the lower twothirds of this figure. Bright Hf-rich precipitates above bands nearly depleted of precipitates was a common feature below many of the pits.

Two additional broad, shallow pits are shown with EDS spectra in Fig 86. The first pit appears sunken but contains burner deposits on the surface indicating that this was, at some time during testing, the external surface. The oxide in this pit is again Al-rich with some Ca, Ti and a trace of Ni (Fig 86c). The outer surface of the second pit is slightly raised and shows the original outer scale with the bright HfO_2 line. This pit also shows some cracking to the left of the pit. Again, it is unknown when this cracking occurred, and no cracks appear on the right half of the pit. The composition of this pit shows the typical Al and O with a small amount of Ti but surprisingly no Ca (Fig 86d).

The elemental distribution in one of the shallow pits in D218 is shown in the x-ray maps of Fig 87. The pit is primarily Al and O (Al_2O_3) with Ca penetrating throughout the pit. There is a Cr enrichment on the outer surface, but no significant enrichment of other measured elements. Although a Ti map was not produced, concentration measurements shown in the following figure (Fig 88) indicate a Ti concentration in the pit slightly less than 1%, approximately that initially in the alloy. The Al map indicates that there is a small depletion of Al from a layer approximately 30 microns thick below the pit. Concentration measurements made in this region by EMP show a decrease of 6% Al from point e to point c (Fig 88). The Ti concentration in the pit is slightly less than that in the alloy with an indication of a slight buildup of Ti in the alloy just below the pit. These measurements indicate that Al is preferentially oxidized to a slightly greater extent than is Ti causing some Ti to diffuse away from the growing pit. There is also a slight Hf concentration gradient towards the pit indicating the preferential oxidation of Hf. Calcium concentrations in the pit were measured at a level less than 0.3%.

The more complete x-ray maps of a small mounded pit in AFN19 (Fig 89) show many similarities to the elemental distributions for D218. The pit is primarily Al and O (Al_2O_3) with Al_2O_3 concentrated at the base of the pit. Ca is present throughout the pit but is enriched on the surface and at the base. Ti is also present throughout the pit and appears correlated with the Al. Cr, present in AFN19 at a level of only 1%, is also present within the pit but is mildly enriched above the Al_2O_3 base. Ni, like the Cr, is present near the center of the pit. The S maps show no enrichment within the pit but only on the outer surface. Si is enriched in the alloy below the pit, and also on the surface but not within the pit. Enrichment of Si and Ti in Heusler and/or NiTiSi particles is evident in the alloy below the pit. The Na map shows that Na is present within the pit. Na was only detected by WDS using the electron microprobe and not EDS because of the low concentrations.

A deeper pit in D218 is shown in Fig 90. A close examination of the alloy microstructure below the pit indicates two bands where the fine Heusler precipitates have changed. This change in microstructure denotes the diffusion-affected region which is twice the depth of penetration of the pit. The magnified view shows an oriented growth of oxide fingers at the bottom of this pit (Fig 90b). The bright cores of these fingers suggest the preferential oxidation of Hf from the Hf-rich Heusler particles aligned along certain crystallographic planes. The continuation of the aligned HfO_2 lines within the primarily Al_2O_3 pit is also apparent. Fine bright lines of presumably HfO_2 in a pattern typical of the Heusler particles in the alloy were commonly observed in other pits in many of the alloys. This observation suggests that the Heusler particles oriented on the specific crystallographic planes are not dissolving prior to being oxidized below growing pits. The aligned oxide fingers below the pit shown in Fig 90b were not uncommon, although the majority of the pits did not show the aligned fingers.

Similar morphologies of possible initiation sites were observed on the high-Ti alloys with and without Cr. Fig 91a shows a small pit on AFN19 similar to that shown in Fig 85b. In Fig 91b, the scale on D219 appears to be thickening both above (point 2) and below (point 1) the bright line of HfO_2 particles. EDS spectra of these two regions show the typical Al- and O-rich scale containing a small amount of Ti and Ca with the Ca/Ti ratio greater in the outer region of the scale (point 2), similar to that observed on D218 (Figs 83 and 84). Pit initiation and the start of small mounds on AFN20 are shown in Fig 91c,d. EDS measurements at the positions indicated by the arrows show similar Al, O, Ti and Ca peaks as previously shown. No γ' phase was observed around any of the small initiating pits.

Intermediate Attack

As the corrosion pits grow, islands of the more-noble Ni are incorporated into the corrosion product. This stage of attack is considered as "intermediate" between the initiation stage and the rampant attack discussed in the following section. Micrographs showing regions of intermediate attack on D218 and D219 are shown in Fig 92. Each of these attacked regions contain islands of relatively pure Ni, either metallic or oxidized. The band of bright Hf-rich precipitates and the precipitate-free band are evident below several of the corrosion pits. EDS analysis of the very bright particle in Fig 92b showed only Hf peaks, implying Hf carbide. Elemental distribution within the attacked region in Fig 92a is shown by the x-ray maps in Fig 93. These maps show that Cr is enriched only on the surface. Calcium is also enriched on the surface but also in the rightmost region of the pit which contains primarily Al and O (Al_2O_3). Both Ti and Si are associated with the Al_2O_3 but are slightly enriched in the lower half of the pit. Hafnium again shows no significant enrichment. Quantitative EMP measurements were made at the points labeled "a" through "e" in Fig 93a. The results show that points a and c are Al_2O_3, with approximately 0.2% Ca at point a but no Ca at point c. The Al_2O_3 contains approximately 0.4-0.8% Ti. The oxide at point b, slightly lighter than the Al_2O_3, has the composition of $NiAl_2O_4$. The bright constituent at point d is metallic Ni with less than 1% other elements.

The pit in AFN19 shown in Fig 94 appears near the transition between initiation and intermediate attack. Although no Ni islands are apparent, the associated x-ray maps show that there is significant Ni within the center of the pit. Like the pits in the initiating attack stage, this pit is primarily Al and O (Al_2O_3) with Ti largely associated with the Al. Ca is again present throughout the pit. Chromium, appears present but not enriched within the pit. The slight Cr enrichment on the surface may be due to deposition from the burner, as observed for D218 (Fig 87). The S and Si maps show an enrichment on the surface but not within the pit. The Na map shows that there is a small presence of Na throughout the pit. It is interesting that Ca is present throughout this pit where Ni appears finely mixed with the Al_2O_3 in contrast to the lack of Ca in the more advanced pit in regions containing Ni, NiO and $NiAl_2O_4$ (Fig 93).

Figure 95 shows other regions of intermediate attack on D219. The NiO trapped in the corrosion product is indicated in Fig 95b. The darkest oxide (points 1 and 3) is again presumably Al_2O_3 based on the EDS spectra with the usual peaks for Ti and Ca. It is interesting that the Ca is detected far within the pit (point 1). Surrounding the NiO is an oxide with an intermediate brightness (point 2). The EDS spectra for this oxide (Fig 94d) indicates the presence of $NiAl_2O_4$ with small additions of Ti and Ca. Fig 96 shows an additional region of intermediate attack on D219. The magnified views show the formation of a lighter phase at the oxide/metal interface (Fig 96b) and the bright HfO_2 particles in the oxide and also in the alloy (Fig 96c). The size of the lighter phase adjacent to the oxide in Fig 96b did not allow for accurate EDS analysis due to beam overlap with the surrounding oxide and metal, however, the phase is likely γ' based on the appearance and location. Formation of γ' adjacent to the oxide, such as shown in Fig 96b, was rare. However, γ' was commonly observed undergoing discontinuous precipitation in front of the advancing corrosion product, as will be shown below.

Regions of intermediate attack in AFN20 are shown in Fig 97. The magnified view of the bottom of a pit (Fig 97d) shows a second oxide with a lighter shade of gray mixed with the darker Al_2O_3 scale. EDS analysis indicates that this lighter oxide contains significant Ti and is likely either TiO_2 or a mixture of TiO_2 and Al_2O_3, possibly containing some HfO_2. This fine, light and dark structure within the Al_2O_3 was common. The x-ray maps in Fig 98 of the corrosion mound shown in Fig 97a clearly show that Ca is distributed throughout the mound. Cr is again enriched on the surface and Hf is enriched near the base of the mound with some HfO_2 fingers, slightly discernible, penetrating into the alloy. The Ni map indicates a small region of NiO in the center of the mound surrounded by a Ni- and Al-rich oxide, presumably $NiAl_2O_4$. Ti is present with the Al_2O_3 throughout the mound and appears slightly enriched in the alloy below the mound . Quantitative probe measurements were made at the points indicated as a-e. All points show primarily Al_2O_3 with varying amounts of Ni, Ti and Ca, and reflect the enrichments and depletions shown in the maps.

The x-ray maps in Fig 99 of the box shown in Fig 97b show the preferential growth of the HfO_2/Al_2O_3 stringers. The discontinuous precipitation of γ' in the β matrix is also apparent. Quantitative probe measurements at the points a-g are shown in the accompanying table. The γ' precipitate indicated at point f has an Al and Ti content of 17.1% and 8.7%, respectively (i.e., $Ni_3[Al,Ti]$). The corrosion pit shown in Fig 100 is a magnified view of that shown in Fig 97c. The EMP concentration profile in the alloy below the pit shows slightly decreasing Al concentrations toward the pit. As previously seen (Fig 88), the Ti is slightly rejected from the pit resulting in a small concentration decrease from the pit into the alloy (within 15 microns of the pit). Although distinct diffusion bands with and without precipitates were observed below this pit, there were no obvious concentration differences within these bands other than the slight concentration gradients mentioned above.

Rampant Attack

Rampant attack exhibited a fairly characteristic microstructure on each of the alloys. This attack morphology always consisted of rapid inward penetration of Al_2O_3 stringers trapping large amounts of Ni within the scale. The Ni was typically depleted of Al and had transformed to either γ' or γ. Regions of rampant attack on D218 and AFN19 are shown in Fig 101. The magnified views show that the depletion of Al has resulted in the formation of γ' (Fig 101b,d). Some γ was also observed near the oxide/γ' interface (Fig 101d) or well within the attacked region. Often the Ni islands had been oxidized to NiO in the outer portion (nearer the oxide/gas interface) of the attacked region. The γ'/β interface shows a feathery γ' phase penetrating into the β in Fig 101d. The light and dark oxide striations are also evident in much of the oxide in this figure. Elemental distributions in the region of Fig 101d is shown in the x-ray maps in Fig 102. The striated oxide is primarily Al and Ti with a small presence of Cr. Regions of γ and γ' can be distinguished from the Al map. Not surprising, the Ti partitions to the feathery γ' below the oxide phase. It is significant that there appears to be no enrichment of Ca, Si or Na in the x-ray maps of Fig 102.

Regions of rampant attack on D219 and AFN20, which exhibited poor overall corrosion behavior, are shown in Fig 103. The magnified view of the inner region of attack in (b) shows the γ and γ' phases. The lighter and darker oxide in this image has a mottled appearance rather than the striated appearance of that in Fig 101d. Elemental distributions in an attacked region of AFN20 are shown in the x-ray maps in Fig 104. Again, most of the oxide is Al-rich (Al_2O_3) with lower concentrations of Ti. A close examination of the Ni and O maps show that many of the Ni islands in the attacked region are metallic with smaller NiO islands in the outer portion of the attacked region. Ca and Cr appear enriched only on the surface. The higher magnification maps of the inner attacked region shown in Fig 105 clearly show the depletion of Al and the association of Ti and Al in the oxide. The concentration profile in this figure clearly shows an Al gradient in the β phase indicating Al transport towards the oxide. There is also a small Ti gradient in the β phase which indicates Ti transport towards the γ' phase and oxide. There are no apparent compositional differences in the inner region of rampant attack between the AFN19 (Fig 102) and AFN20 (Figs 104,105) although the overall corrosion behavior of the alloys was significantly different. Figure 106 shows regions in AFN19 which appear to be in transition from intermediate to rampant attack. Oxide fingers are penetrating into the alloy, however isolated γ' precipitates are still present below the oxide fingers. Some of the oxide shows the dark and light striations whereas other regions appear mottled.

Oxidation of one of the large Heusler particles at the inner region of rampant attack on AFN20 is shown in Fig 107. It is interesting that although the particle is enriched in Hf, the particle is not being oxidized more rapidly than the surrounding β phase. EDS measurements of the oxide in the particle yielded significant Al, Ti and Hf peaks. Other partially oxidized Heusler particles were observed but also showed no tendency for accelerated oxidation. Observation of a large, oxidized Heusler particle at the surface did indicate that some of the oxide had grown outward which could be the result of the oxidation of Ti from the particle.

Discussion

It is clear from the weight change data that increasing the Ti concentration from 1% in D218 to 5% in AFN20 and D219 significantly degrades the hot corrosion resistance of this material. Although the weight change of D219 is somewhat greater than that for AFN20 in Series II, the weight change for both alloys during Series III is similar indicating the difference in Ga content between the two alloys (0.05 to 0.2%) appears of little consequence. Other comparisons between the better alloys indicate that Ga plays an insignificant, or minor role in the hot corrosion resistance. However, comparisons between AFN19, AFN21 and AFN22, each of which exhibited a similar, low weight change during Series II testing, indicate that 1% Cr is able to compensate for the deleterious effect of Ti additions of 4-5%. Hence, it can be concluded that alloys containing only 1%Ti (e.g., D218) showed a low susceptibility to the hot corrosion test performed in this study.

Considering the behavior of D218 as the baseline, increasing the Ti content to 5% (e.g., AFN20, D219) significantly degraded the hot corrosion resistance in comparison to the baseline, while the addition of 1-2% Cr to the high-Ti alloys again restored the hot corrosion resistance to the level of the baseline.

Mechanically polishing the surface of D219 improved the hot corrosion behavior over that of the chemically milled D219 samples. This improvement was primarily in delaying the rapid weight gain of the mechanically polished samples for approximately 100 hrs over that of the chemically milled samples (Fig 38). This delay suggests that the mechanical polishing treatment delayed initiation of the hot corrosion attack. However, figures of the samples after 50 hrs showed that distinct mounds had formed even after 50 hrs and that no new mounds were apparent with further testing (Figs 72, 73). It is clear that the mechanical polishing favored discrete corrosion mound formation over the more uniform type of attack morphology observed on the chemically milled samples. It is also clear that the rate of weight gain is initially lower for the mechanically polished samples. However, after approximately 200 hrs, the rate of weight gain for the mechanically polished samples appears roughly the same as that of the chemically milled samples (Fig 38). The cause for the change from the uniform type of attack morphology to the mound formation following mechanical polishing is unclear. It is not known whether the mechanical polishing further removed damaged surface layers from the EDM process, or whether the polishing removed some detrimental effect of the chemical milling treatment. It would be interesting to test additional samples which were mechanically polished directly after the EDM treatment (not following chemical milling as in the present case) and also to chemically mill samples following mechanical polishing. This additional testing could better isolate the beneficial effect of the mechanical polishing, and indicate whether the chemical milling treatment merely fails to adequately remove the detrimental effect of the EDM process, or whether the chemical milling treatment itself degrades the corrosion resistance of the surface.

No significant difference was observed between the mechanically polished and chemically milled D218 samples within the 300 hr test period. It is possible that mechanical polishing had improved the corrosion resistance of the D218 alloy although the testing time was too short to observe the benefit in this alloy which exhibited good corrosion behavior. It would also be interesting to test both chemically milled and mechanically polished D218 samples for longer times to see if rapid weight gains on the alloy eventually occurred.

The baseline alloy, D218, with low Ti and no Cr, obviously responded differently to the chemical milling treatment than the alloys containing higher Ti levels. For the high-Ti alloys, the addition of Cr appeared to make little difference in the response to the chemical milling treatment. However, certain regions on several samples showed significant differences in both the response to the chemical milling treatment and in the hot corrosion response. One such sample was AFN24, shown after electropolishing and chemical milling in Fig 10 and after 300 hrs of testing in Fig 50. Since other samples did not show this significant difference in the surface after electropolishing and chemical milling, it is not thought to be a consequence of the processing but of a chemical inhomogeneity in the sample. In this sample, the shiny, bumpy end following chemical milling (Figs 10a and 50a) showed poor hot corrosion resistance. In contrast, the shiny, flat surface after chemical milling the AFN25 sample (see arrow in Fig 11b) did not show any indication of increased hot corrosion attack after 300 hrs (see arrow in Fig 53a). However, one of the other irregular surfaces on the curved surface of AFN25 which exhibited the typical flat matte finish after chemical milling, did undergo severe hot corrosion attack (Fig 53b). Hence, the different responses of a surface to the chemical milling treatment do not necessarily indicate the hot corrosion resistance. It again appears most likely that chemical inhomogeneities within the sample may be the cause for the widely different hot corrosion response on the same sample. Widely different responses to hot corrosion on the same sample was observed with numerous alloys (AFN20, Fig 59, Fig 82; D219A, Fig 68; AFN26, Fig 77d,e; to a lesser extent on D219B, Fig 69). Compositional inhomogeneities in AFN23 tested in Series II appears the only reasonable explanation for the anomalous behavior of this alloy which exhibited a higher weight gain in Series II than in Series III. The scale morphology of this alloy did show a localized accelerated attack on part of the curved surface during Series II testing.

Corrosion Morphology

Two general types of corrosion morphology were produced on the surface, distinct mounds, and a uniform type of attack. The distinct mound formation is typified by the mounds shown on D219E after 50 hrs of testing in Fig 72 and after 300 hrs in Fig 73. The surprising feature of this type of attack is that although the mounds grew and coalesced with time, there is little indication of attack between the mounds, nor the formation of new mounds with additional testing. This feature was typical of the alloys which exhibited the distinct mound morphology. Since sea salt was continuously deposited during the test, it is curious that mounds were not continuously formed unless mound formation could occur only at select sites on the surface. Hence, mounds may have been initiated at most of these sites within the first 50-100 hrs. The surface contained many imperfections, such as cracks, pores and pits. However, the mounds did not show a preference or partiality for formation at these defects. Hence, it is possible that the mounds were initiated at a chemical inhomogeneity at or near the surface rather than some irregular surface feature. The presence of large Heusler particles near the surface are not believed to initiate mounds for several reasons. The large Heusler particles were not observed in D218, although mounds were observed on this alloy. The number of mounds formed on the surface of many of the alloys far exceeded the abundance of the large Heusler particles. Lastly, the large Heusler particles showed little tendency for accelerated attack over the β phase (Fig 107).

The uniform attack morphology was observed primarily on the two alloys with the poorest corrosion behavior, AFN20 and D219, but to a lesser extent on other alloys. The entire D219C sample showed this type of attack in Series III, as shown in Figs 75 and 76. However, D219D, also tested in Series III, only showed this uniform type of attack on the curved surface and on one end (Fig 74b,c). The other end showed the typical mound formation (Fig 74a). Other D219 and AFN20 samples tested in Series II also showed this form of attack on all (D219B, Fig 69) or some surfaces (AFN20, Fig 58a,d; D219A, Fig 68a). In addition, the morphology on portions of samples with better corrosion behavior also showed what appeared to be this type of attack (AFN23, Fig 49a and region 2 in Fig 49b; AFN26, Fig 82d-f). It is clear that some samples showed both distinct mound formation as well as the uniform attack (Figs 59a,b, 68a,b, 74a,b, 82a,d). As previously stated, mechanically polishing the surface of D219 resulted in a change from the uniform attack morphology to only mound formation (Figs 71-73). However, as indicated above, it is unclear what surface conditions or compositions lead to mound formation versus the uniform attack morphology.

Microstructures

The "pre-initiation" scale on D218 (Fig 83a,b) is distinctly different from that on D219 (Fig 83c,d). The scale on D218 appears thinner and more uniform (compare Figs 83a and 83c). In addition, this scale also appears duplex, with the HfO_2 only in the inner layer and with a higher volume fraction of the HfO_2 than that in D219 (compare Figs 83b and 83d). The HfO_2 particles serve as markers in both alloys to indicate that at some time, Al_2O_3 was growing outward. Since α alumina grows inward, it is very likely that early during the test, θ-Al_2O_3 formed and grew on the surface. θ-Al_2O_3, a metastable phase, commonly forms during oxidation of NiAl at temperatures below 1000°C and can remain on the surface for extended periods. θ-Al_2O_3 is also known to grow rapidly outward at a rate nearly two orders of magnitude faster than α-Al_2O_3.[20,21] At higher temperatures (i.e., >1100°C), θ-Al_2O_3 typically transforms rapidly to α-Al_2O_3 although this transformation is also affected by various elements in the alloy.[20,21] Since no θ-Al_2O_3 was detected by x-ray diffraction in the current study, any θ-Al_2O_3 could have transformed to α-Al_2O_3 within the first 50 hrs. Elements within the alloy or deposited on the surface from the burner could have aided the transformation at 900°C.

In regard to the seeming differences in the HfO_2 volume fraction in the scales, D218 and D219 each contain 0.5% Hf differing only in Ti content (1 and 5%, respectively). However, this difference does affect the precipitate morphology within these two alloys. In addition, D219 contains the large multiphase regions consisting of primarily Heusler, β NiAl and Ni(Hf,Ti)Si. It is possible that the higher Ti content in D219 stabilizes the Heusler phase (Ni2Al(Hf,Ti)) altering the solubility of Hf within the matrix which could affect the selective oxidation of the Hf. Examination of other "pre-initiation" scales on other high-Ti alloys, which exhibited both good and poor corrosion behavior, indicated that these scales appeared similar to those on D219. However, since the alloys appear to contain significant compositional inhomogeneities, variations of other elements could have affected the solubility of the Hf affecting the formation of HfO_2 in the scale. For instance, a higher Si content in one of the alloys could have reduced the Hf solubility in the alloy by the formation of NiHfSi particles.

The small, bright precipitates below the growing pits (e.g., Fig 85b,c, Fig 90) are likely HfO_2. Although the O solubility in NiAl would be extremely small, some O will diffuse into the alloy and internally oxidize the oxygen-active Hf. Since the Heusler phase precipitates (Ni2Al[Hf,Ti]) are enriched in Hf, it seems likely that the internal oxidation of the Hf would cause dissolution of the Heusler phase in the internally oxidized region. This dissolution has been observed in some cases, but not others. The different morphologies of the HfO_2 precipitates could be related to the original Heusler particle orientations.

In most corrosion pits and internal oxide formations, EDS analysis repeatedly showed that Ti was associated with Al. However, current phase diagram studies[22,23] indicate little solubility between Al_2O_3 and TiO_2 suggesting that the oxides are mixed and not solutions. The striated and mottled appearance of the oxide fingers and pits also suggest an Al_2O_3 and TiO_2 mixture, similar to that observed on TiAl alloys oxidized in air at 900°C.[24]

The discontinuous precipitation of γ' below the growing pits prior to rampant attack is likely due to the presence of Ti. The Ti appears to be rejected from small growing pits (Fig 88). However, as the inward growth of the pits increases, the Ti concentration in the β phase below the pits will also increase until the solubility of Ti in the β phase is exceeded resulting in the precipitation of the γ' ($Ni_3[Al,Ti]$) phase. Quantitative EMP measurements of the discontinuously precipitated γ' indicated a Ti content of almost 9% (Fig 99).

Rampant Attack

Despite the curious mix of possible sulfates, some process/es obviously occurred to inhibit the formation of, or breach the protective Al_2O_3 scale. Something deposited on the surface appears to have caused, or allowed, the corrosion pits to form. The protective scale could have been partially or locally dissolved (fluxed) or cracked and damaged by thermal cycling. Ca, and to a lesser extent, Mg were observed throughout the initiating pits and could induce the hot corrosion process. However, it is puzzling that S was only detected near the surface and Na was only detected at trace levels within smaller pits. The role the porous HfO_2 stringers might play in allowing a molten sulfate to penetrate the scale is uncertain. The effect of significant TiO_2 on the protectiveness of the Al_2O_3 scale is also unknown. In TiAl alloys, mixed Al_2O_3 and TiO_2 scales, formed in air at 900°C, grew rapidly and were poorly protective.[24] It is possible that mixed Al_2O_3/TiO_2 scales would also provide little protection against a molten sulfate. Lastly, since deposition occurs continuously, it is unclear why the pits are initiated early during testing and continue to grow, but new pits are not continuously nucleated throughout the remainder of the test.

The lack of alkali metals (Ca, Na, Mg) at the inner attack front during rampant attack suggests a non-corrosive mechanism for the rapid inward growth of the Al_2O_3. Grabke and Meier[25] observed accelerated, inward-growing Al_2O_3 during oxidation of NiAl between 800-900°C at very low partial pressures of oxygen (Po_2) when the protective Al_2O_3 scale was prevented from forming. Two conditions, in separate studies, were observed by Grabke to prevent the protective Al_2O_3 formation and result in rapid inward attack. The first was the formation of Ni silicides on the surface of the NiAl (the source of Si was the silica container vessels) and the second was the formation of Al sulfide on the surface when a $1\%H_2S$ environment was used. In both cases, rapid inward growth of Al_2O_3 occurred over hundreds of microns in as short as 42 hrs.[25] The morphology of the inward-growing Al_2O_3 show similarities to the current hot corrosion morphology during rampant attack. Both studies also show formation of γ' below the attack front, and the incorporation of nearly-pure Ni islands in the attacked region.

A possible explanation for the development of the rampant attack morphology is that molten sulfates on the surface or in pits provide the two conditions observed by Grabke to produce the internal attack. Firstly, the sulfate reduces the Po_2 at the base of the pit. Secondly, chemical reactions, such as fluxing, either damages or dissolves the protective scale, and/or the presence of the sulfate hinders reformation or healing of the protective scale if it is damaged by another means (i.e., cracked by thermal cycling). In addition, although the concentration of Si in the NiAl alloys in the present study was low, Si was typically enriched near the surface during testing. Si may also have acted to reduce the Po_2 within the pit or to hinder the formation of the protective Al_2O_3 scale. Once the rampant attack morphology is initiated, sufficient Al is oxidized within the alloy to produce a γ' layer below the attack front.

Grabke and Meier[25] proposed a mechanism whereby the inward growth of the Al_2O_3 "protrusions" was sustained by O transport via Ni corridors to the surface. In the present study, the innermost "tips" of the Al_2O_3 protrusions, where growth would be occurring, is clearly in the γ' phase which Grabke acknowledges has a negligible solubility for oxygen. The transition from intermediate to rampant attack also appears to occur prior to γ formation, with only discontinuous precipitation of γ' in the β phase below the attack front. Hence, a different means of rapidly transporting O inward to sustain the growth of the Al_2O_3 protrusions is required.

Since fine-grained, mixed Al_2O_3 and TiO_2 scales are known to grow fast and be poorly protective on TiAl alloys,[24] it seems possible in the present study that this mixed oxide scale could allow significant O transport through the scale. In addition, the presence of HfO_2 "stringers" within the Al_2O_3 could also contribute to the inward O transport. In addition, it is also possible that O transport occurs within pores within the Al_2O_3 protrusions. Although pores are evident in the internal Al_2O_3 formations, it is impossible to know to what extent the porosity is due to the polishing procedures. Close examination of the oxide protrusions after etching away the matrix might indicate the true extent of the porosity. Rapid O transport via TiO_2 and/or HfO_2 "channels," as well as interconnected porosity within the oxide, could possibly sustain the rapid, inward oxide growth during rampant attack.

Unresolved Issues

Previous deposition studies in the same burner rig, at 900°C and at 2 ppm sea salt concentration, the same conditions used in this study, showed that Na, Mg, Ca and K sulfates were deposited on an inert target from the burner flame. Analysis of the deposits has shown that the Na content is 3.5 times that of Mg, and 15 times that of Ca (in at.%) (the Mg was actually oxidized on the inert target; see Appendix A). The ternary phase diagram for Na_2SO_4, $MgSO_4$ and $CaSO_4$ is shown in Fig 108.[26] The ternary melt could remain molten at 900°C if only a small amount of $MgSO_4$ remains in solution at the Na_2SO_4-$CaSO_4$ eutectic composition (53%Na_2SO_4, T=918°C). However, it is known that Fe, Ni, Cr, and Mn are deposited on the surface from the corrosive degradation of the burner and nozzle. Some of these elements may be deposited as liquid sulfides. The effect of the addition of these elements on the melting point of the sulfate deposit is unknown. It is possible that their addition further reduces the melting point of the sulfate deposit causing the solution to be molten at 900°C over a wide composition range.

Although the present work was not a mechanistic study, a general question of the basic chemical mechanism remains unanswered. First, it is unclear what chemical reactions are occurring on the surface to break down the protective Al_2O_3 scale which should be formed on these alloys. As stated above, it is likely that a molten NaSO4-$MgSO_4$-$CaSO_4$ solution was deposited on the sample surface. However, the relative abundance of Na, Mg and Ca observed in the corroded NiAl samples does not resemble the proportions deposited on the inert target. Little Na was observed either on the surface or in the polished cross-sections and the EDS analysis almost always showed a greater quantity of Ca than Mg. The concentration of Ca in the water soluble corrosion product also greatly exceeded that for either Mg or Na. Although the fuel to air ratio (F/A) in the burner was lower for the deposition studies (Appendix A), it is not expected that the F/A would have a significant effect on the relative proportions of the deposited sulfates. Hence, the composition of the deposited sulfates and the chemical reactions occurring on the surface remain unclear.

Summary and Conclusions

1. Increasing the Ti from 1% to 5% increases the susceptibility of these alloys to hot corrosion attack.

2. The addition of 1-2% Cr to alloys containing 4-5% Ti reduces the susceptibility of these alloys to hot corrosion attack and negates the deleterious effect of the Ti addition.

3. Mechanically polishing the surface improved the hot corrosion response over that of the chemical milling surface treatment.

4. Differences in composition, and possibly inhomogeneities in composition, resulted in a different response of the surface to the chemical milling treatment. The different response to the surface treatments resulted in either a shiny (e.g., D218) or flat matte finish (e.g. D219).

5. Pits, grooves and many other unusual features existed on the surface after the electropolishing and chemical milling treatments, especially in the alloys containing 4-5%Ti. Crack openings at the surface were widened although many crack tips were not affected by the surface treatments (i.e., not blunted).

6. However, in view of Conclusions 4 and 5, the presence of pits and grooves on the surface did not strongly influence the hot corrosion response. Alloy D218, with few pits and grooves, exhibited good resistance to hot corrosion attack, as did AFN19, which possessed a typical surface with pits and grooves. Similarly, the formation of corrosion mounds did not show a distinct association with the highest pitted regions. Furthermore, although cracks existed in the surface after electropolishing and chemical milling, the cracks did not appear to significantly influence the hot corrosion response of the material.

7. Attack on some samples was strongly localized. The most likely explanation for this localized attack was compositional inhomogeneity within the sample. This same inhomogeneity is also the most likely cause for the localized differences in the response of the surface to the chemical milling treatment.

8. The morphology of the hot corrosion attack was either as corrosion mounds or uniform, inward attack which preserved surface features.

9. Corrosion mound formation was initiated early during testing but appeared to stop. Although mounds continued to grow and coalesce with time, few new corrosion mounds were observed after 50-100 hrs.

10. The hot corrosion morphology (mounds versus uniform attack) was affected by, but not dependent on, the surface preparation treatments (chemical milling versus mechanical polishing). Mechanical polishing resulted in a change from uniform attack to mound formation on D219. A similar corrosion morphology was observed on the electropolished

and chemically milled samples.

References

1. R. Darolia, JOM, **43**, 43, 1991.

2. R. Darolia, W.S. Walston and M.V. Nathal, "NiAl for Turbine Airfoils" in *Superalloys 1996*, R.D. Kissinger, D.J. Deye, D.L. Anton, A.D. Cetel, M.V. Nathal, T.M. Pollock, and D.A. Woodford, editors, TMS, Warrendale, 1996, p. 561-570.

3. R.D. Noebe, R.R. Bowman, and M.V. Nathal, "Review of the Physical and Mechanical Properties and Potential Applications of the B2 Compound NiAl," NASA TM 105598, April 1992.

4. D.B. Miracle, Acta. Metall. Mater., **41**, 649, 1993.

5. W.S. Walston, R.D. Field, J.R. Dobbs, D.F. Lahrman and R. Darolia, "Microstructure and High-Temperature Strength of NiAl Alloys," in *Structural Intermetallics*, R. Darolia, J.J. Lewandowski, C.T. Liu, P.I. Martin, D.B. Miracle and M.V. Nathal, editors, TMS, Warrendale, 1993, p. 523-532.

6. J.A. Nesbitt, C.A. Barrett and P.O. Dickerson, "Cyclic Oxidation of Single-Crystal NiAl-X Alloys," NASA TM 107346, 1996.

7. G.C. Fryburg, F.J. Kohl, C.A. Stearns and W.L. Fielder, J. Electrochem. Soc., **129**, 571, 1982.

8. N.S. Bornstein, JOM, **48**, 37, 1996.

9. J. Stringer, J. De Physique IV, **3**, 43, 1993

10. G.H. Meier, Mater. Sci. and Eng. **120**, 1, 1989.

11. J. Stringer, Mater. Sci. and Tech., **3**, 482, 1987.

12. F.S. Pettit and C.S. Giggins, "Hot Corrosion," in *Superalloys II*, C.T. Sims, N.S. Stoloff and W.C. Hagel, editors, John Wiley and Sons, New York, 1987, p. 327-358.

13. M. Kaufman, Trans ASM, **62**, 590, 1969.

14. G. Romeo and D.W. McKee, J. Electrochem. Soc., **122**, 188, 1975.

15. R.L McCarron, N.R. Lindblad, and D. Chatterji, Corrosion, **2**, 476, 1976.

16. D.L. Ellis, "Hot Corrosion of the B2 Nickel Aluminides," NASA CR191082, March 1993.

17. A. Garg, R.D. Noebe and R. Darolia, "Characterization of the Microstructure of a Hf-

Doped NiAl Single Crystal Alloy Containing Different Levels of Si Contaminant," HiTemp Review, 1995, NASA CP 10178, Paper 28, 1995.

18. R.D. Noebe, P.O. Dickerson, A. Garg, "Hierarchial Characterization of the Microstructure of Single Crystal NiAl Alloy AFN12," NASA TM 107029, 1995.

19. I.E. Locci, R.M. Dickerson, A. Garg, R.D. Noebe, M.V. Nathal, and R. Darolia, "Microstructure and Phase Stability of Single Crystal NiAl Alloyed with Hf and Zr," J. Materials Research, **11**, 3024, 1996.

20. G.C. Rybicki and J.L. Smialek, Ox. Met., **31**, 275, 1989.

21. B.A. Pint, M. Treska and L.W. Hobbs, Ox. Met., **47**, 1, 1996.

22. E.H. Copland, B. Gleeson and D.J. Young, "Factors Affecting the Sub-Surface Formation of a TixAlyOz Phase During Oxidation of γ-TiAl Based Alloys," in *13th International Corrosion Congress*, Melbourne Australia, Nov. 1996, p. 1-11.

23. X.L. Li, R. Hillel, F. Teyssandier, S.K. Choi and F.J.J. Van Loo, Acta Metall. Mater. **40**, 3149, 1992.

24. S. Becker, A. Rahmel, M. Schorr and M. Schutze, Ox. Met., **38**, 425, 1992.

25. H.J. Grabke and G.H. Meier, Ox. Met., **44**, 147, 1995.

26. Phase Diagrams for Ceramists, Vol II, Americal Ceramic Society, Westerville, OH, 1969, Fig 2923.

Table I
Alloy Designations and Compositions* (at.%)

Alloy	Ni	Al	Hf	Ga	Ti	Cr	Si	Hf/Si
D218	50.0 (48.5)	48.3 (49.7)	0.50 (0.51)	0.2 (0.12)	1.0 (1.0)	-	(0.15)	(3.4)
D219	50.0 (48.2)	44.3 (45.4)	0.50 (0.57)	0.2 (0.19)	5.0 (5.4)	-	(0.32)	(1.78)
AFN19	50.0 (51.5)	43.3 (41.3)	0.50 (0.59)	0.2 (0.2)	5.0 (4.8)	1.0 (0.9)	(0.65)	(0.91)
AFN20	50.0 (51.4)	44.45 (42.8)	0.50 (0.58)	0.05 (0.06)	5.0 (4.8)	0.0 (0.0)	(0.32)	(1.81)
AFN21	50.0 (51.5)	43.8 (42.4)	0.50 (0.58)	0.2 (0.13)	4.5 (4.4)	1.0 (0.8)	(0.32)	(1.81)
AFN22	50.0 (51.4)	44.3 (42.8)	0.50 (0.58)	0.2 (0.13)	4.0 (3.9)	1.0 (0.9)	(0.32)	(1.81)
AFN23	50.0 (51.5)	43.3 (41.7)	0.50 (0.61)	0.2 (0.13)	4.0 (4.1)	2.0 (1.7)	(0.32)	(1.91)
AFN24	50.0 (51.3)	43.45 (42.3)	0.50 (0.56)	0.05 (0.04)	5.0 (4.8)	1.0 (0.8)	(0.16)	(3.5)
AFN25	50.0 (51.3)	43.95 (42.6)	0.50 (0.58)	0.05 (0.04)	4.5 (4.4)	1.0 (0.8)	(0.32)	(1.81)
AFN26	50.0 (51.5)	44.15 (42.4)	0.65 (0.77)	0.2 (0.13)	4.0 (4.0)	1.0 (0.9)	(0.32)	(2.4)

* Compositions in parentheses determined at NASA Lewis Research Center

TABLE II
ELECTROPOLISHING CONDITIONS

25-40 volts
1-1.5 amps
5 minute Immersion
Solution:
    400 ml Methanol
    50 ml Perclorate
Liquid Nitrogen bath

Table III
X-ray Results for Series II after 300 hrs

Alloy	Al_2O_3	NiO	Spinel	HfO_2	TiO_2	$Ca_3Al_2O_6$	Unknown Peak	Substrate	Comments
AFN 19	✓	✓	A_o=8.30	✓		✓	d=3.75 I/I_o=5	✓	Both ends similar except unknown peak not present on one end. Curved surface: spinel peak stronger; NiO peak much weaker, no unknown peaks.
AFN 20	✓	✓	A_o=8.30	✓	✓	✓	d=3.73 I/I_o=24	✓	Both ends similar. Curved surface, smooth side: spinel stronger, NiO weaker; rough side: NiO stronger than smooth side, but not as strong as on ends. No unknown peaks on curved surfaces.
AFN 21	✓	✓	A_o=8.30	✓	trace	✓	d=3.77 I/I_o=24	✓	Curved surface: spinel increased, NiO greatly decreased; No unknown peaks on curved surface.
AFN 22	**Similar to AFN 21**						d=3.77 I/I_o=7	✓	Similar to AFN 21

AFN 23	✓	✓	A_o=8.30	✓	trace	✓	d=3.75 I/I_o=0.6	✓	Both ends similar. Curved surface, smooth scale: spinel increased, NiO greatly decreased; rough scale: spinel increased, NiO greatly increased. No unknown peaks on smooth scale.
AFN 24	✓	✓	A_o=8.30	✓	trace	✓	d=3.78	✓	Both ends similar. Curved surface, smooth scale: spinel strongly increased, NiO greatly decreased; rough scale: spinel decreased, NiO greatly increased. No unknown peaks.
AFN 25	✓	✓	A_o=8.30	✓		✓	d=3.82 I/I_o=0.8		Curved surface, smooth scale: spinel strongly increased, NiO greatly decreased; rough scale: spinel decreased, NiO greatly increased. No unknown peaks.
AFN 26	✓	✓	A_o=8.30	✓		✓	d=3.76 I/I_o=3	✓	On curved surface, spinel strongly increased, NiO greatly decreased, no unknown peaks.
D218A	✓	✓	A_o=8.30	✓			d=3.76 I/I_o=3	✓	Both ends similar. Curved surface, Spinel stronger, NiO weaker. No $Ca_3Al_2O_6$ detected on any surface. No unknown peaks on curved surfaces.
D219A	✓	✓	A_o=8.05 (strong) A_o=8.30 (weak)		✓	✓	d=3.74 I/I_o=6	✓	Both ends similar. Curved surface, rough scale: NiO and spinel (A_o=8.05) weaker, spinel (A_o=8.30) increased; Smooth scale: NiO and spinel (A_o=8.05) weaker still, spinel (A_o=8.30) increased. No unknown peaks on curved surfaces.
D219B	**Similar to D219A**								

Table IV

Composition of Soluble Reaction Products*

Alloy	Al	Cr	Si	Ca	Mg	Na	B	Sr
AFN20	0.8	0.3	4.8	11.5	0.09	0.6	0.3	0.16
AFN23	2.9	0.5	6.5	16.0	0.09	1.4	0.5	0.22
AFN26	2.5	0.4	9.5	15.7	0.06	0.8	0.8	0.18
D218	0.7	0.8	1.9	24.3	0.11	1.7	0.9	0.22
D219	5.9	1.0	13.3	32.0	0.13	2.4	0.9	0.41

* Compositions reported in µg/ml

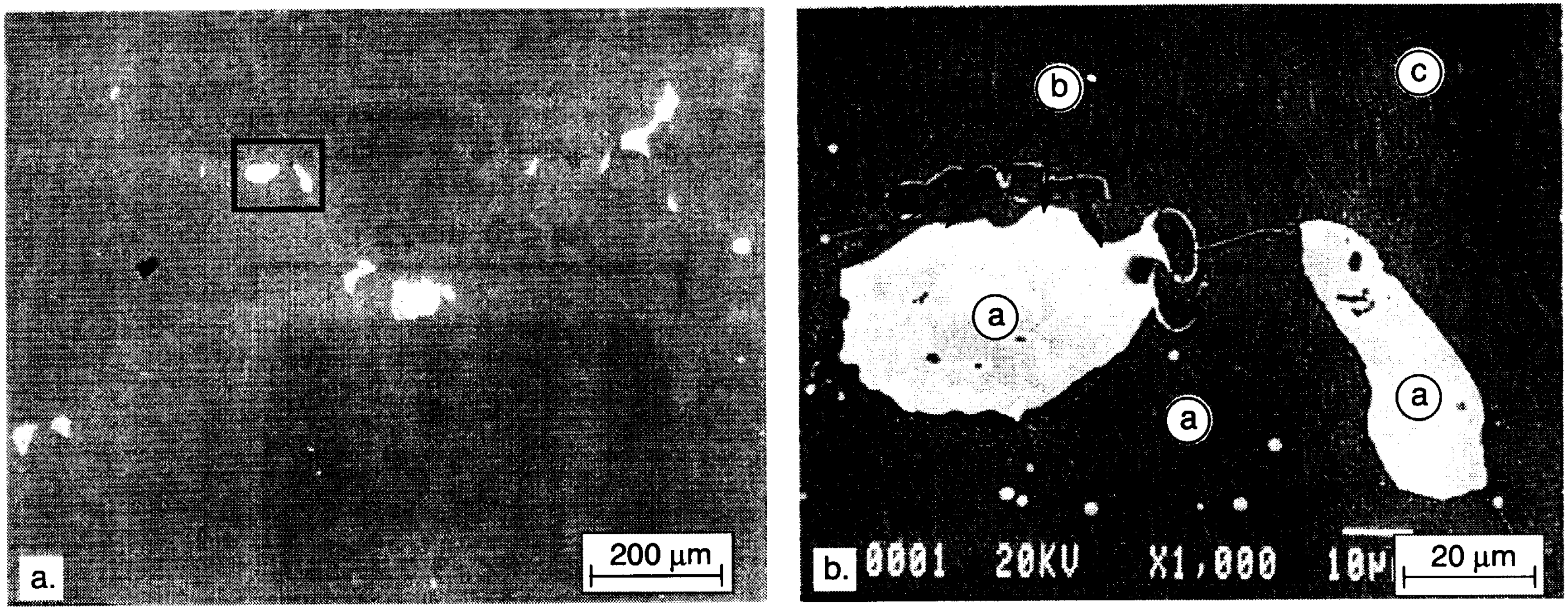

Location	Ni	Ti	Al	Hf	Si	Phase
a	49.0	16.0	28.4	5.8	0.7	Heusler
a (2nd spot)	49.2	15.0	31.5	3.5	0.7	Heusler
b	35.2	13.4	0.7	19.0	31.7	NiHfSi
c	49.0	7.1	42.9	0.7	0.2	β - NiAl, Matrix

Fig. 1 Large multiphase precipitates found in all alloys except D218. Compositions in the table refer to labeled points a-c in the image.

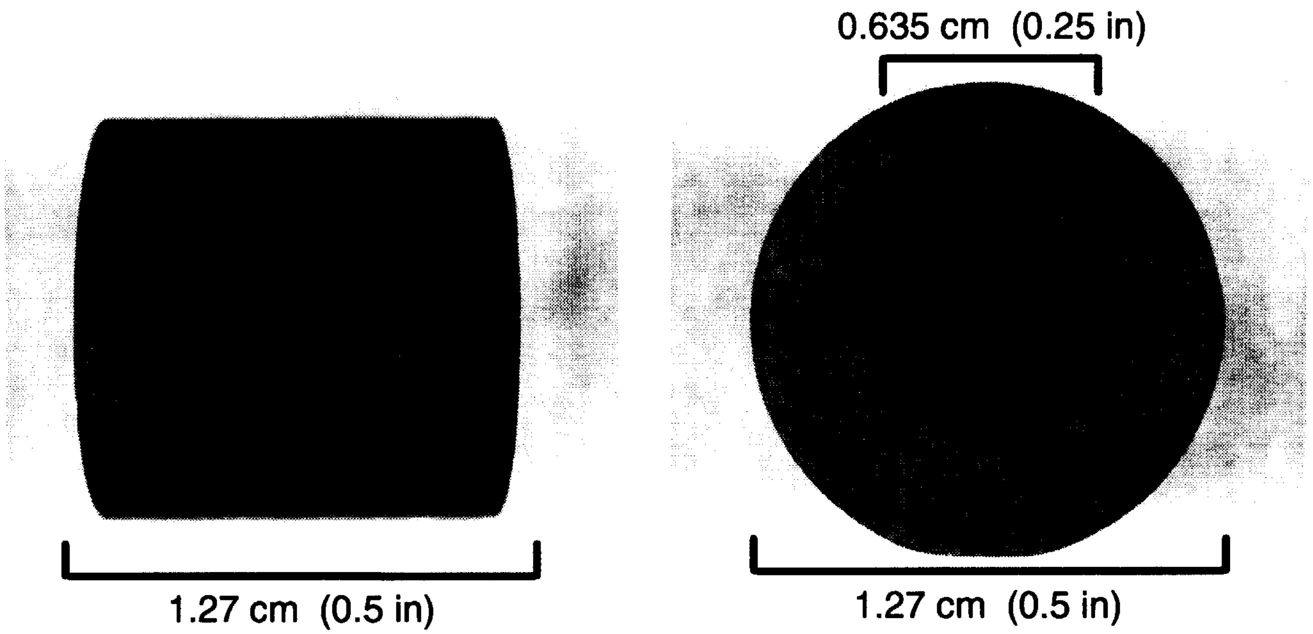

Fig. 2 Dimensions of the samples tested in the burner rig. (AFN26 shown after electropolishing and chemical milling.)

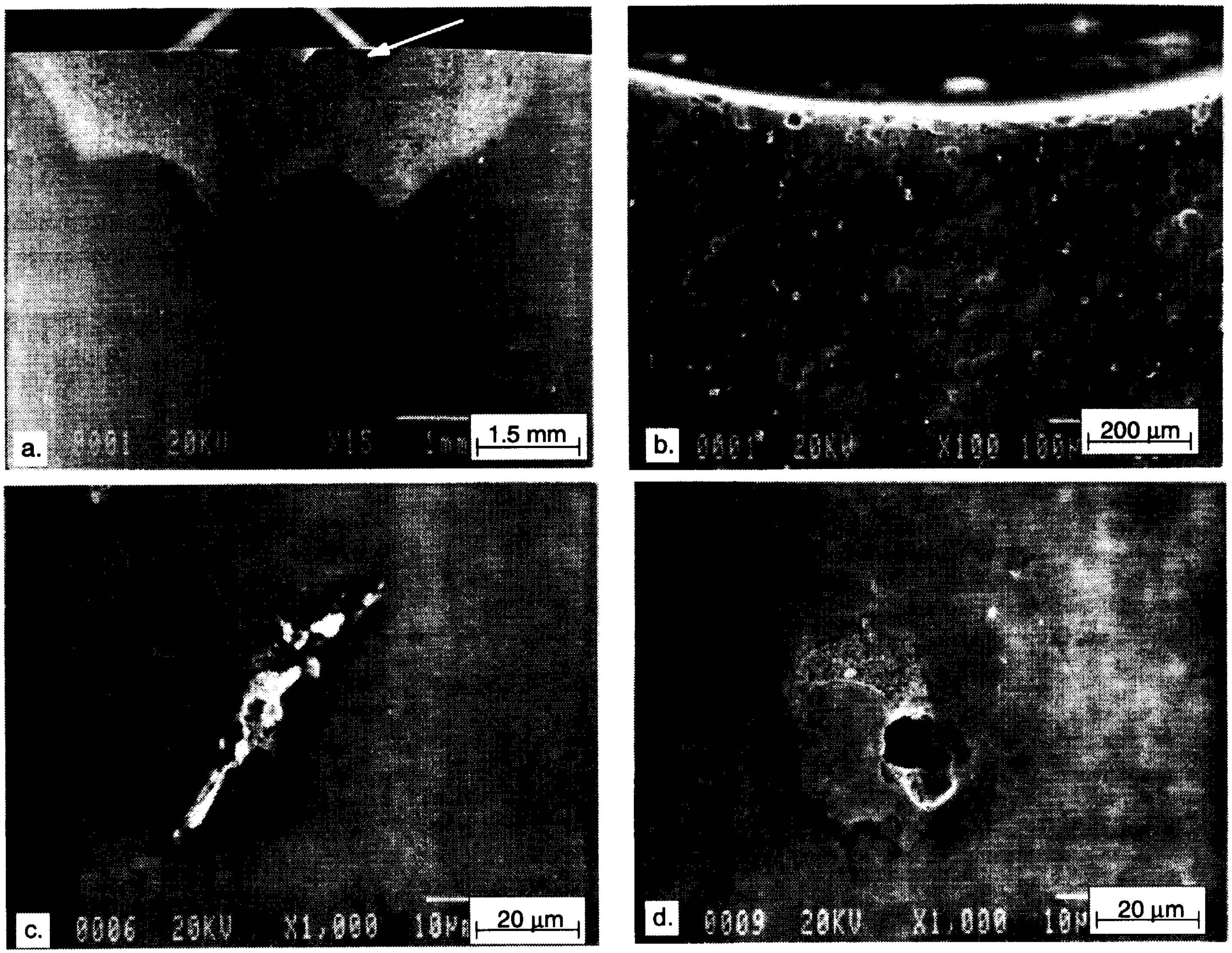

Fig. 3 SEM photos of AFN 26 after electropolishing (a) unusual region near one end, (b) etch pits in region indicated by arrow in (a) (many pores contain epoxy from previous mounting), (c) exposed Hf oxide particle, (d) multiphase Heulser, β-NiAl and Ni(Hf,Ti)Si particle with pore.

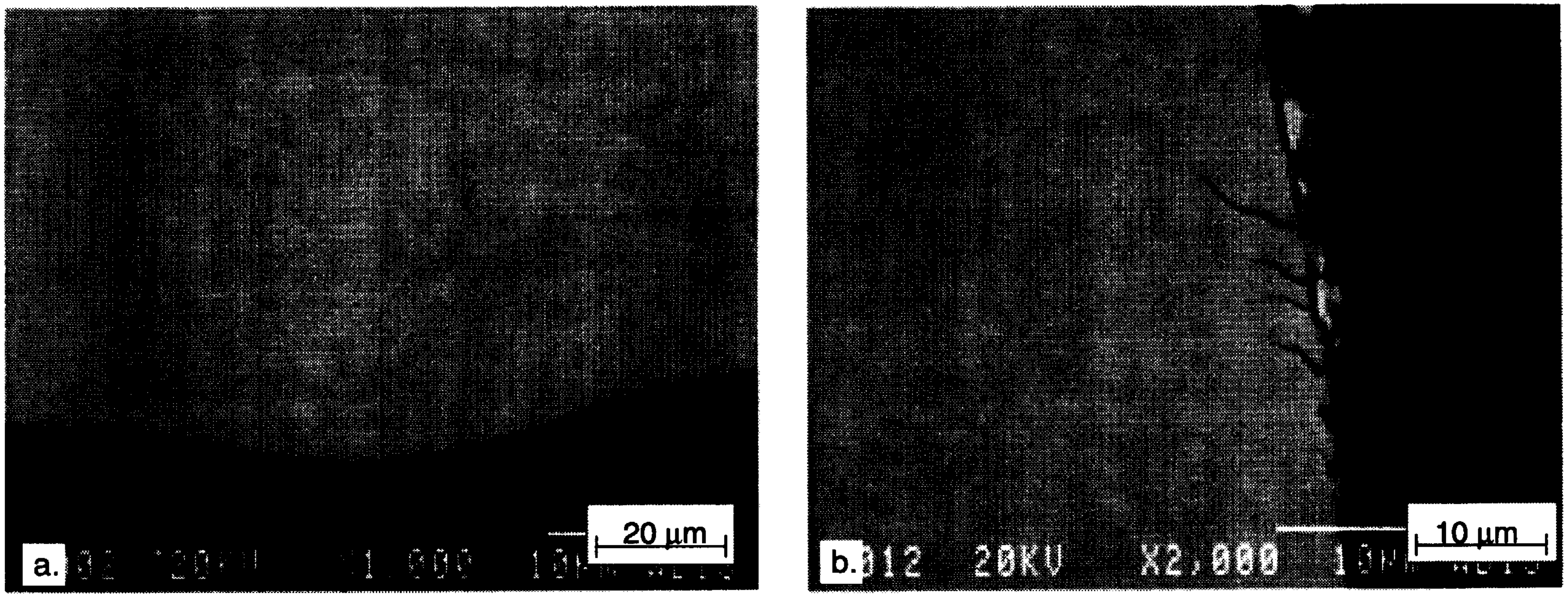

Fig. 4 SEM photos of polished cross section of AFN26 showing (a) typical smooth surface (ID surface shown) and (b) typical fine cracks from EDM cutting (OD edge shown).

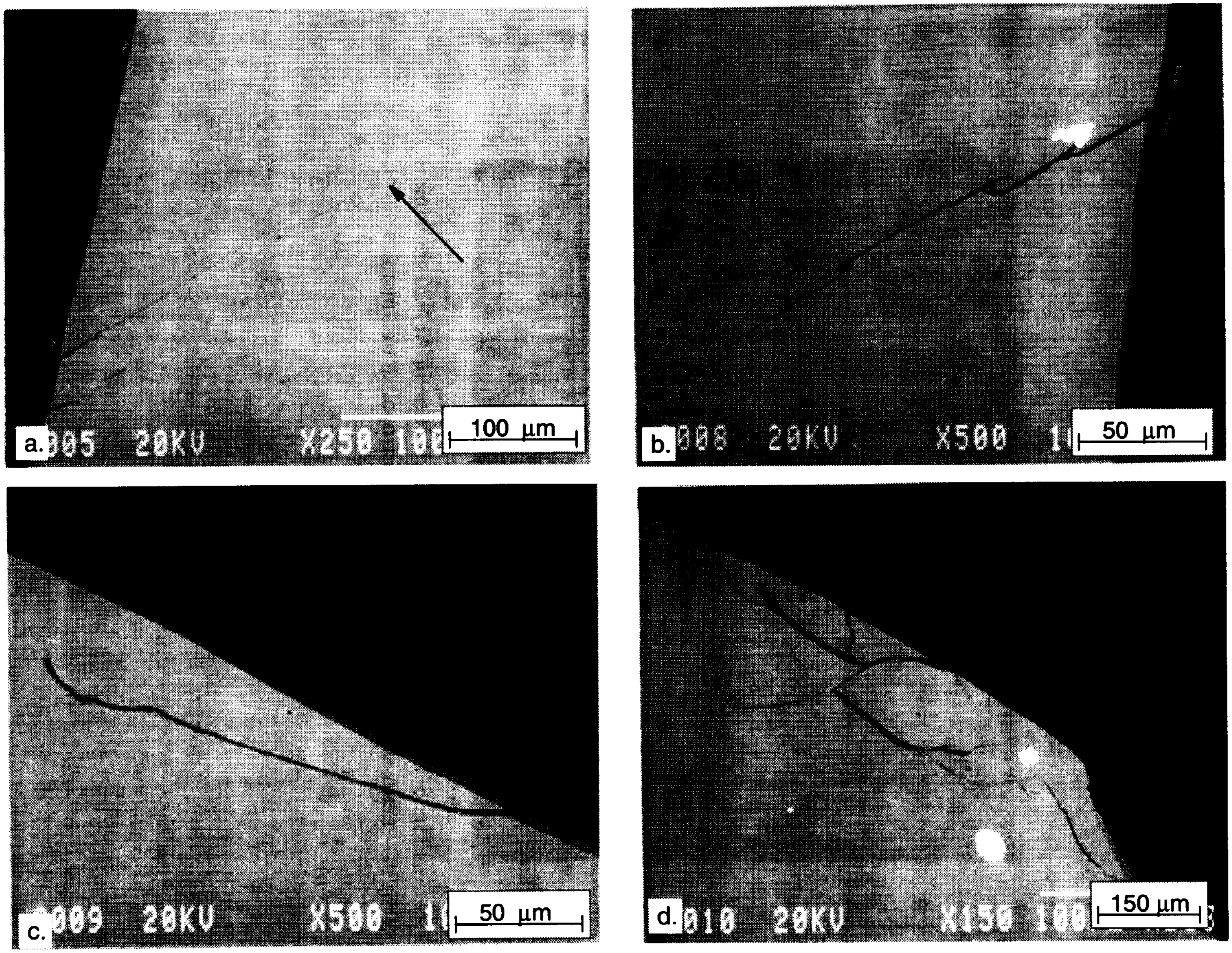

Fig. 5 SEM photos of AFN26 showing cracks from EDM cutting (a),(b) at the ID edge, and (c),(d) at the OD edge. Arrow shows depth of penetration in (a). (Bright particles in (b) and (d) are Hf-rich Heusler and/or NiHfSi particles.

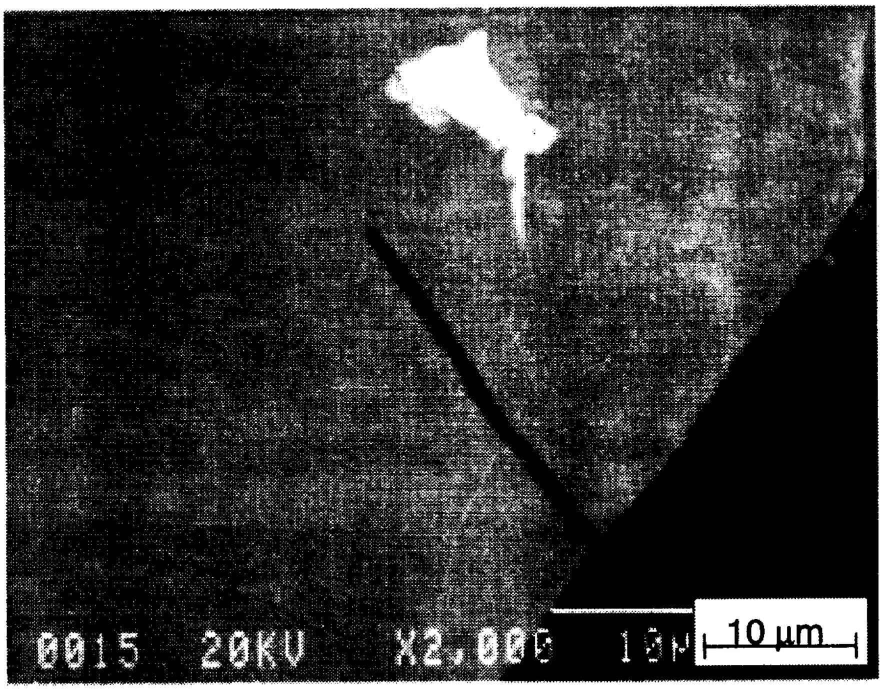

Fig. 6 SEM photos of polished cross section of AFN26 showing crack which appears blunted by electropolish treatment.

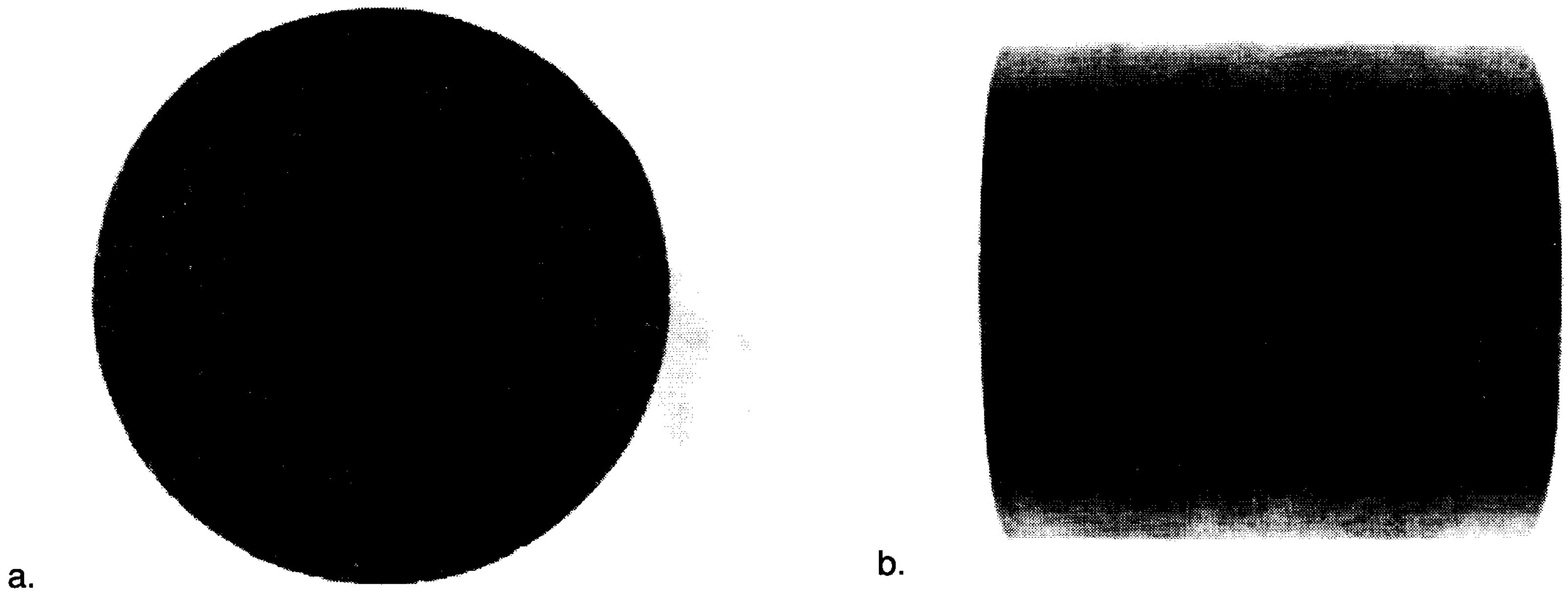

Fig. 7 Macrophotos of D218 after chemical milling showing shiny metallic surface finish (a) top, (b) curved surface.

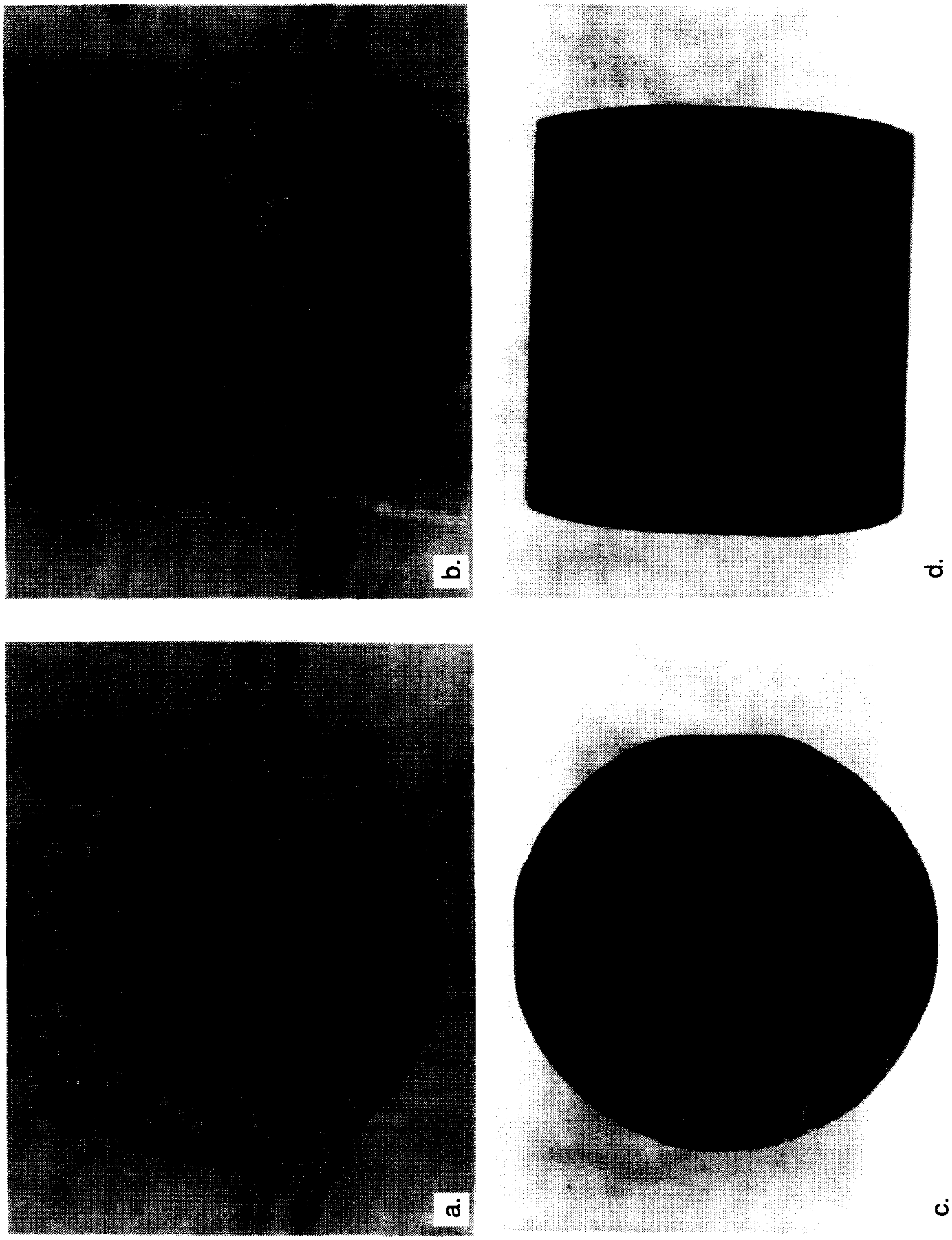

Fig. 8 Macrophotos of samples after electropolish and chemical milling (a),(b) AFN21, (c),(d) AFN19 (e),(f) AFN22.

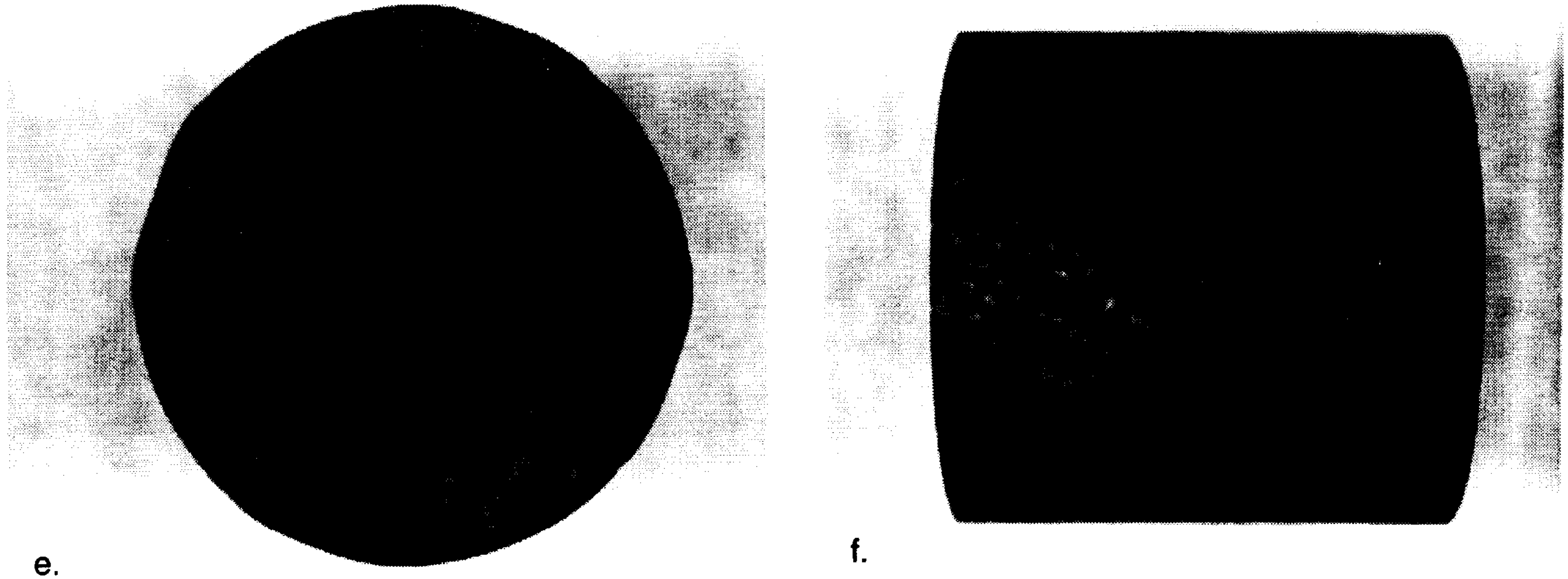

Fig. 8 (cont.) Macrophotos of samples after electropolish and chemical milling (a),(b) AFN21 , (c),(d) AFN19 (e),(f) AFN22.

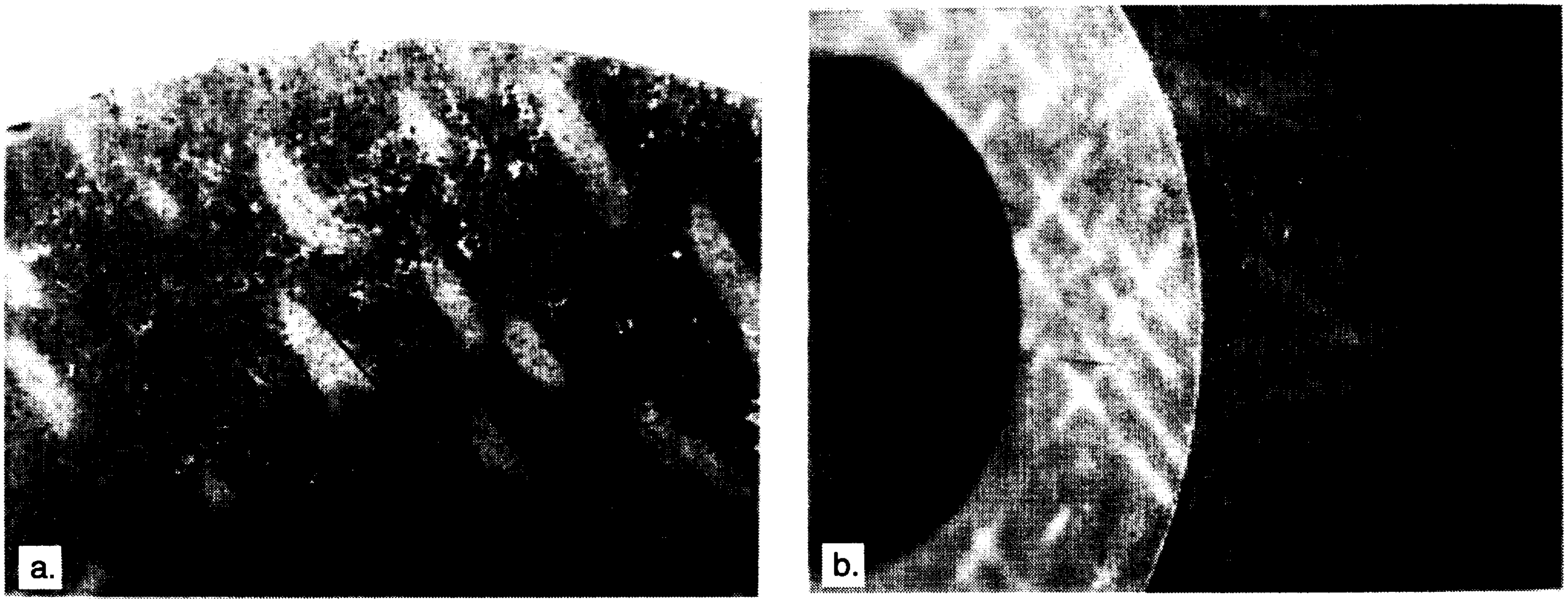

Fig. 9 Macrophotos of samples after electropolish and chemical milling showing cracks (a) at ID edge in AFN19, and (b) at OD edge of AFN20.

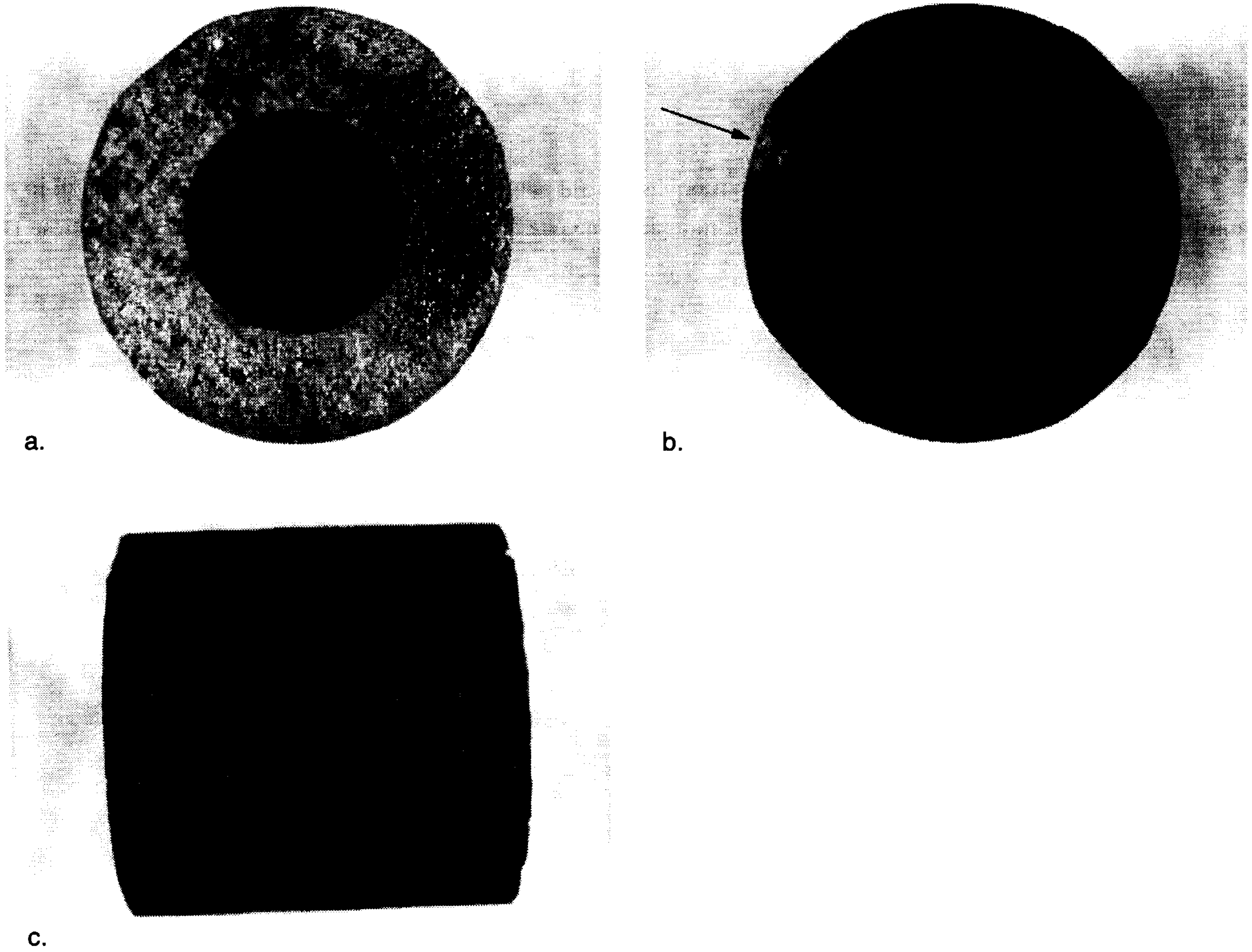

Fig. 10 Macrophotos of AFN24 after electropolishing and chemical milling, (a) shiny but rough, metallic surface (b), (c) dark, flat matte surface typical on high-Ti containing samples.

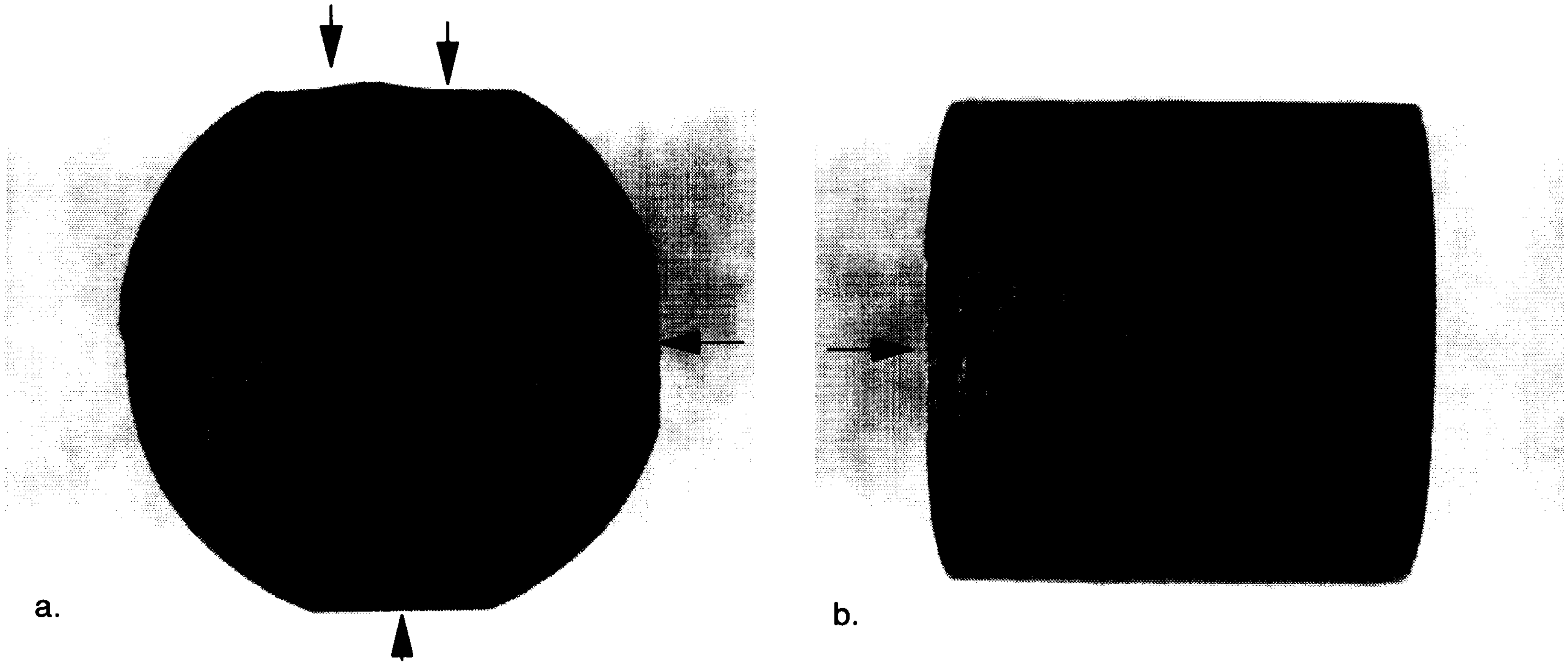

Fig. 11 Macrophotos of AFN25 after electropolishing and chemical milling. Arrows indicate beveled or flat regions from the side of the ingot or where mechanical test samples had previously been cut from the ingot.

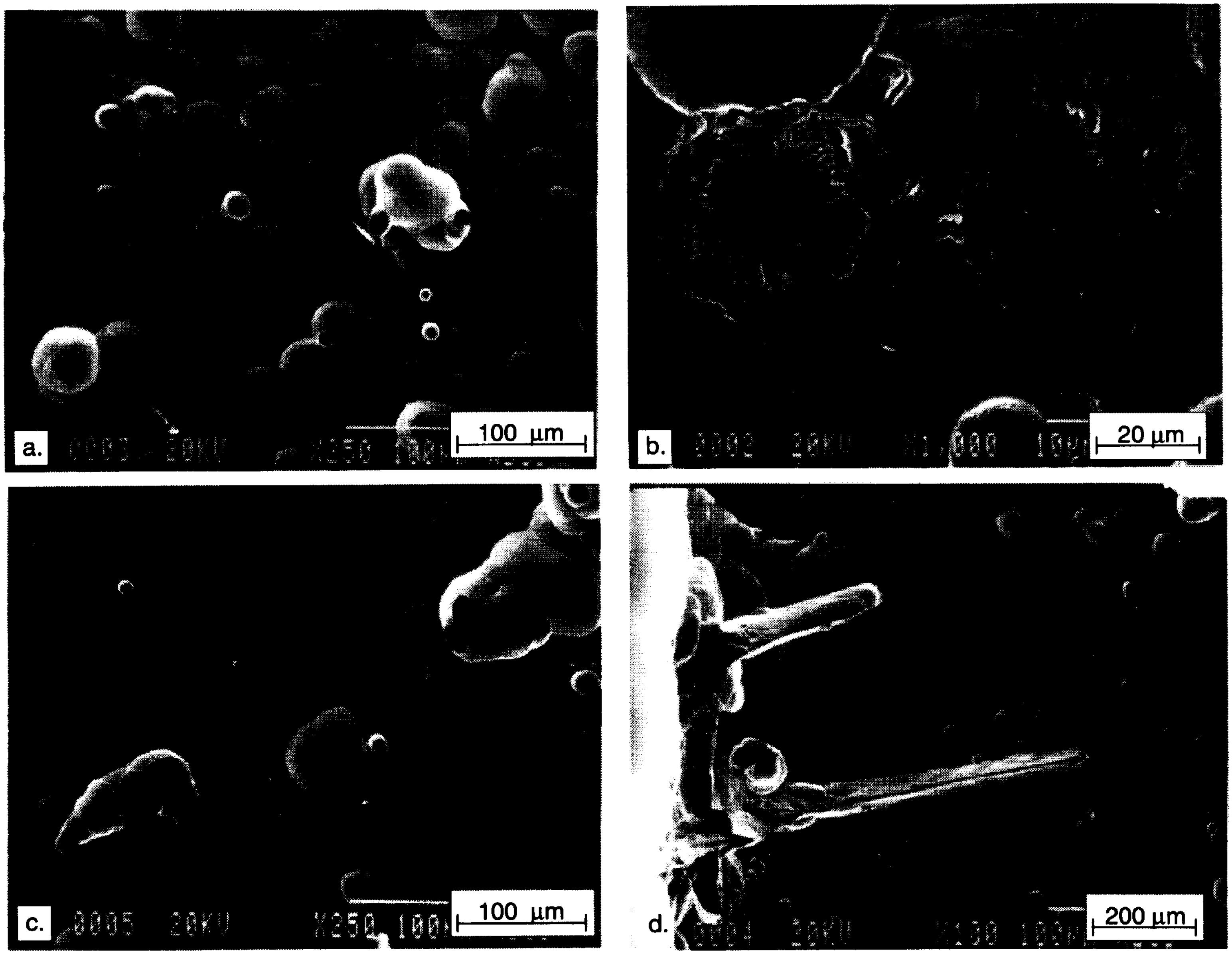

Fig. 12 SEM photos of the surface of D218 after chemical milling (a,b) general surface features, (c) porosity, and (d) blunted cracks.

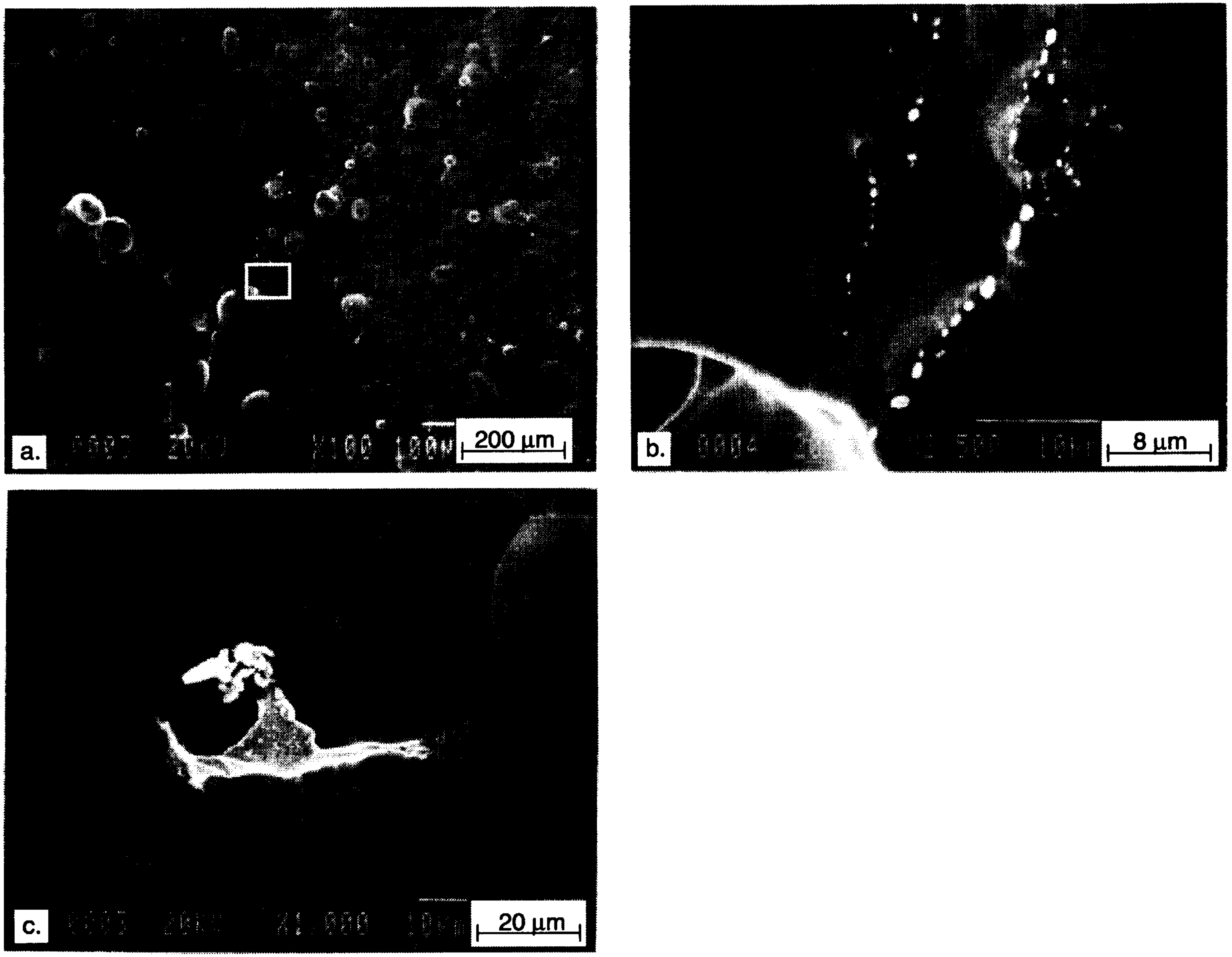

Fig. 13 SEM photos of the surface of D218 after chemical milling (a) general surface features, (b) high magnification of inset in (a) showing HfO2 particles, (c) oxide/carbide particles.

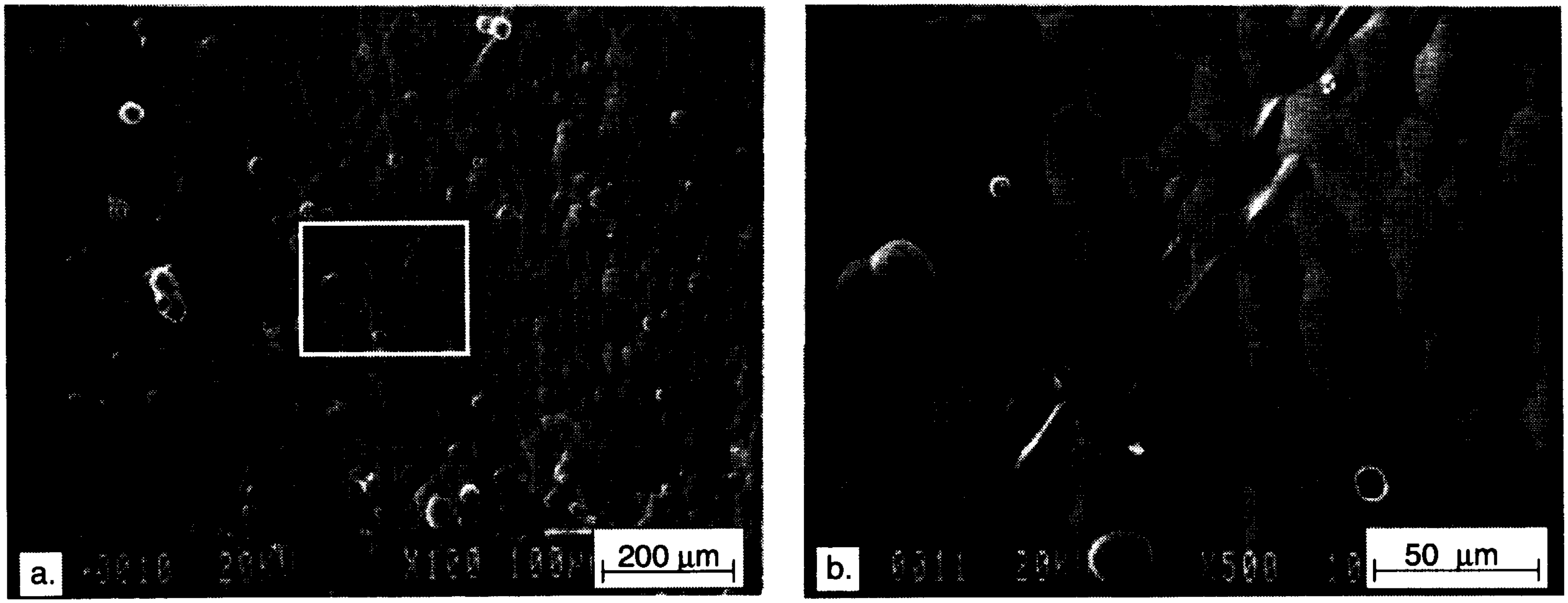

Fig. 14 SEM photos of the surface of D218 after chemical milling (a) general surface features, (b) high magnification of inset in (a) showing unidentified linear feature.

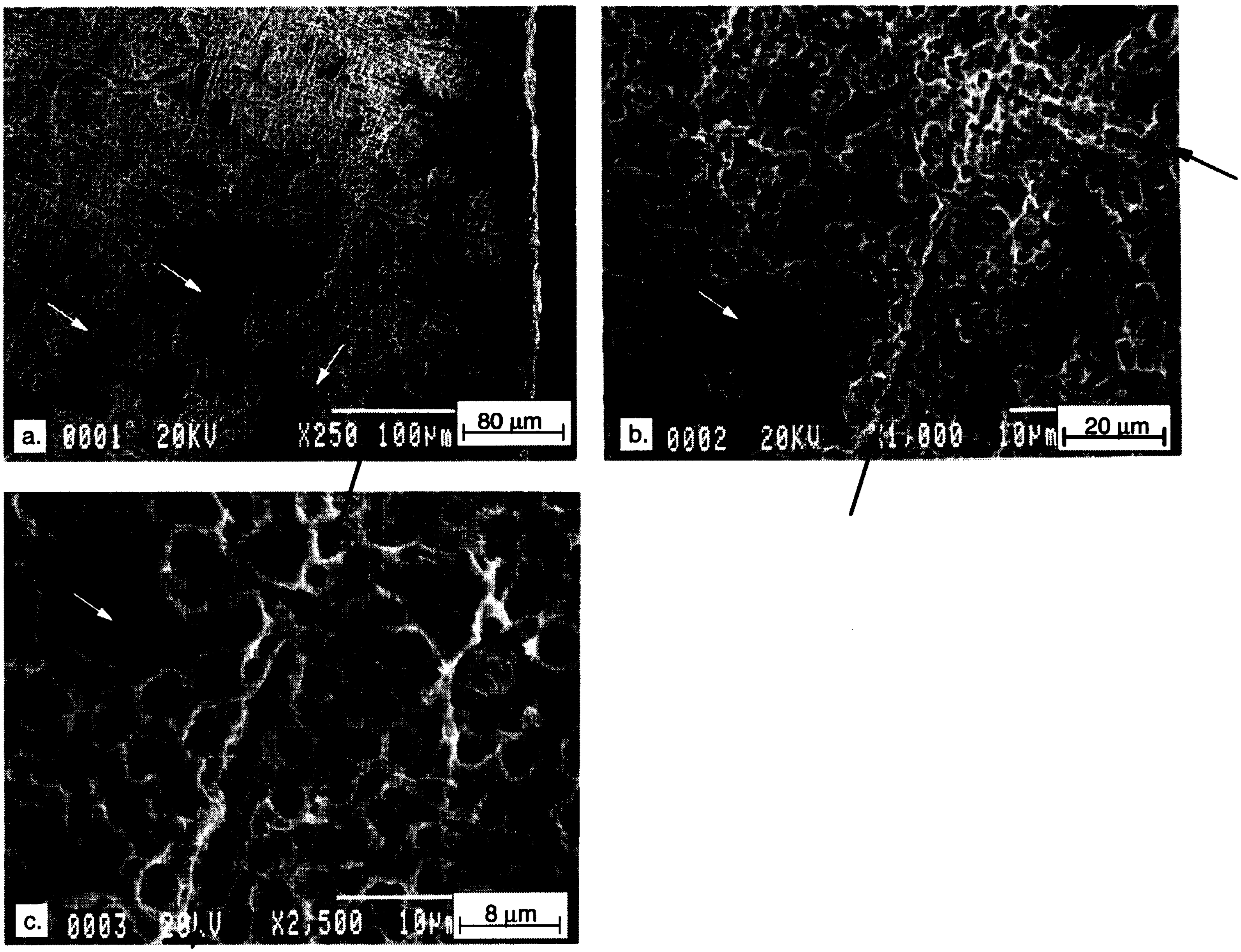

Fig. 15 SEM micrographs of D219 after chemical milling showing "less etched" regions indicated by white arrows, etch pits, and etched subgrain boundaries indicated by dark arrows.

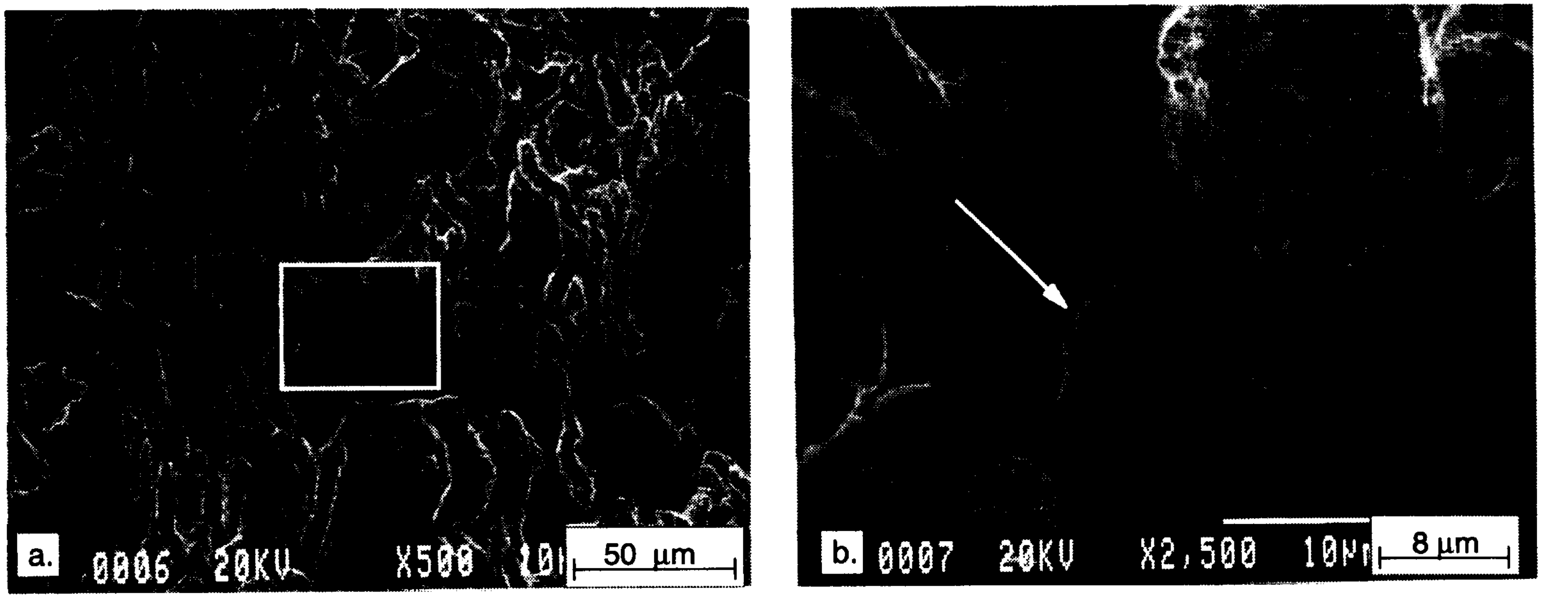

Fig. 16 SEM micrographs of D219 after chemical milling showing "less etched" regions, (b) is a higher magnification of the box shown in (a).

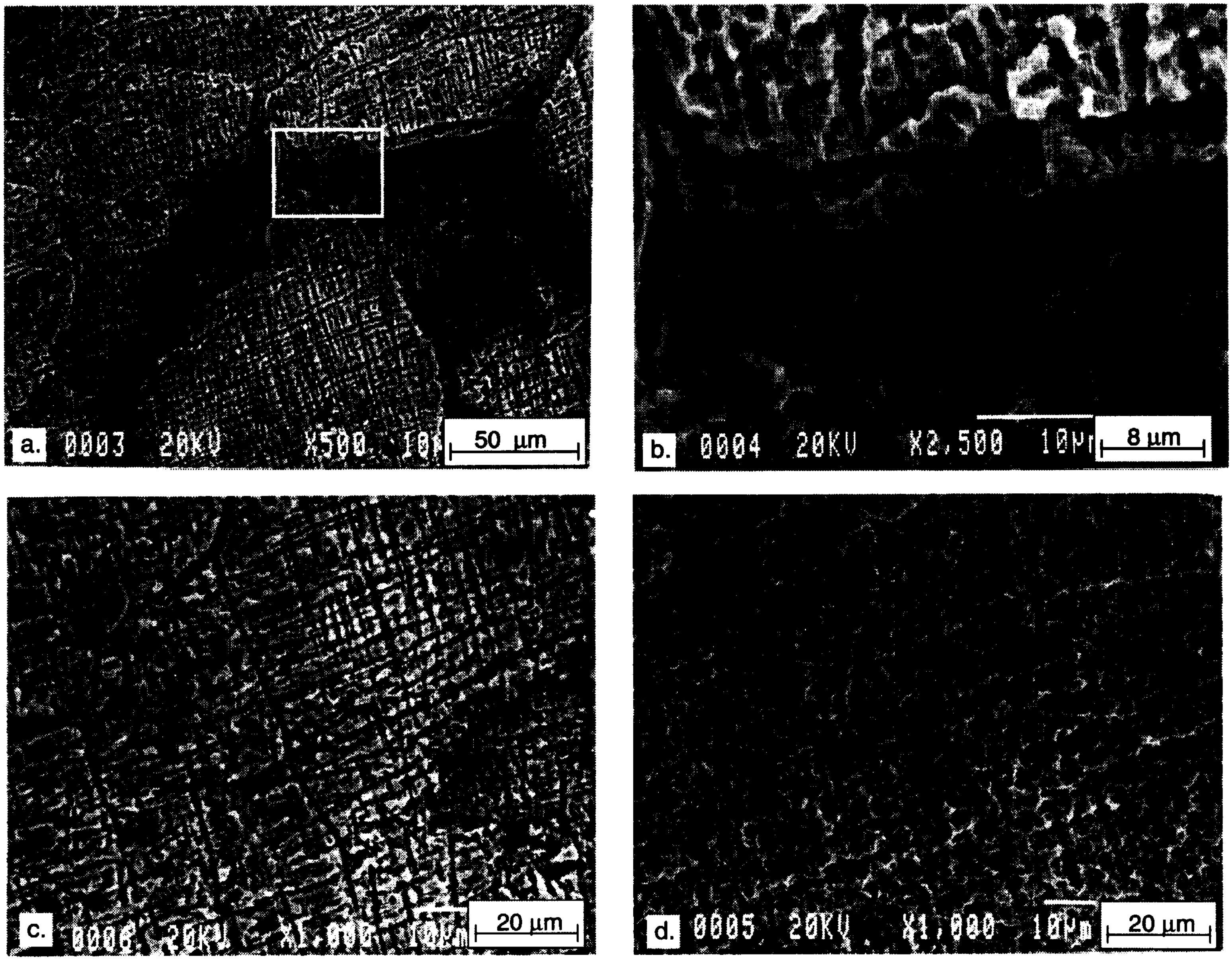

Fig. 17 SEM micrographs of D219 after chemical milling showing various morphologies of etched surface.

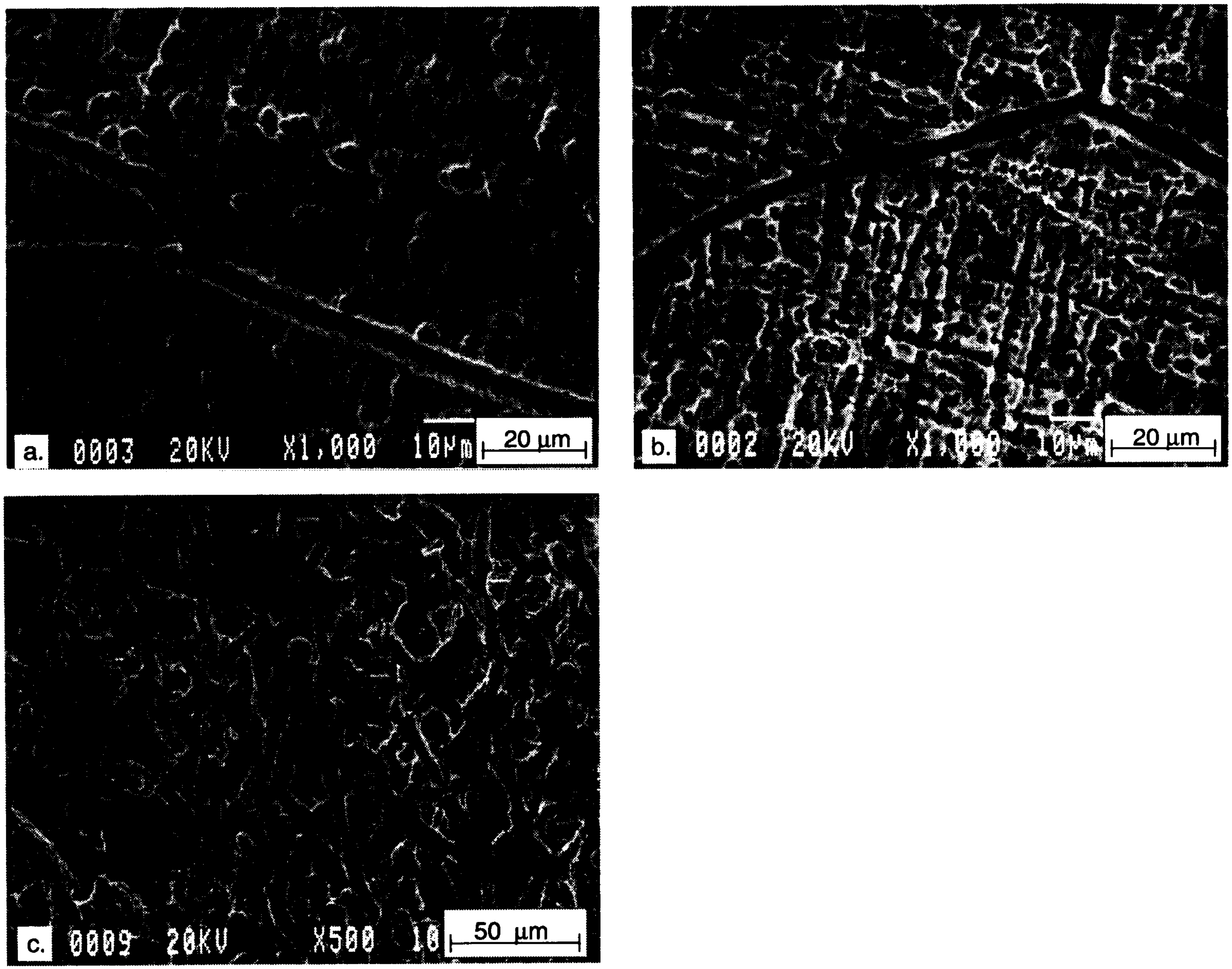

Fig. 18 SEM micrographs of D219 after chemical milling showing (a,b) etched subgrain boundaries and (c) trench-like pits.

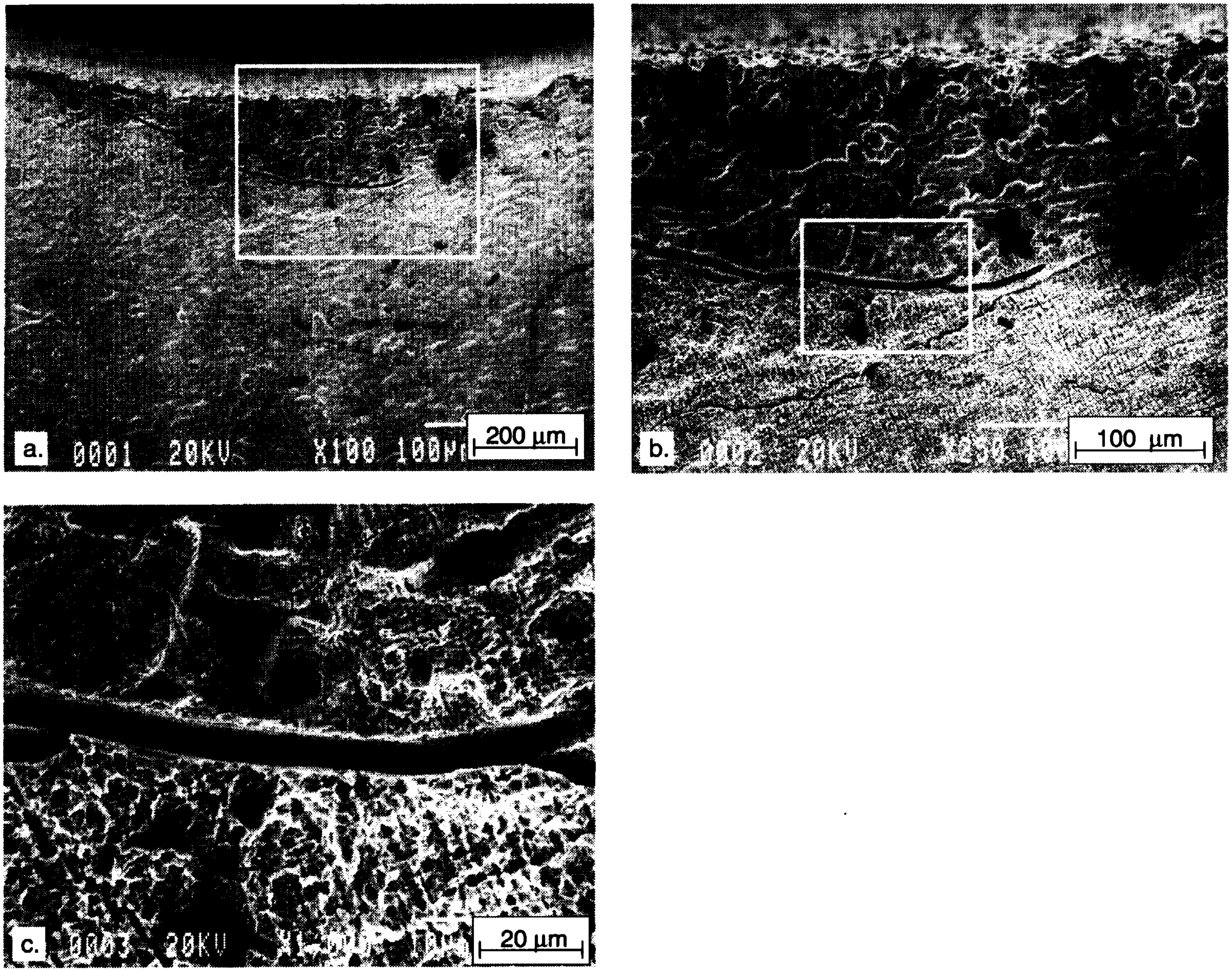

Fig. 19 SEM micrographs of AFN20 after chemical milling showing different etching patterns on either side of a crack or etched subgrain boundary, (b,c) are higher magnifications of boxes shown in (a,b).

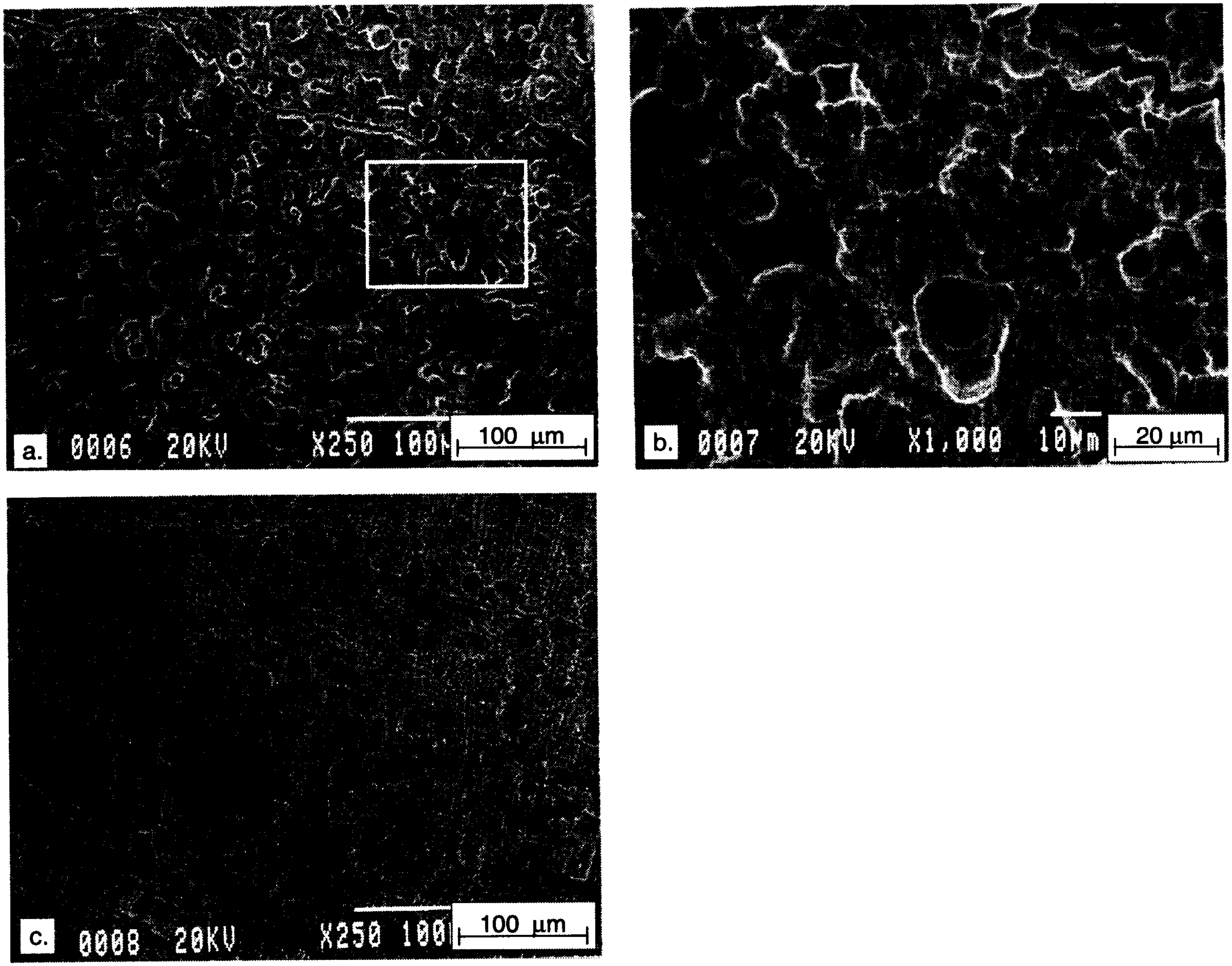

Fig. 20 SEM micrographs of D219 after chemical milling showing porosity, pits and attack at a subgrain boundary.

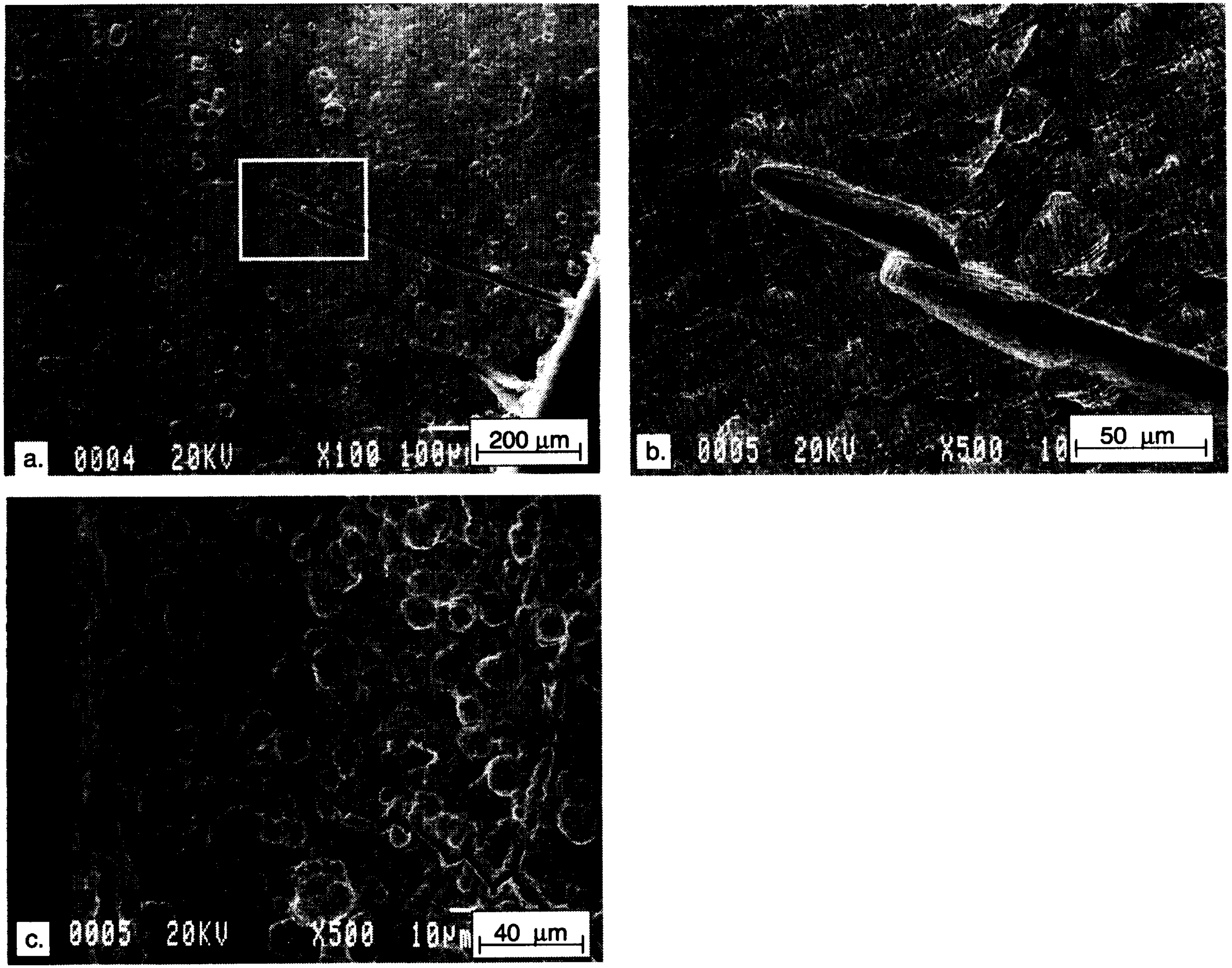

Fig. 21 SEM micrographs of cracks at the surface after chemical milling (a,b) AFN20, (c) D219.

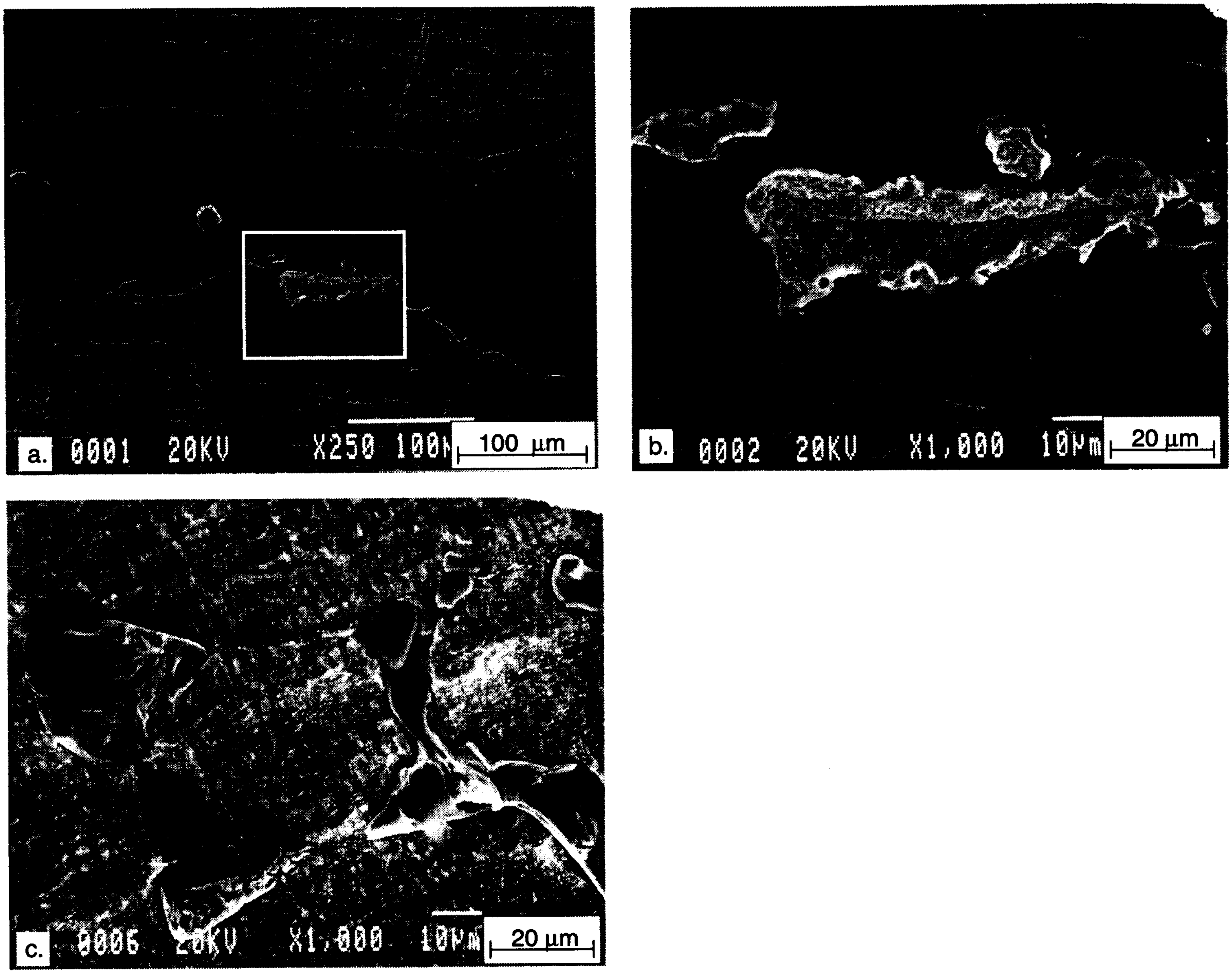

Fig. 22 SEM micrographs of oxides or carbides at the surface after chemical milling (a,b) D219, (c) AFN20.

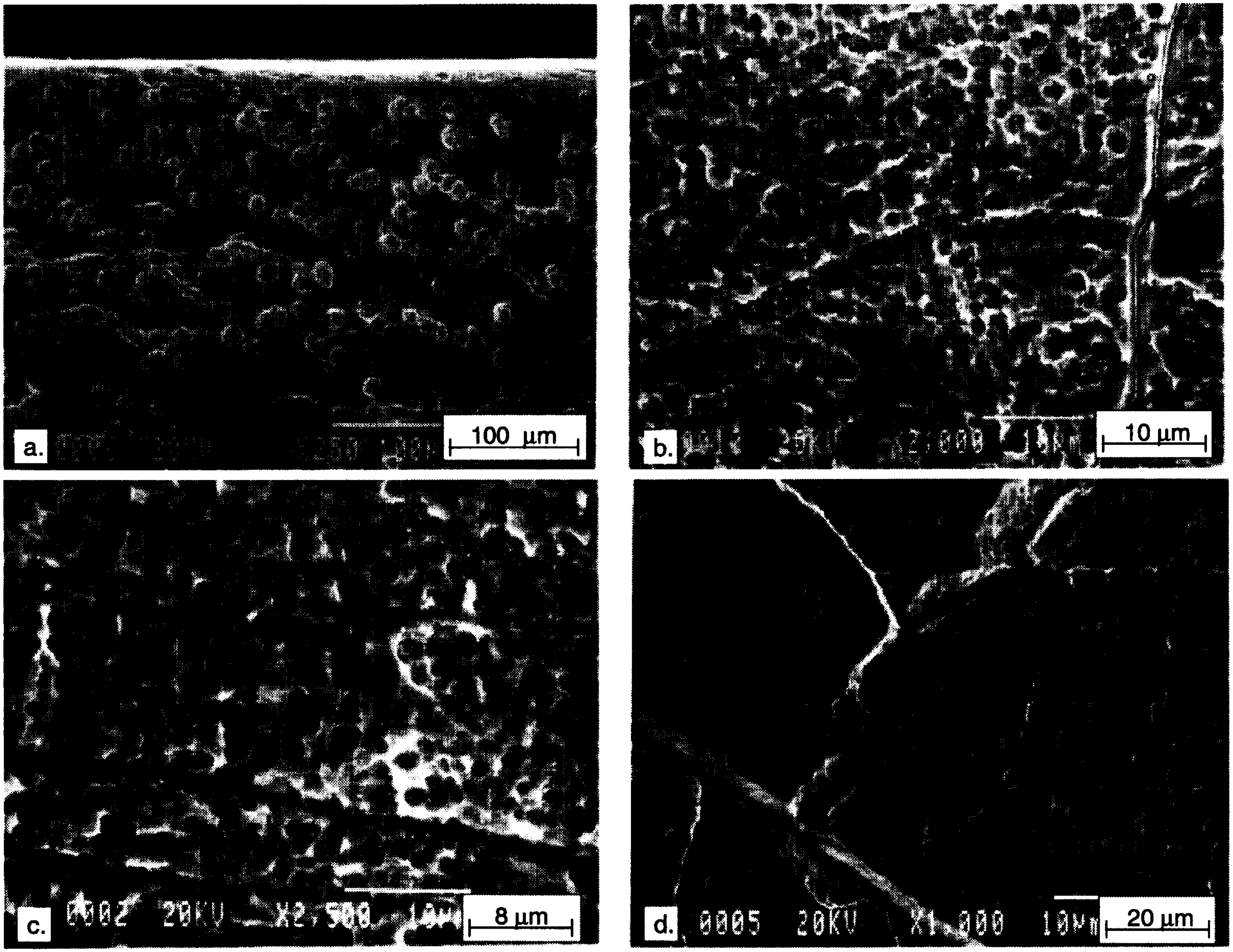

Fig. 23 SEM micrographs after electropolish and chemical milling showing pits and preferential etching of subgrains. Heusler precipitates are apparent in pits (a,b) AFN23, (c,d) AFN26.

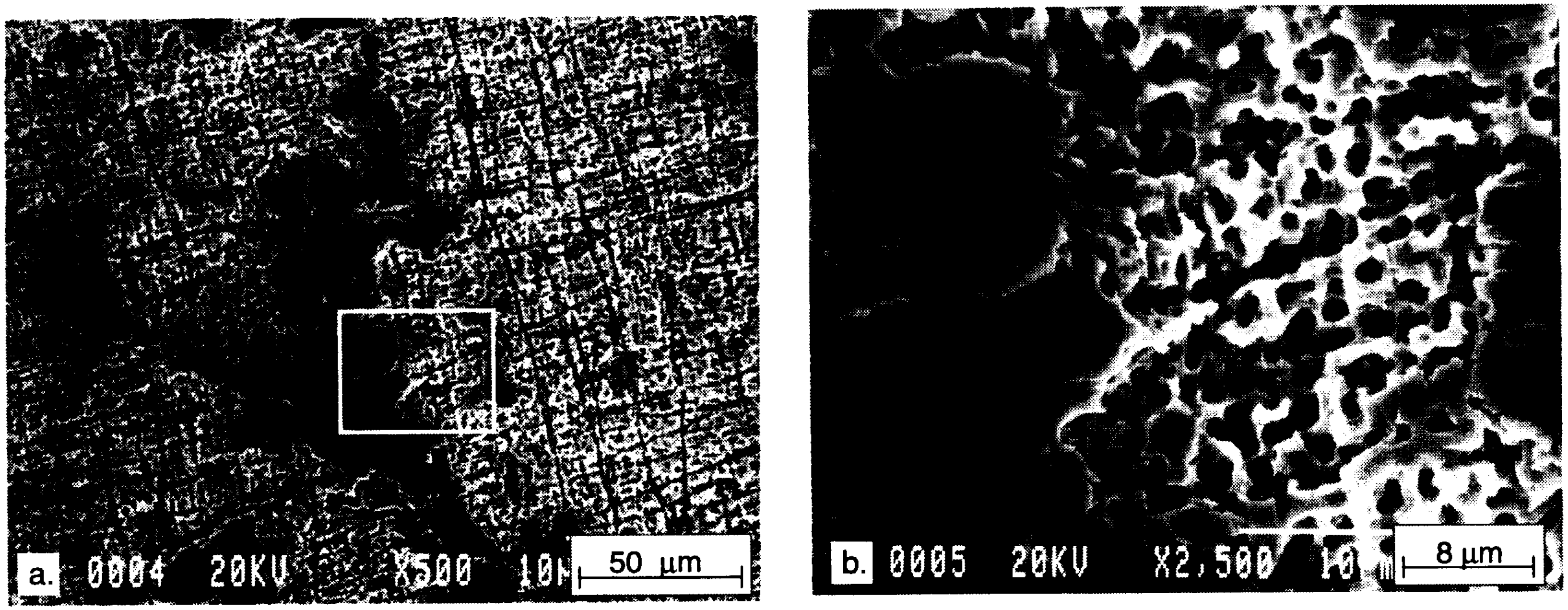

Fig. 24 SEM micrographs after electropolish and chemical milling of AFN26 showing dark regions not equally etched as surrounding material.

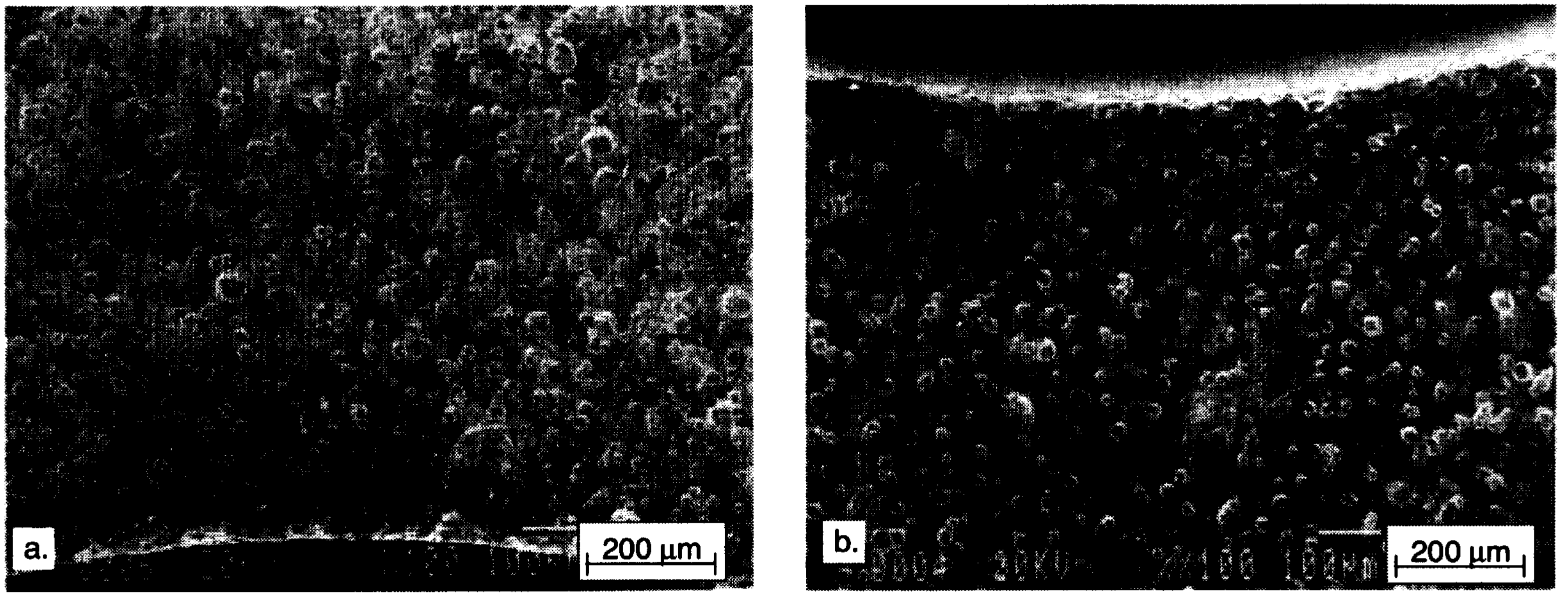

Fig. 25 SEM micrographs after electropolish and chemical milling of AFN23 showing porosity and pits on the same end of the sample.

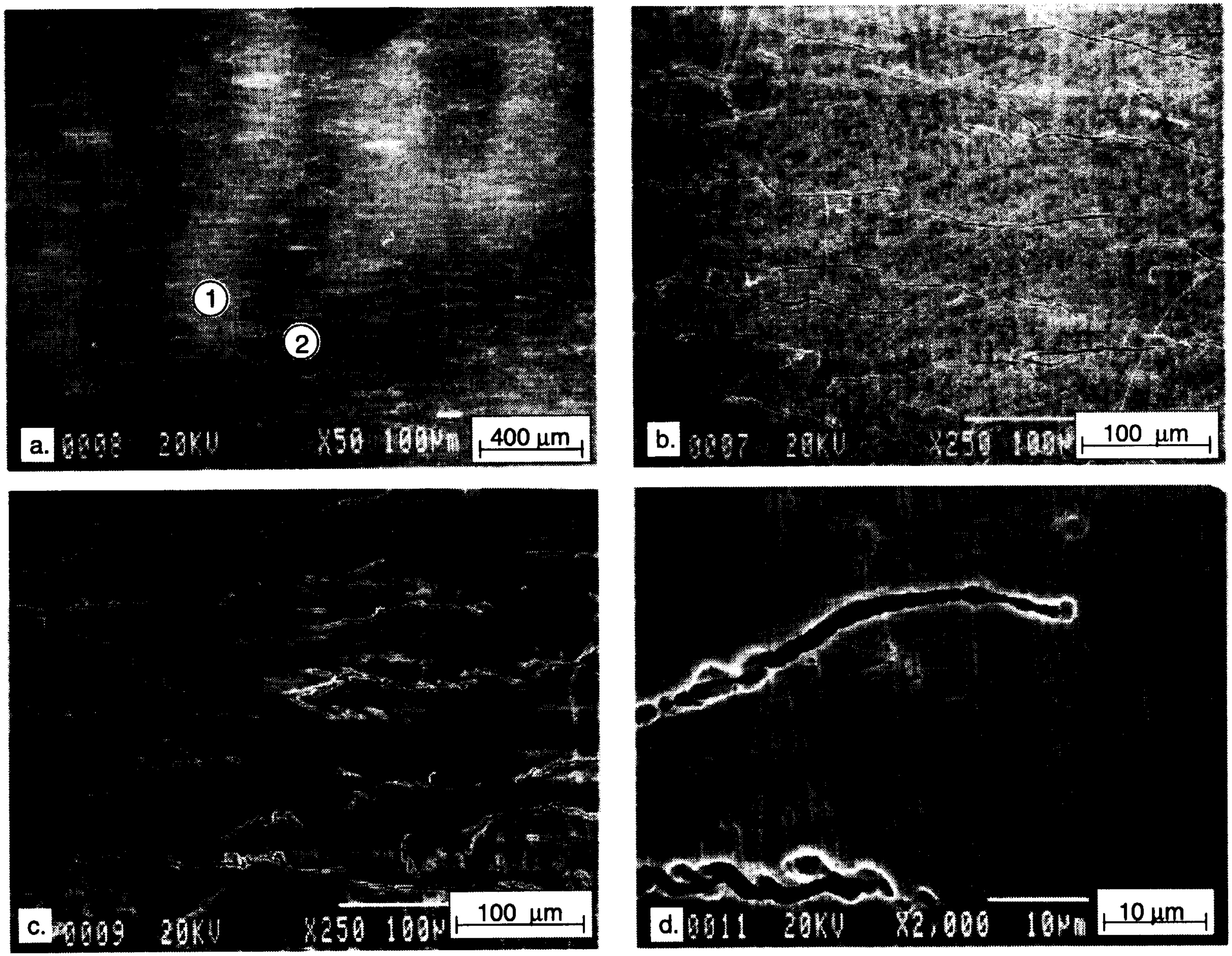

Fig. 26 SEM micrographs after electropolish and chemical milling of AFN23 (a) showing light (1) and dark (2) regions on curved surface of sample (b) magnified view of light region 1, (c,d) magnified view of dark region 2.

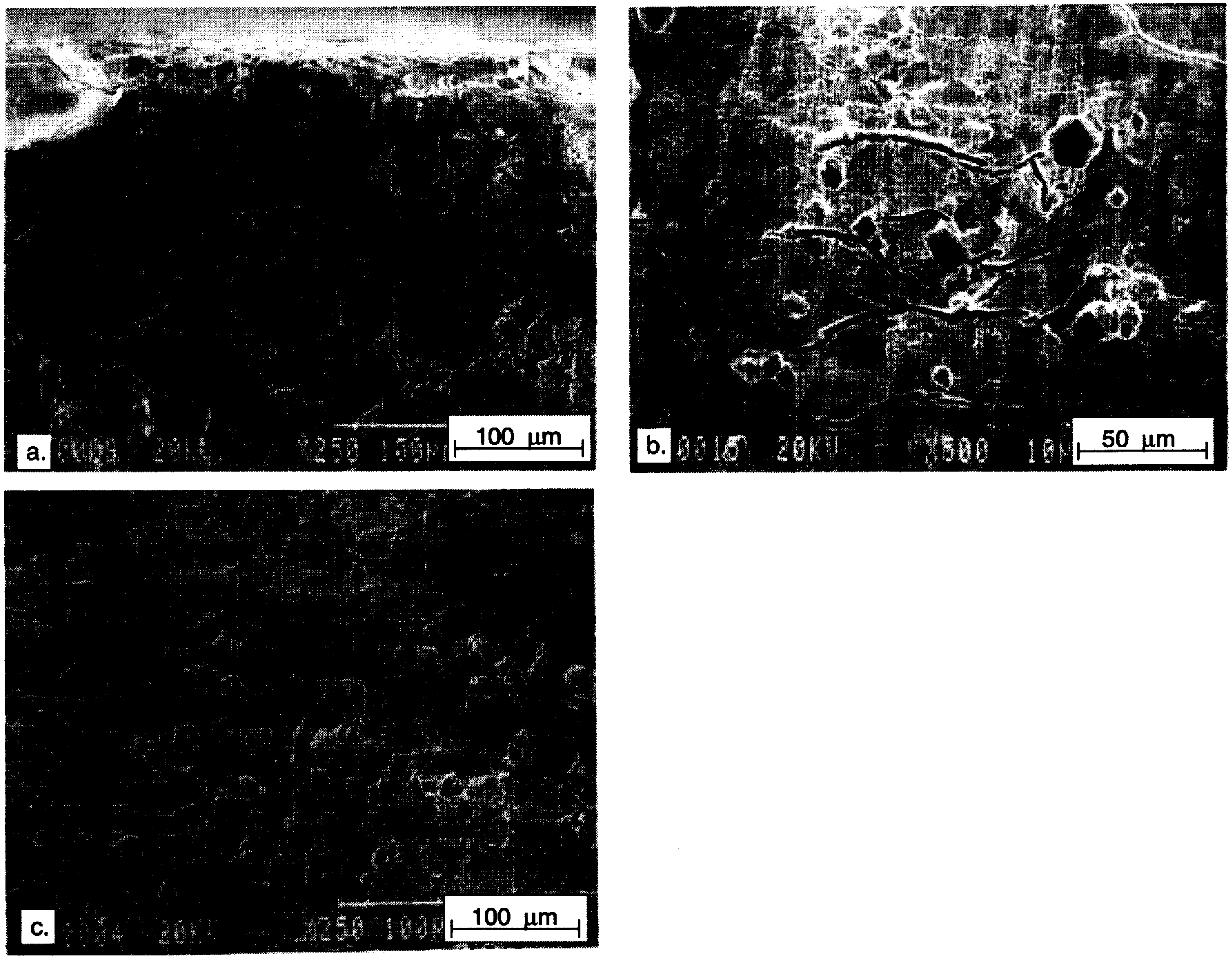

Fig. 27 SEM micrographs after electropolish and chemical milling showing cracks in the surface of AFN23 (a,b) at the ends, and (c) on the curved surface.

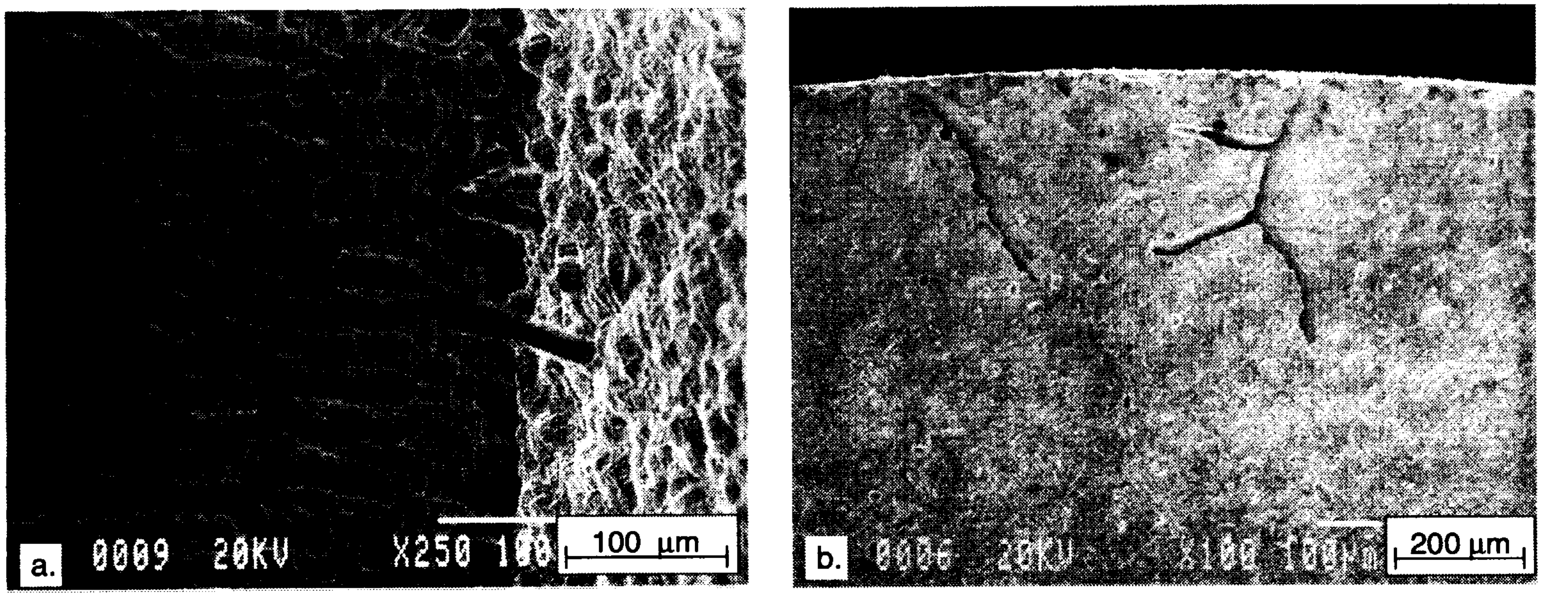

Fig. 28 SEM micrographs after electropolish and chemical milling of AFN26 showing etched cracks..

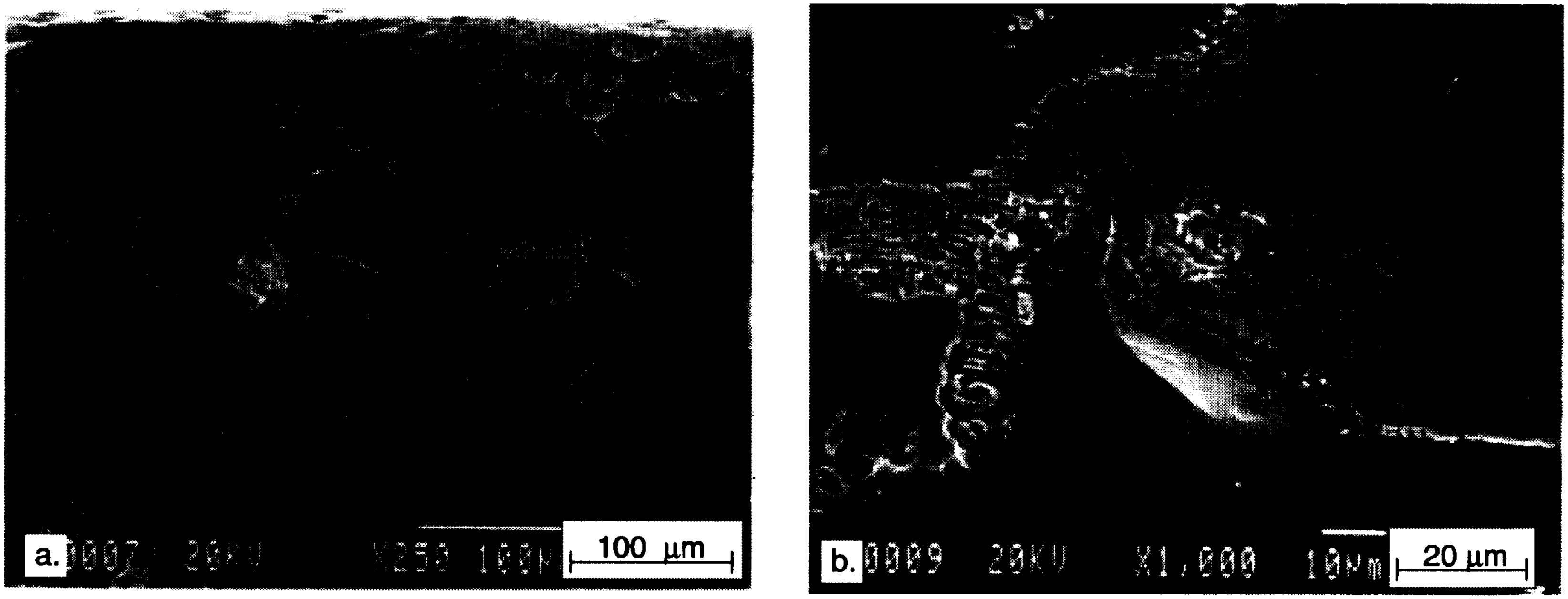

Fig. 29 SEM micrographs after electropolish and chemical milling of AFN23 showing unusual etch features on surface.

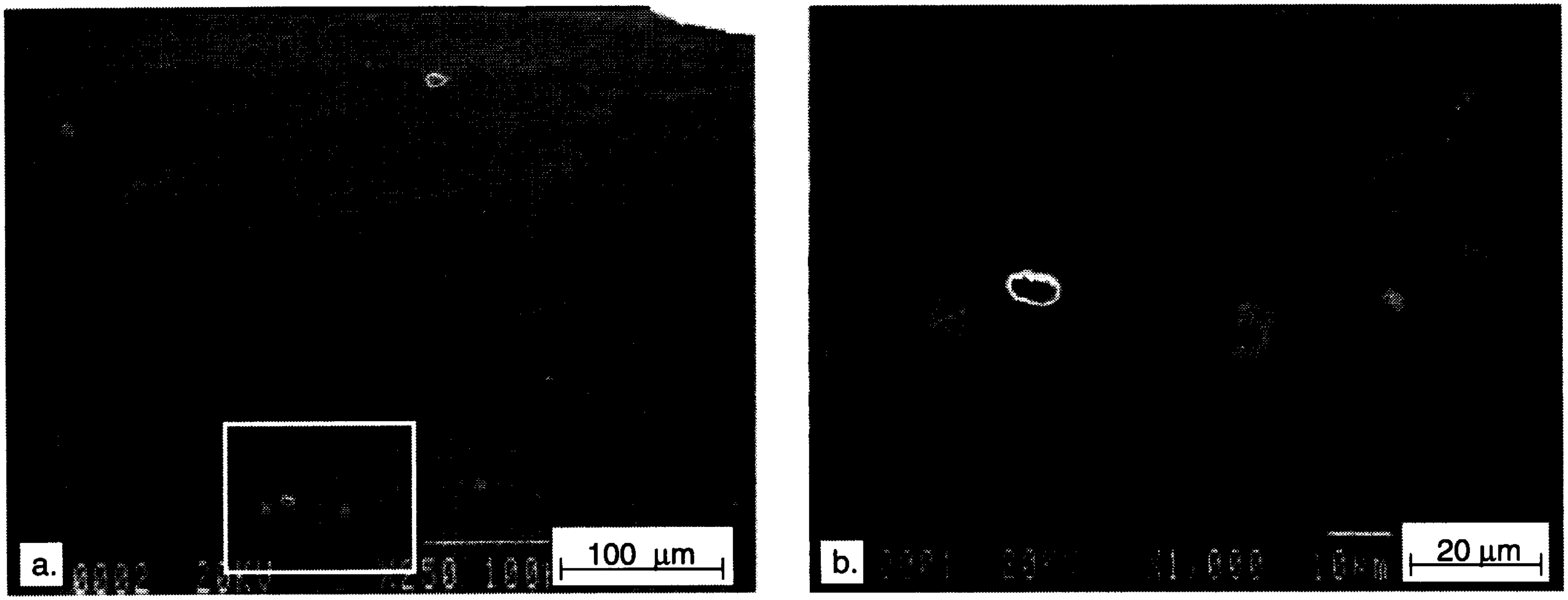

Fig. 30 SEM micrographs of D218 after mechanical polish through 600 grit SiC paper.

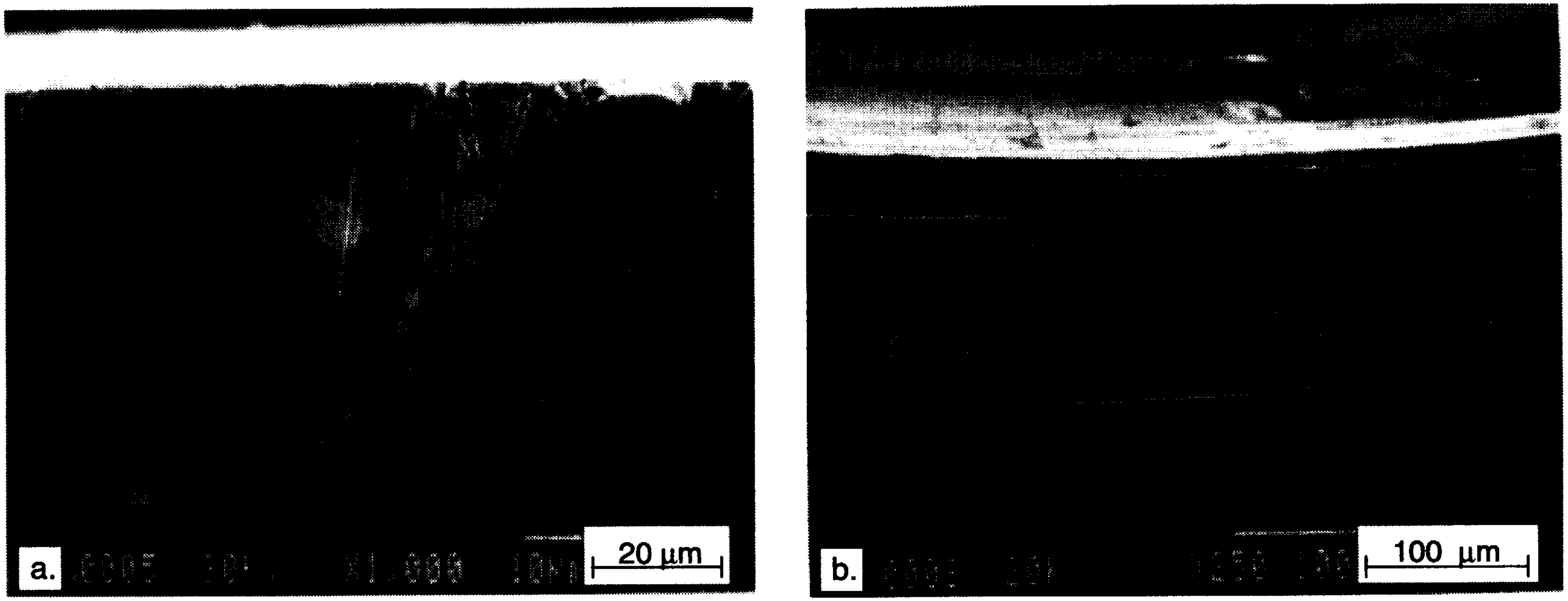

Fig. 31 SEM micrographs of D218 after mechanical polish through 600 grit SiC paper showing polishing marks remaining on the surface.

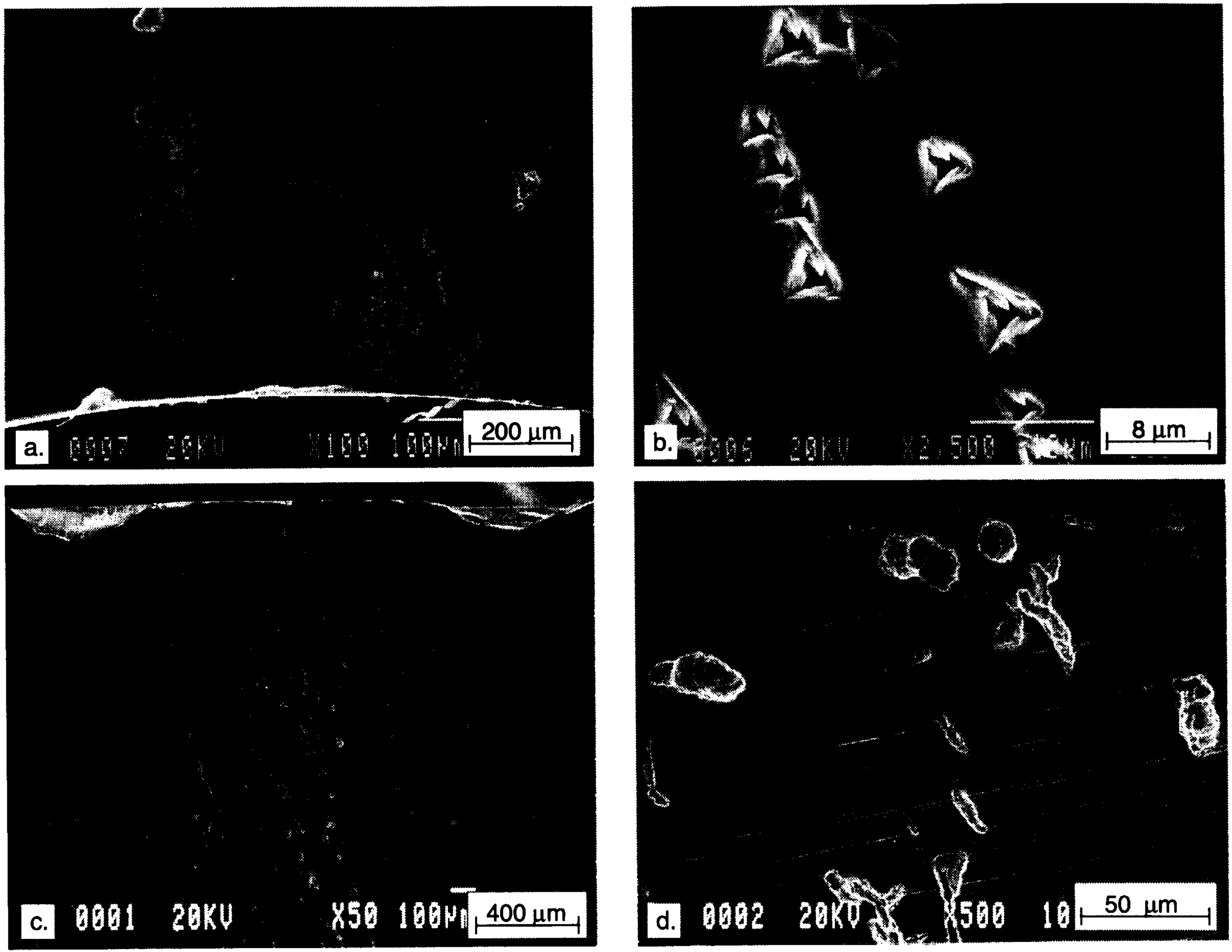

Fig. 32 SEM micrographs after mechanical polish showing fine pores remaining on the surface of (a,b) D218, (c,d,e,f) D219. Images (b,d and f) are magnified views of pores in (a,c and e).

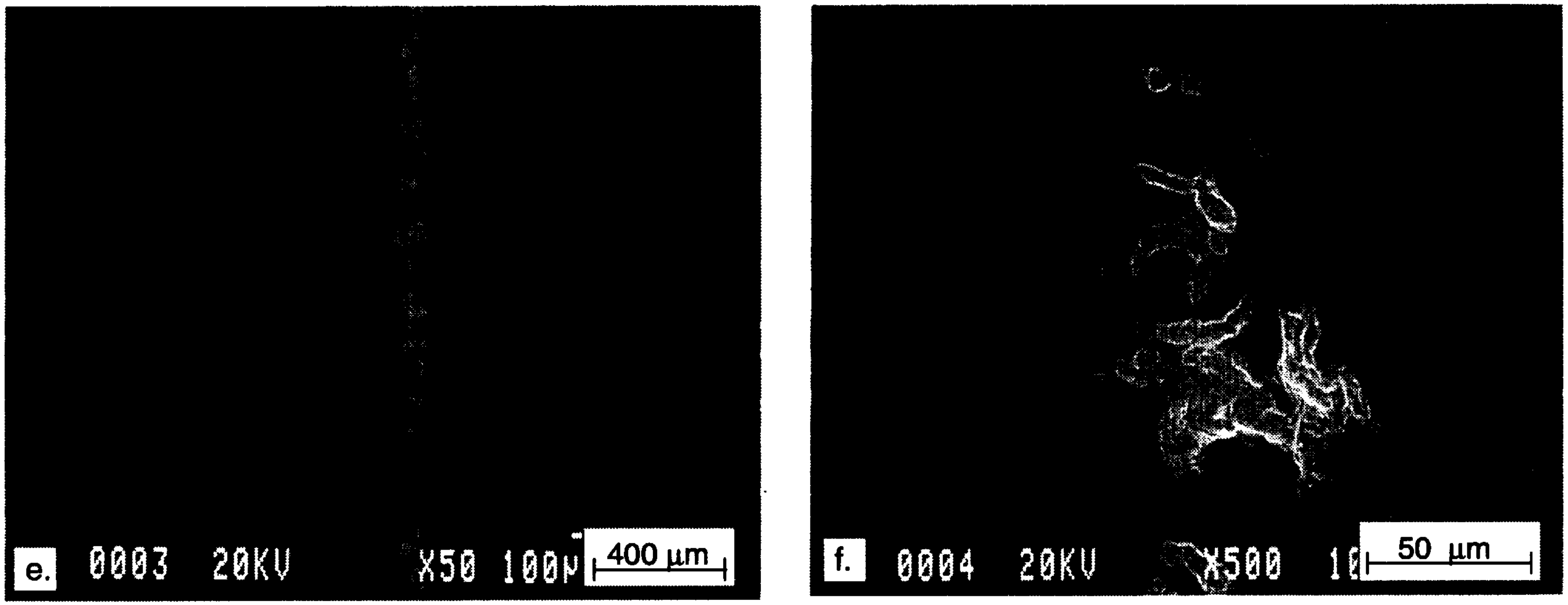

Fig. 32 (cont.) SEM micrographs after mechanical polish showing fine pores remaining on the surface of (a,b) D218, (c,d,e,f) D219. Images (b,d and f) are magnified views of pores in (a,c and e).

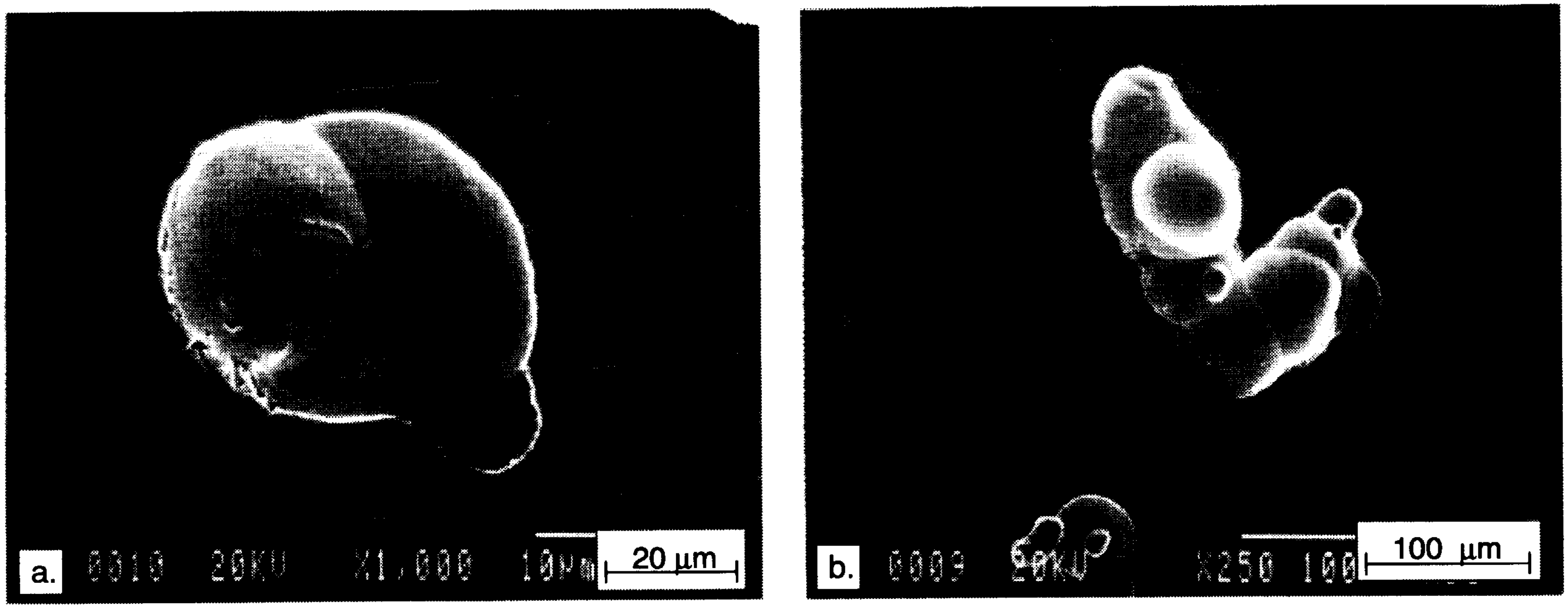

Fig. 33 SEM micrographs after mechanical polish showing large pores remaining on the surface of D218.

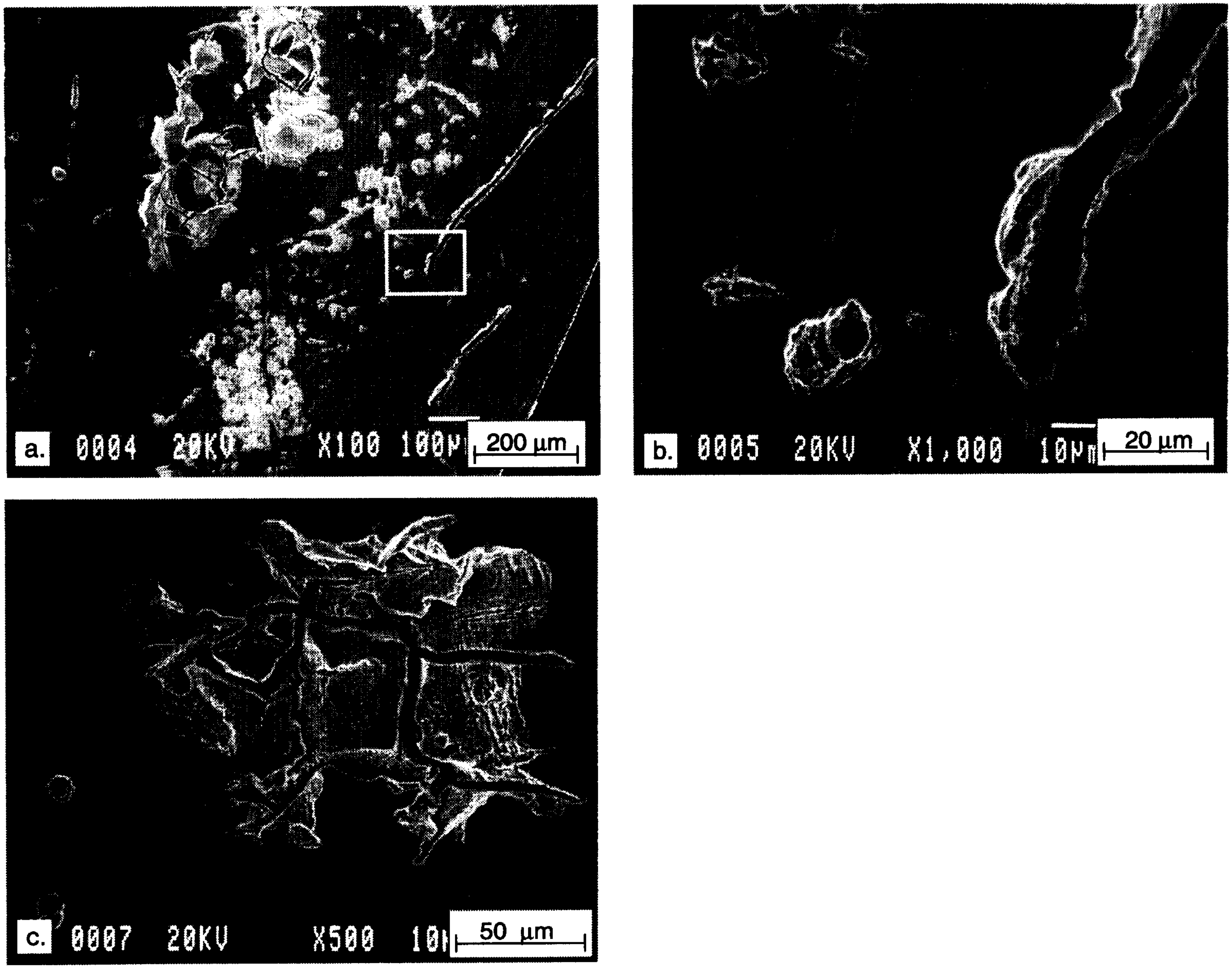

Fig. 34 SEM micrographs after mechanical polish showing large cracks on the surface of D219.

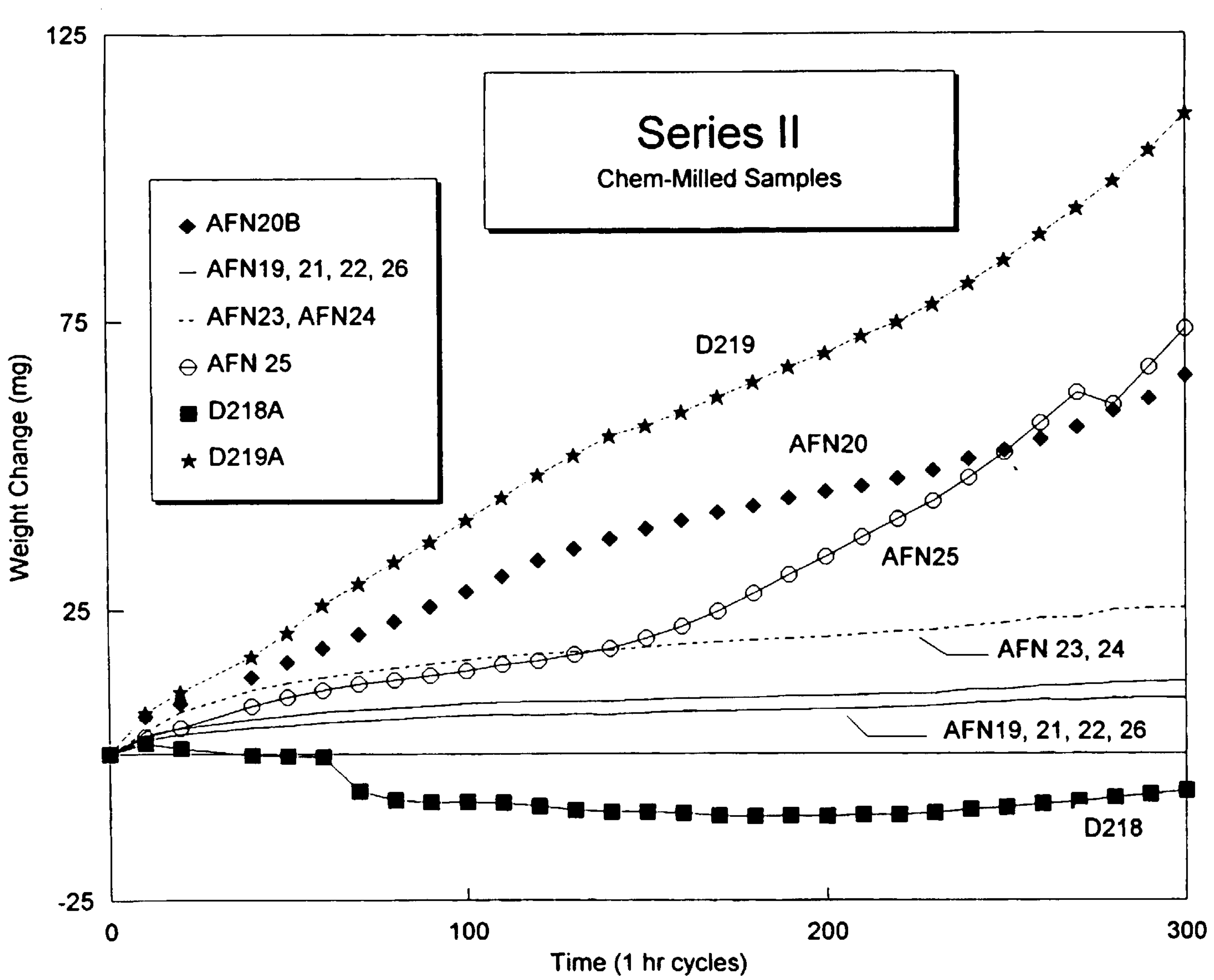

Fig. 35 Weight change during burner rig testing for Series II.

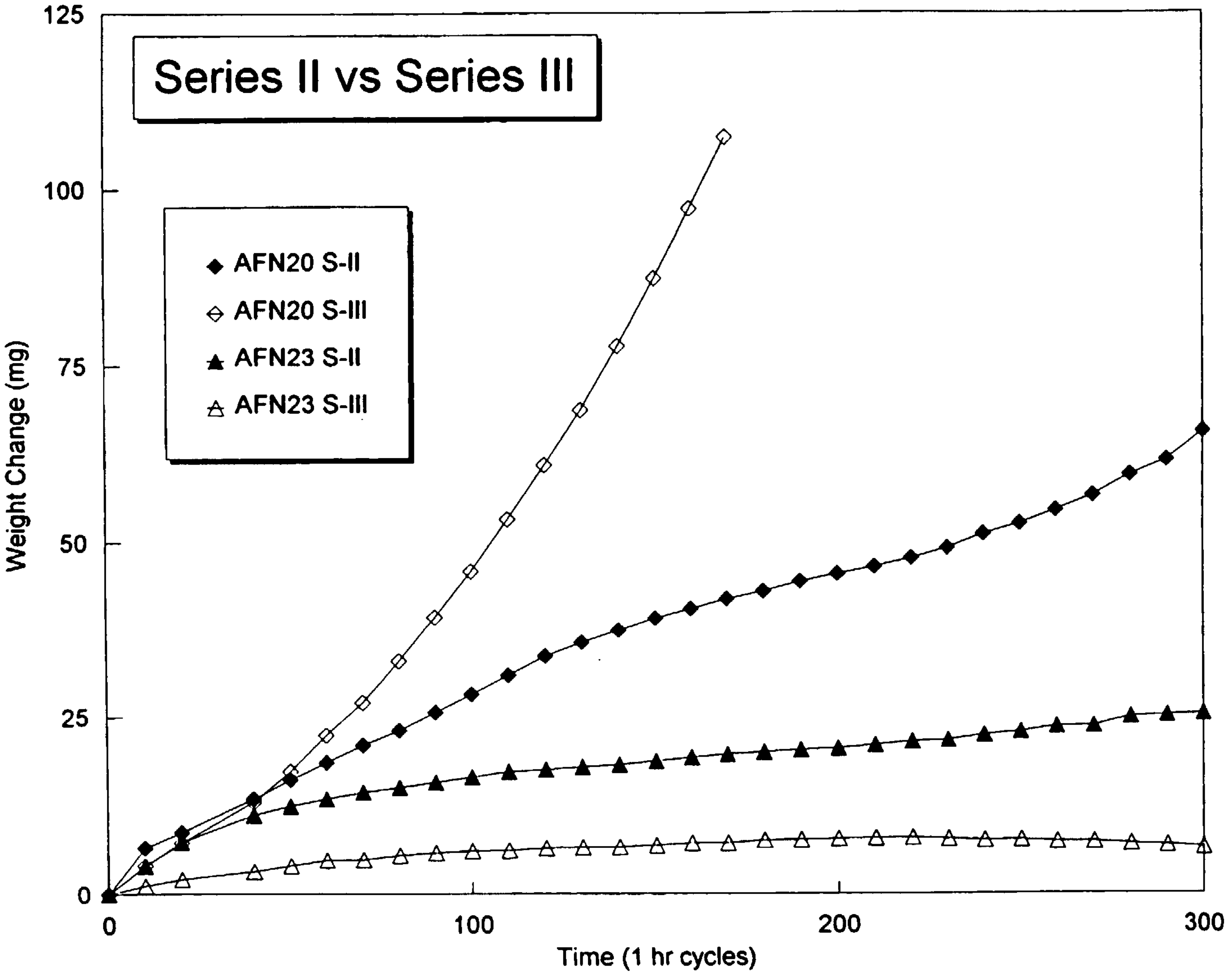

Fig. 36 Weight change during burner rig testing for Series II versus Series III for AFN20 and AFN23 alloys.

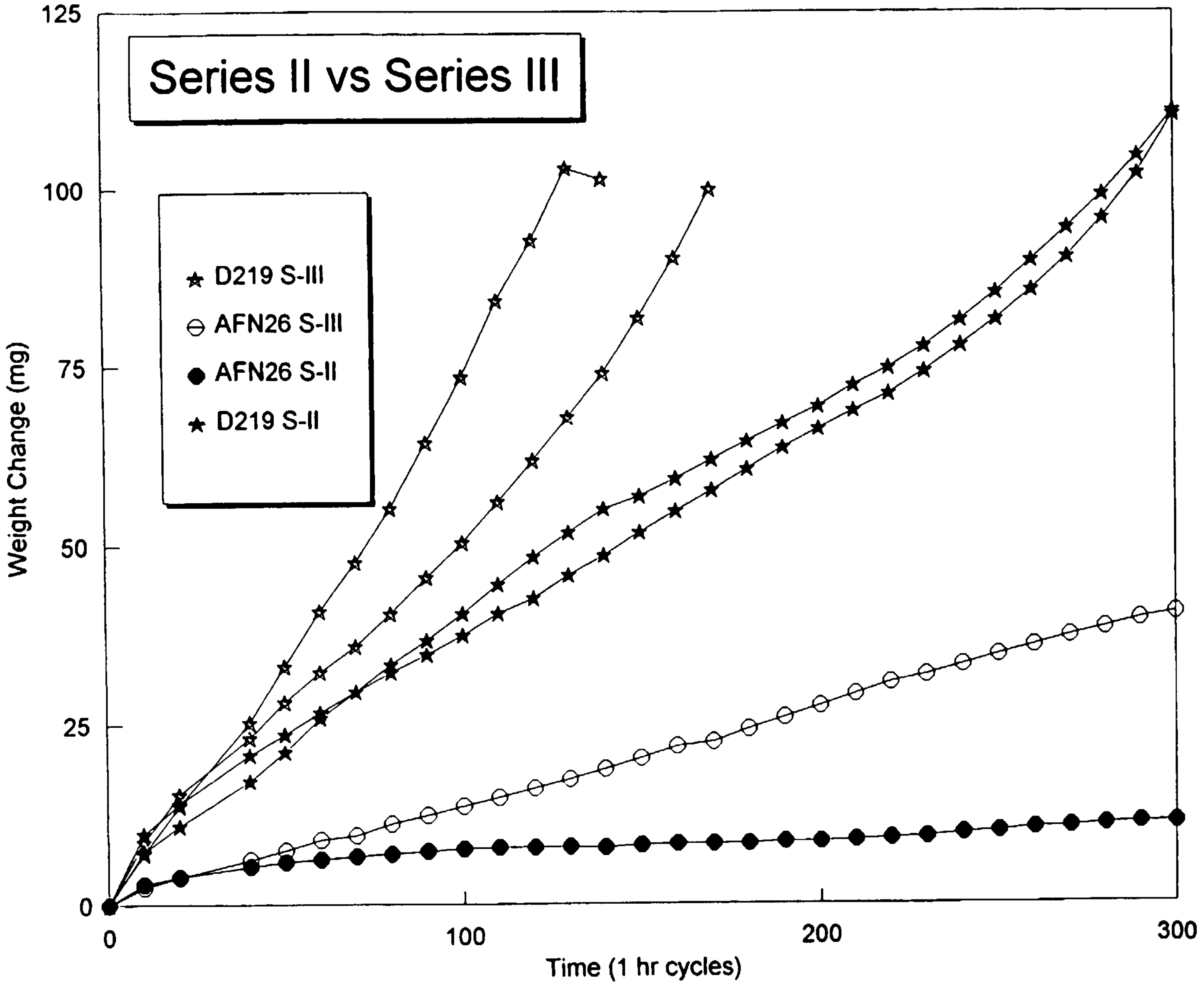

Fig. 37 Weight change during burner rig testing for Series II versus Series III for AFN26 and D219 alloys.

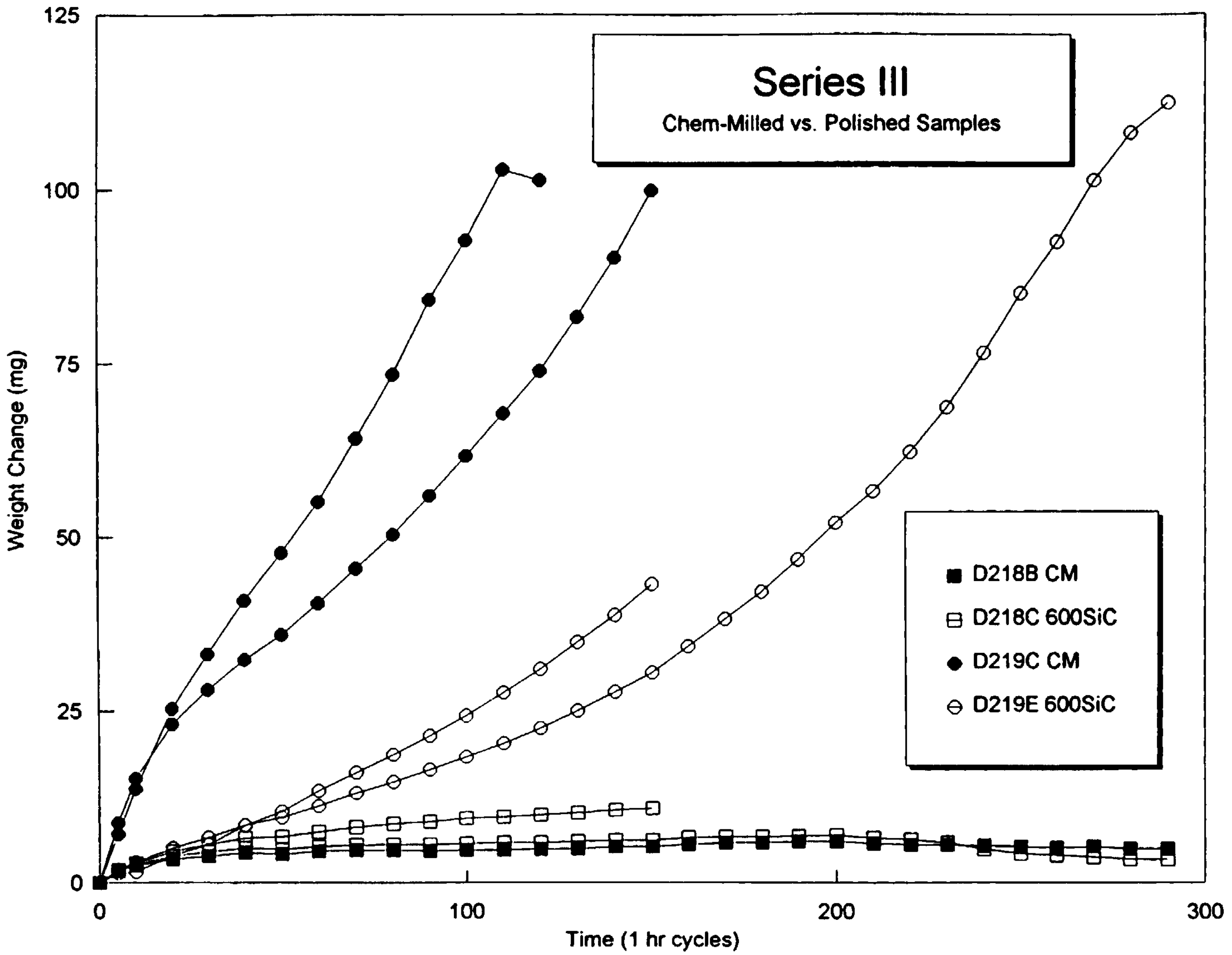

Fig. 38 Weight change during burner rig testing for Series III, chemically milled (CM) versus mechanically polished through 600 grit SiC (600 SiC) surface finishes (D218 and D219 alloys).

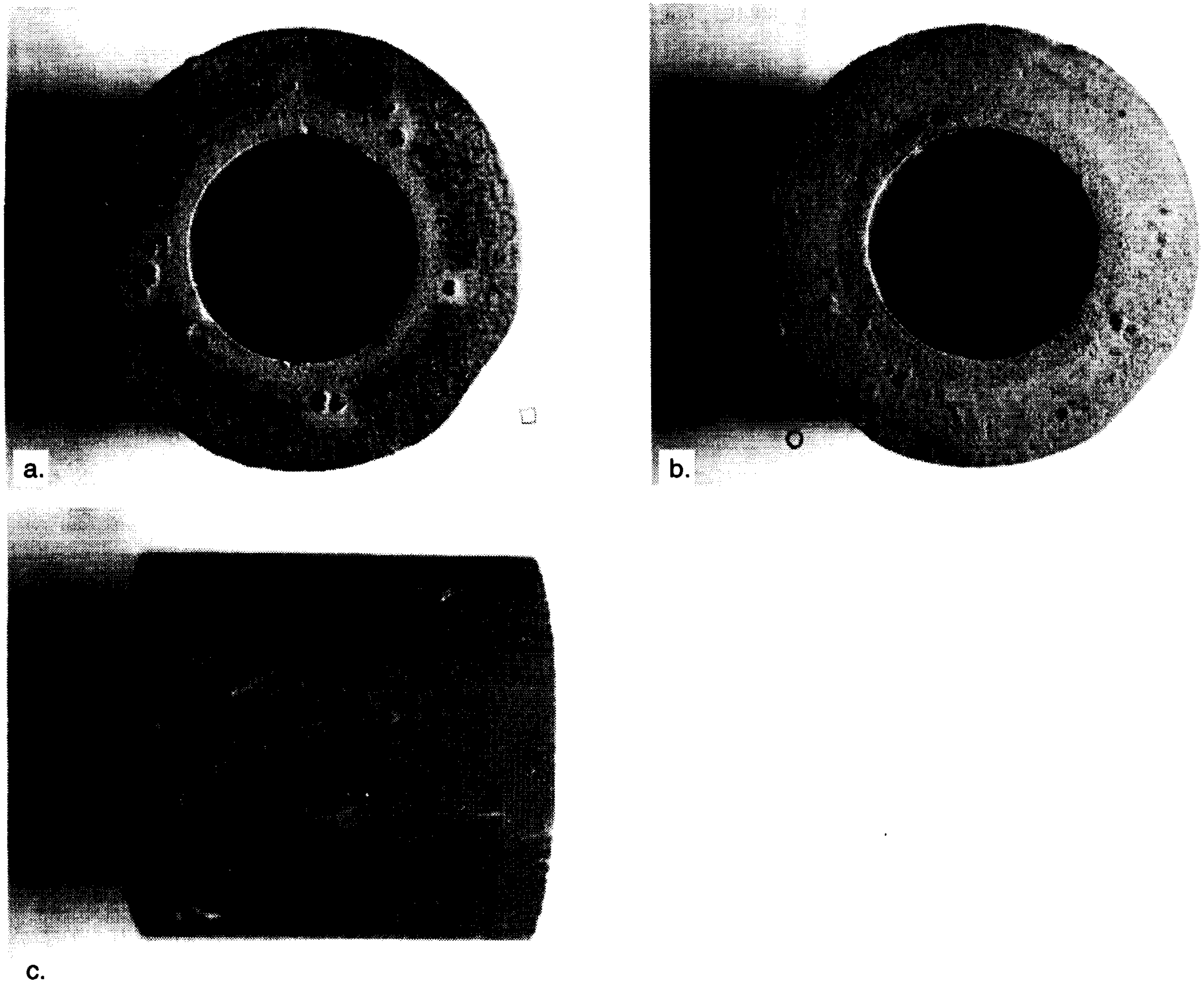

Fig. 39 Optical macrographs of AFN19 after 300 cycles, (a), (b) ends, and (c) curved surface.

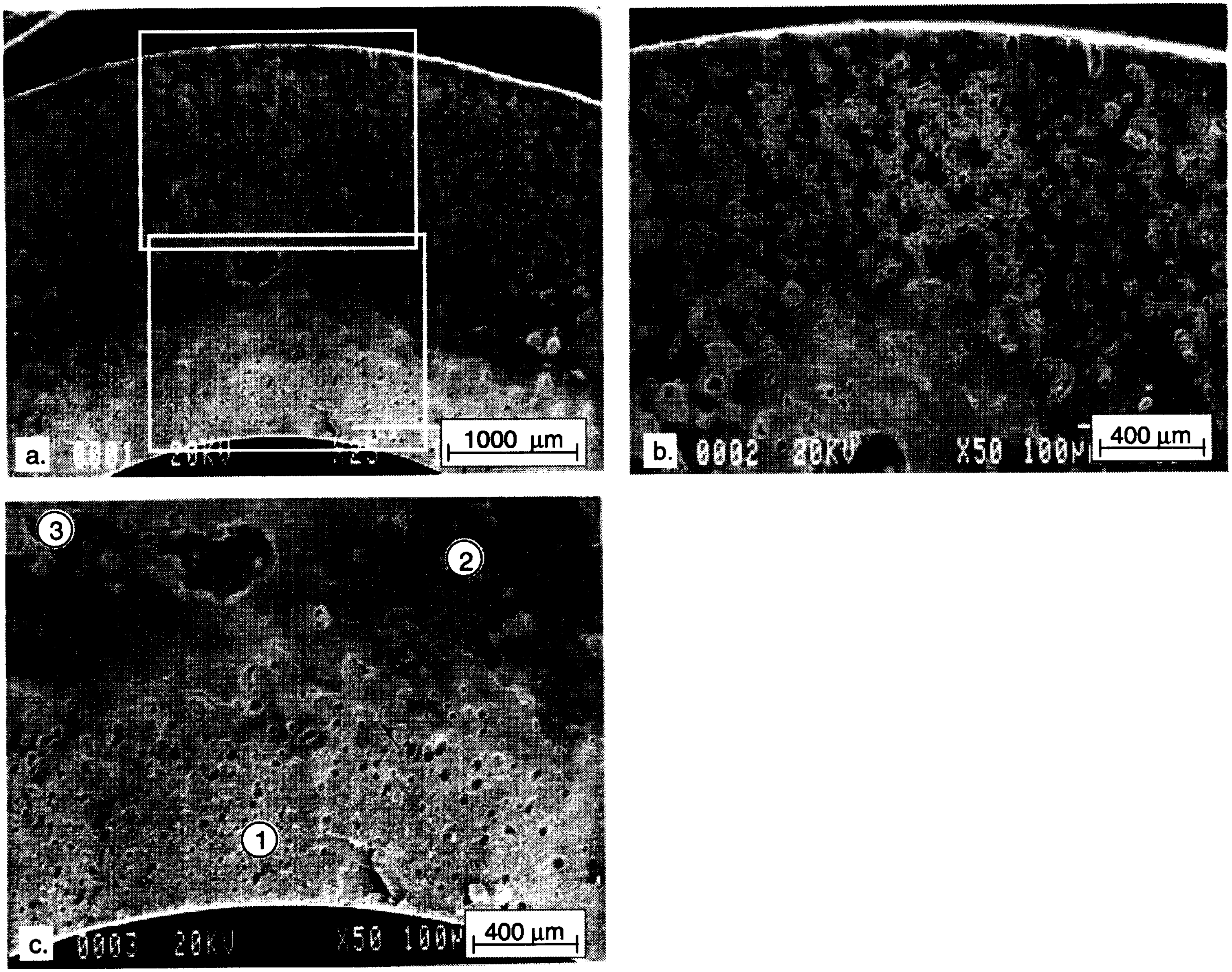

Fig. 40 SEM micrographs of (a) end of AFN19 shown in Fig. 39a, (b) and (c) are magnified views of the ID and OD edges. Arrow in (b) points to a corrosion mound.

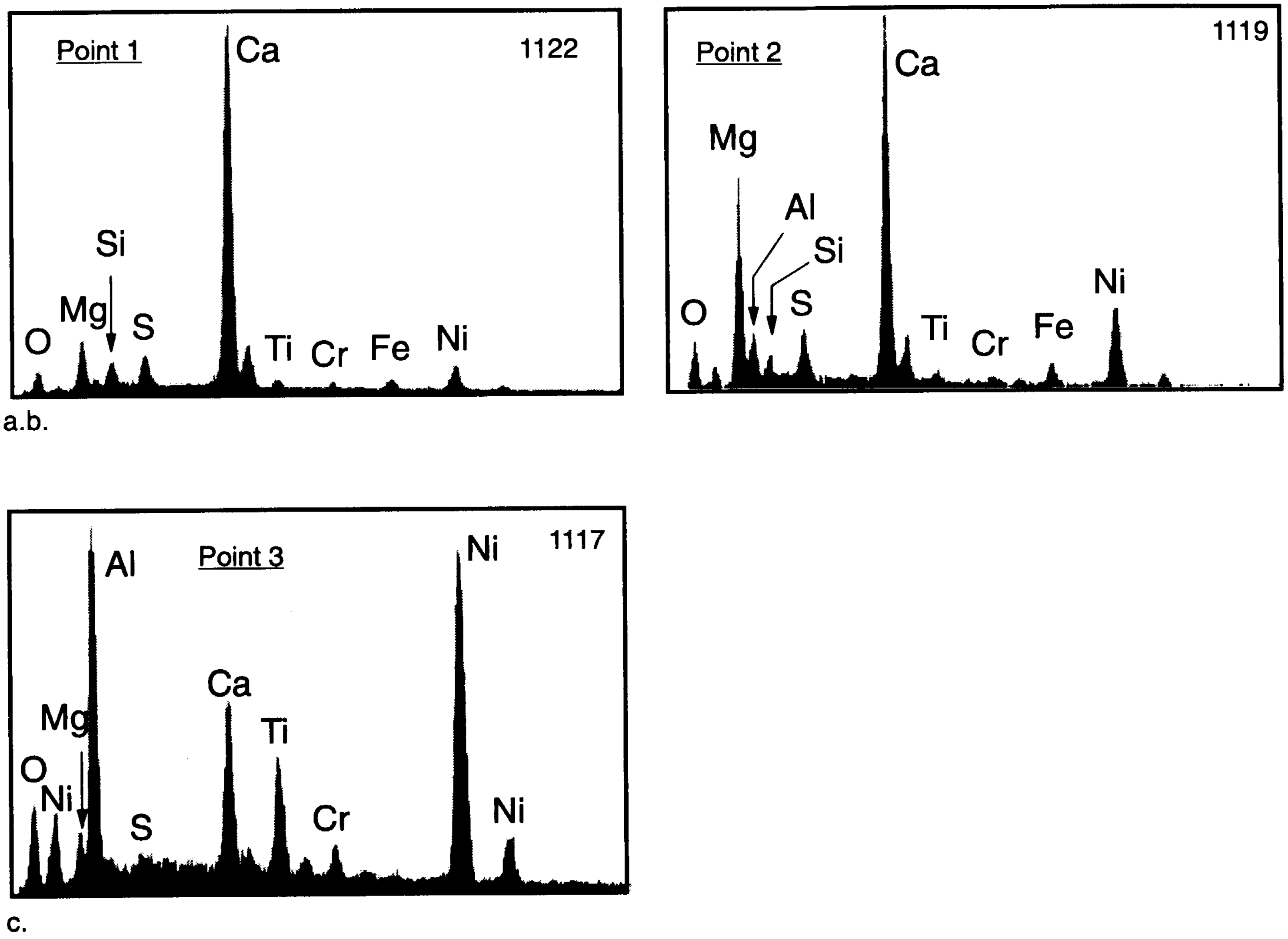

Fig. 41 EDS spectra of (a) point 1, (b) point 2, (c) point 3 shown in Fig. 40b.

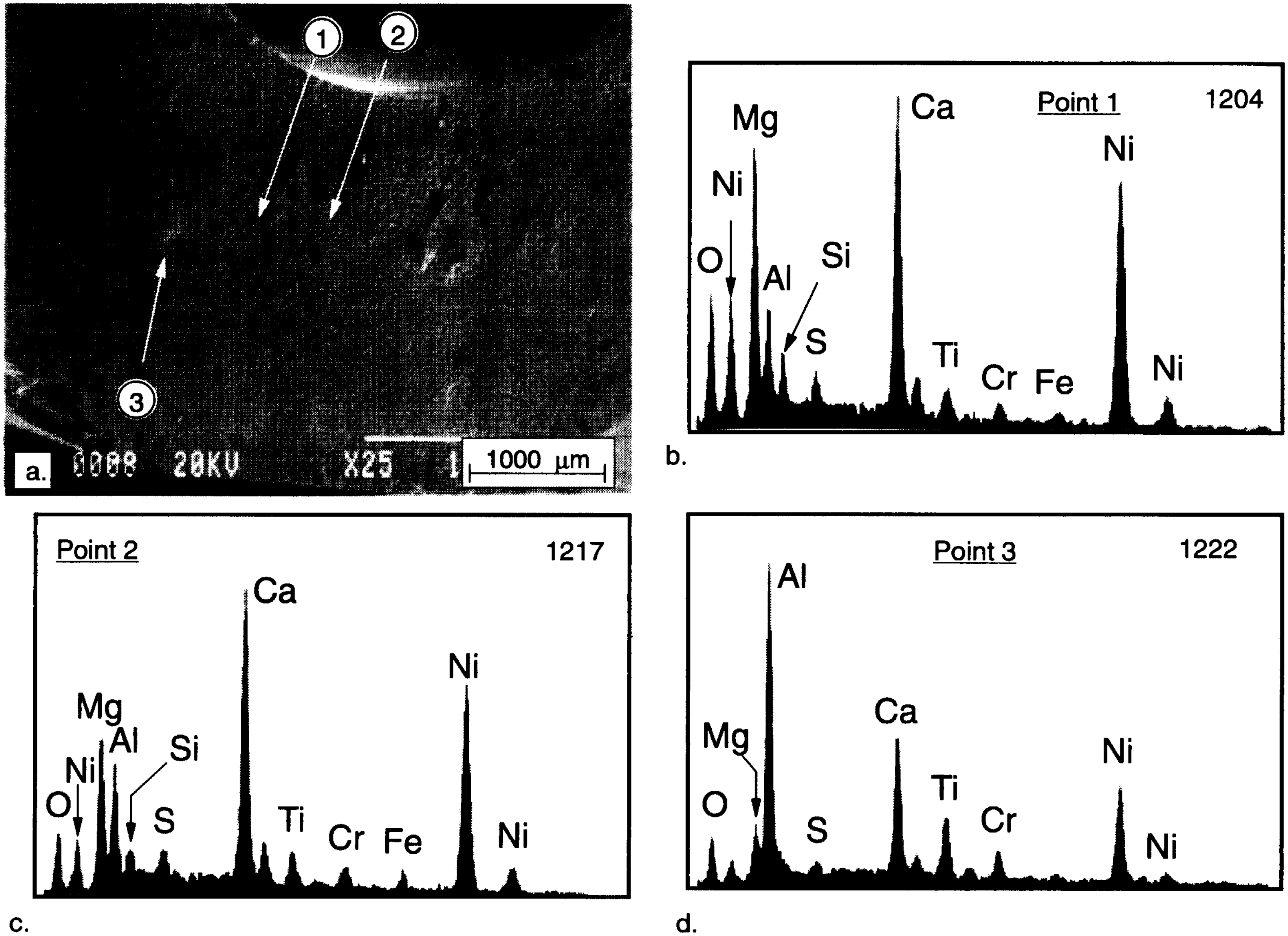

Fig. 42 SEM micrograph of (a) end of AFN19 shown in Fig. 39b (b), (c) and (d) are EDS spectra of points 1, 2 and 3 in (a). Black arrows in (a) point to corrosion mounds.

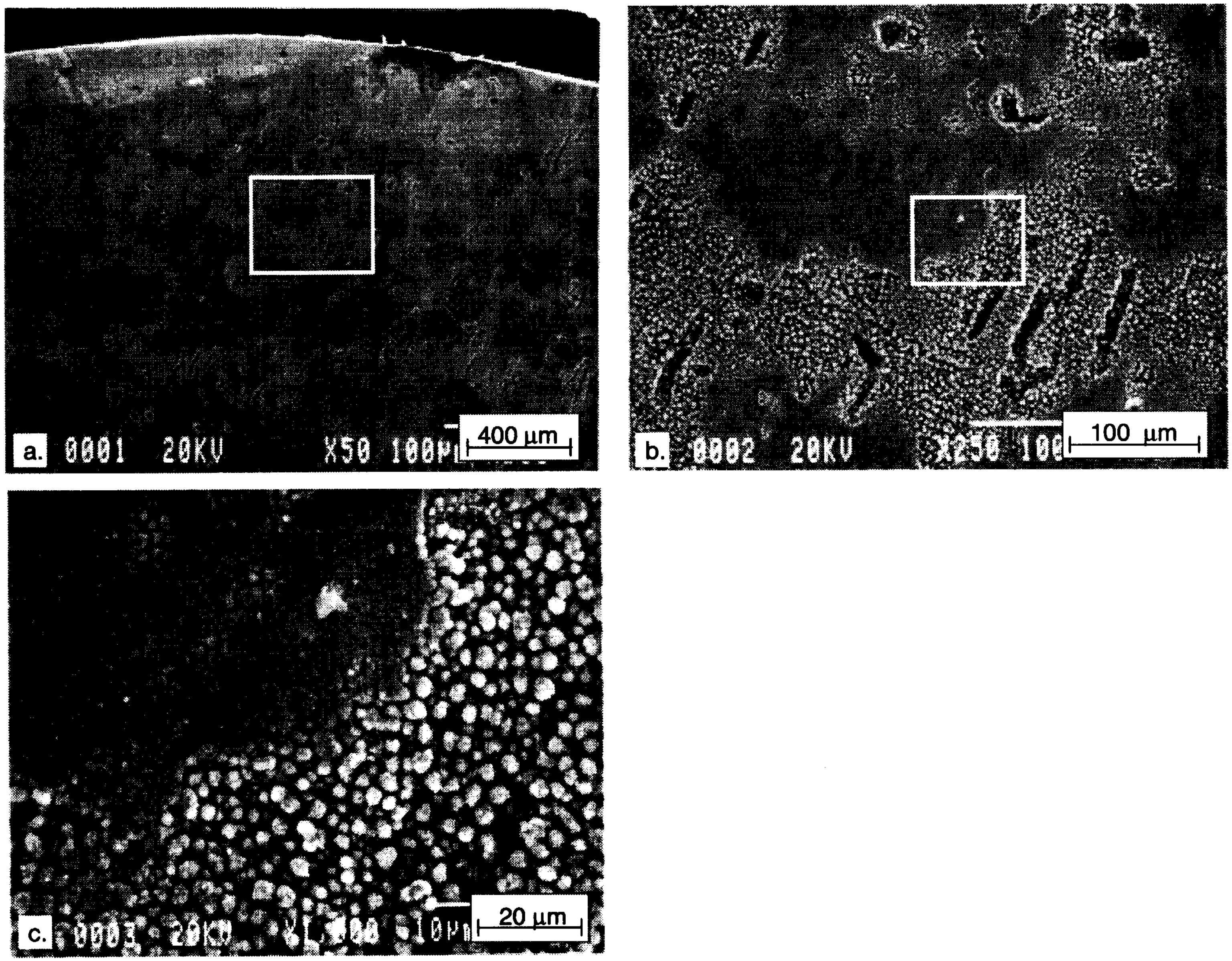

Fig. 43 SEM micrographs of end 2 of AFN19 after 300 cycles, (b) and (c) are magnified views of (a) and (b).

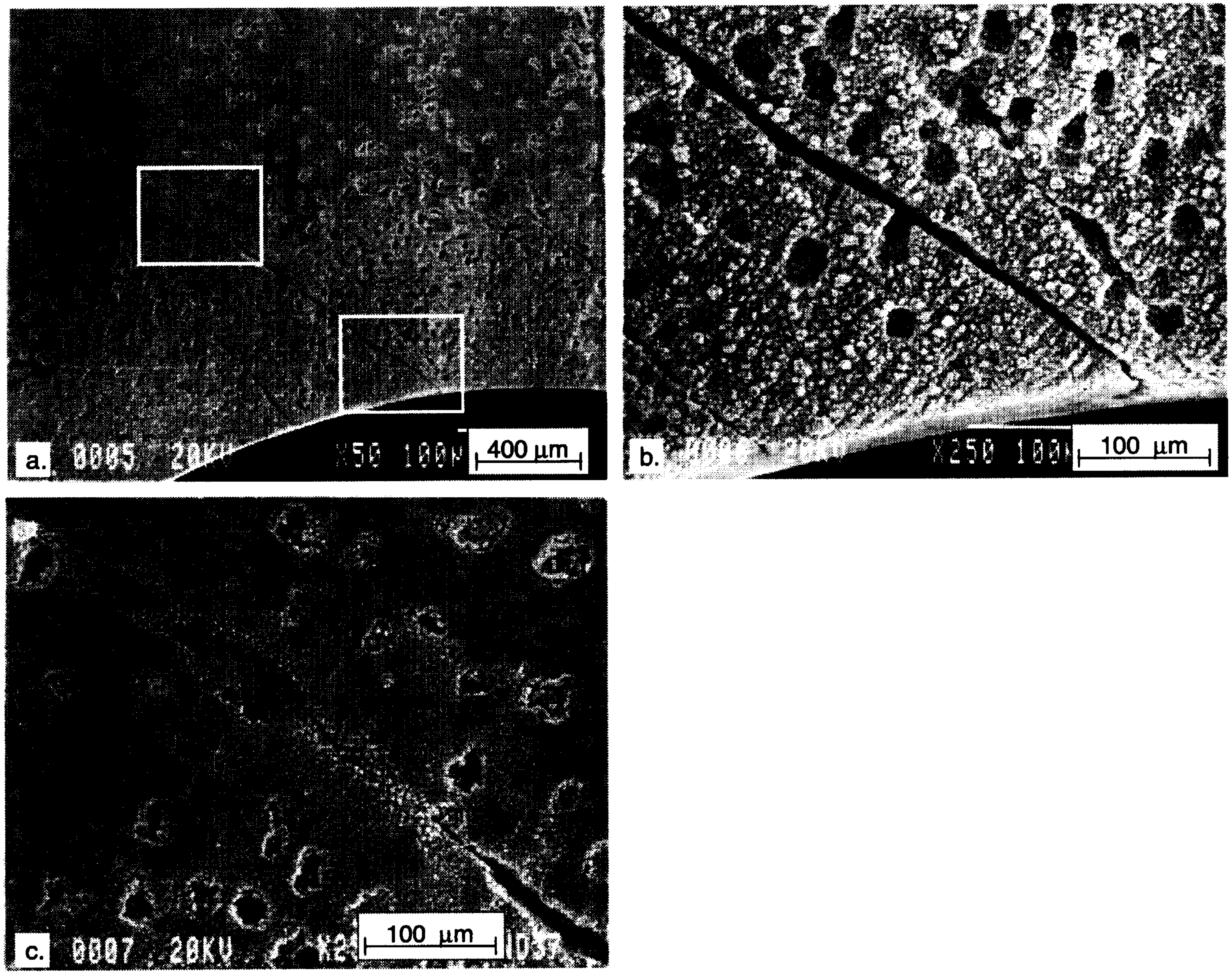

Fig. 44 SEM micrographs of end 2 near the ID edge of AFN19 after 300 cycles, (b) and (c) are magnified views of (a) and (b).

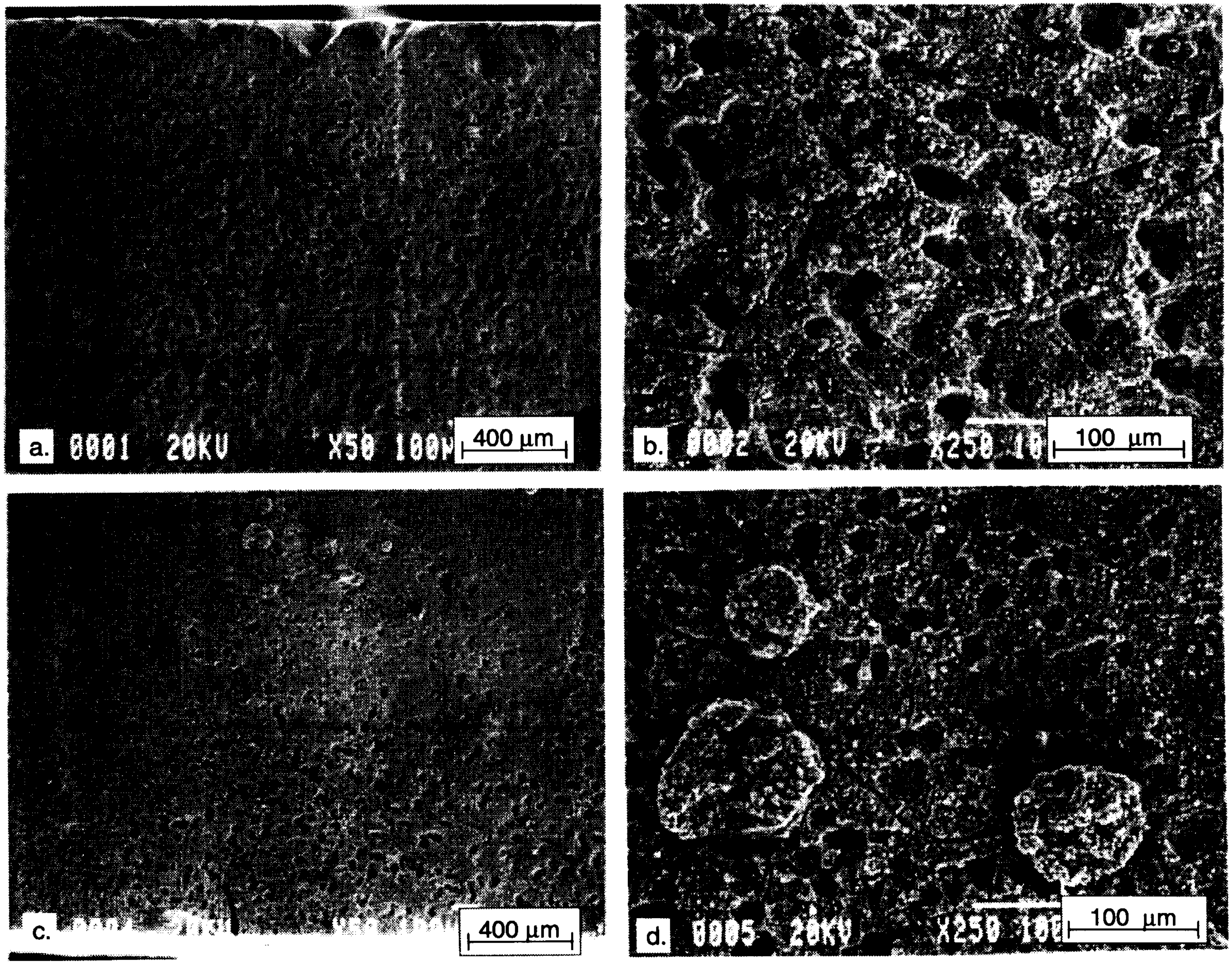

Fig. 45 SEM micrographs of the curved surfaces near each end of AFN19 after 300 cycles, (b) and (d) are magnified views of (a) and (c). The large particles in (d) are rich in Fe and Ca.

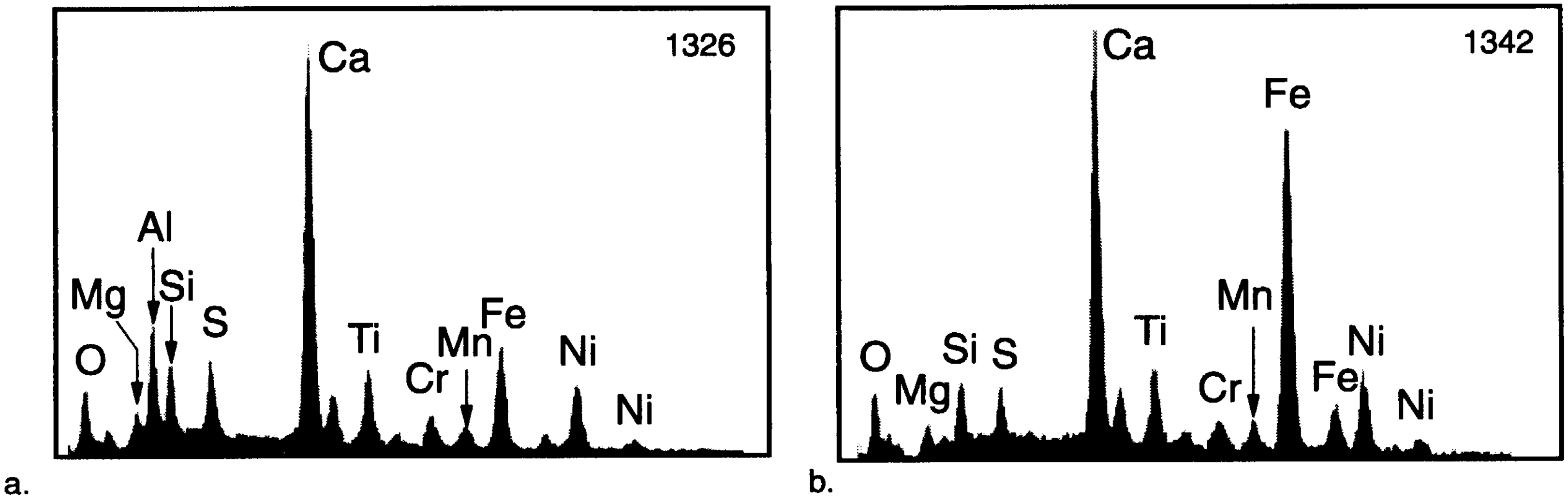

Fig. 46 EDS spectra of (a) the porous regions shown in Fig. 45a,b, and (b) the large particles in (d).

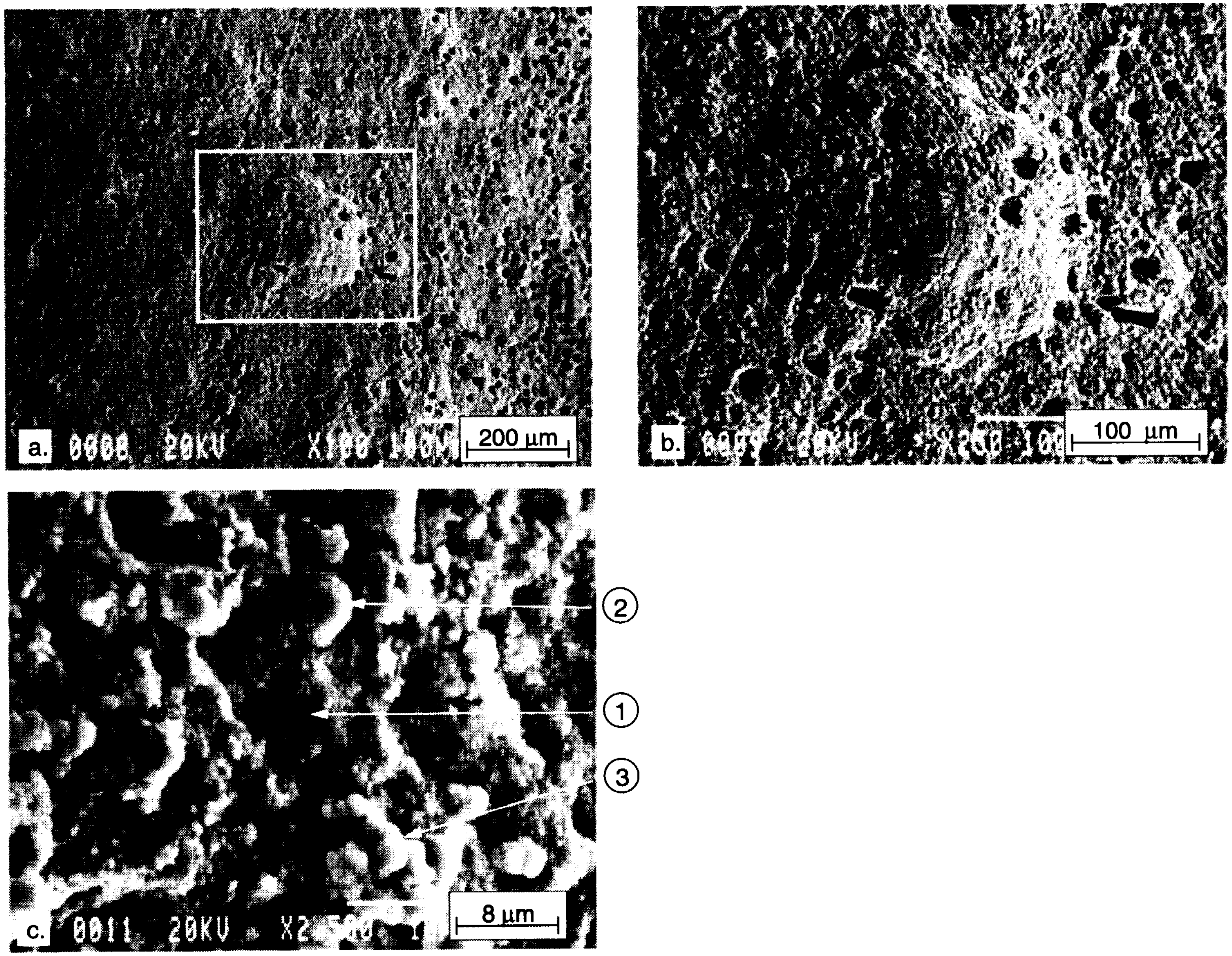

Fig. 47 SEM micrographs of the curved surfaces of AFN19 after 300 cycles showing corrosion mounds (b) is a magnified view of (a) and (c) is a magnified view of the top of mound in (b).

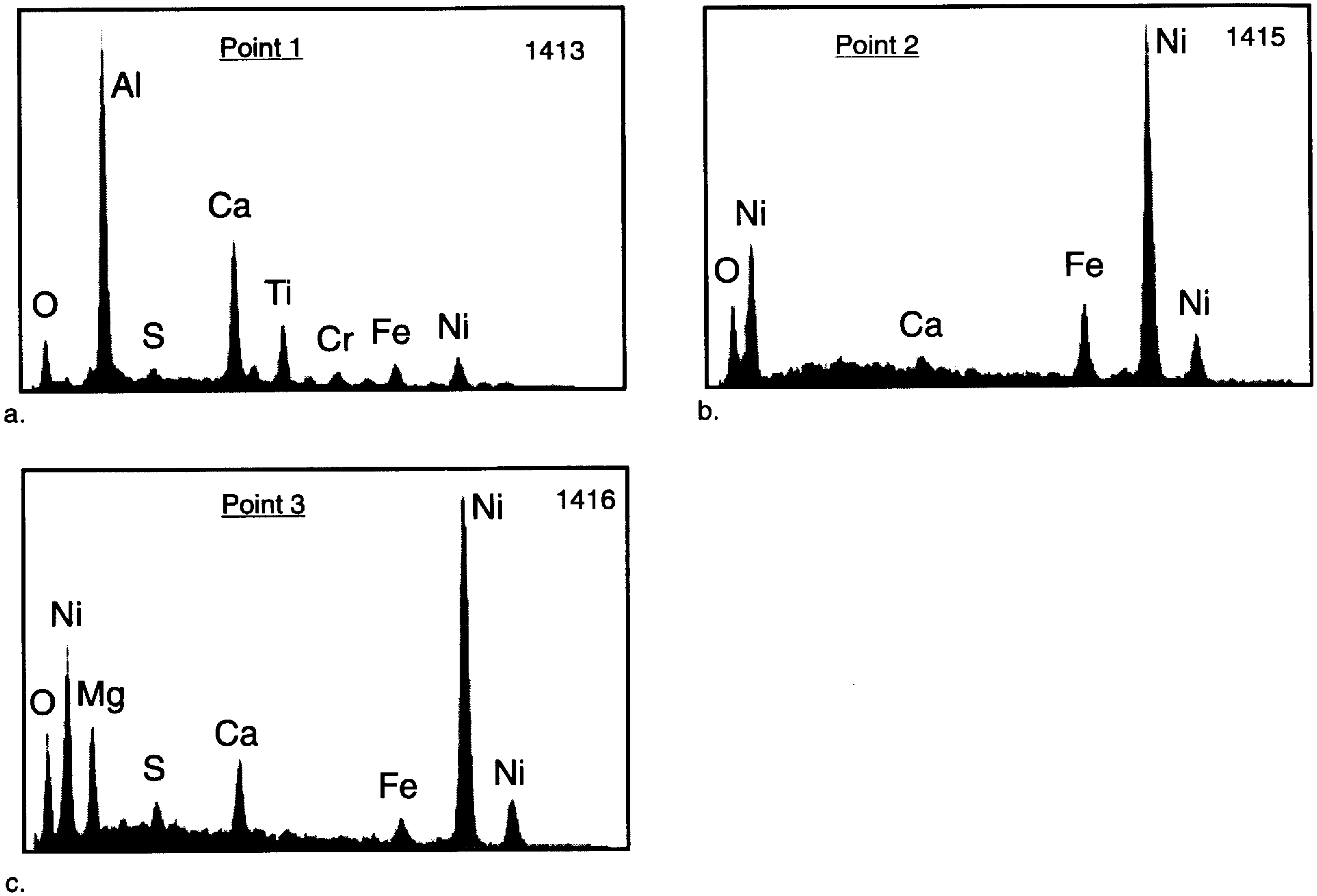

Fig. 48 EDS spectra of points (1), (2) and (3) in Fig. 47c.

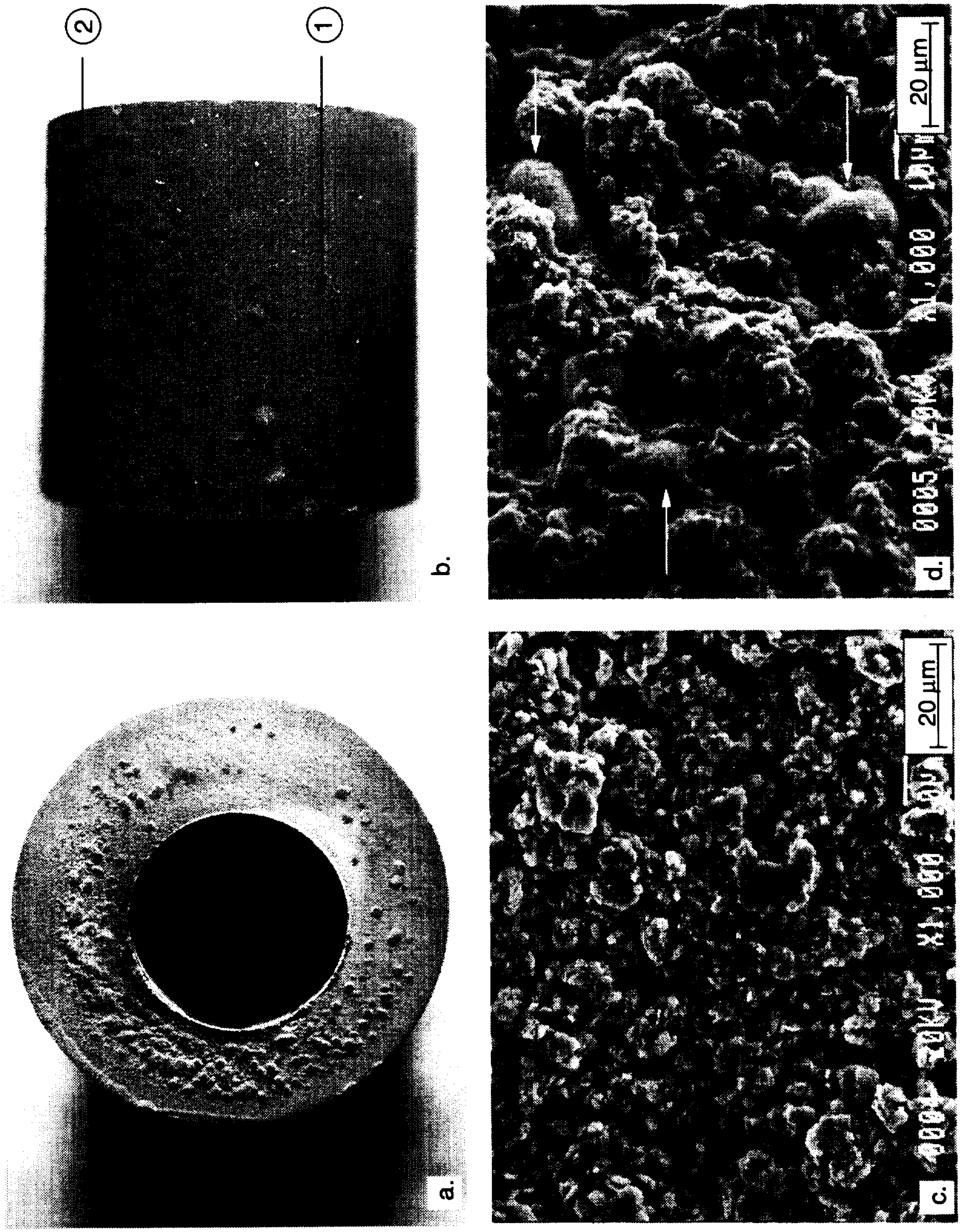

Fig. 49 Optical (a,b) and SEM micrographs of AFN23 after 300 cycles showing the (c) smooth scale in region indicated "1" and (d) rough scale in region indicated "2" with arrows indicating NiO.

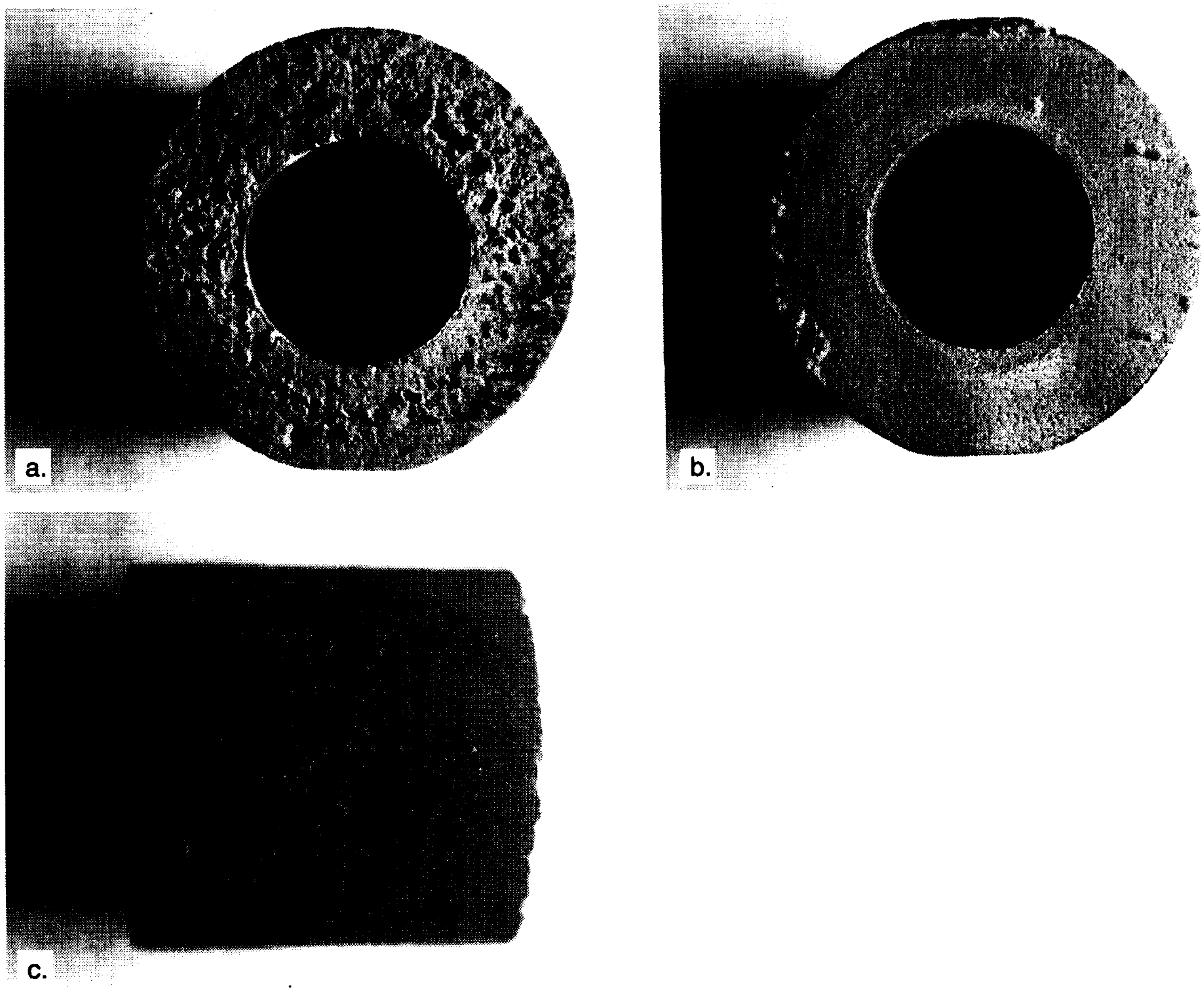

Fig. 50 Optical macrographs of the ends and curved surface of AFN24 after 300 cycles.

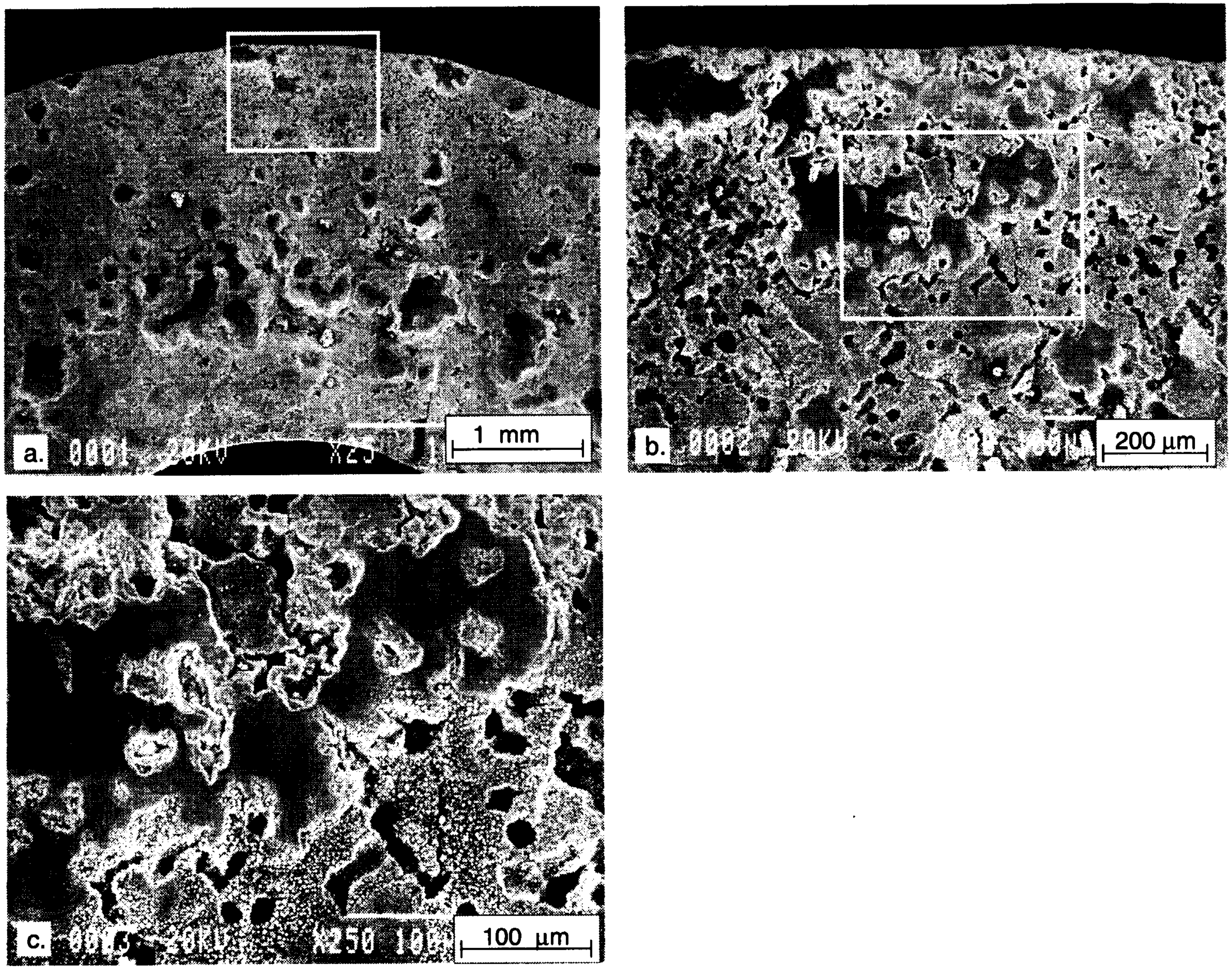

Fig. 51 SEM micrographs of the end of AFN24 after 300 cycles, (b) and (c) are magnified views of (a) and (b), respectively.

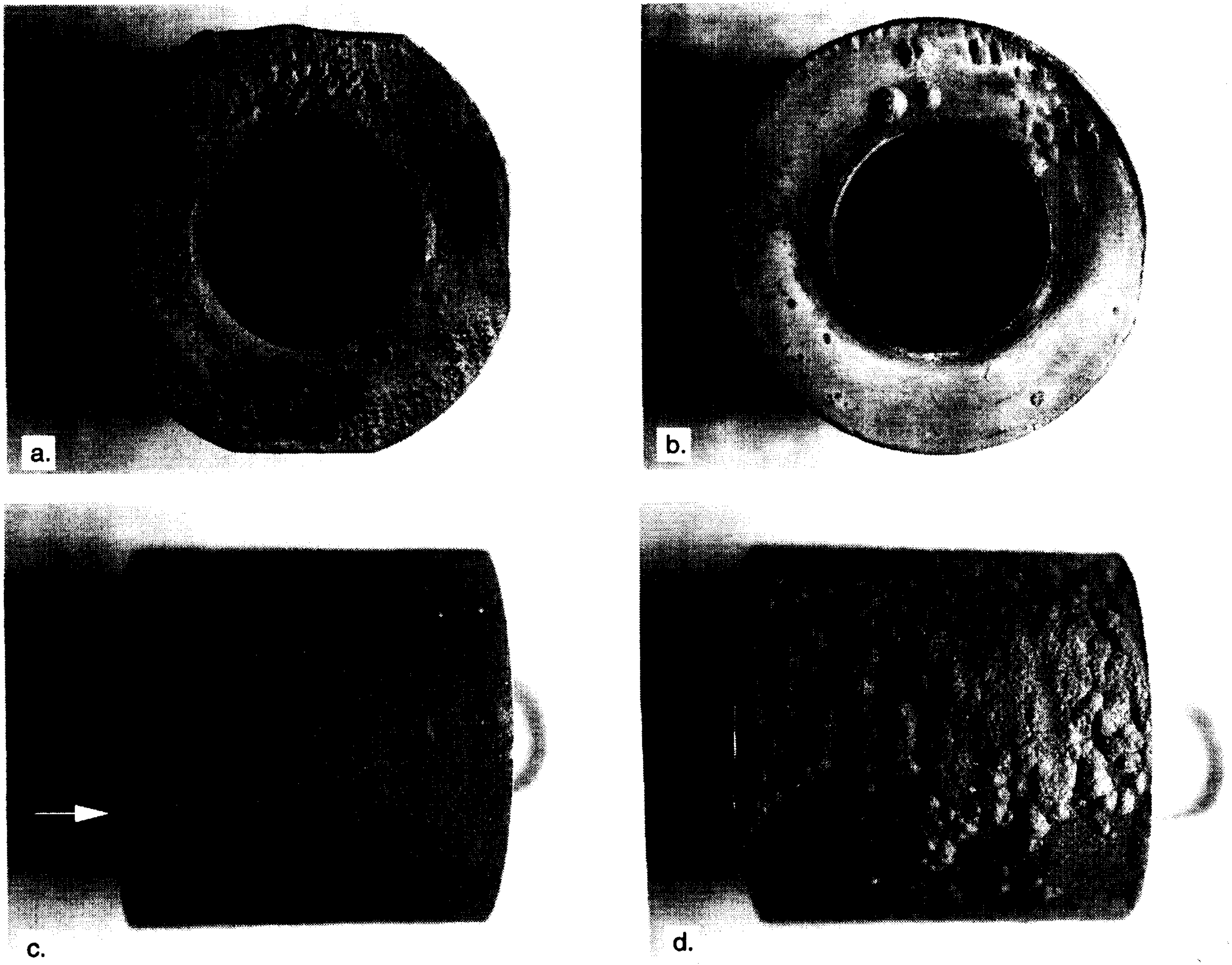

Fig. 52 Macrophotographs of the same AFN25 sample as shown in Fig. 11 after 200 hrs of testing. The arrow in (c) shows the same irregular region on the curved surface as in Fig. 11b.

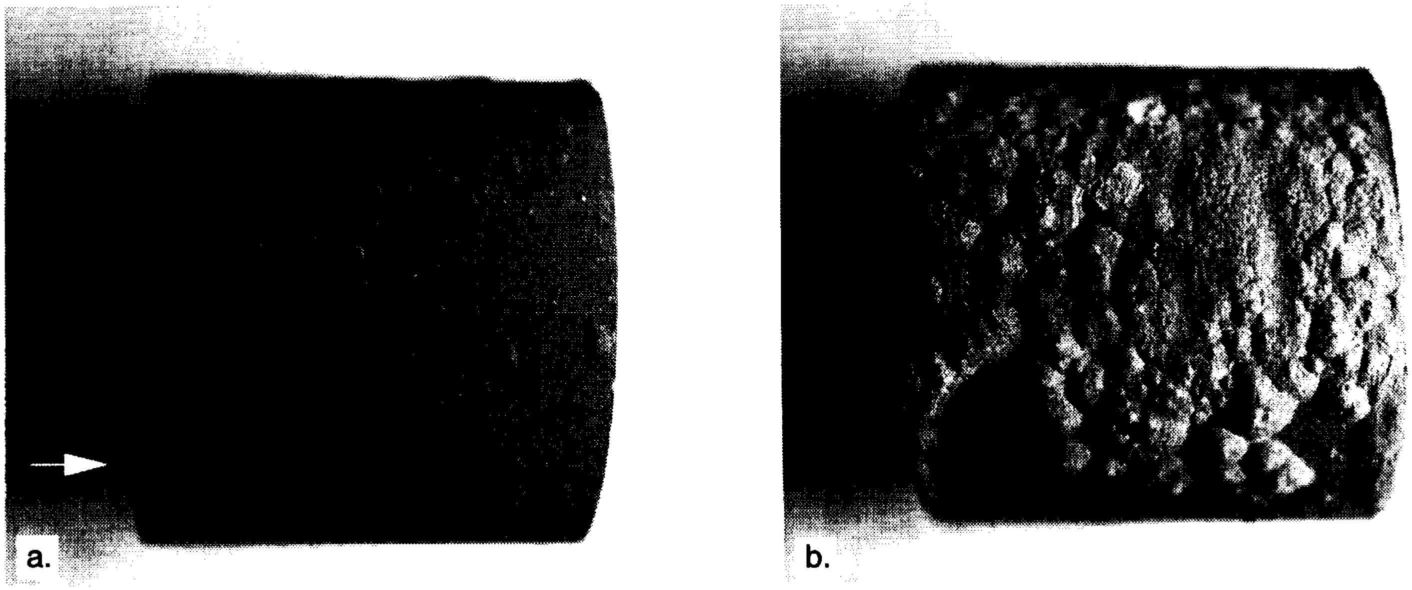

Fig. 53 Macrophotographs of AFN25 sample after 300 hrs. The arrow in (a) shows the same irregular region as in Fig. 52c and Fig. 11b.

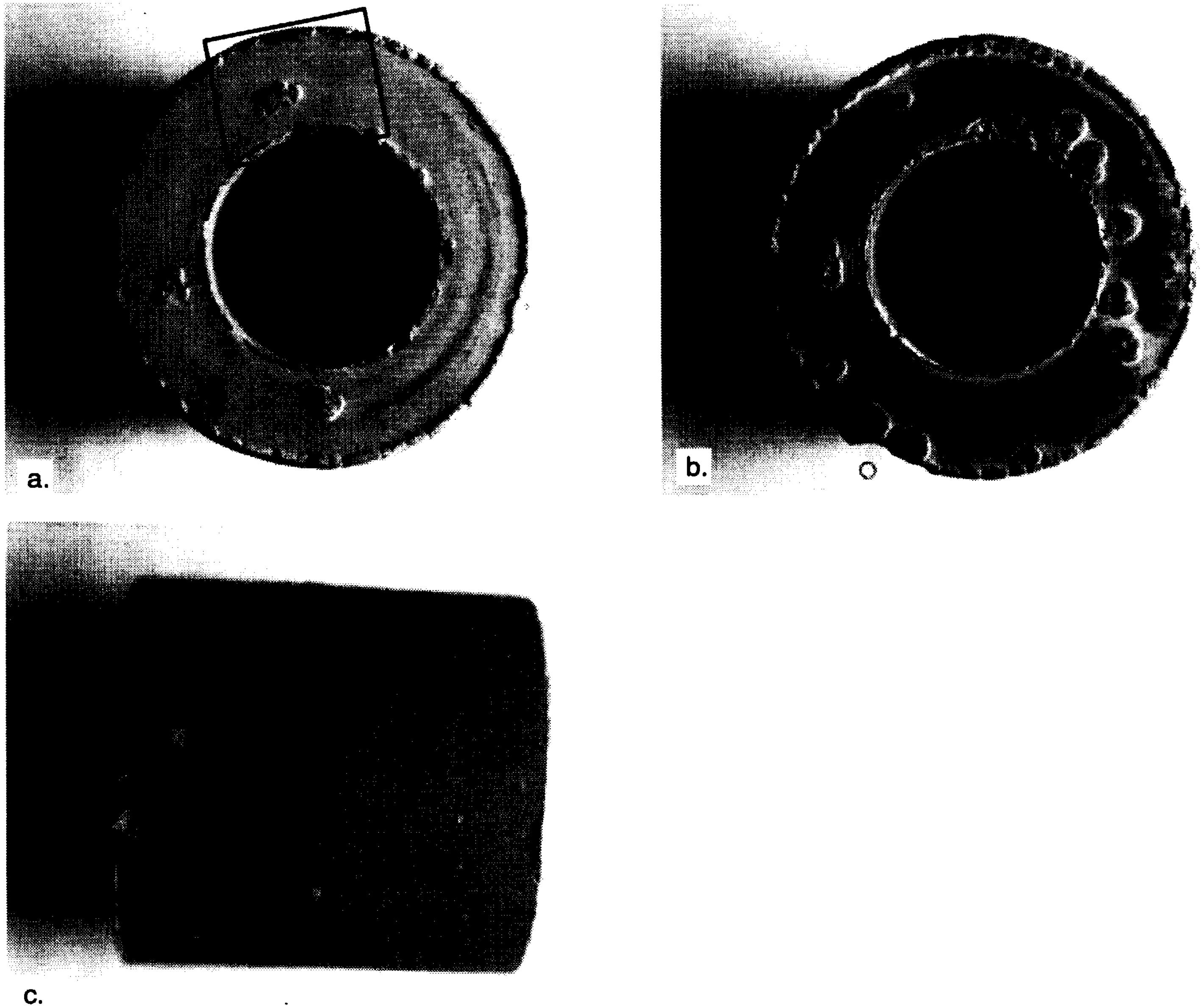

Fig. 54 Optical macrographs of D218 after 300 cycles. Box in (a) shows area of view in Fig. 55a.

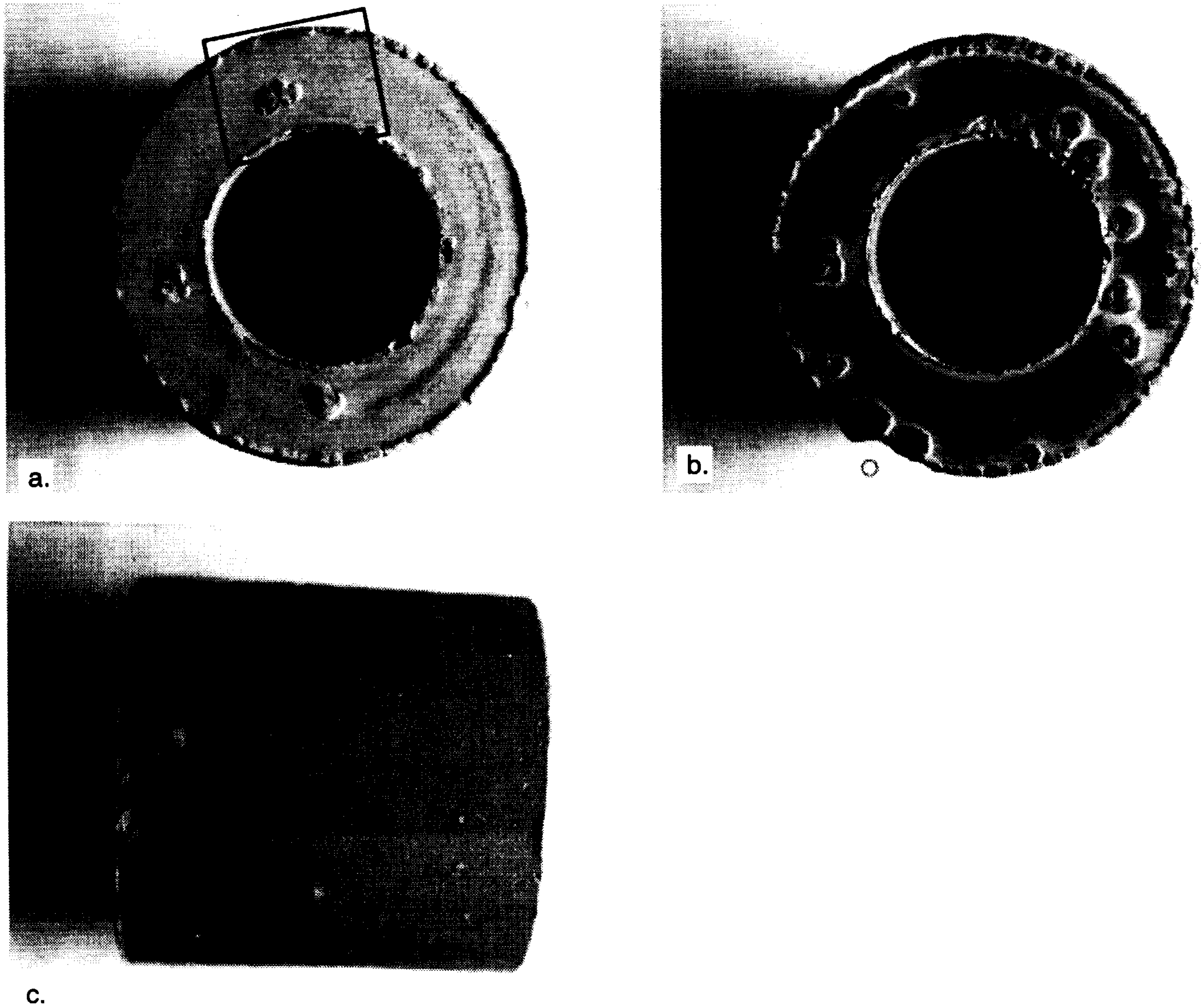

Fig. 54 Optical macrographs of D218 after 300 cycles. Box in (a) shows area of view in Fig. 55a.

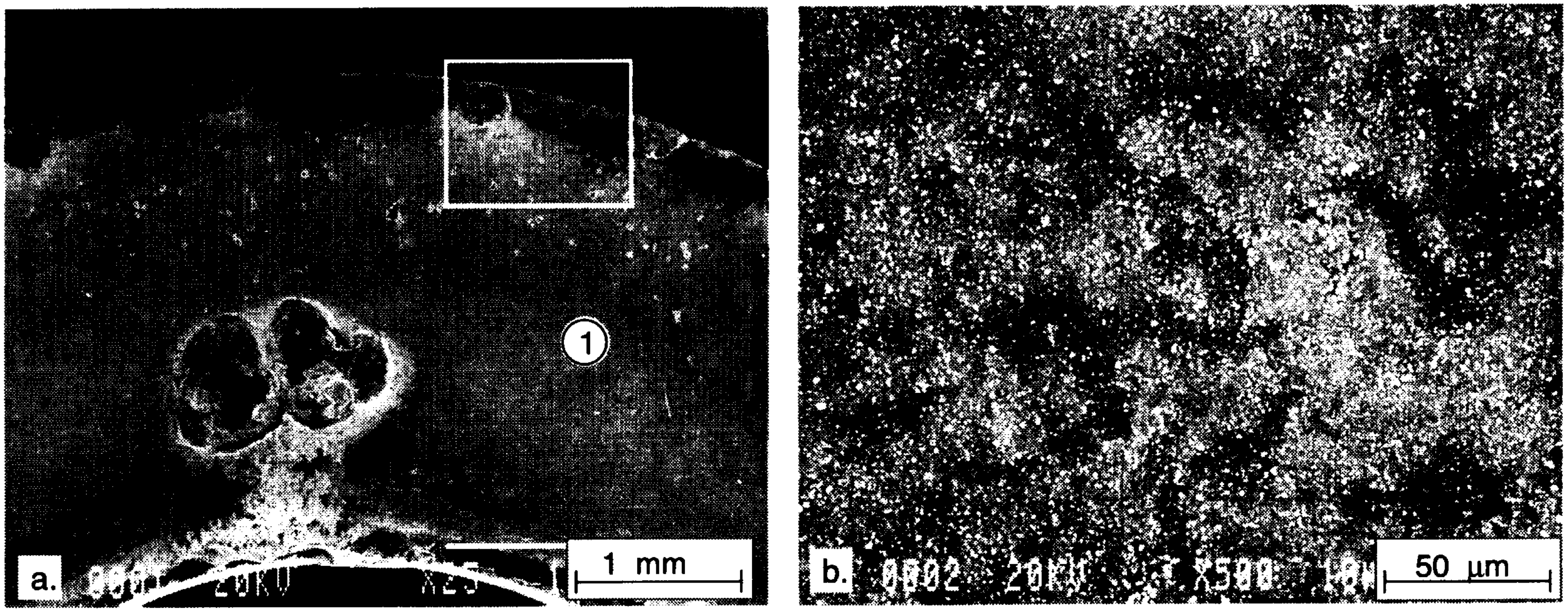

Fig. 55 SEM micrographs of the end of D218 shown in the box in Fig. 54a, (b) is a magnified view of the smooth scale near region indicated as (1). Box in (a) shows area of view shown in Fig. 56a.

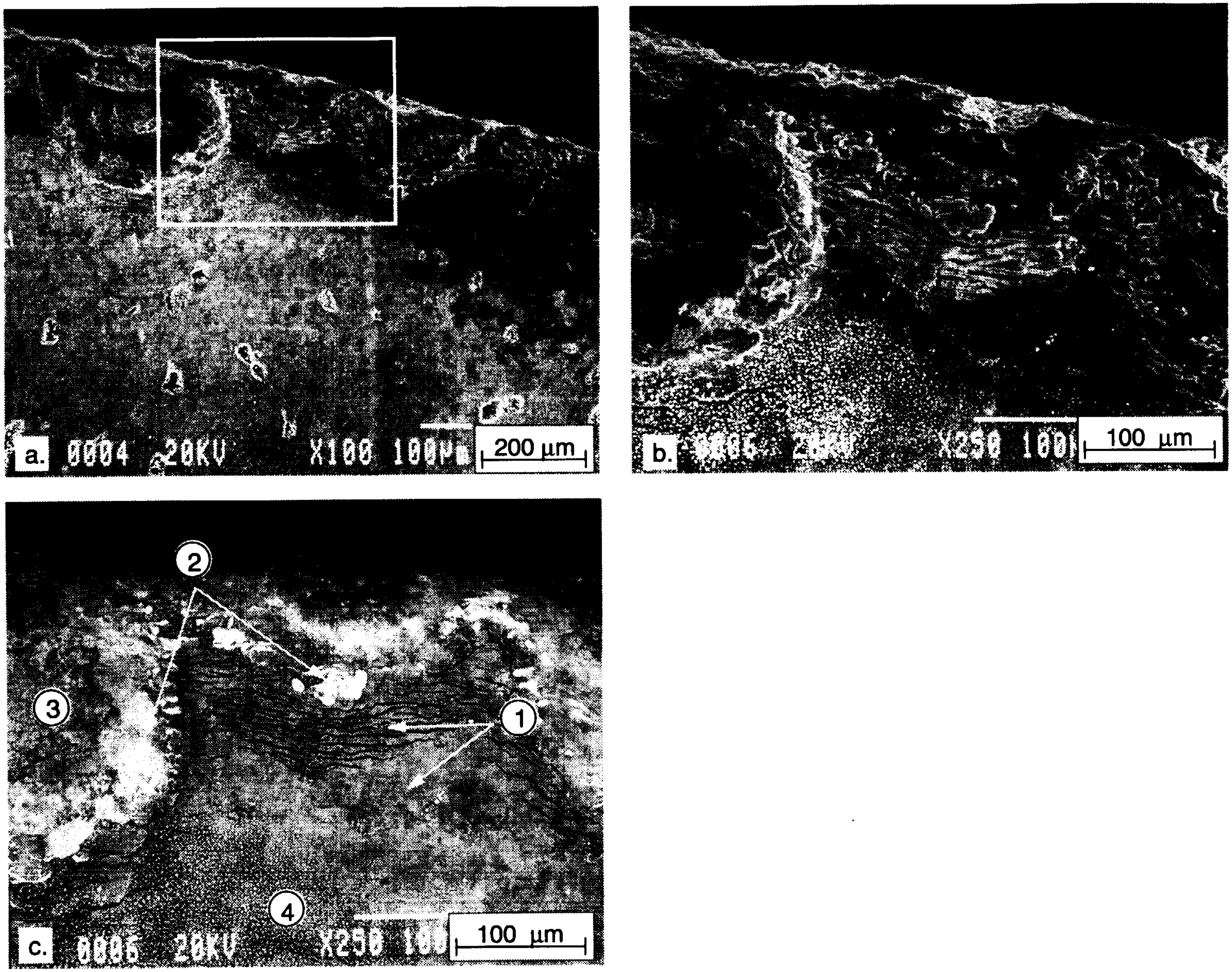

Fig. 56 SEM micrographs of the end of D218 shown in the box in Fig. 55a, (b) is a magnified view of (a) and (c) is a BSE image of (b).

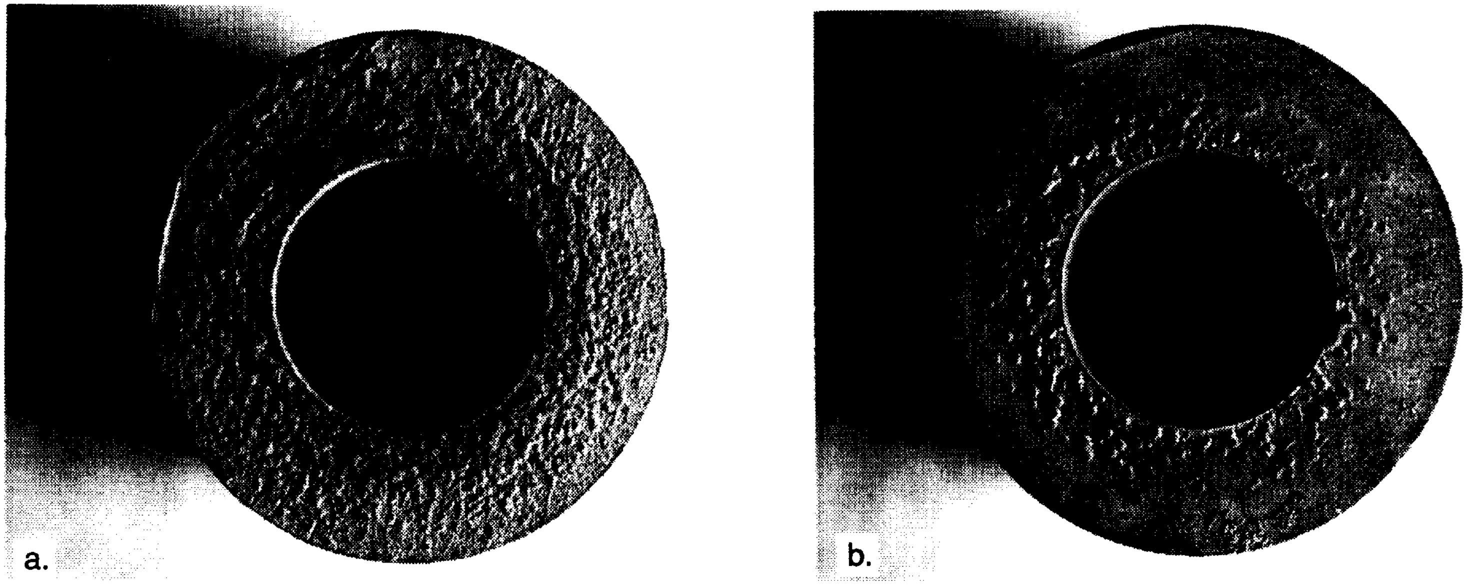

Fig. 57 Macrophotographs of AFN20 after 100 hrs showing different degree of attack on ends.

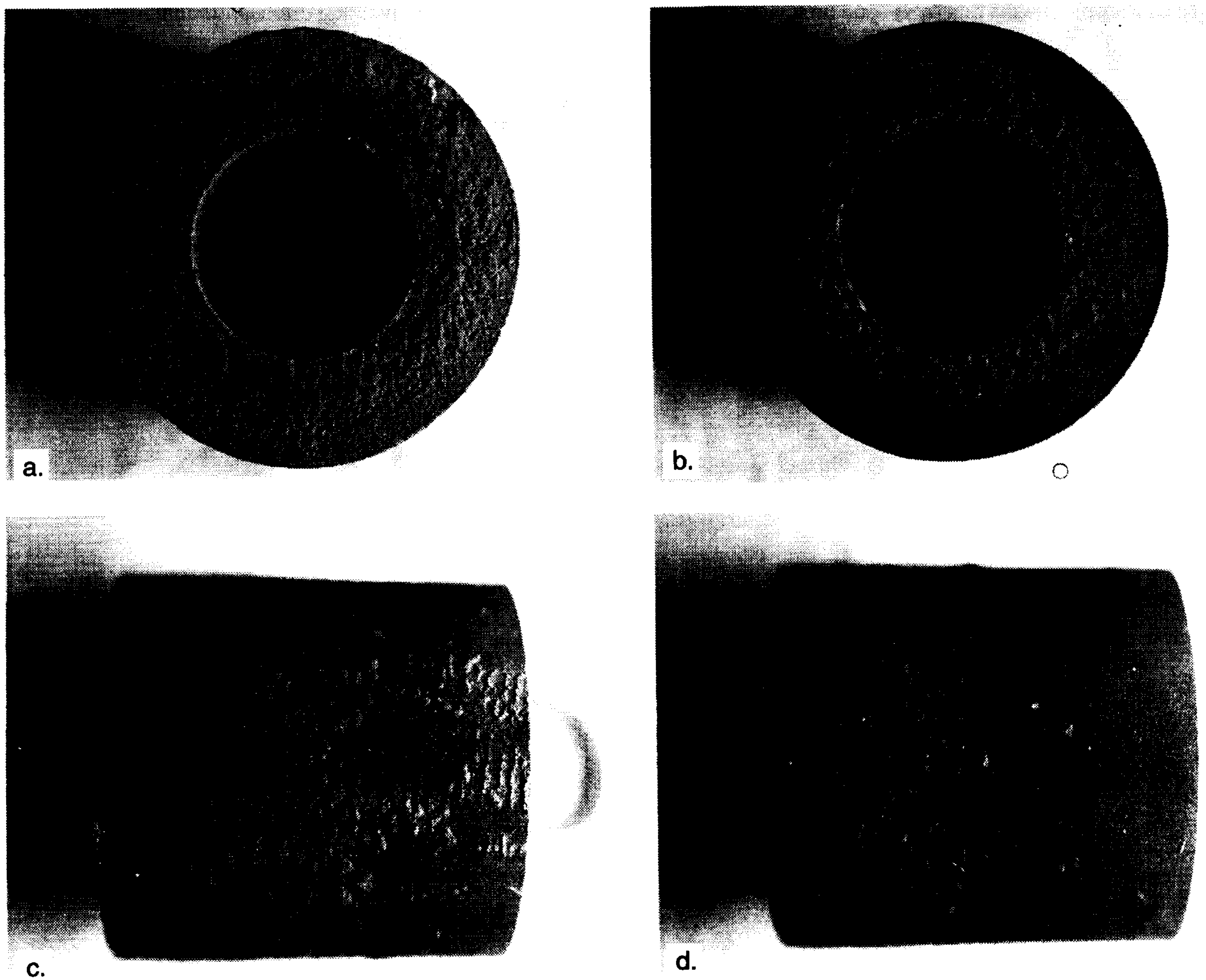

Fig. 58 Macrophotographs of AFN20 after 200 hrs showing coarsening of attack on ends (a,b) and accelerated attack on left half of curved surface (c,d).

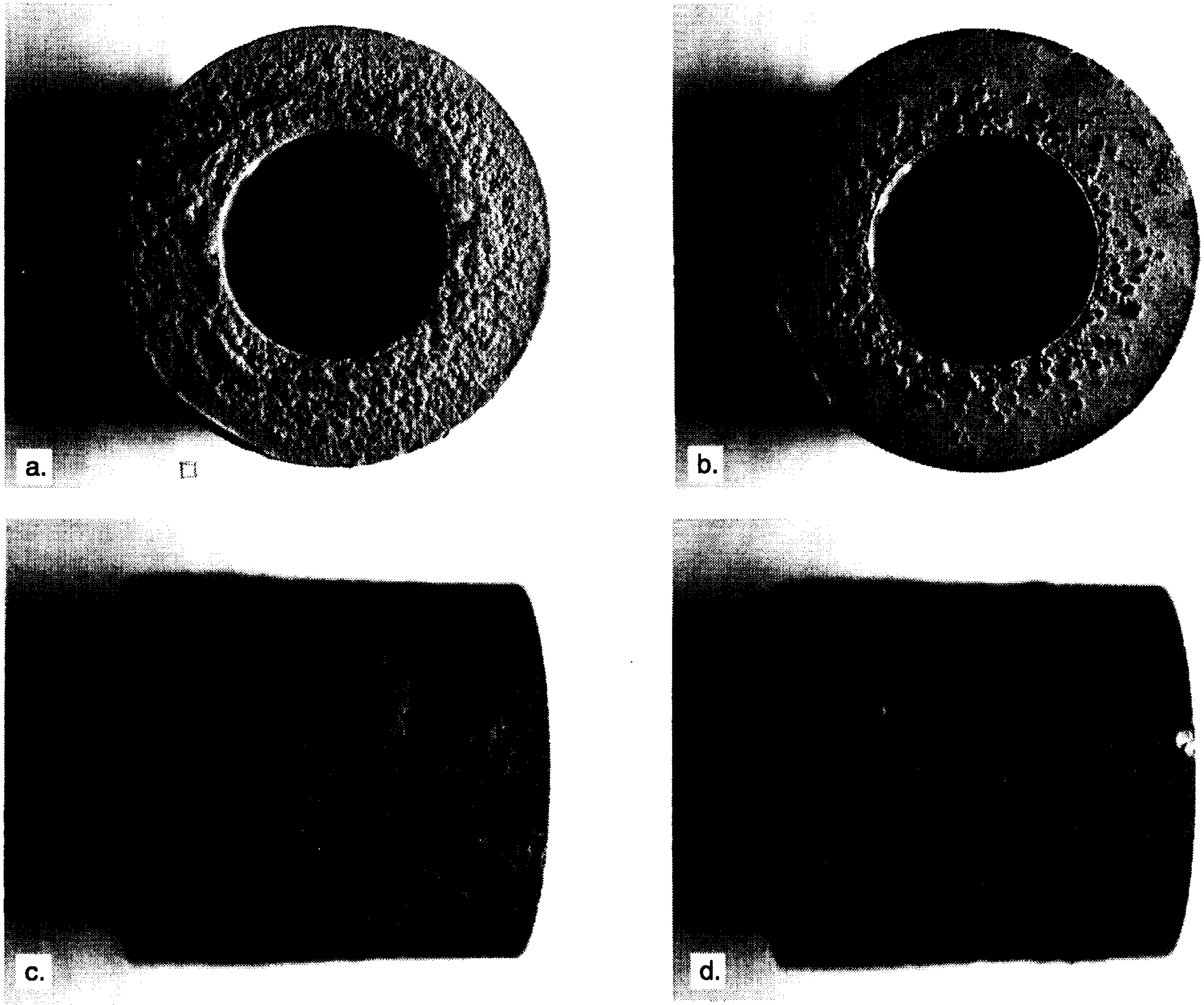

Fig. 59 Macrophotographs of AFN20 after 300 hrs showing coarsening of attack on ends (a,b) and curved surface (c,d).

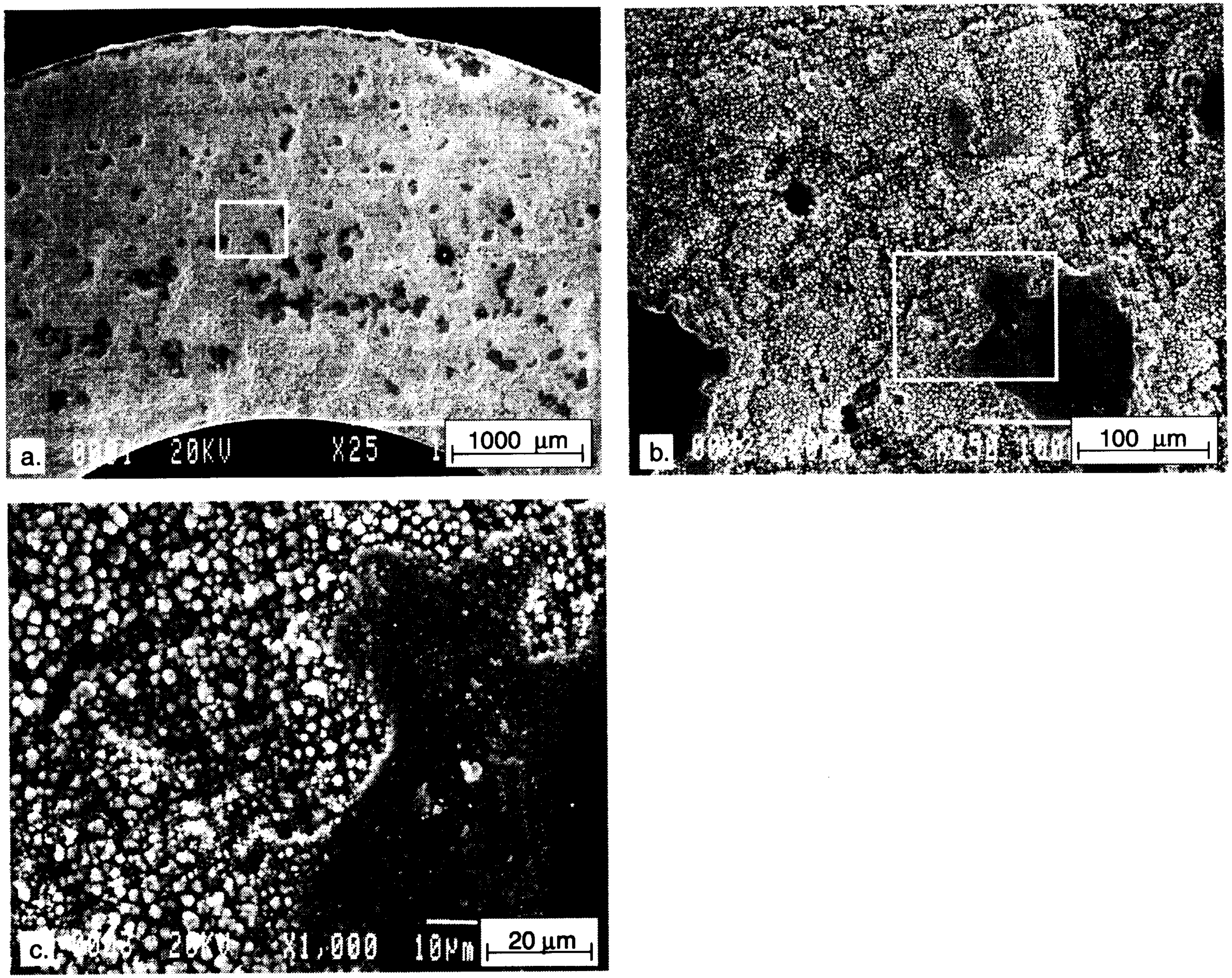

Fig. 60 SEM micrographs of the rough end of AFN20 after 300 cycles, (b) and (c) are magnified views of (a) and (b), respectively.

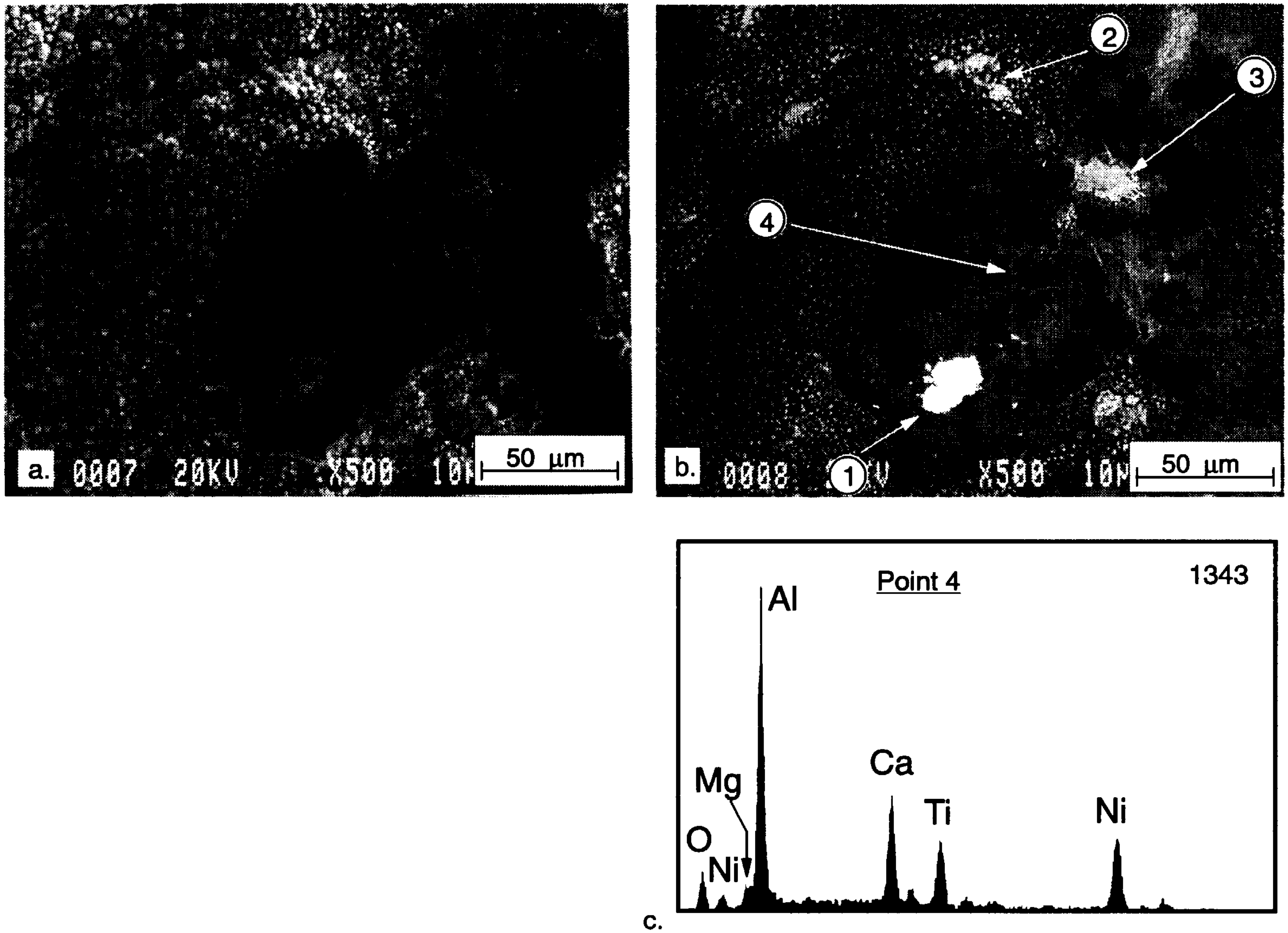

Fig. 61 SEM micrographs of the top of a corrosion mound on the rough end of AFN20 after 300 cycles, (a) SEI image, (b) BSE image, and (c) EDS spectra of point 4.

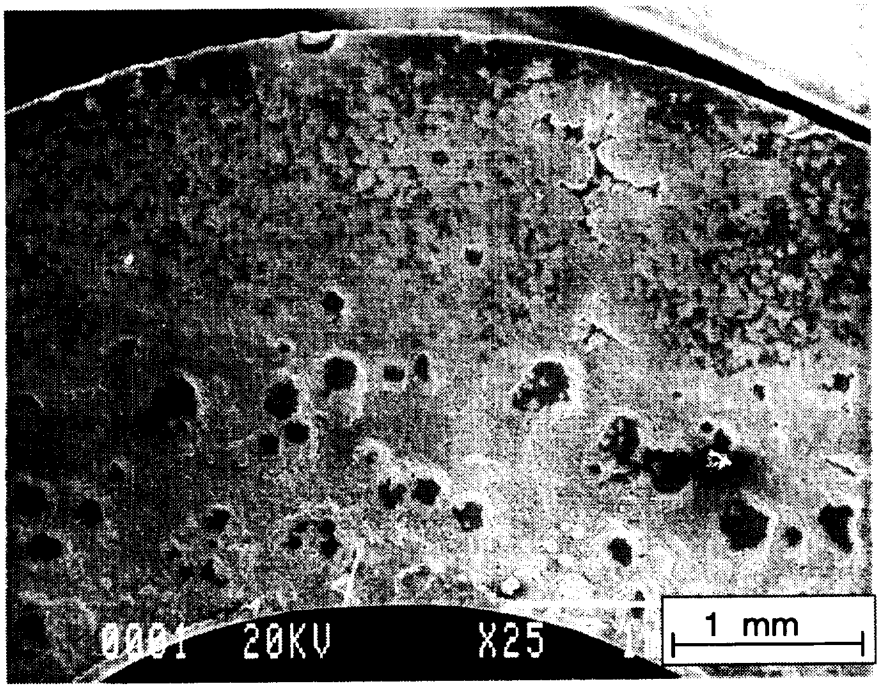

Fig. 62 SEM micrograph of the smoother end of AFN20 (see Fig. 59b) after 300 cycles.

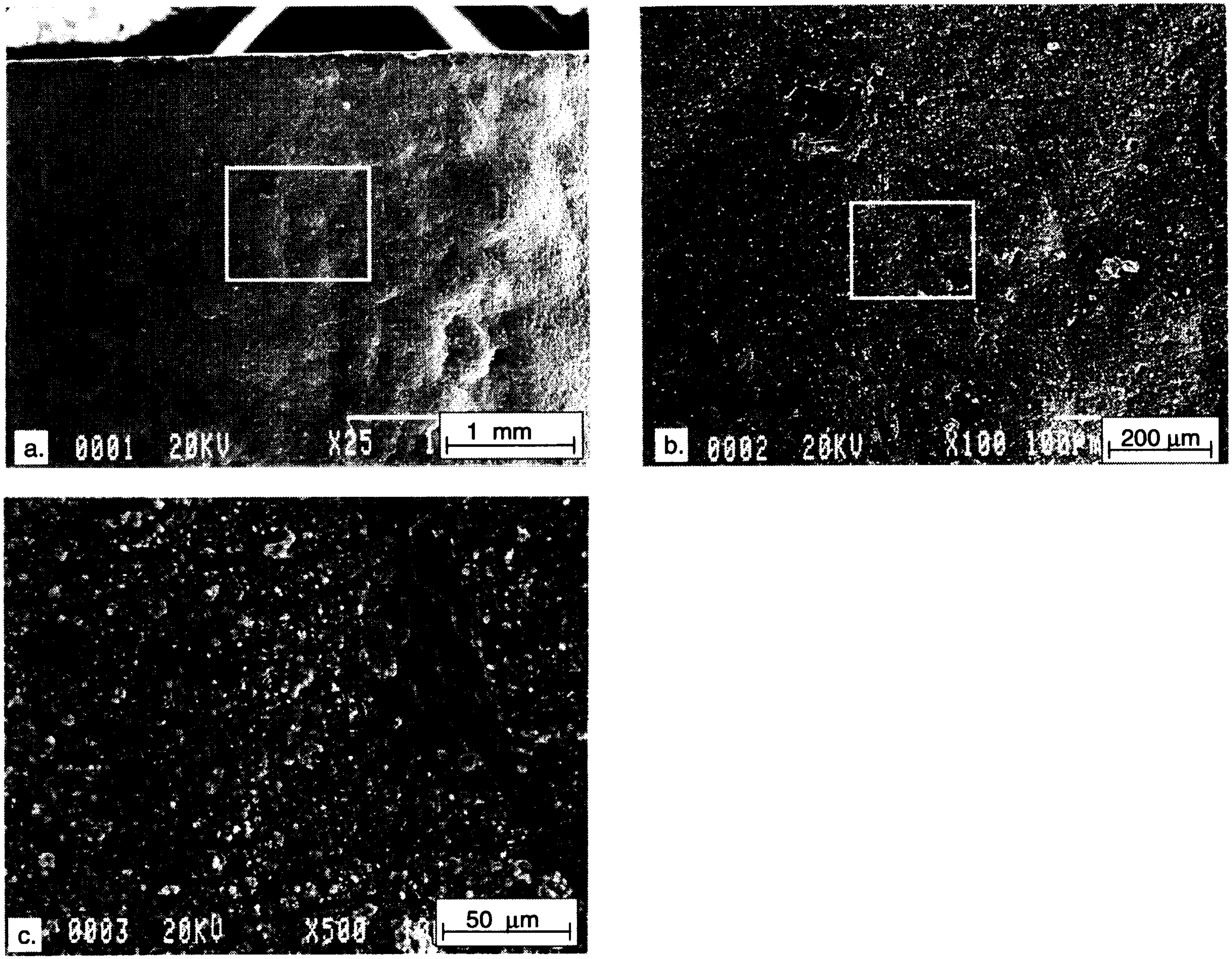

Fig. 63 SEM micrographs of the curved surface of AFN20 after 300 cycles. (b) is a magnified view of the box in (a), and (c) is a magnified view of the box in (b) (End in (a) is that to the left in Fig. 59c.)

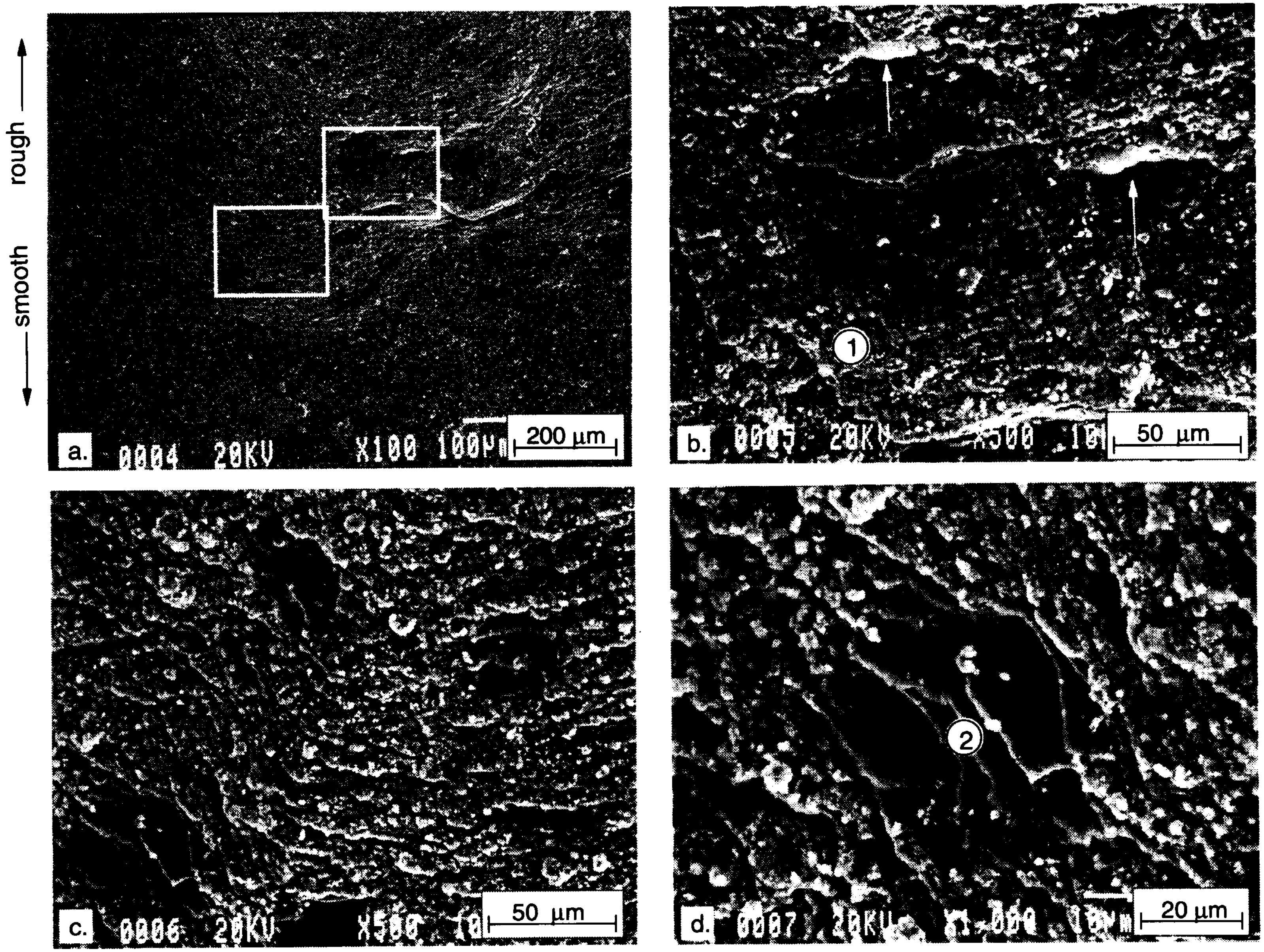

Fig. 64 SEM view (a) overlapping the rough and smooth regions on the curved surface of AFN20 after 300 cycles, (b) and (c) are magnified views of upper and lower boxes, respectively, in (a), and (d) is magnified view of (c).

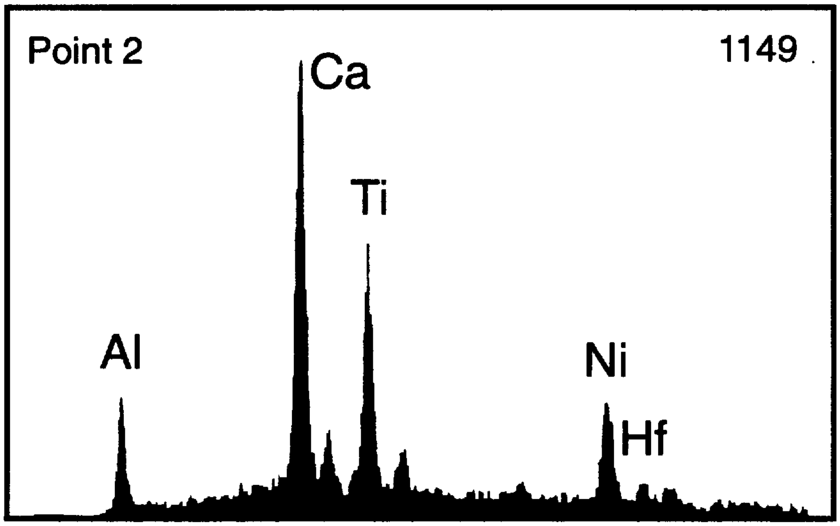

Fig. 65 EDS spectra of the dark plates (point 2) shown in Fig. 64d.

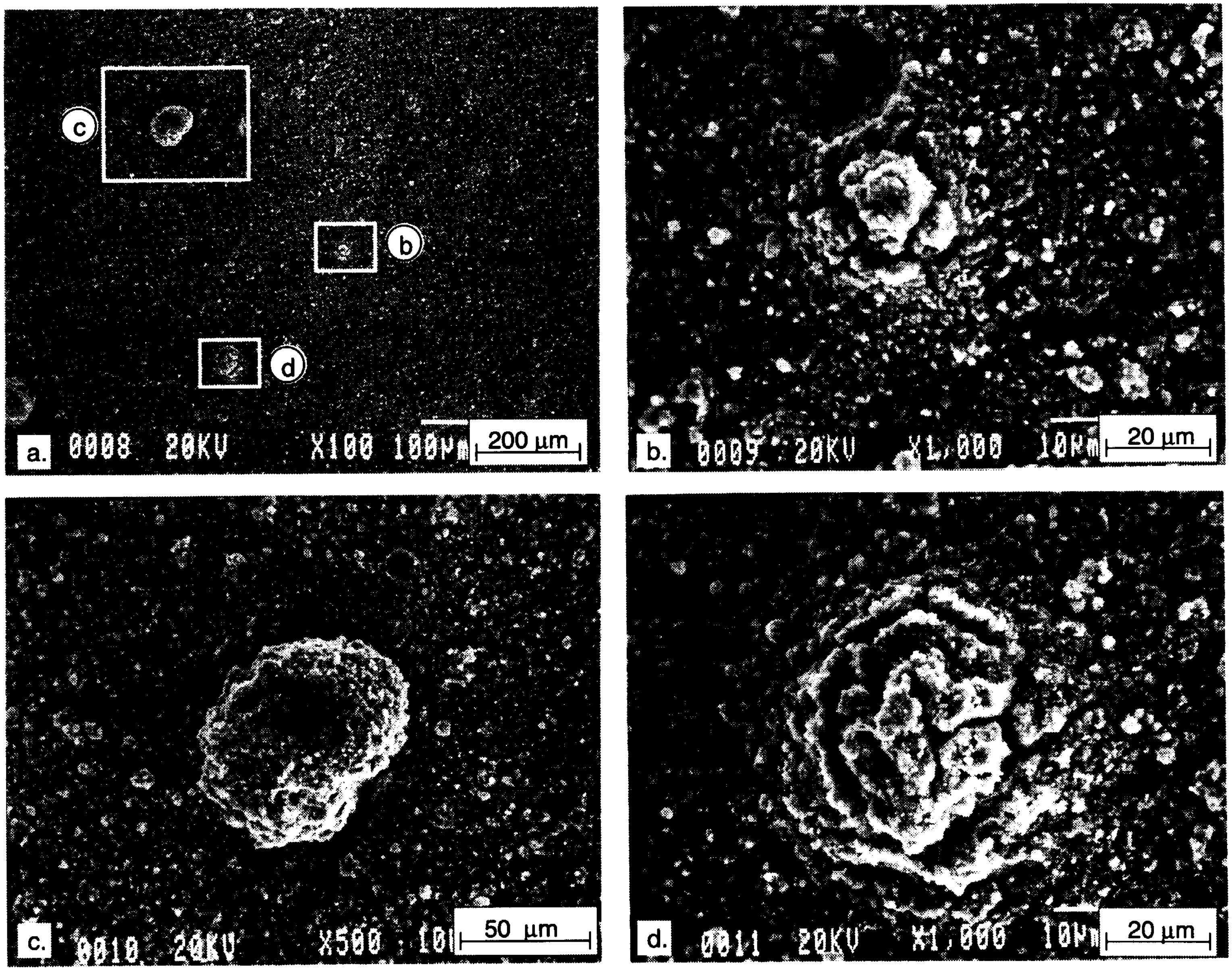

Fig. 66 SEM micrographs of the "smooth" curved surface of AFN20 after 300 cycles (right end of Fig59c,d), (b),(c) and (d) are magnified views of the boxed areas in (a).

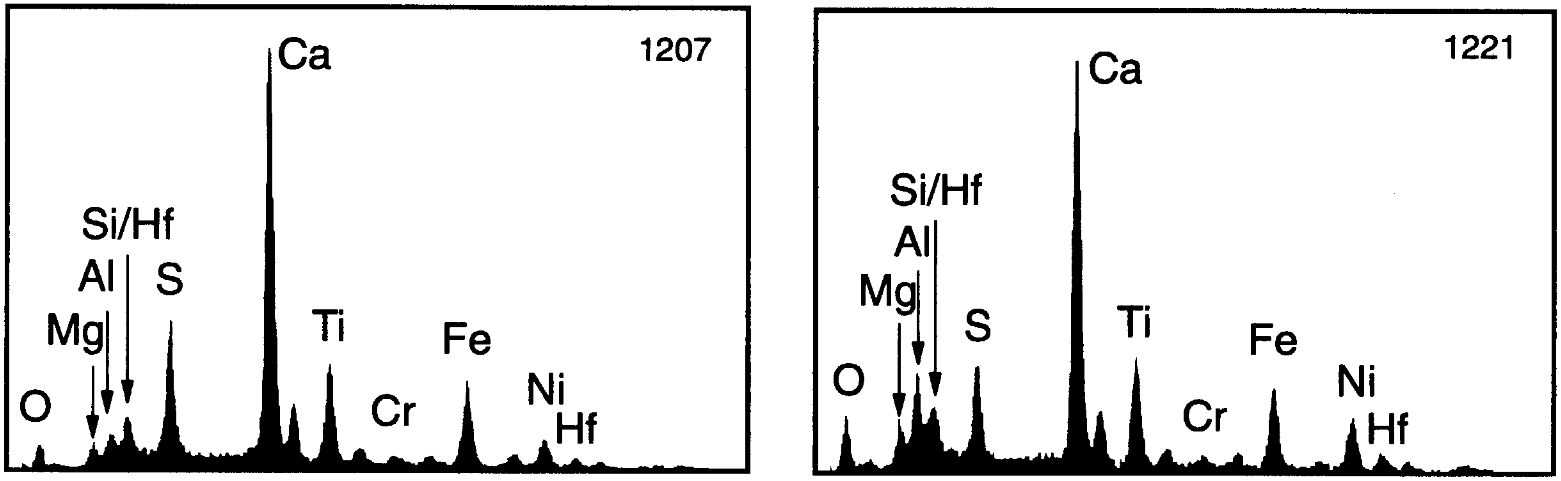

a.

b.

Fig. 67 EDS spectra of the nodule shown in Fig. 66c and the mound in Fig. 66d.

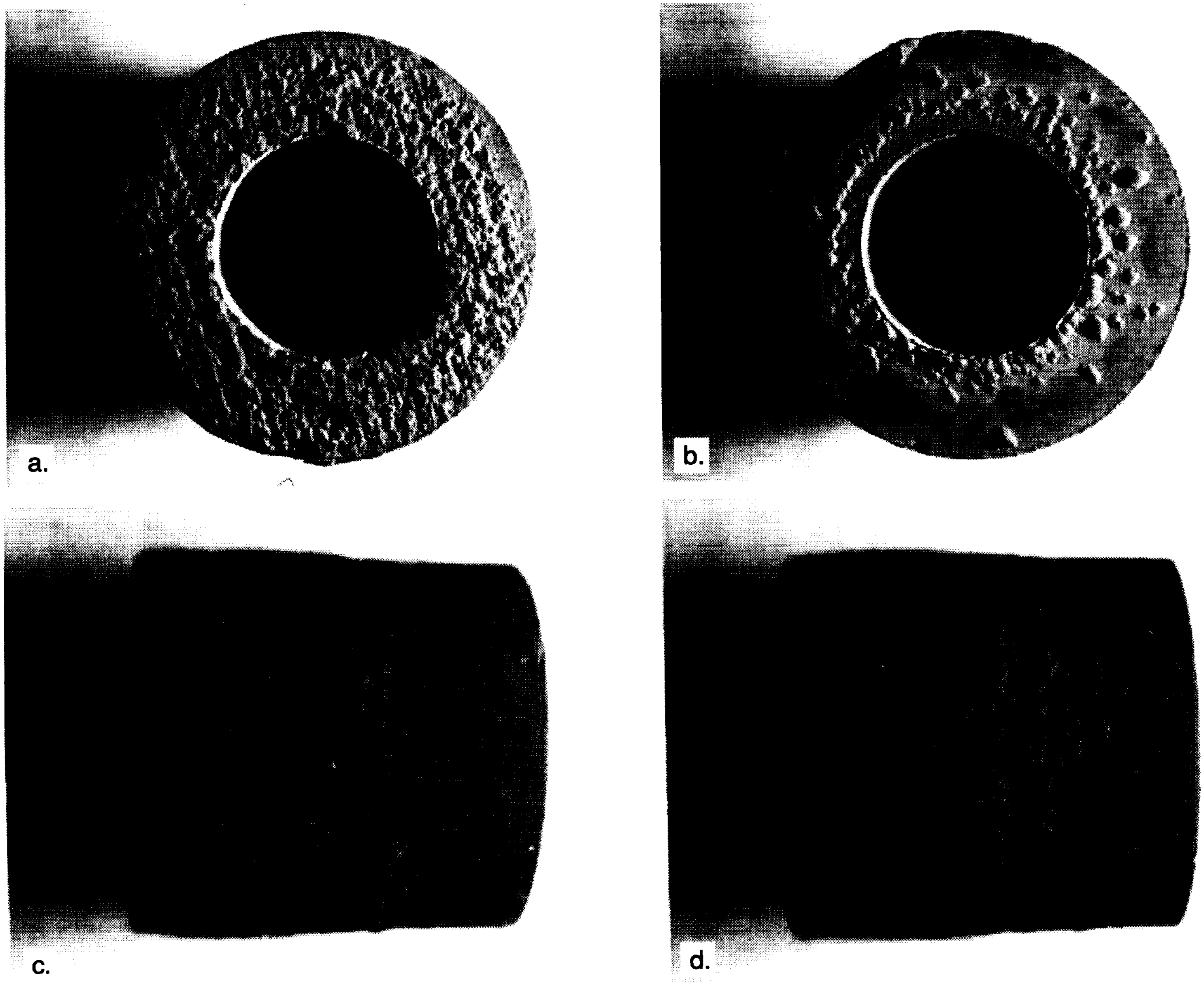

Fig. 68 Macrophotographs of D219A after 300 hrs showing different degrees of attack on end (a,b) and on curved surface (c,d).

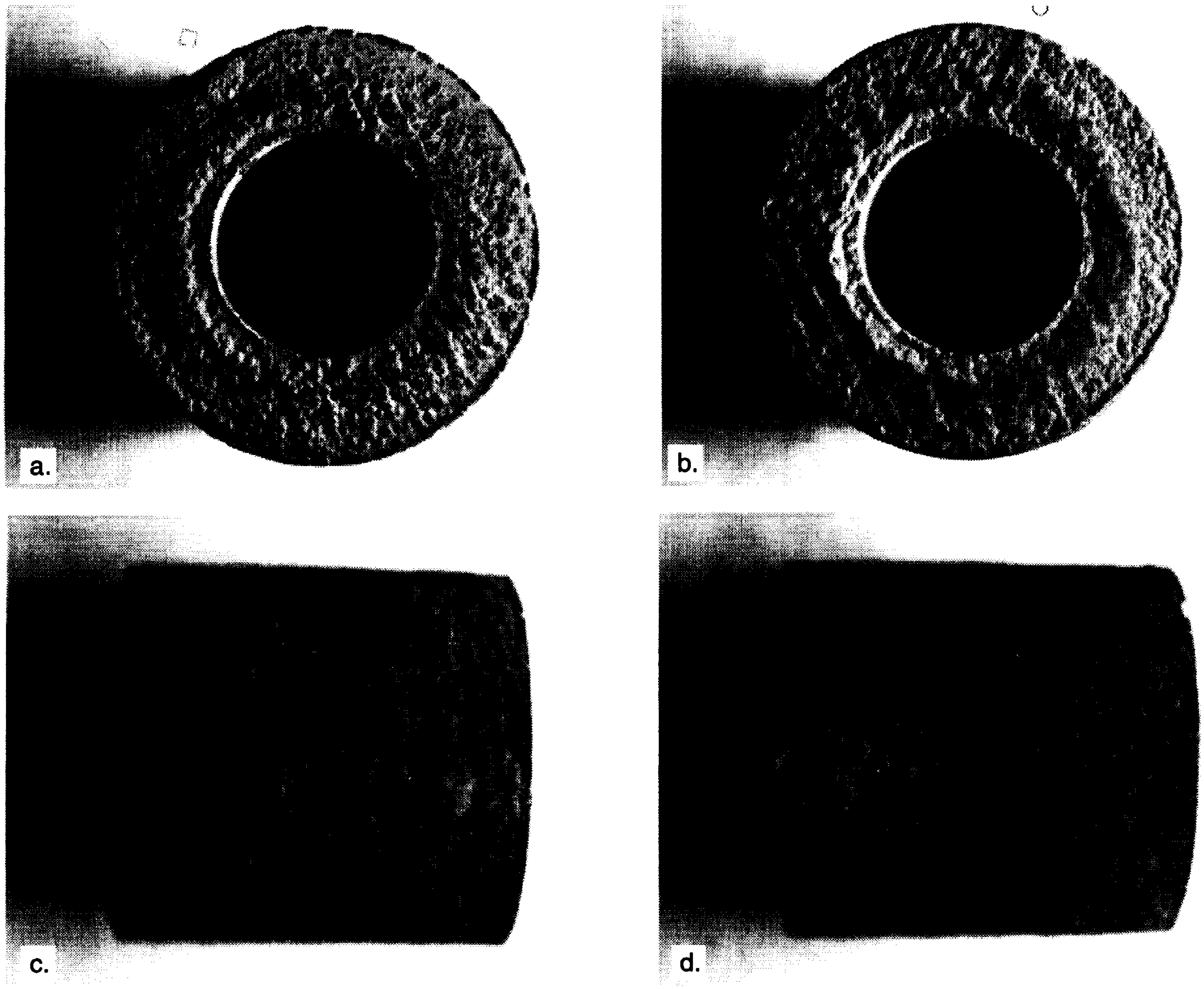

Fig. 69 Macrophotographs of D219B after 300 hrs showing similar degrees of attack on ends (a,b) and on most of curved surface (c,d).

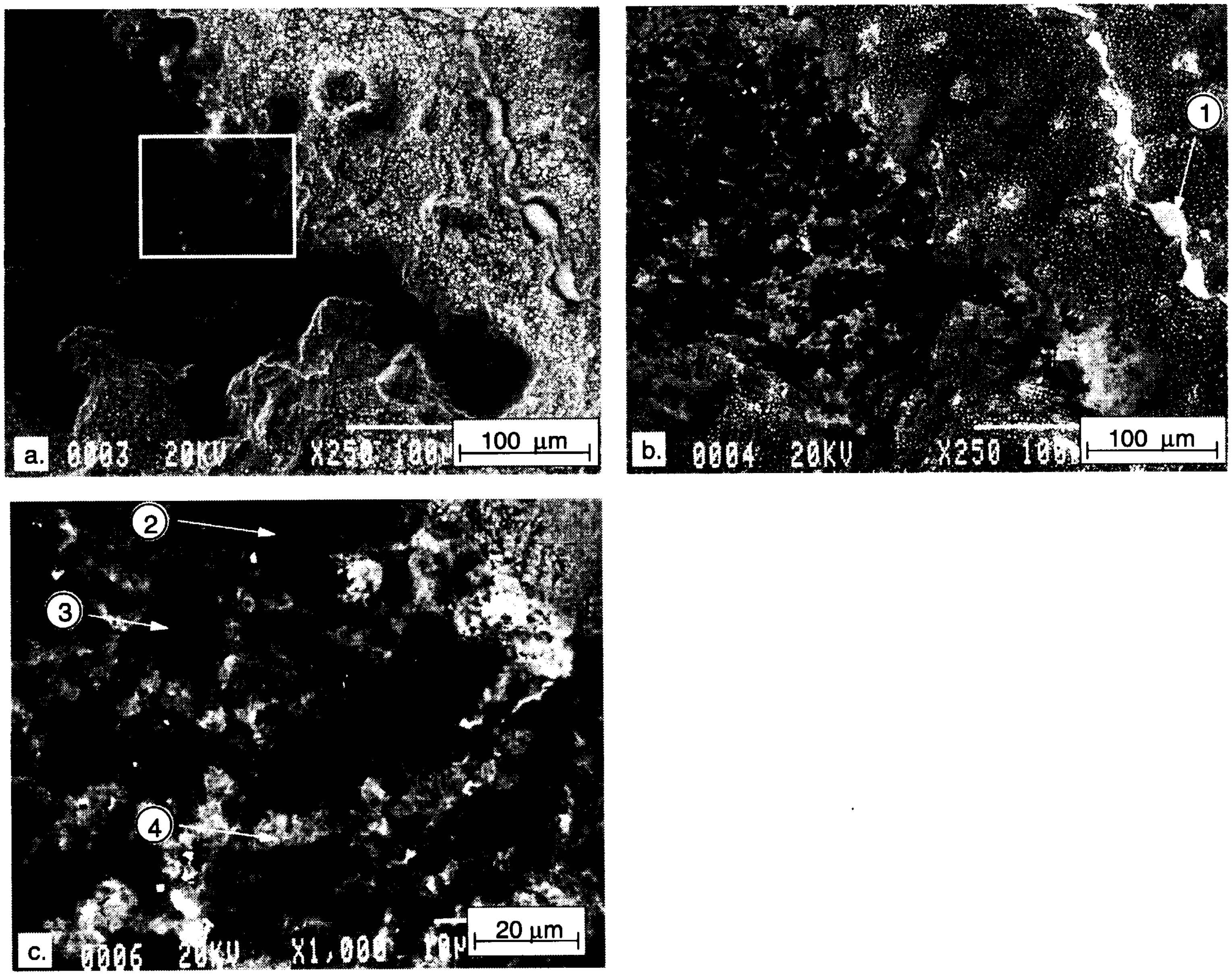

Fig. 70 SEM micrographs of the rough end of D219A after 300 cycles, (b) is a BSE image of (a) and (c) is a magnified BSE image of the box in (a).

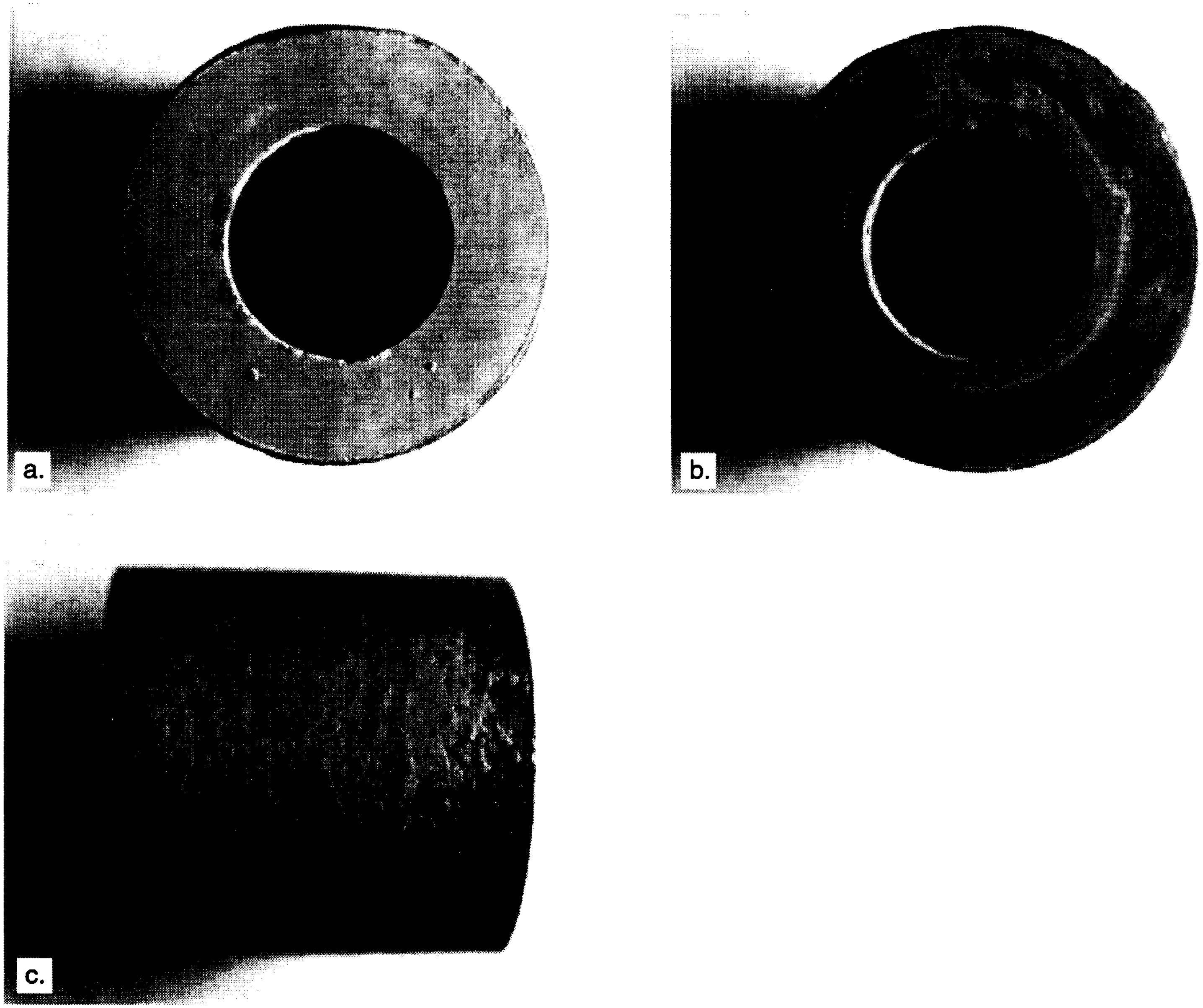

Fig. 71 Macrophotographs of D219F after 50 hrs of testing (Series III). Sample surface had been polished through 600 grit SiC paper.

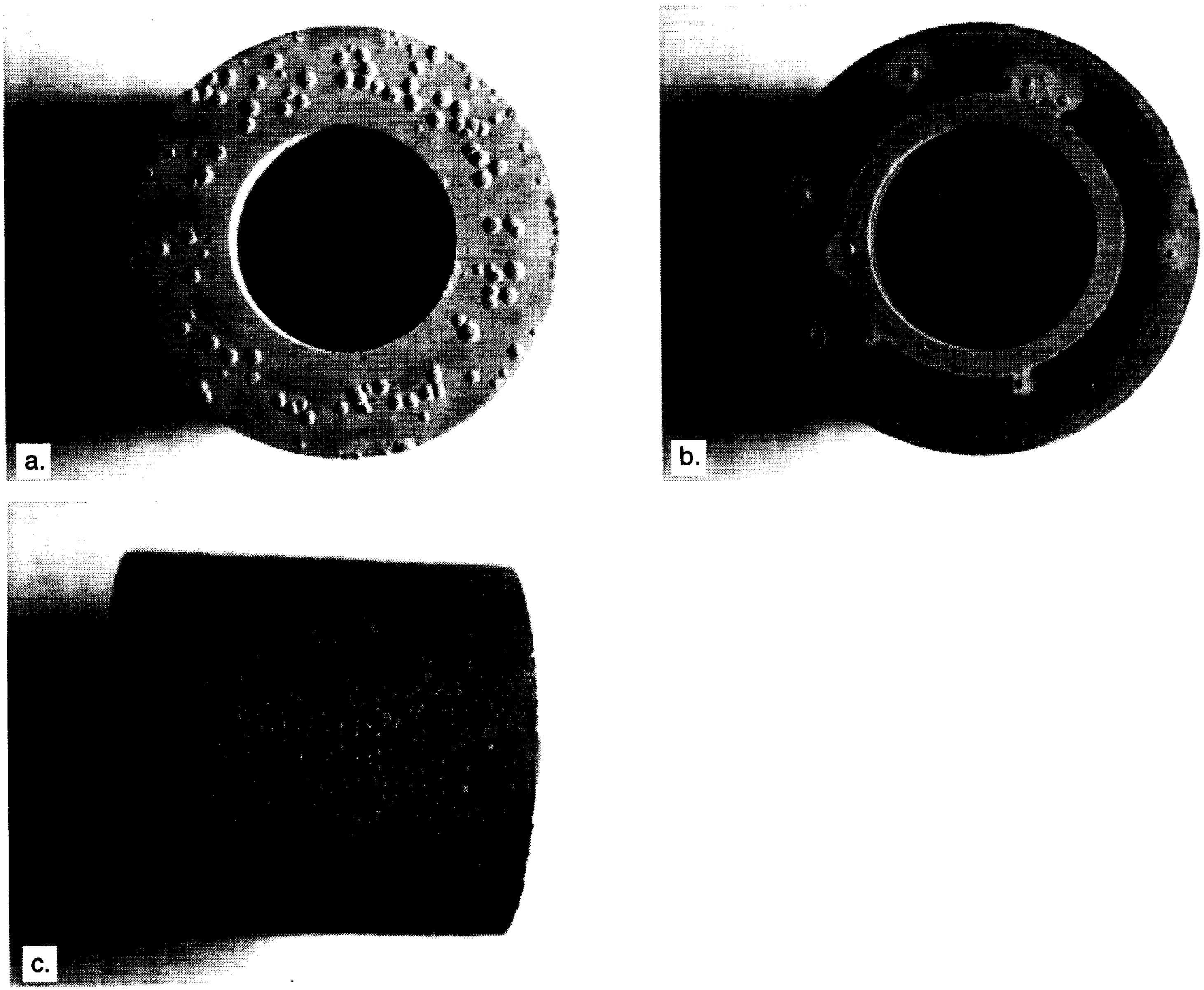

Fig. 72 Macrophotographs of D219E after 50 hrs of testing (Series III). Sample surface had been polished through 600 grit SiC paper.

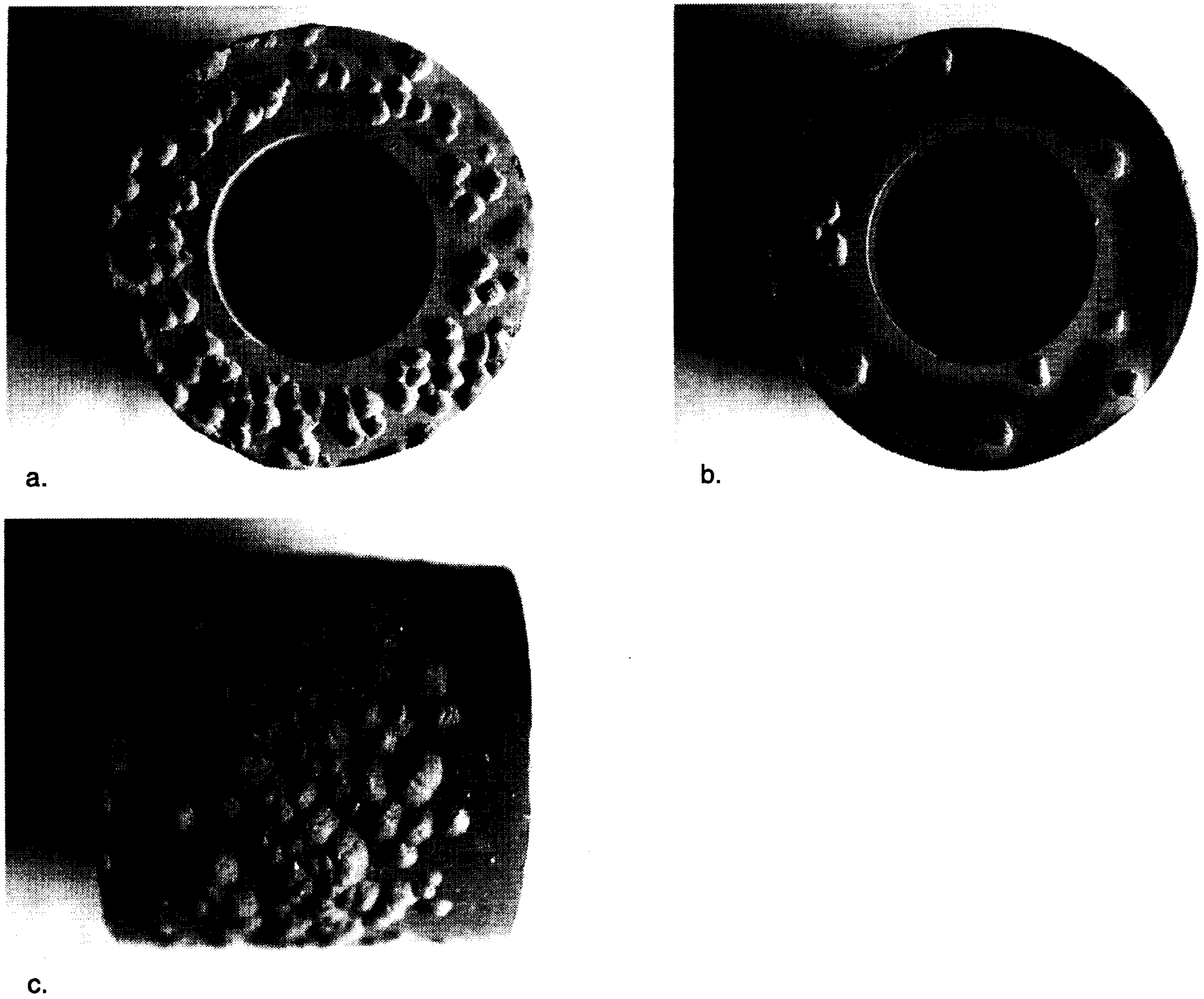

Fig. 73 Macrophotographs of D219E after 300 hrs (Series III). Sample surface was polished through 600 SiC paper.

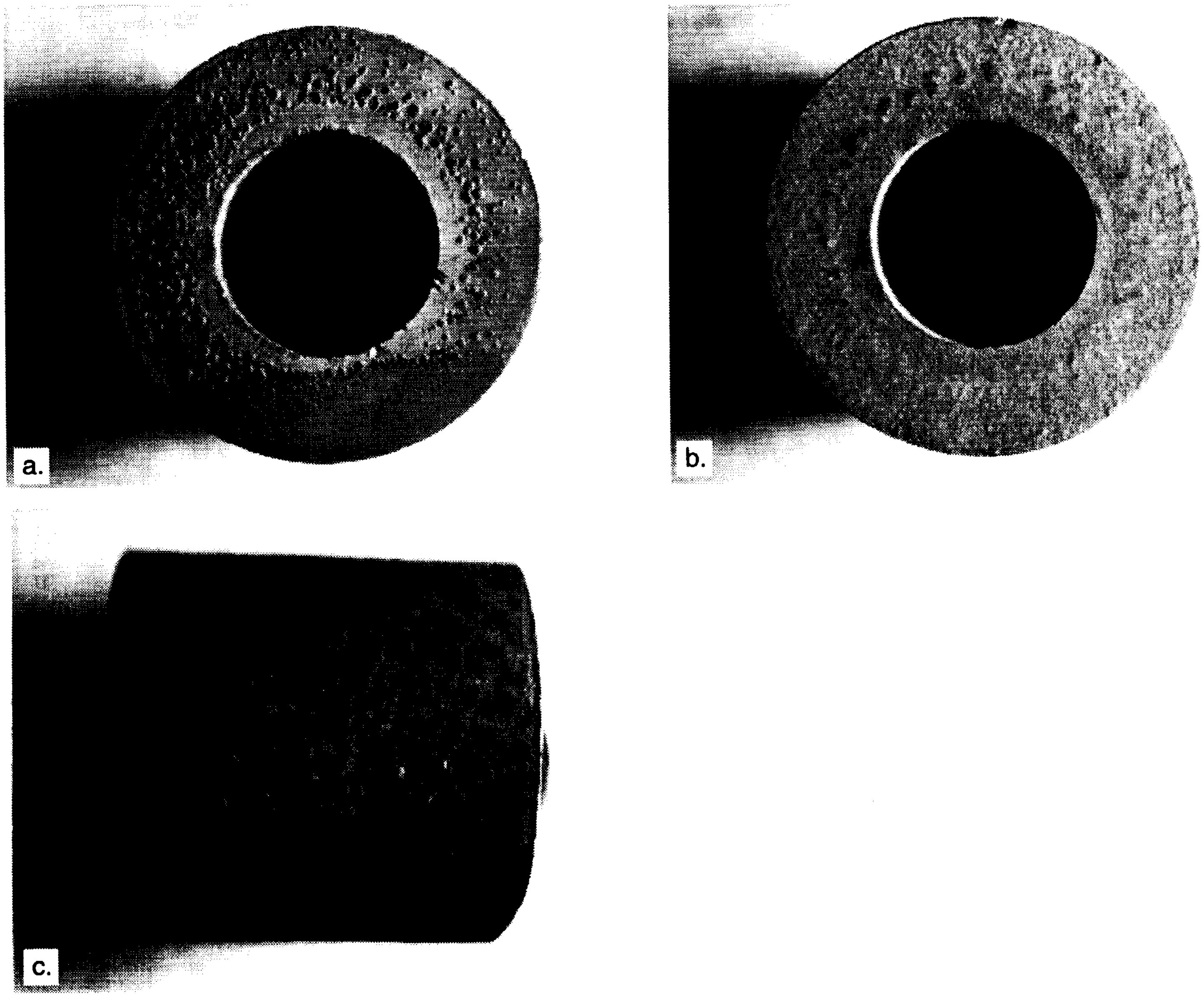

Fig 74 Macrophotographs of D219D after 50 hrs of testing (Series III). Sample surface had been chemically milled.

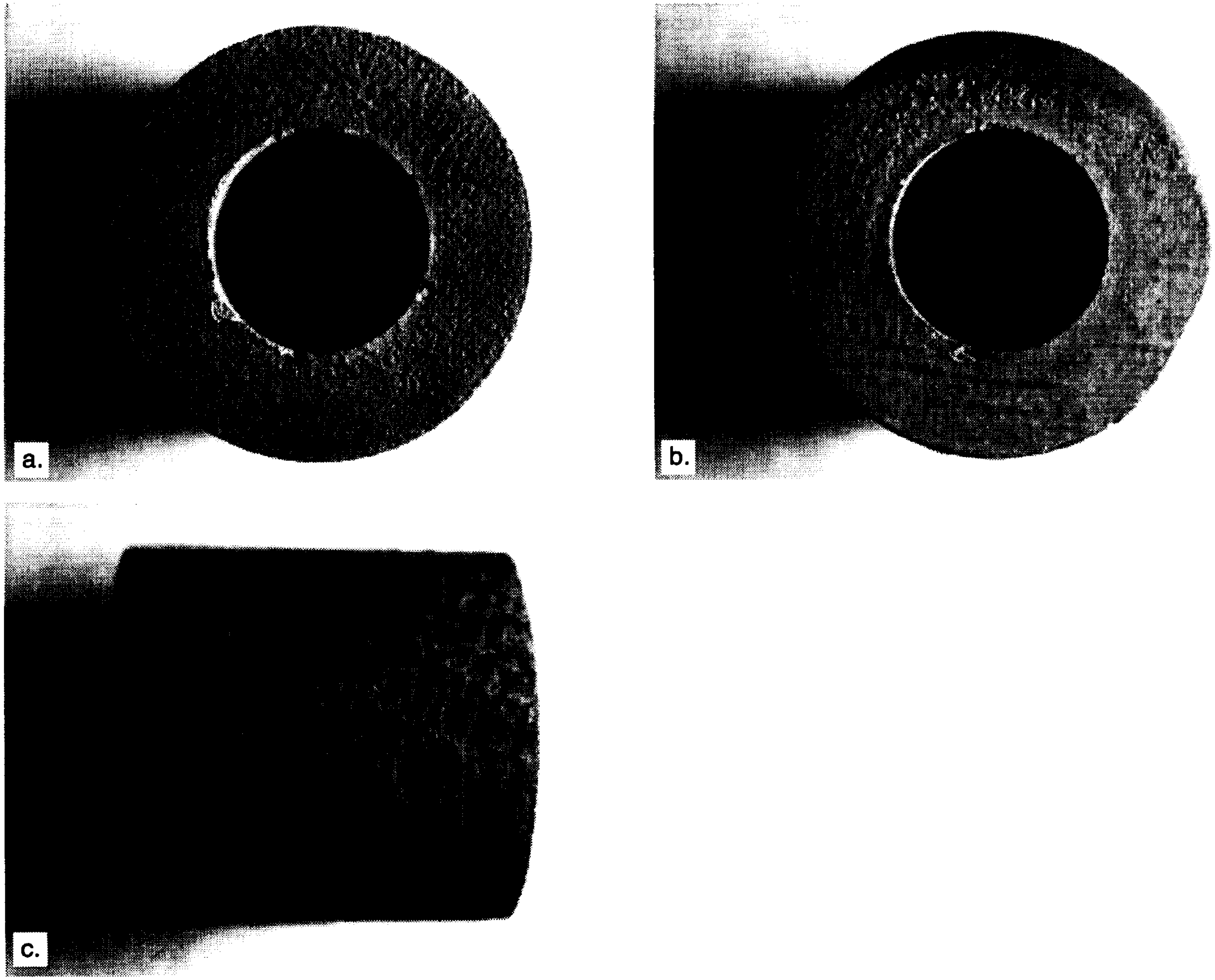

Fig. 75 Macrophotographs of D219C after 50 hrs of testing (Series III). Sample surface had been chemically milled.

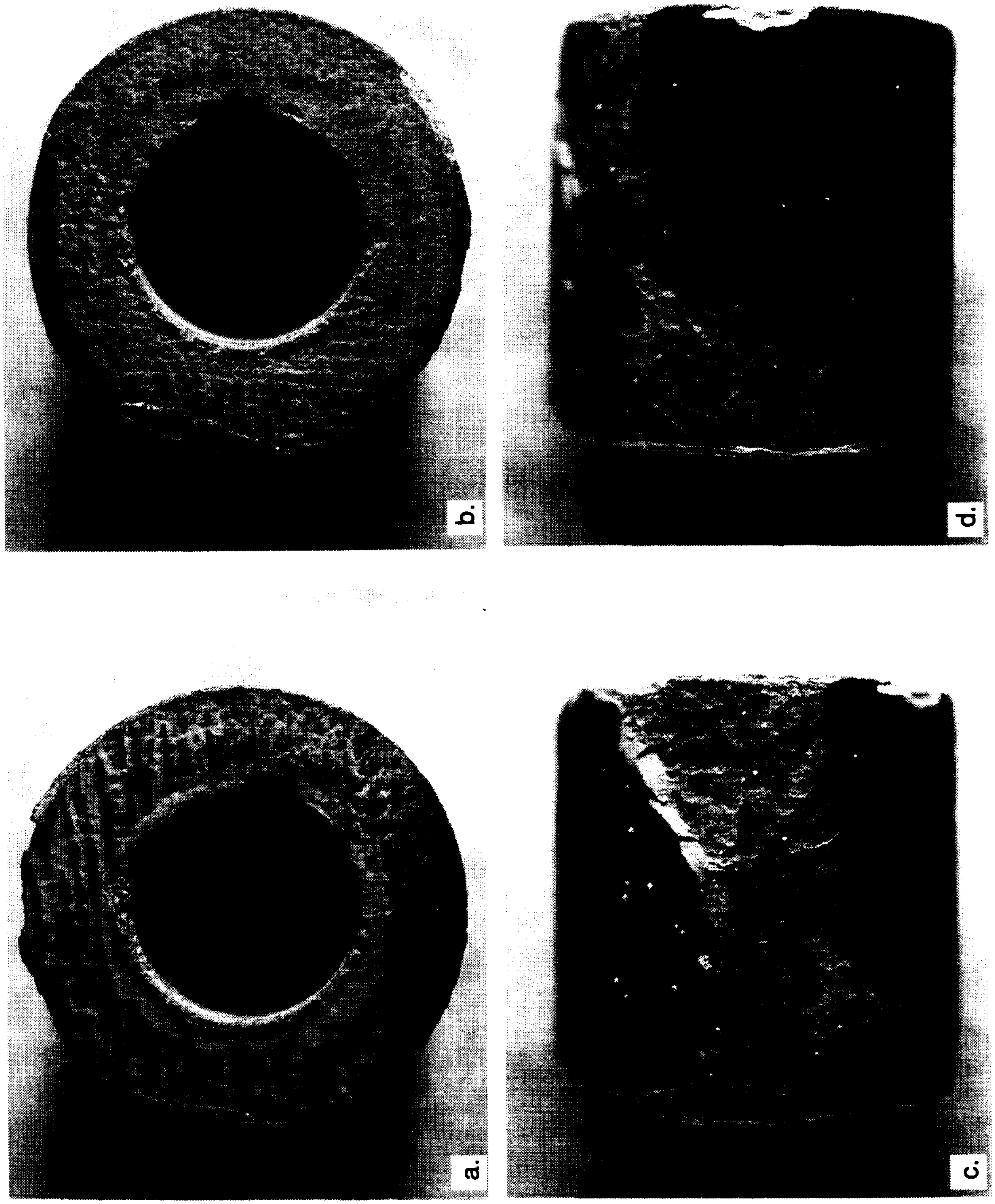

Fig. 76 Macrophotographs of D219C after 200 hrs (Series III). Sample surface was chemically milled.

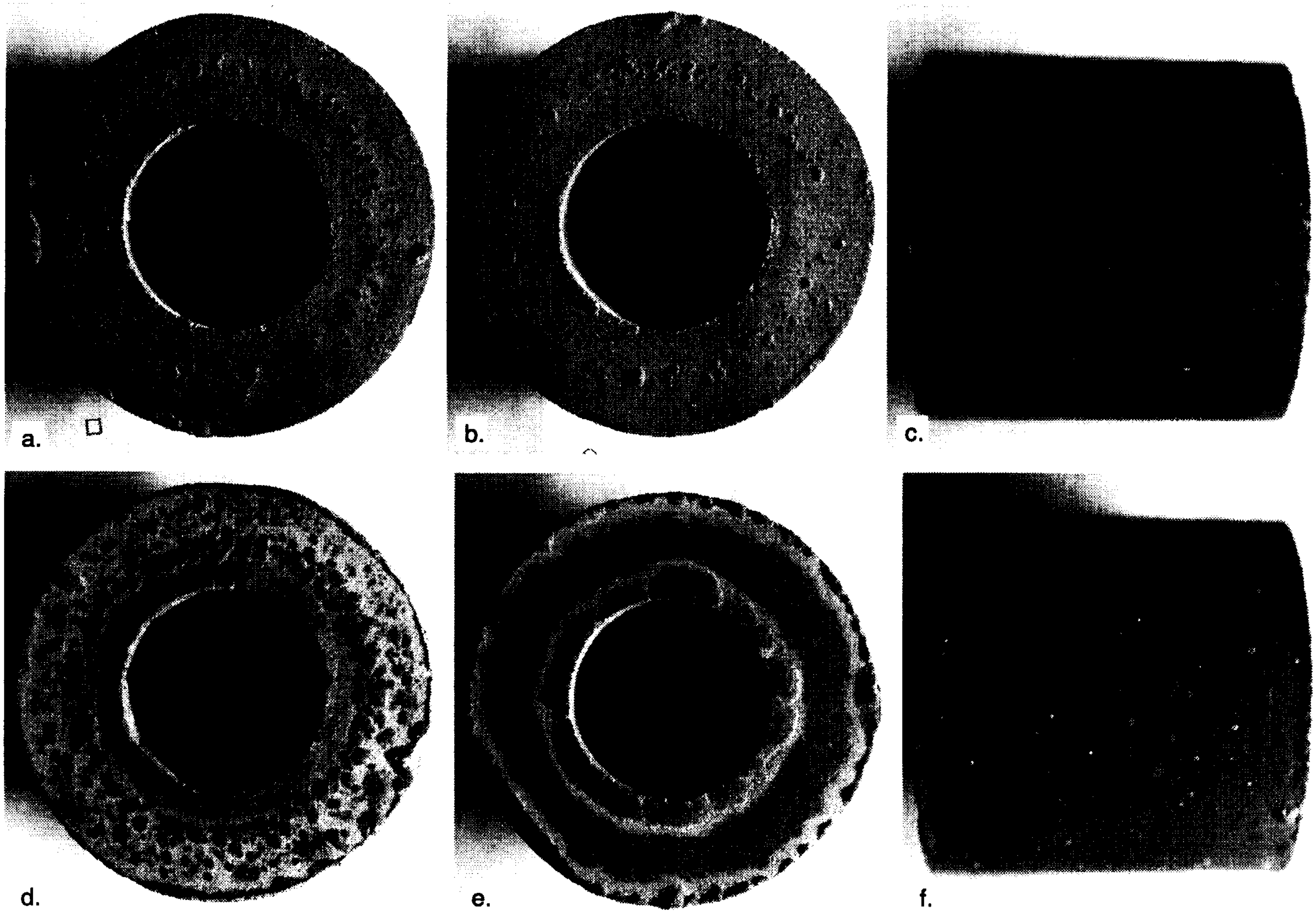

Fig. 77 Optical macrographs of the end and curved surface of AFN26 after 300 hrs (a-c) Series II, (d-f) Series III. Both samples were electropolished and chemically milled.

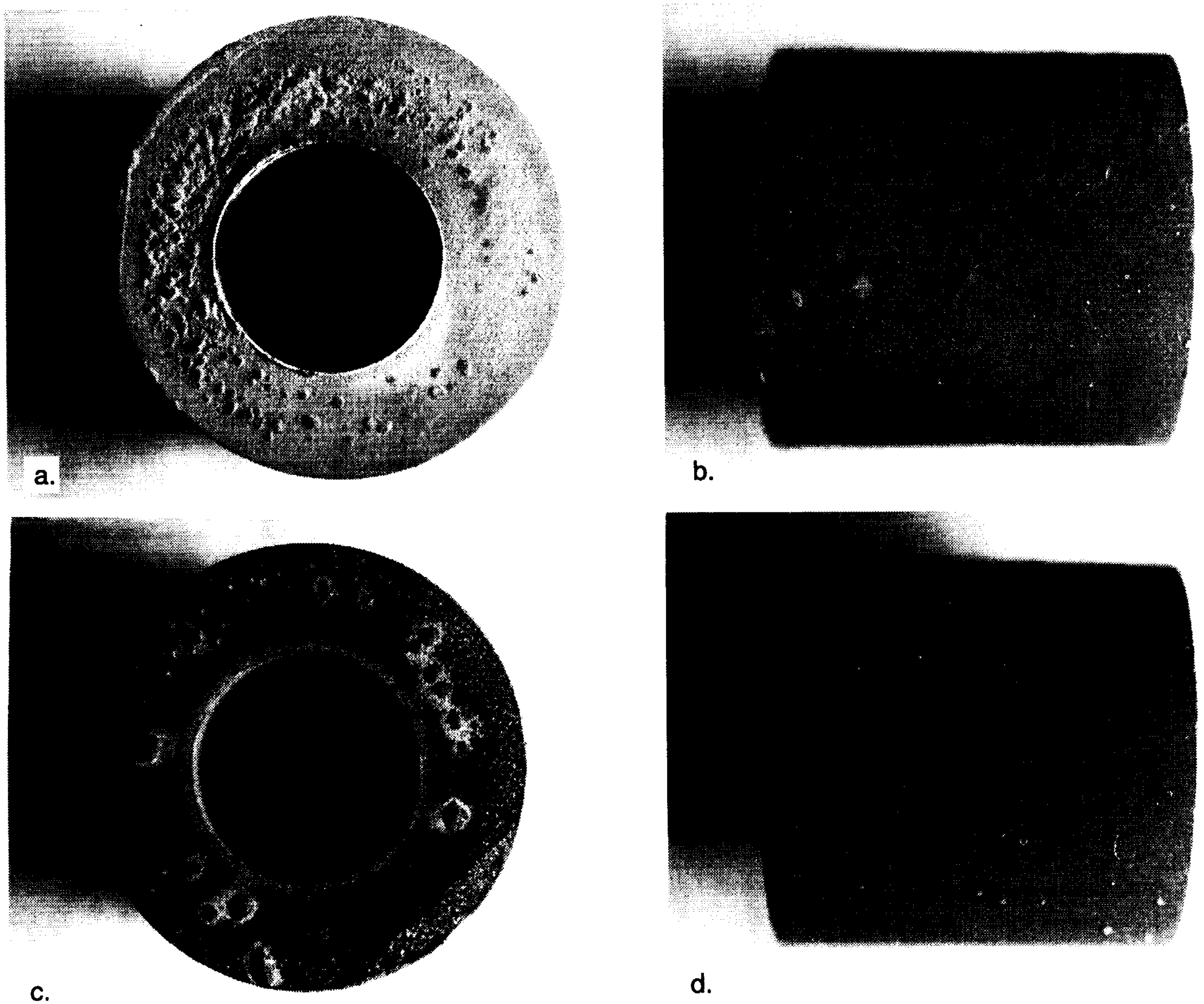

Fig. 78 Macrophotographs of the end and curved surface of AFN23 after 300 hrs (a,b) Series II, (c,d) Series III. ((a,b) previously shown in Fig. 49 are reproduced here for convenience.)

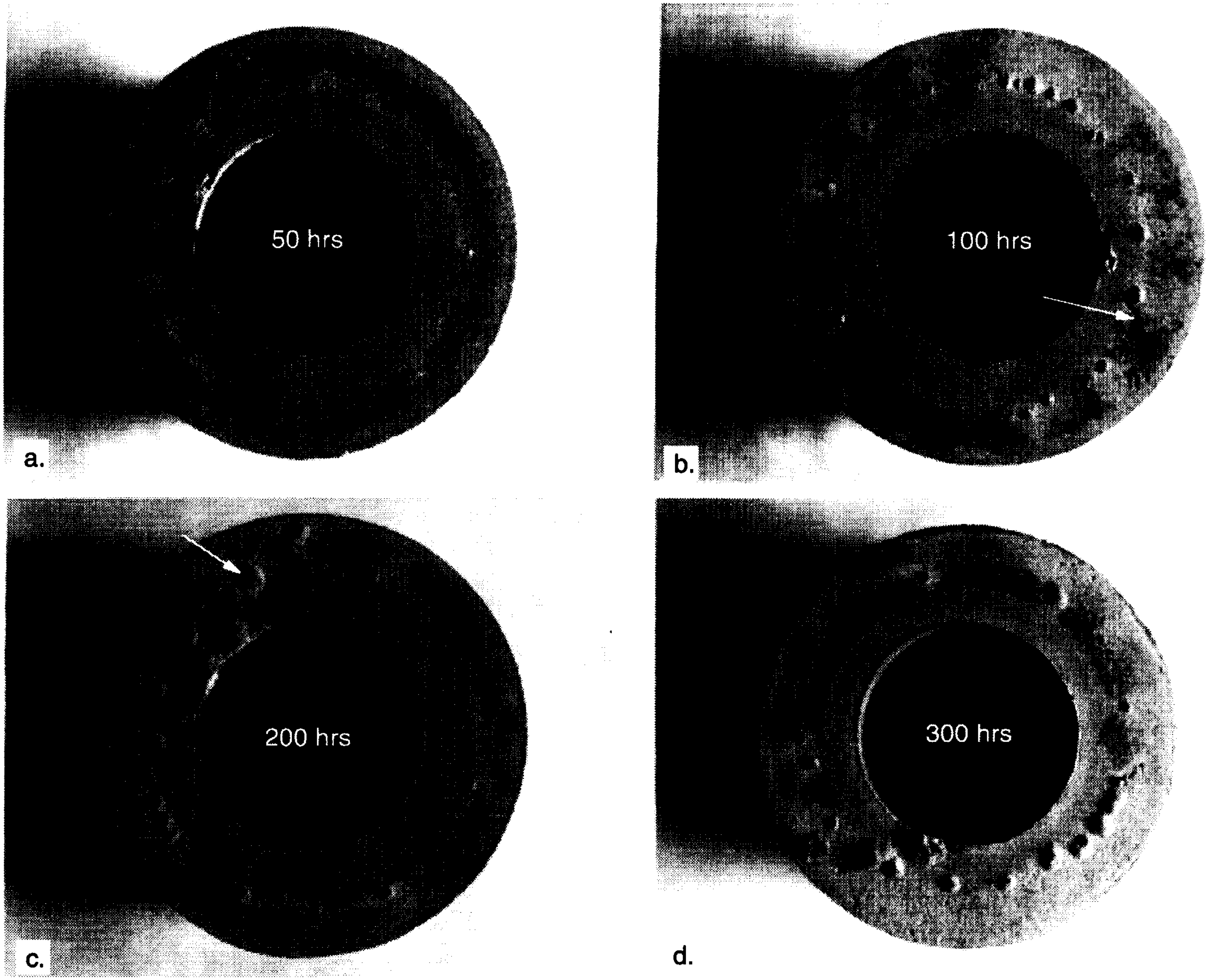

Fig. 79 Macrophotographs of the ends of D218B after (a) 50, (b) 100, (c) 200, and (d) 300 hrs (Series III). Sample surface was chemically milled.

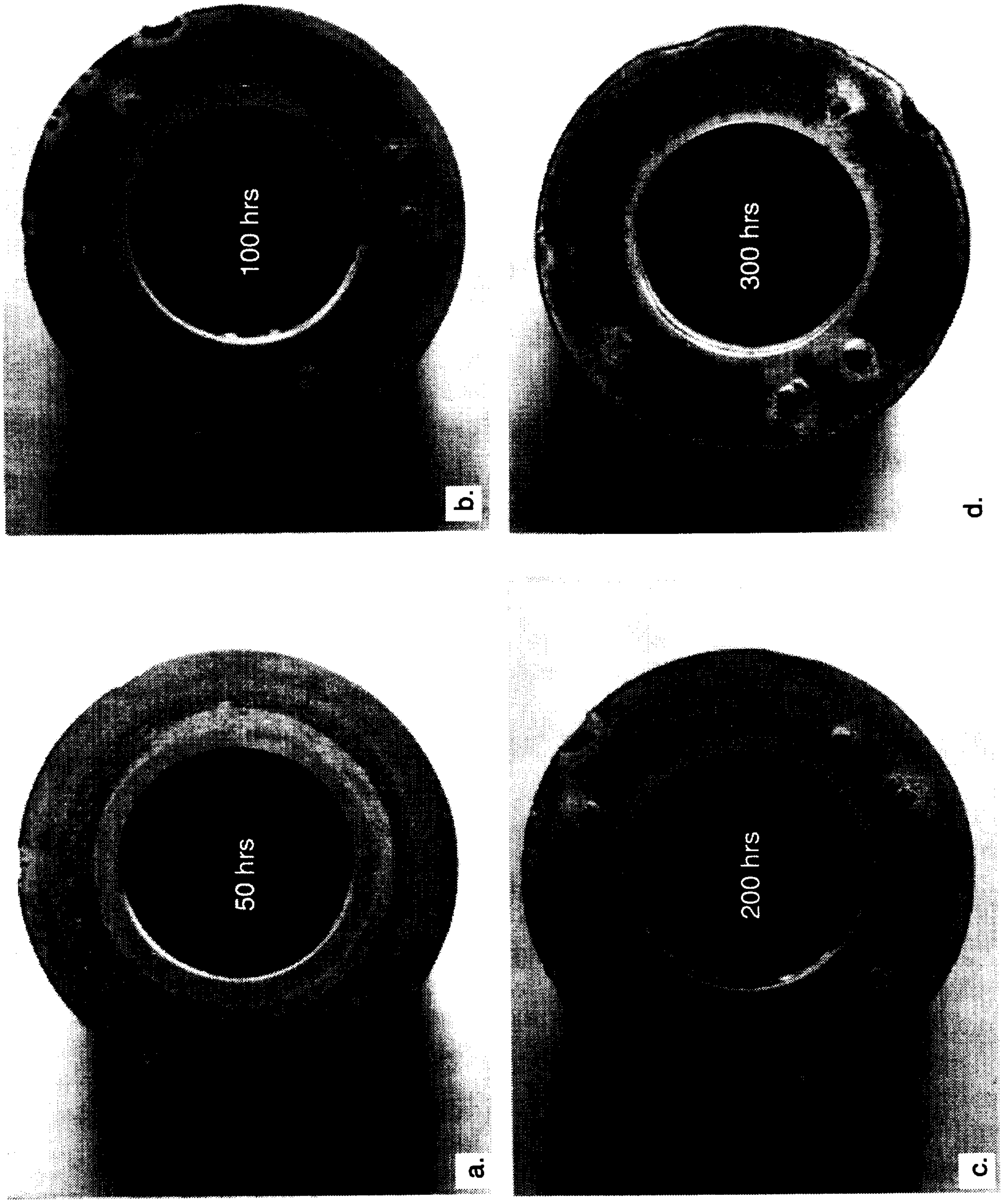

Fig. 80 Macrophotographs of the ends of D218D after (a) 50, (b) 100, (c) 200, and (d) 300 hrs (Series III). Sample surface was polished through 600 SiC paper.

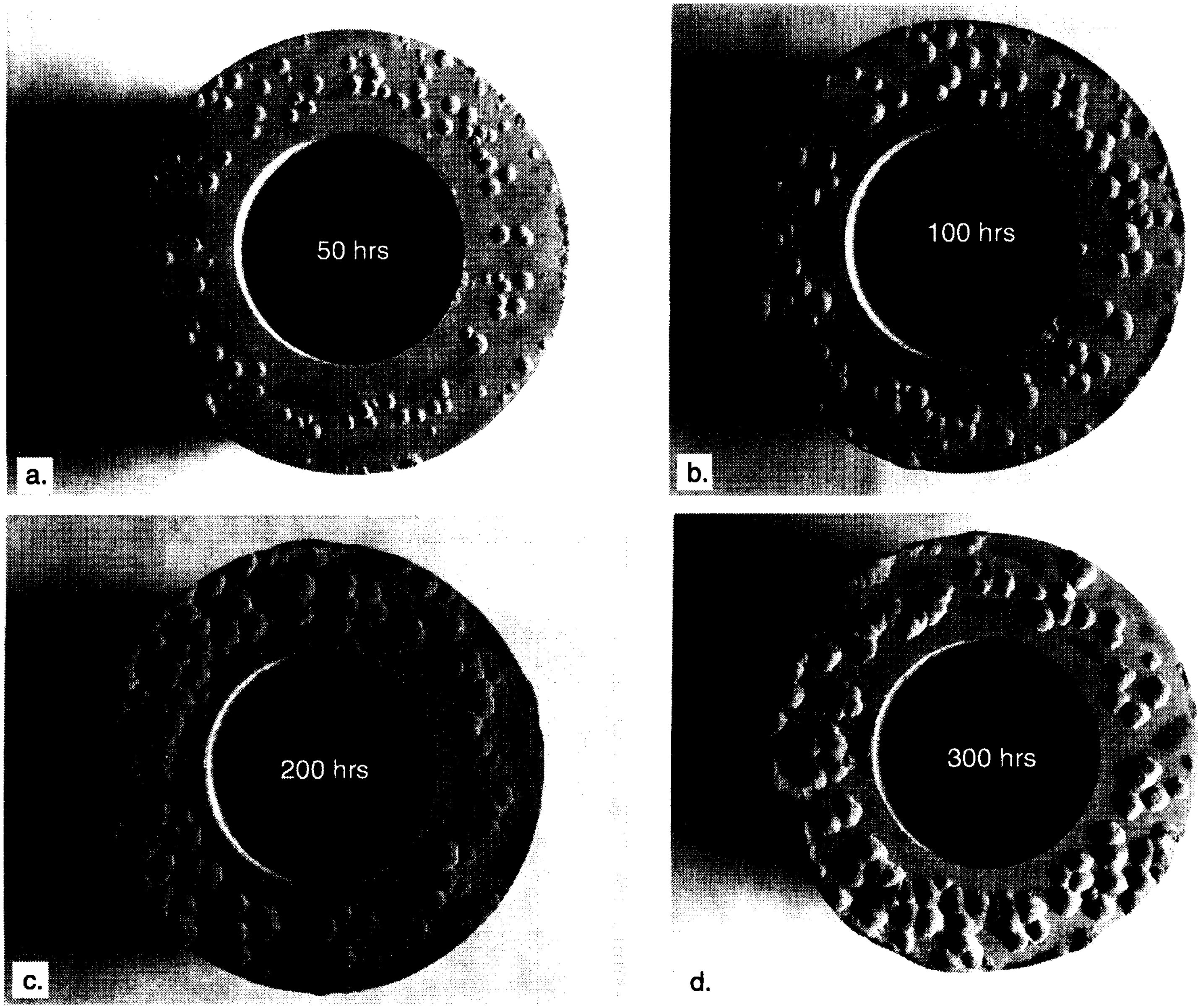

Fig. 81 Macrophotographs of D219E after 50, 100, 200 and 300 hrs (Series III). Sample surface was polished through 600 SiC paper.

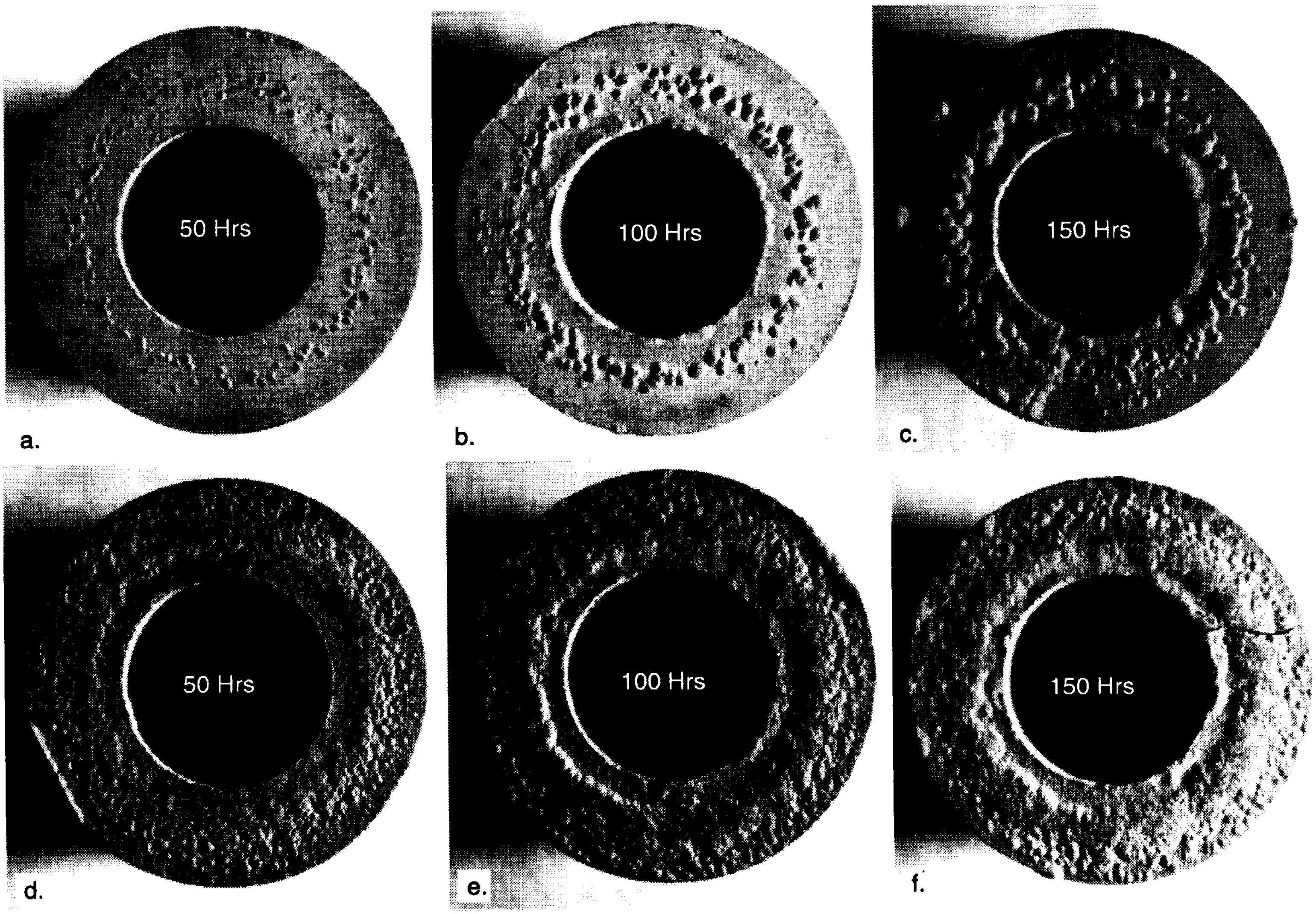

Fig. 82 Macrophotographs of the two ends of AFN20 after (a,d) 50, (b,e) 100 and (c,f) 150 hrs.

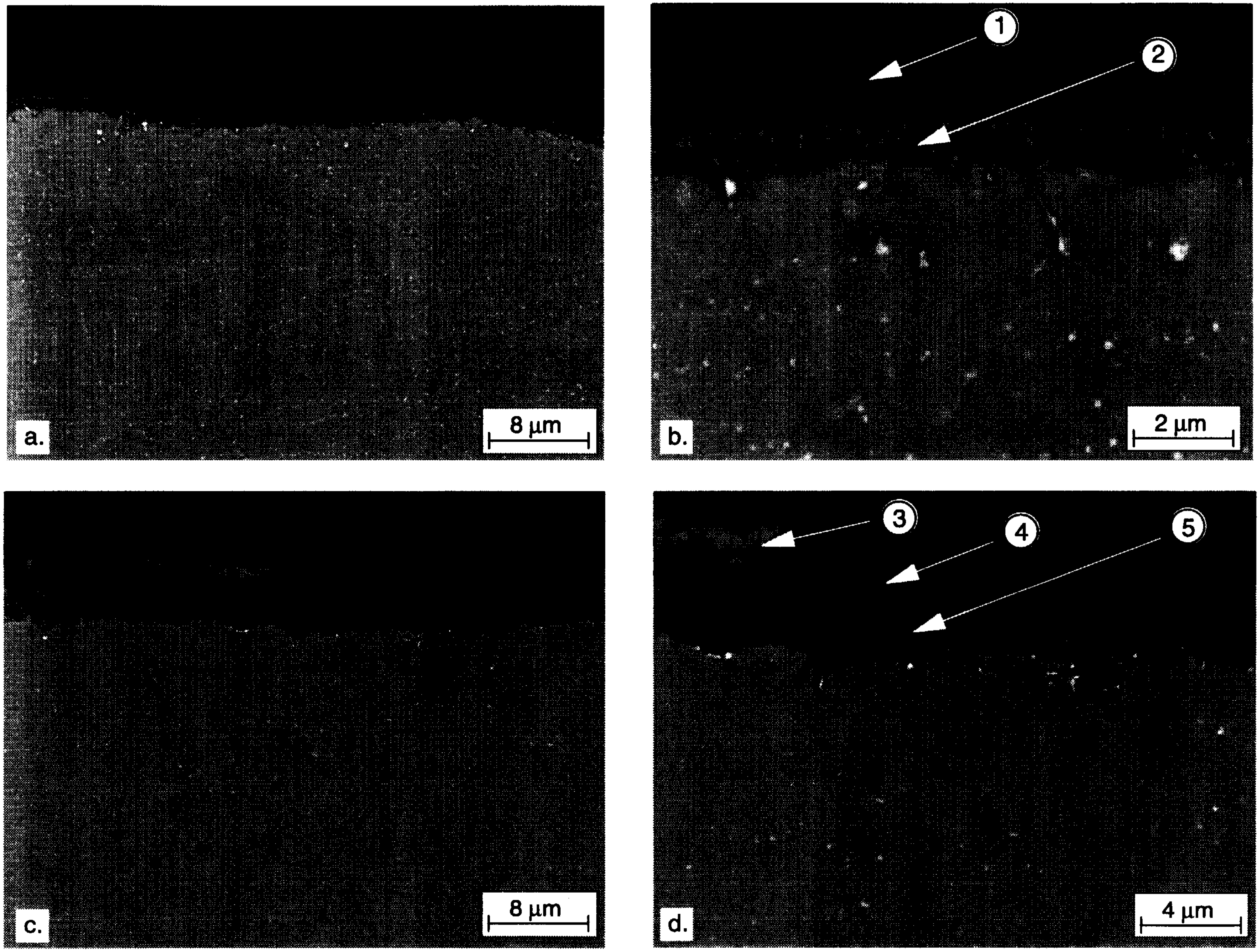

Fig. 83 "Pre-initiation" scale in (a,b) D218 and (c,d) D219. Numbered locations correlate with EDS spectra in Fig. 84.

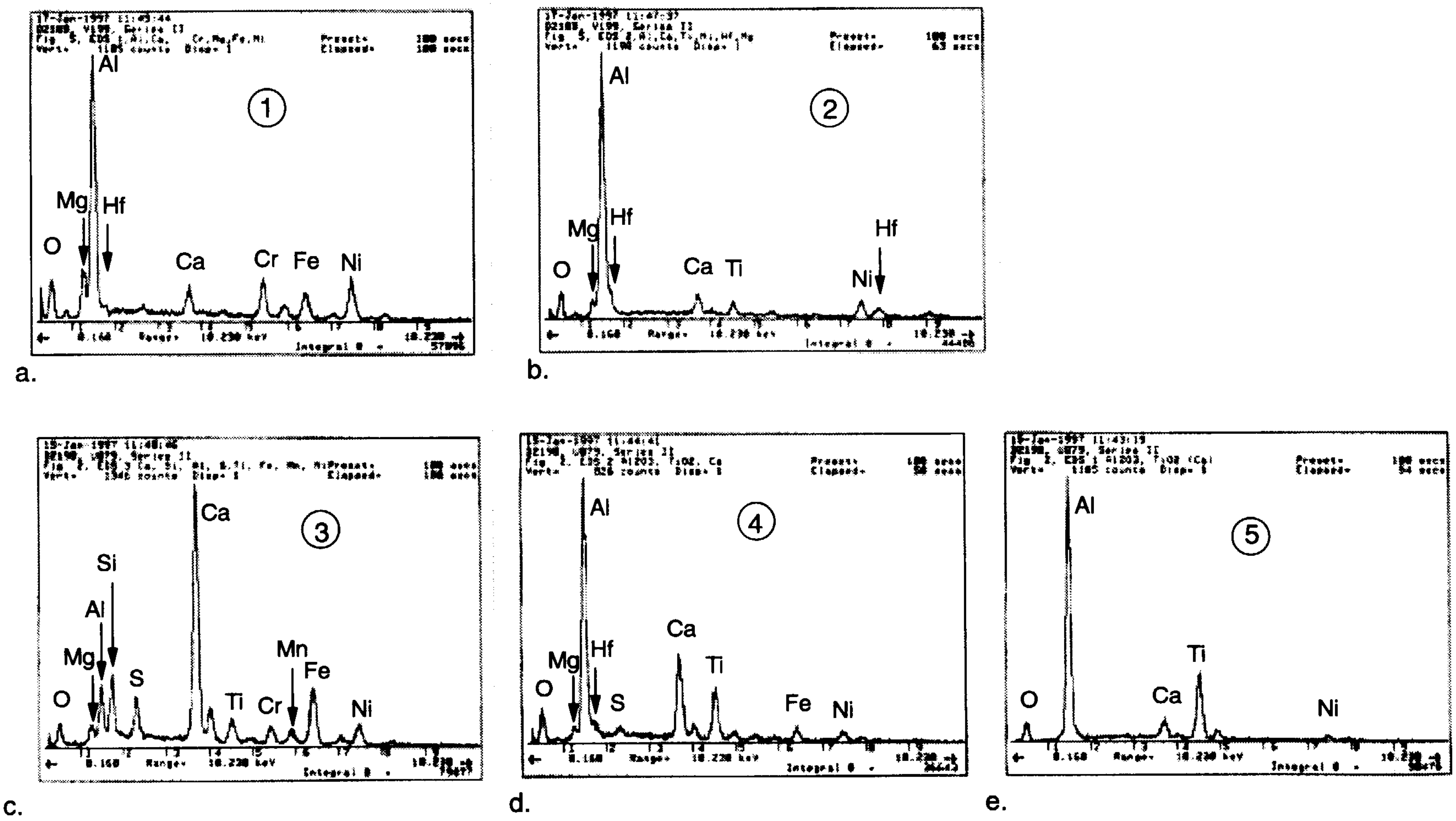

Fig. 84 EDS spectra of "pre-initiation" scales. The numbers in the spectra correlate with the numbered locations in Fig. 83.

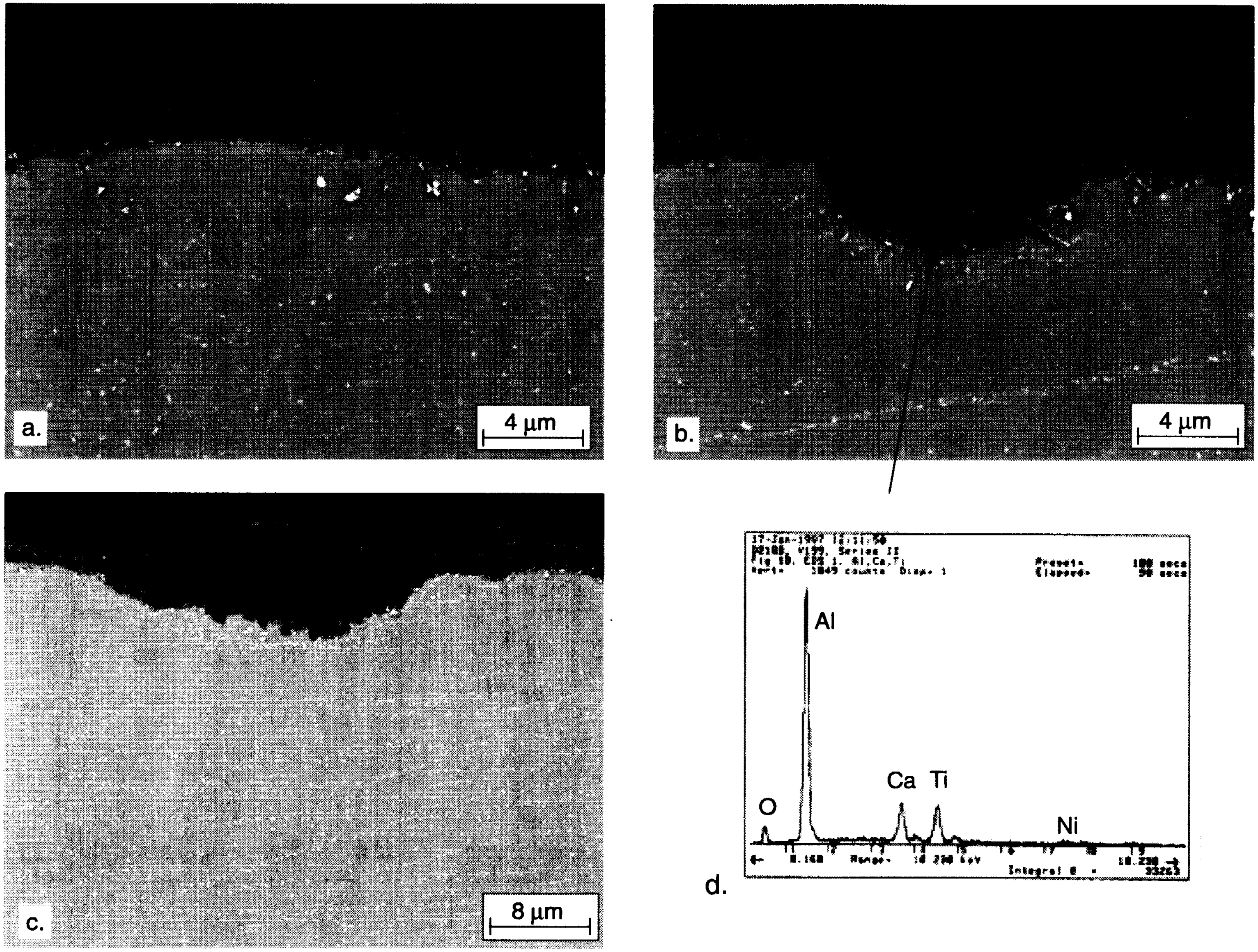

Fig. 85 Possible initiation sites in D218, (a) thicker, fractured scale, (b) "bulb" shaped pit (c) broader, shallow pit, (d) EDS spectra from pit in (b)

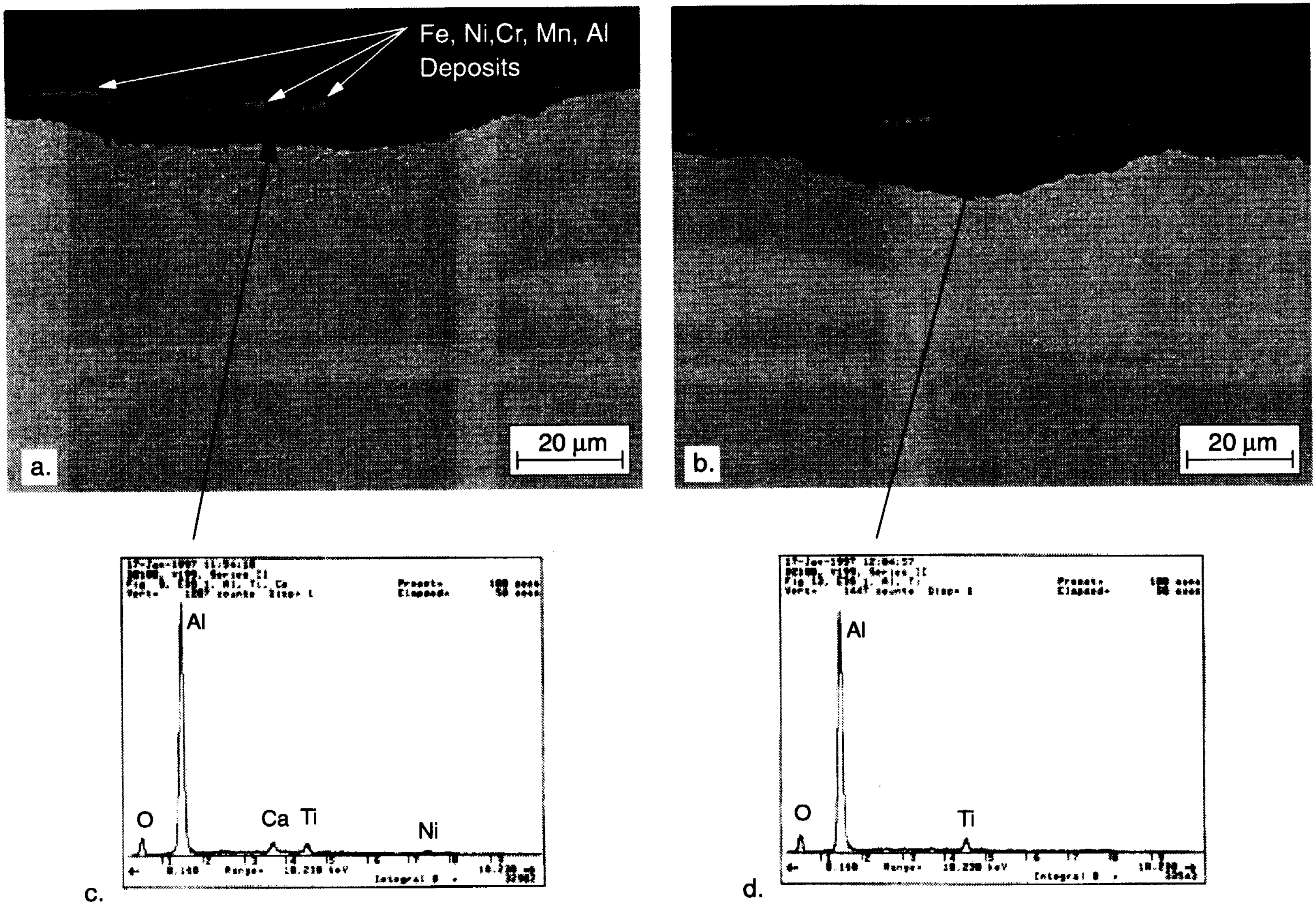

Fig. 86 Possible initiation sites in D218, (a) shallow, sunken pit and (b) shallow but raised pit, (c,d) associated EDS spectra from the center of the pits.

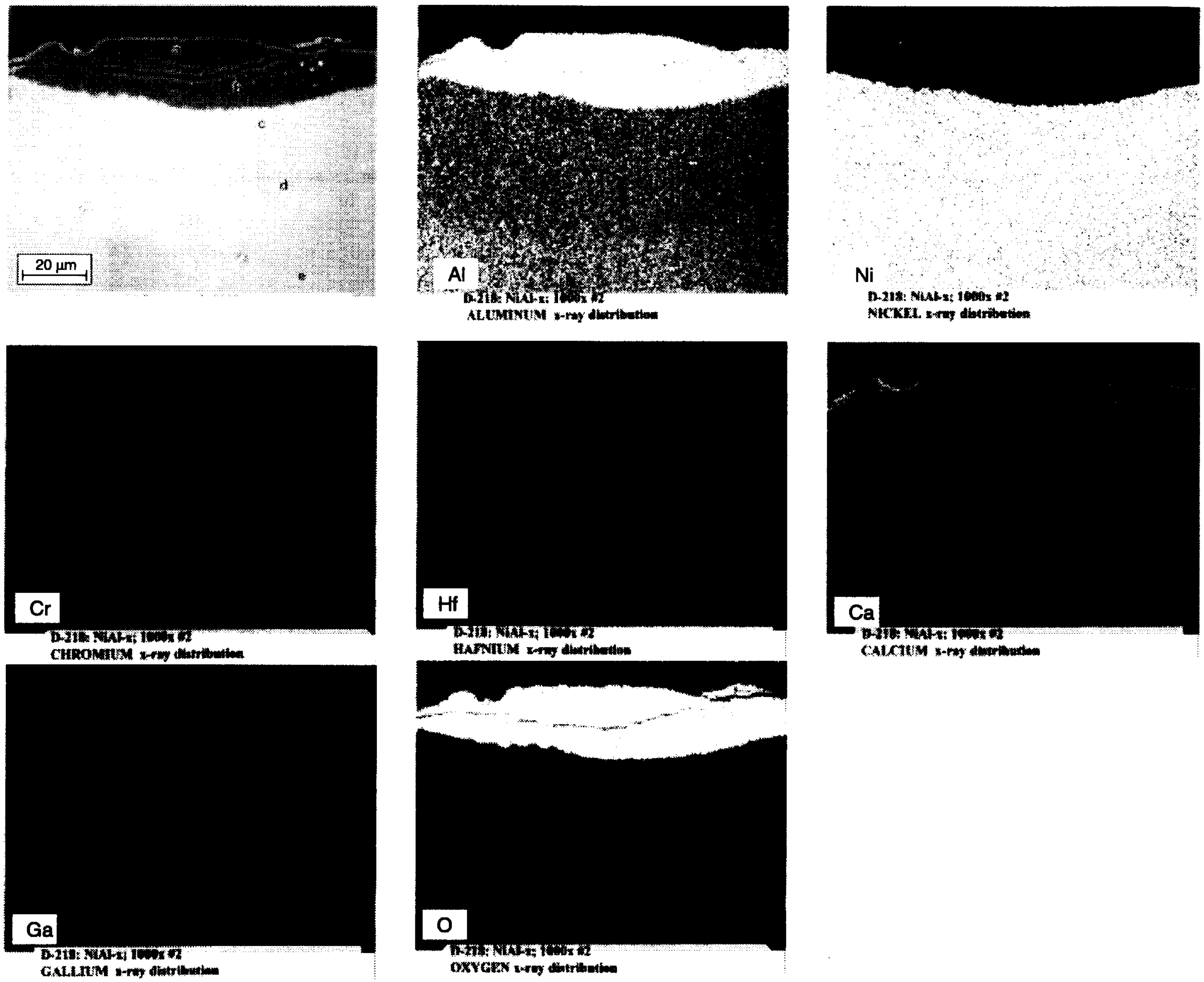

Fig. 87 X-ray maps of a broad, shallow pit in D218.

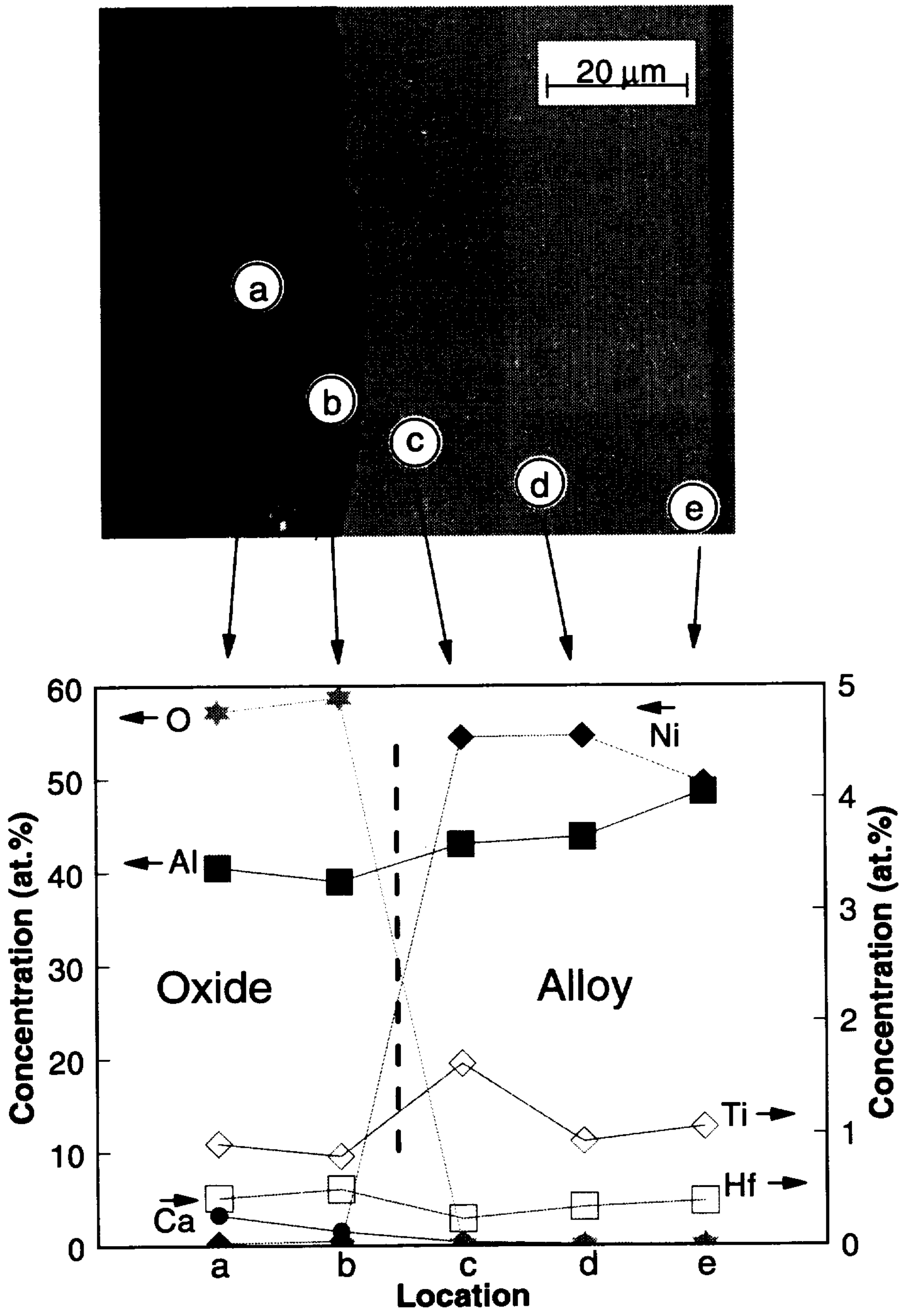

Fig. 88 Concentration profile below shallow pit shown in Fig. 87.

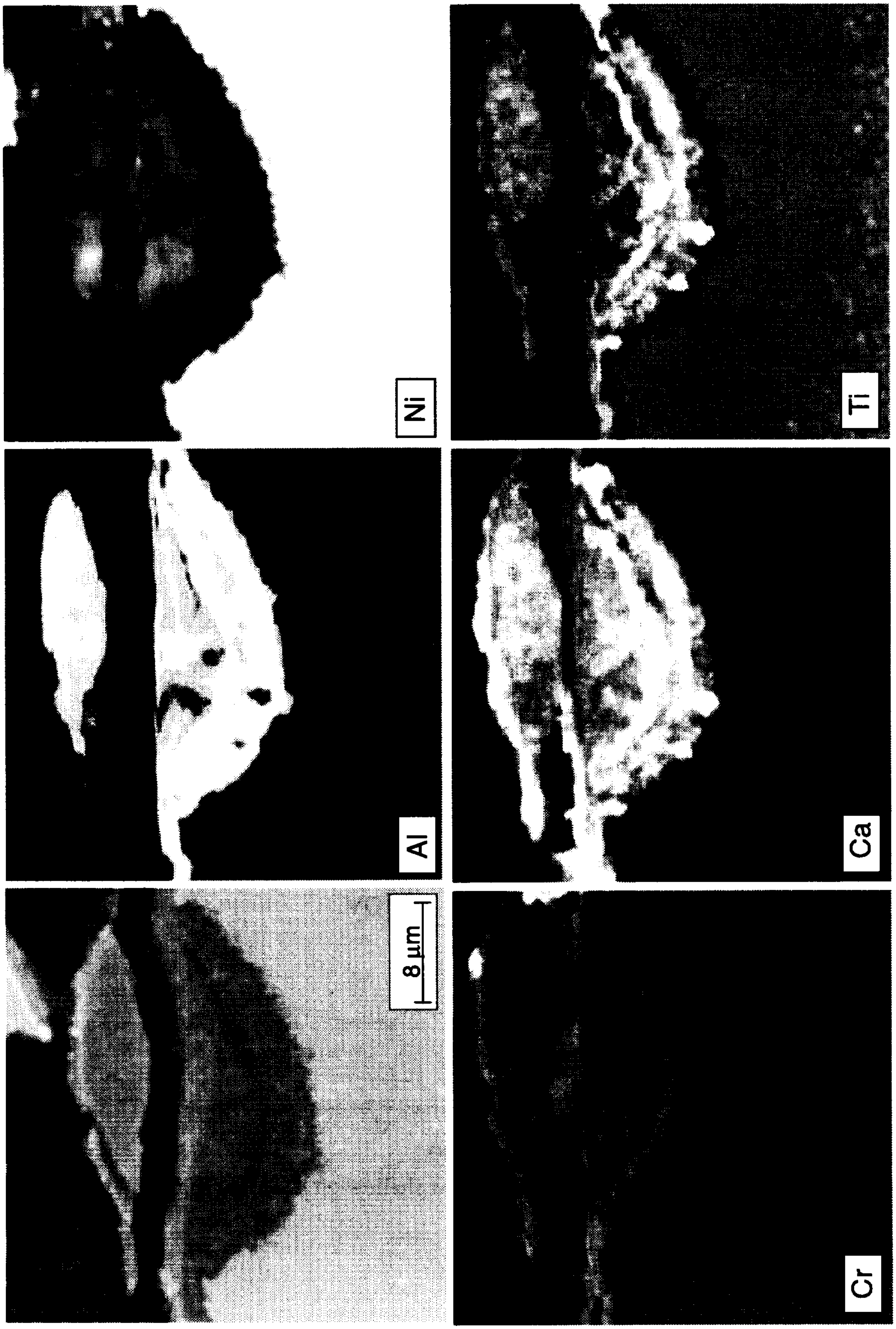

Fig. 89 X-ray map of attack initiation on AFN19 after 300 hrs.

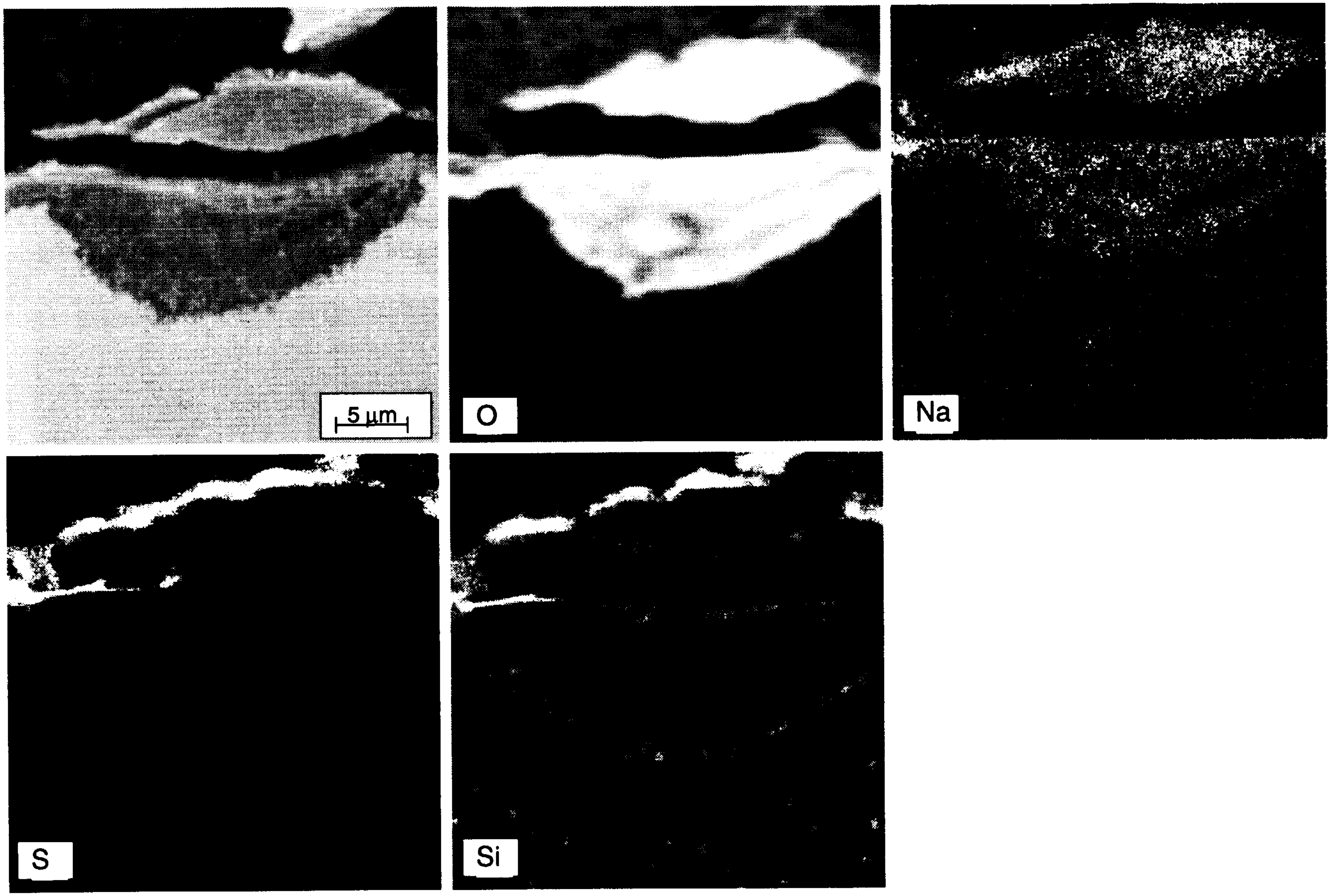

Fig. 89 (cont.) X-ray map of attack initiation on AFN19 after 300 hrs.

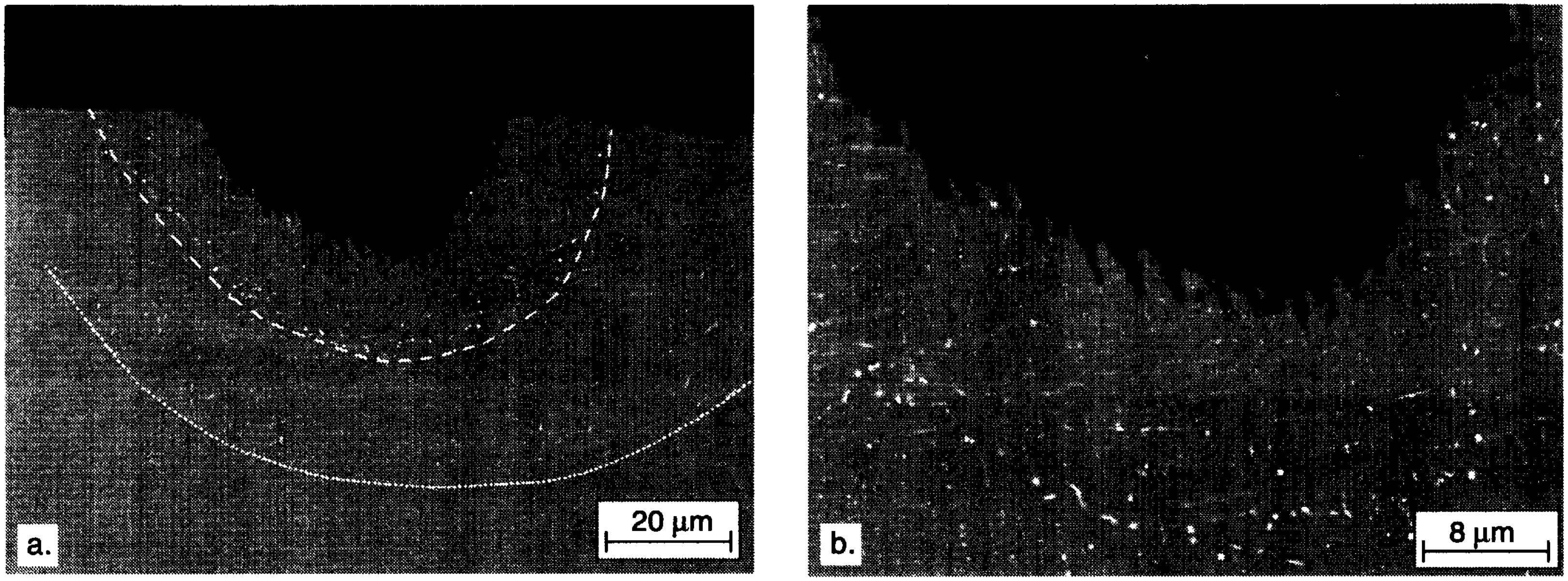

Fig. 90 Deeper pit in D218 showing preferential growth along crystallographic planes (a) dashed lines indicate diffusion affected bands below pit (b) higher magnification showing precipitates aligned with previous Heusler precipitates.

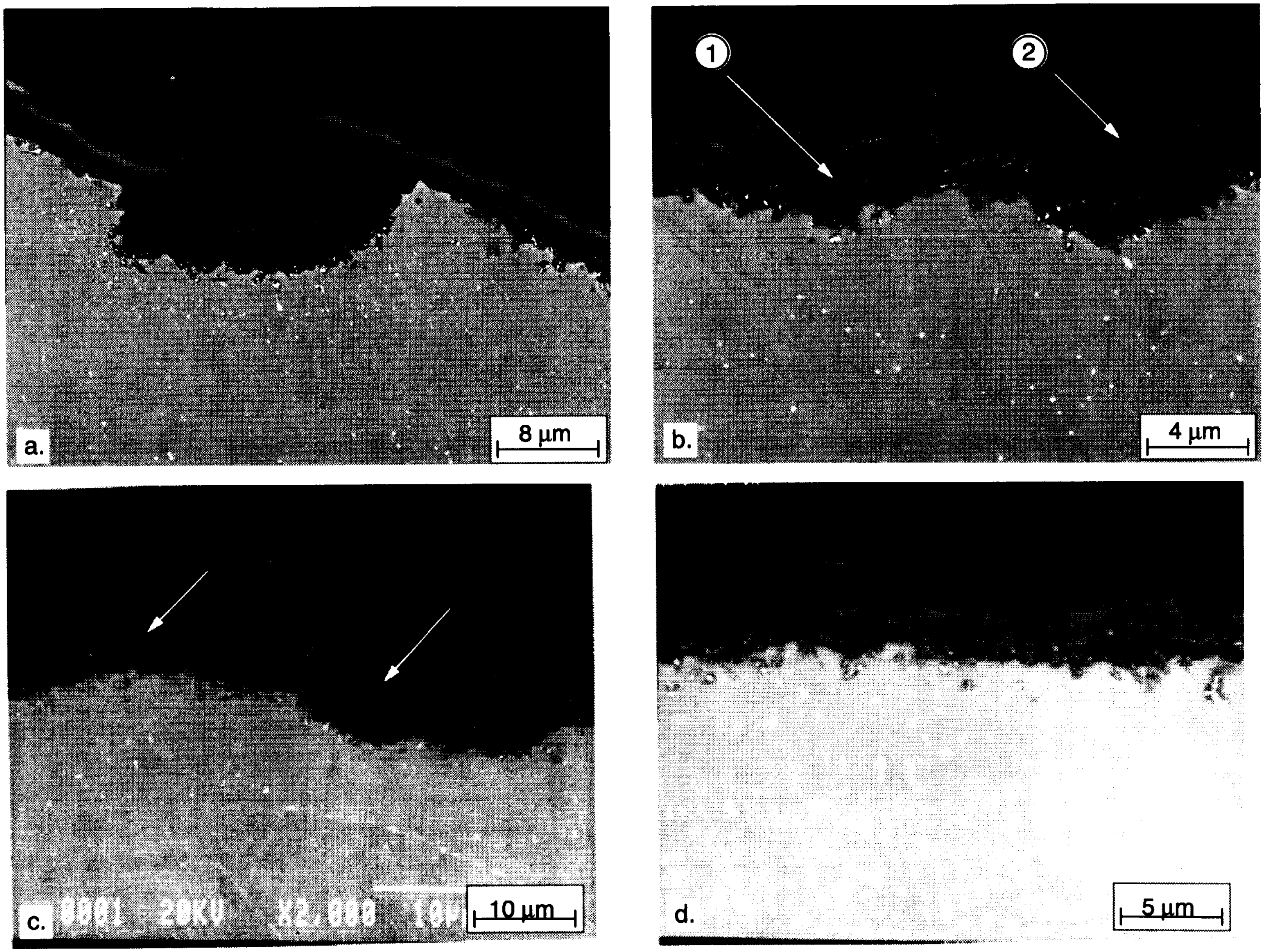

Fig. 91 Possible initiation sites in (a) AFN19, (b) D219 and (c,d) AFN20.

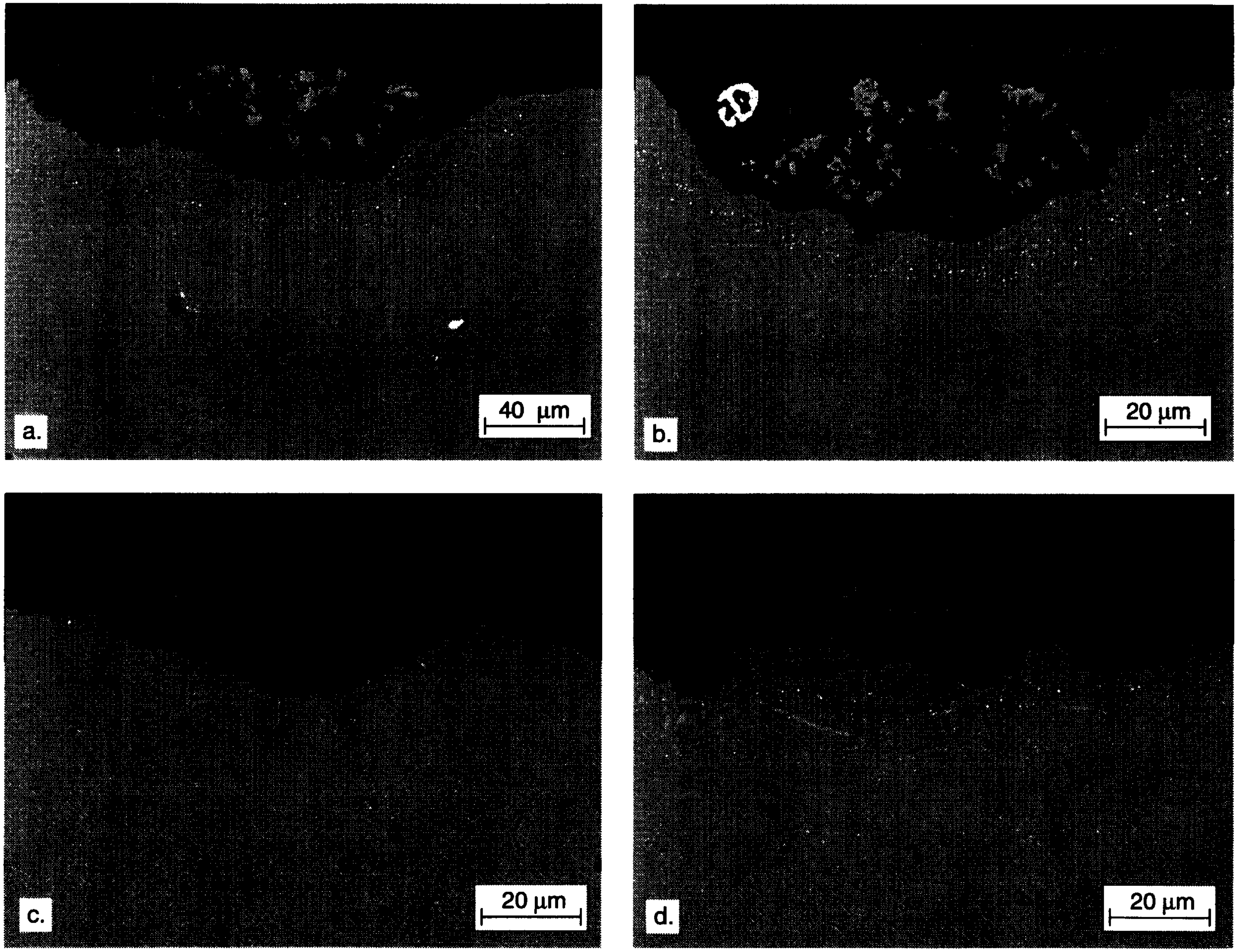

Fig. 92 Intermediate attack (a,b) in D218 (c,d) in AFN19.

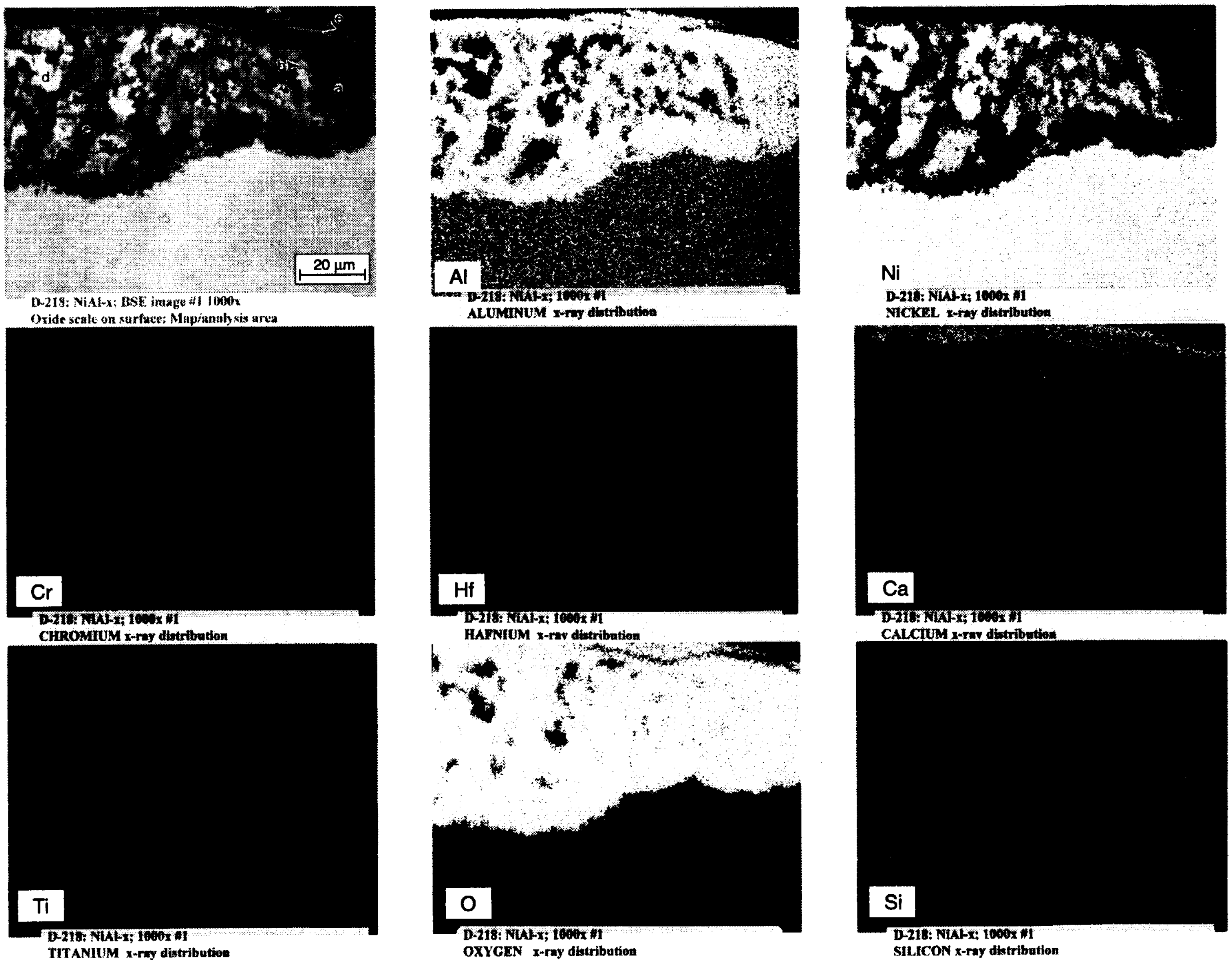

Fig. 93 X-ray maps of intermediate attack in D218 shown in Fig. 92a (Probe image is inverted from that in Fig. 92a)

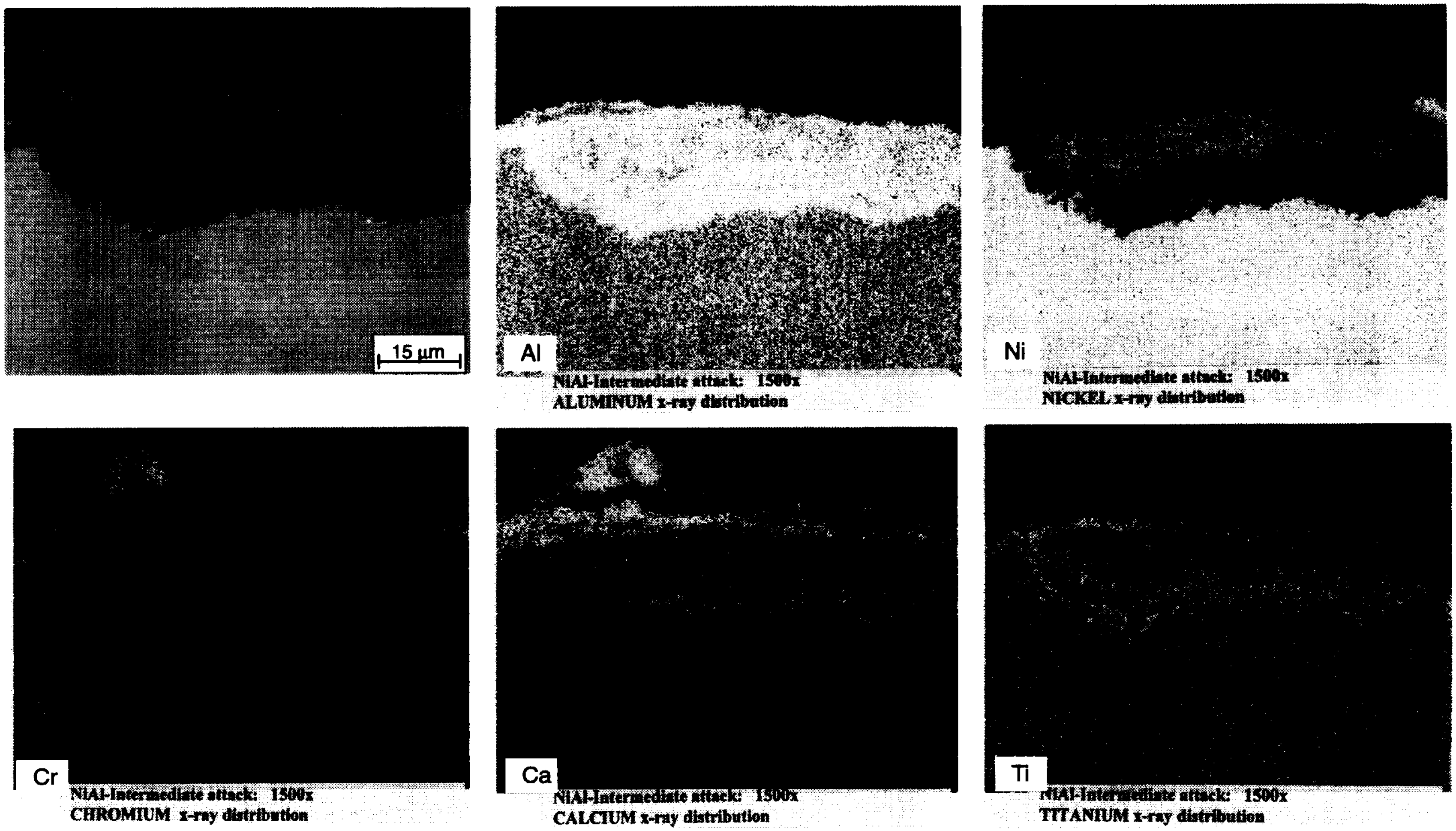

Fig. 94 X-ray map of pit in transition between initiation and intermediate attack on AFN19 after 300 hrs.

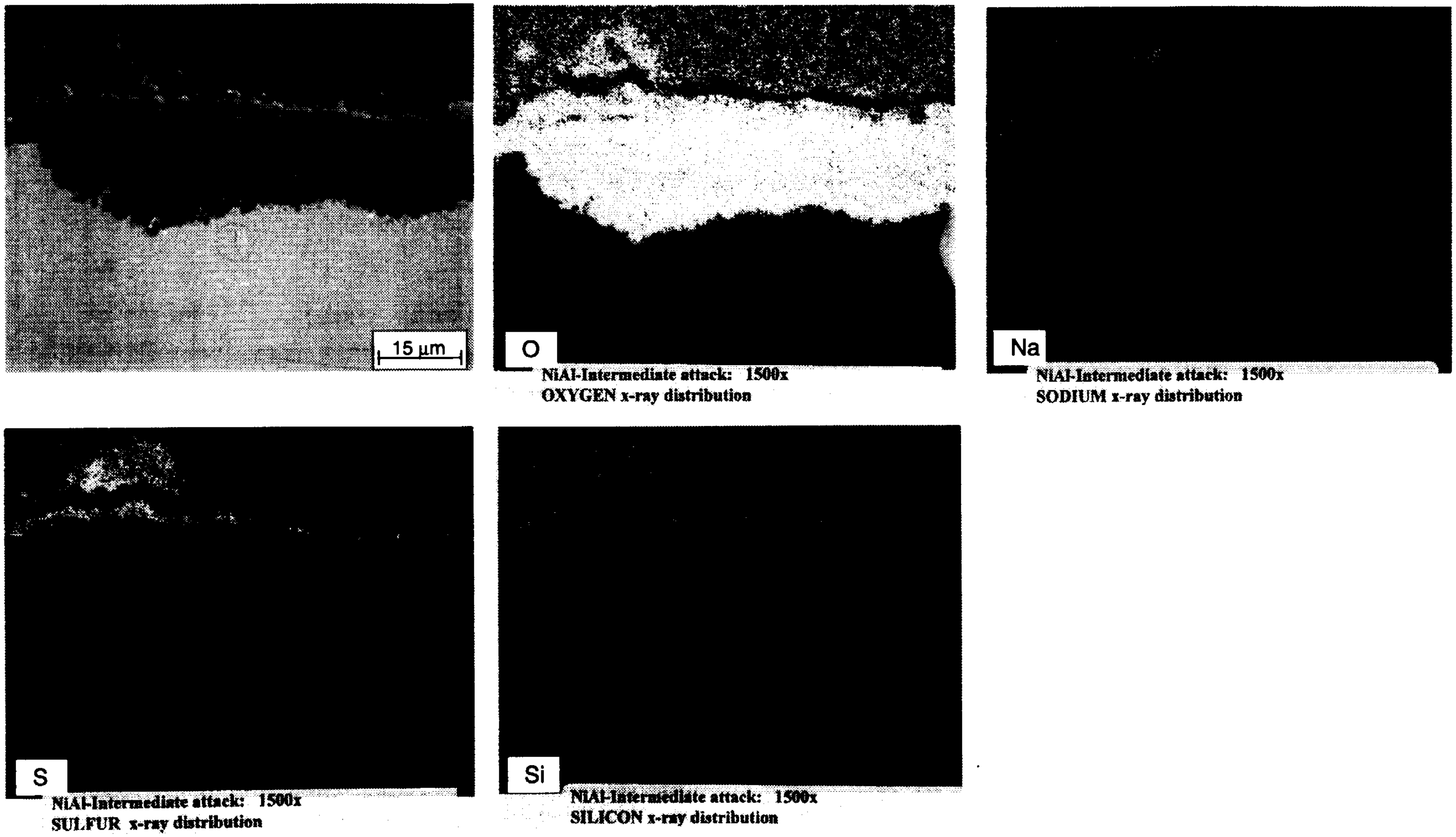

Fig. 94 (cont) X-ray map of pit in transition between initiation and intermediate attack on AFN19 after 300 hrs.

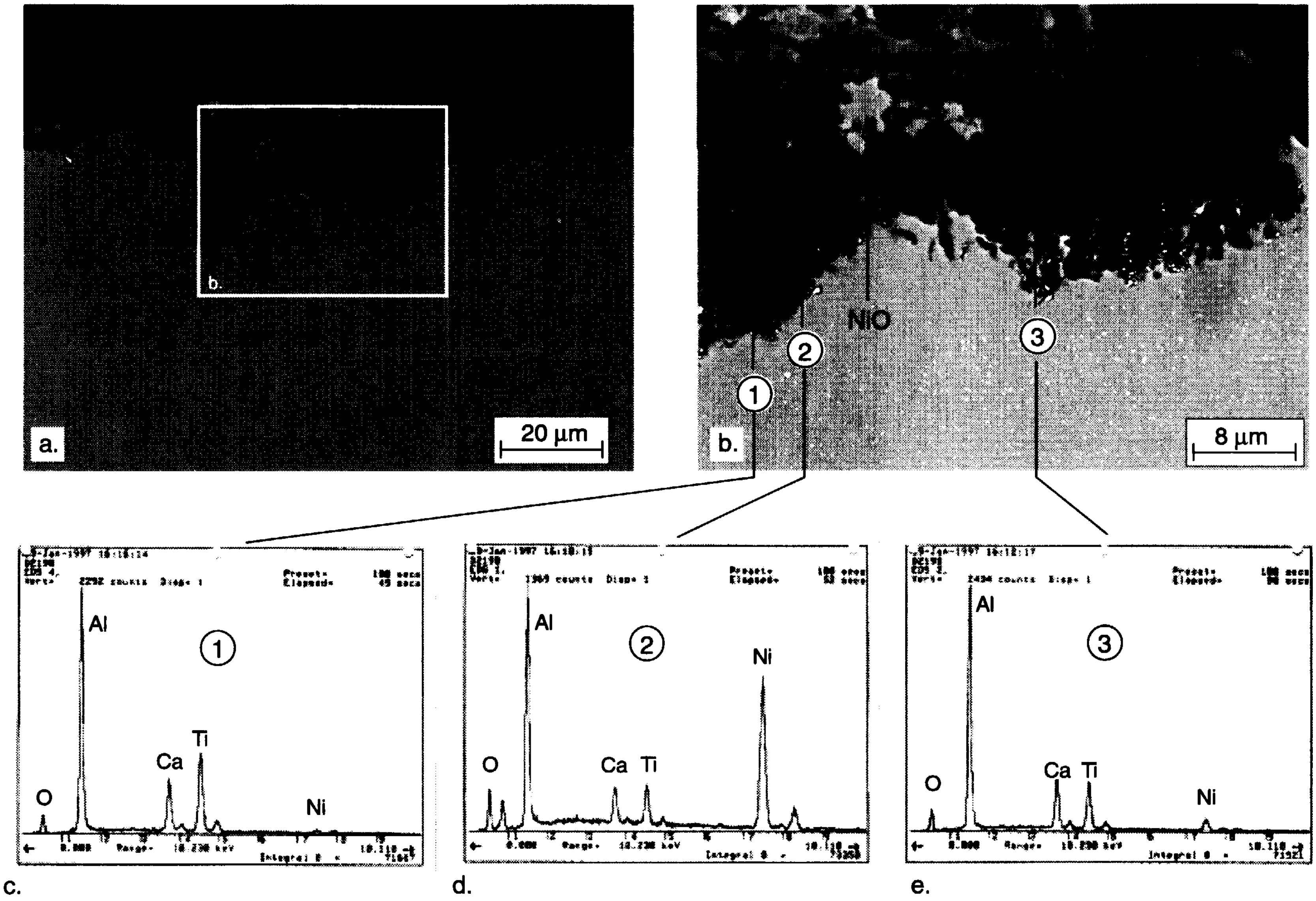

Fig. 95 Intermediate attack in D219. EDS spectra show various oxide compositions in (b).

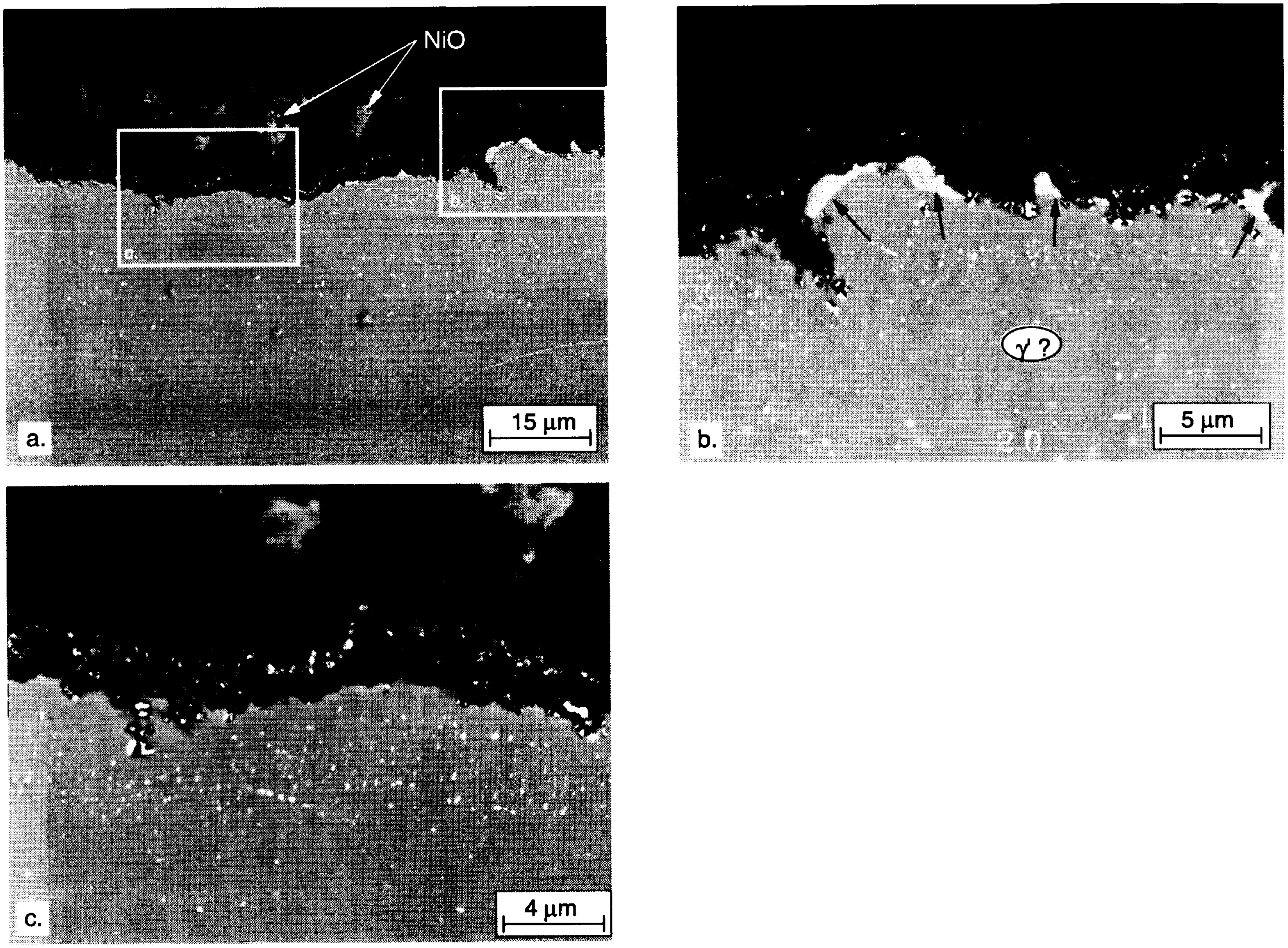

Fig. 96 Intermediate attack in D219. Arrows in (b) indicate likely γ' formation.

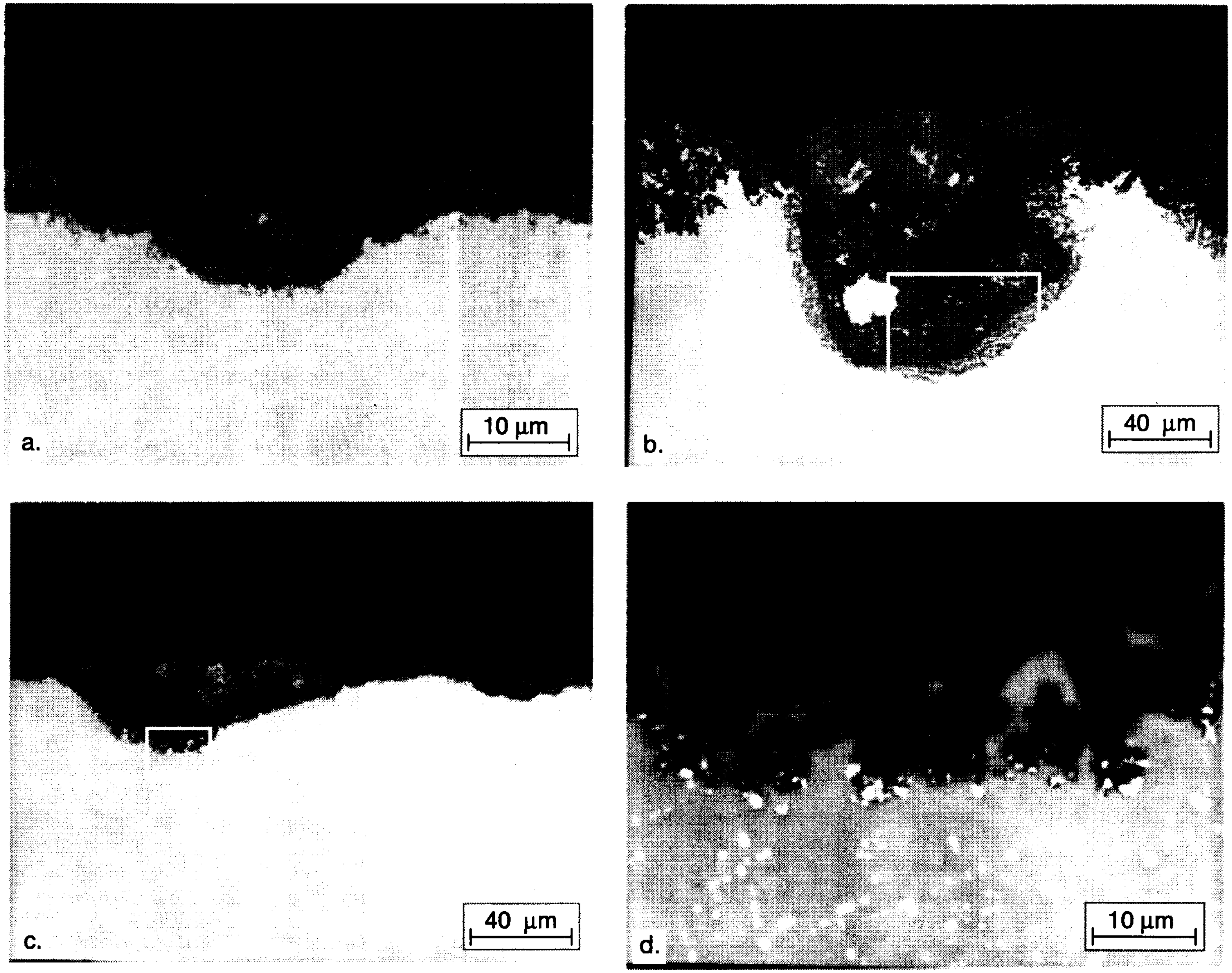

Fig. 97 Intermediate attack in AFN20. Image (d) is a higher magnification of the box shown in (c).

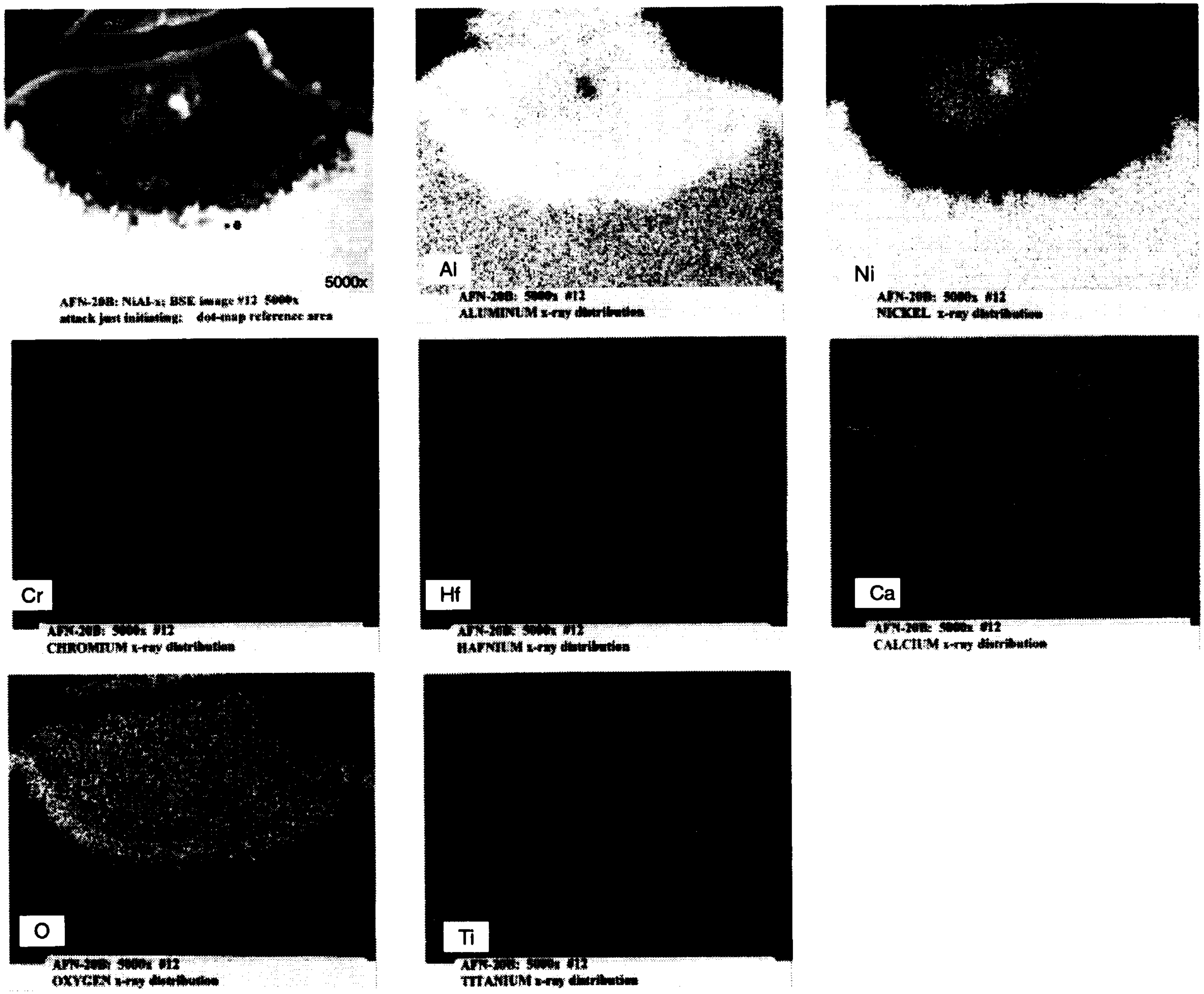

Fig. 98 X-ray maps of intermediate attack in AFN20 shown in Fig. 95d.

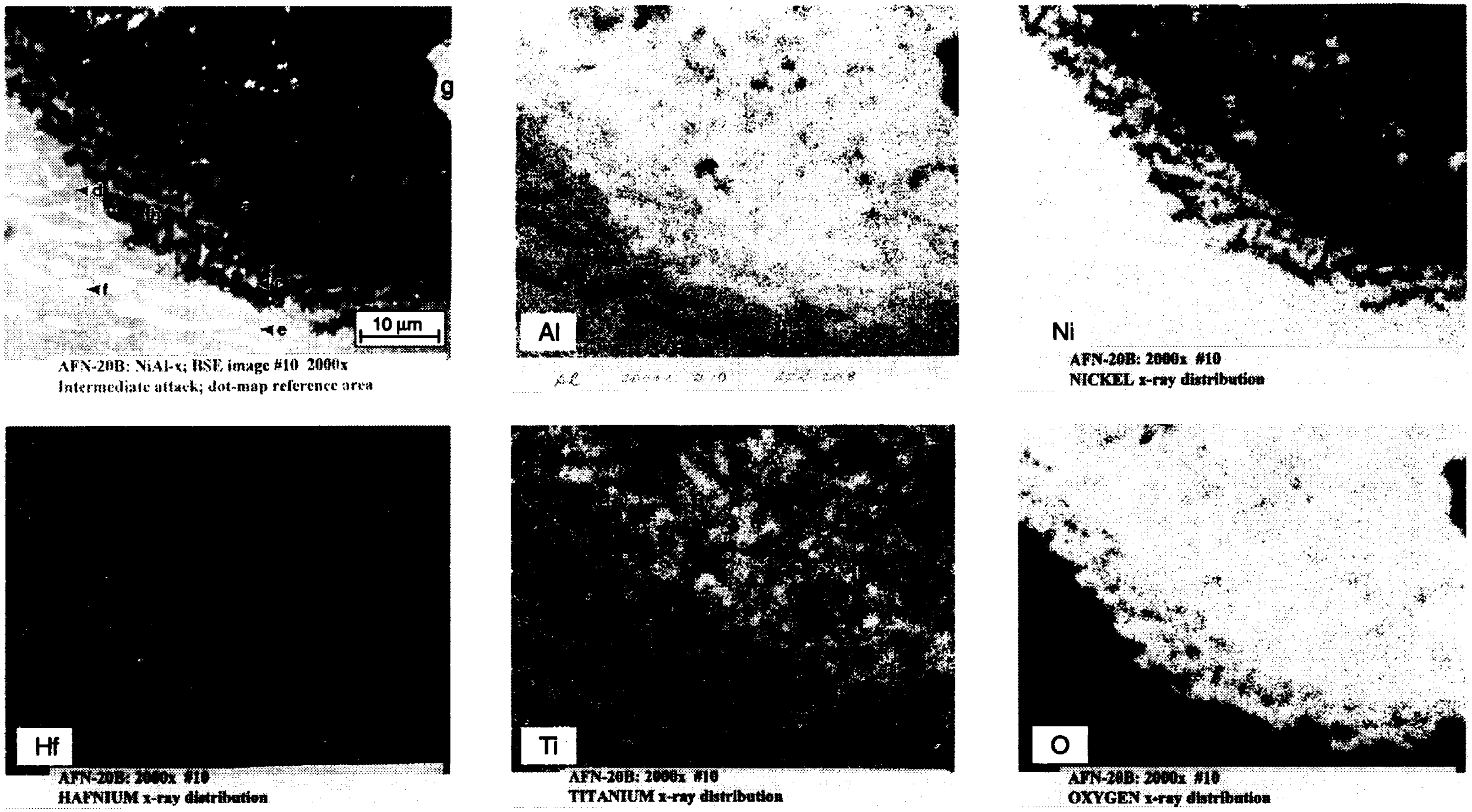

Fig. 99 X-ray maps of intermediate attack in AFN20 shown in box in Fig. 97b. Compositions in Table refer to lettered points a-g in (a).

	Ni	Ti	Al	Hf	Si	O	
a	2.5	6.4	31.5	0.6	0.1	58.9	Al2O3 (Ti)
b	5.9	3.7	35.1	1.4	0.09	53.8	Al2O3(Ni,Ti)
c	57.9	1.1	40.1	0.01	0.29	0.48	β - NiAl
d	57.8	1.6	40.5	0.04	0.07	0	β - NiAl
e	37.3	30.4	19.9	12.2	0.27	0	β - NiAl+HfO2
f	73.2	8.7	17.1	1.0	0.04	0	γ' - Ni3(Al,Ti)
g	87.9	1.5	10.5	0.05	0	0	γ - Ni(Al,Ti)

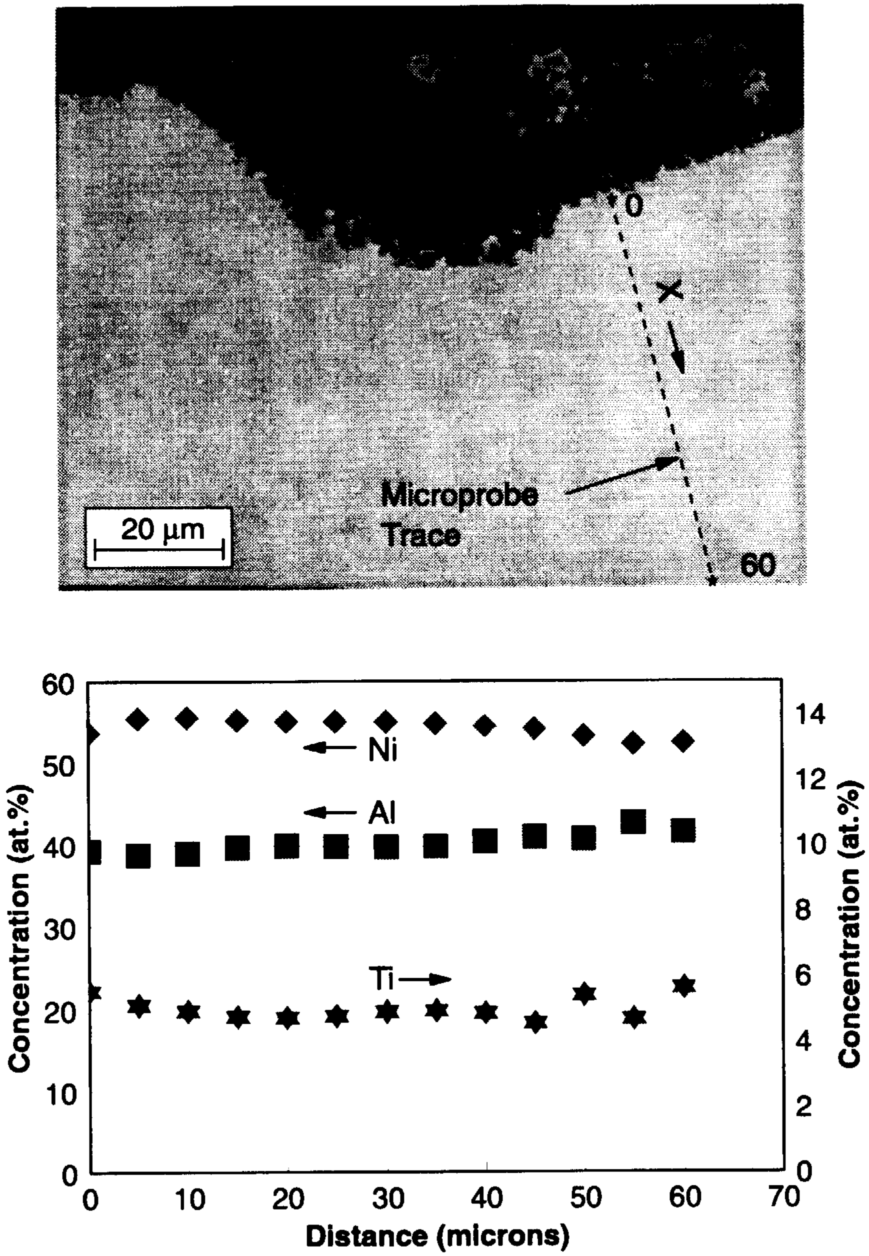

Fig. 100 Concentration profile in AFN20 below region of intermediate attack shown in Fig. 97c.

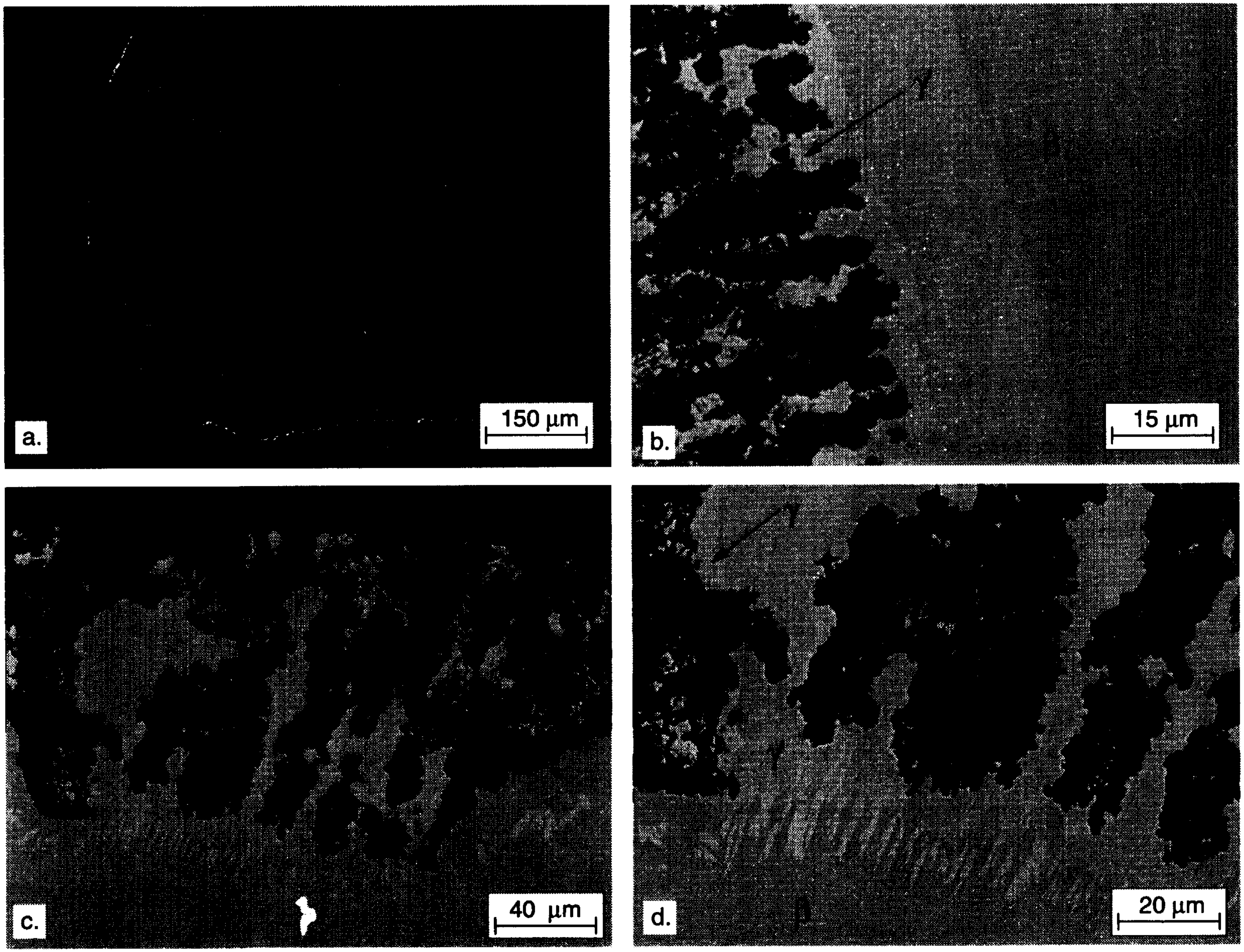

Fig. 101 Regions of rampant attack on (a,b) D218 and (c,d) AFN19. Images (b) and (d) are higher magnifications of (a) and (c).

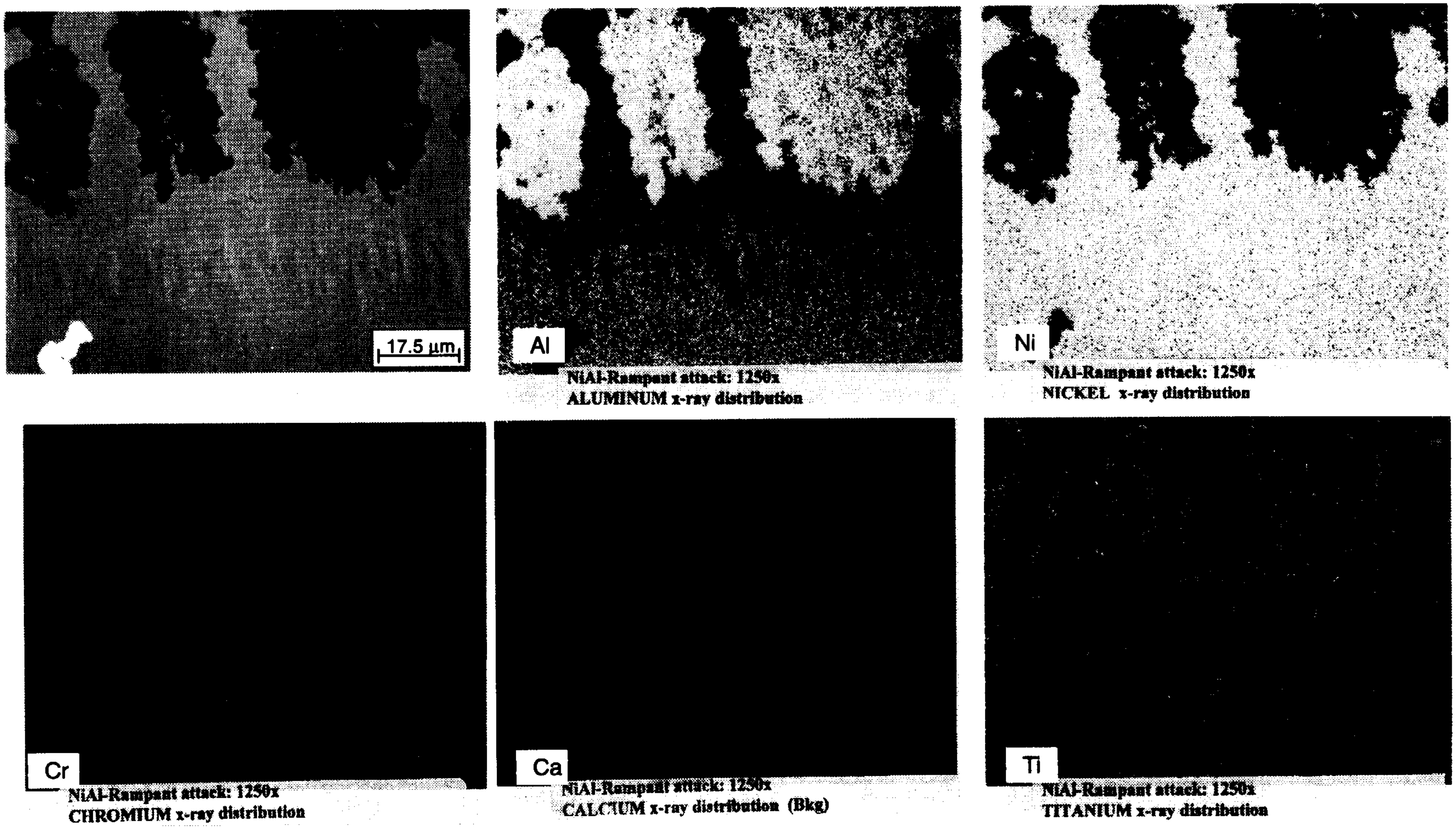

Fig. 102 X-ray map of inner region of rampant attack shown in Fig. 101d (AFN19 after 300 hrs).

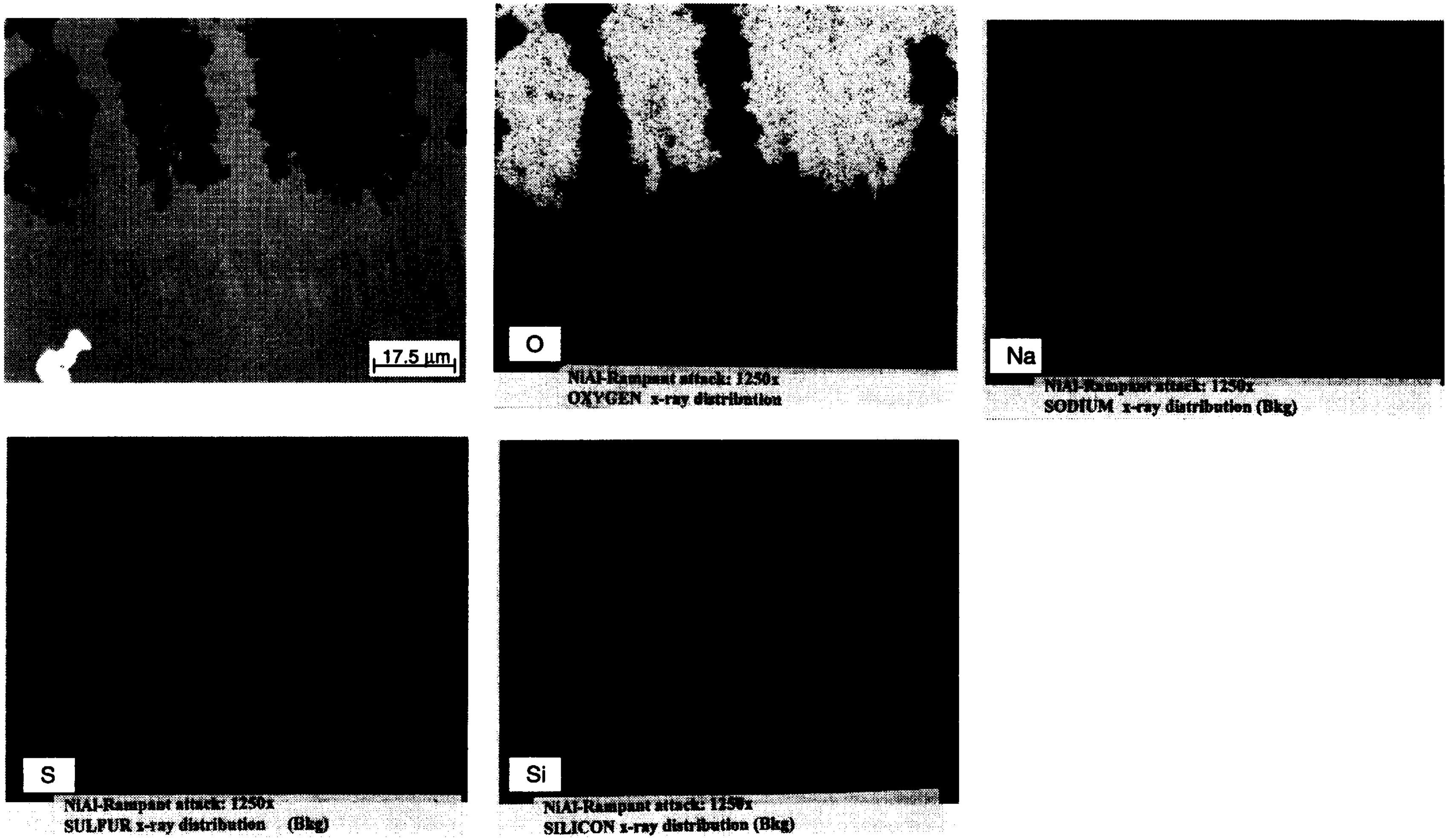

Fig. 102 (cont.) X-ray map of inner region of rampant attack shown in Fig. 101d (AFN19 after 300 hrs).

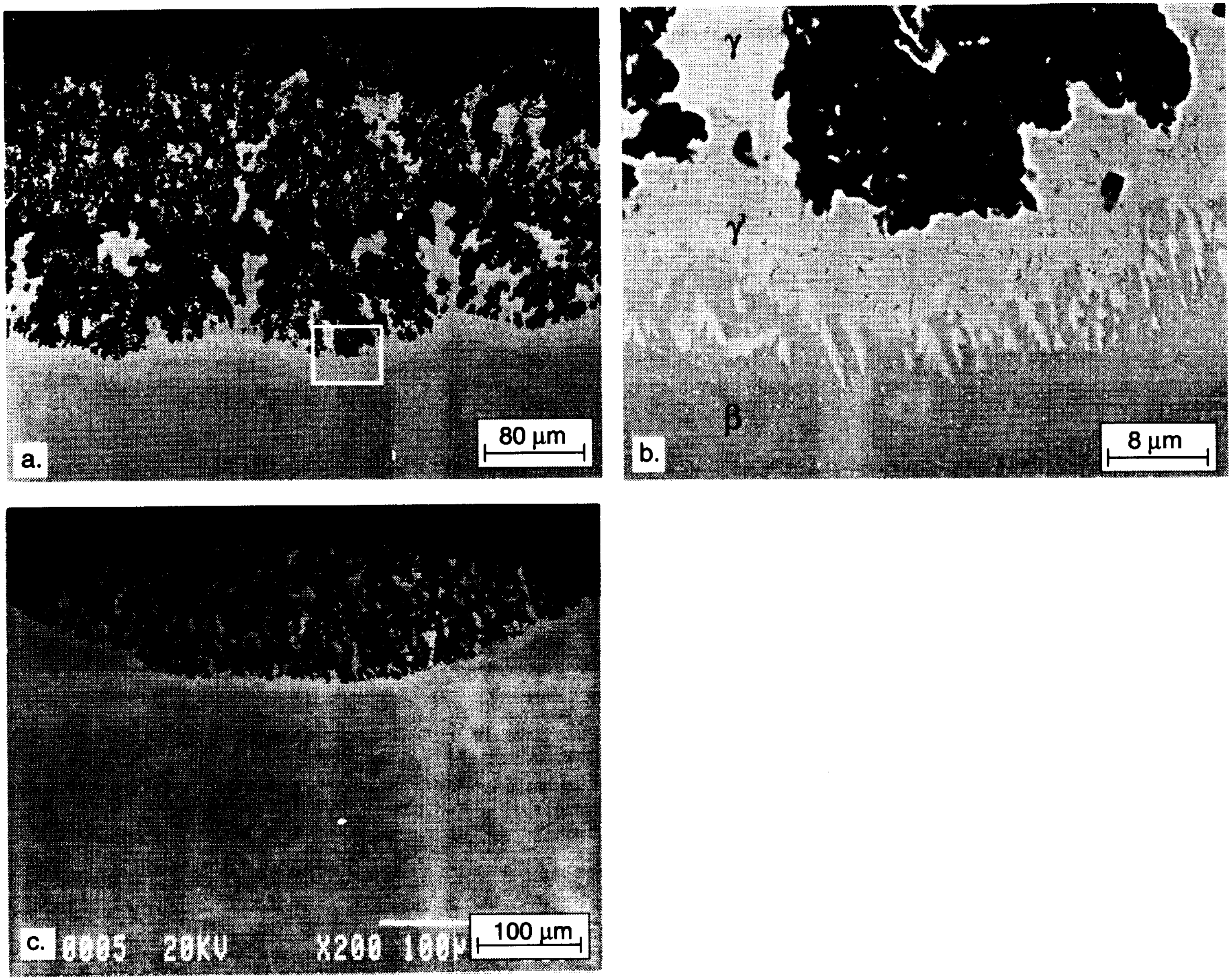

Fig. 103 Regions of rampant attack on (a,b) D219 and (c) AFN20. Image (b) is a higher magnification of the box in (a).

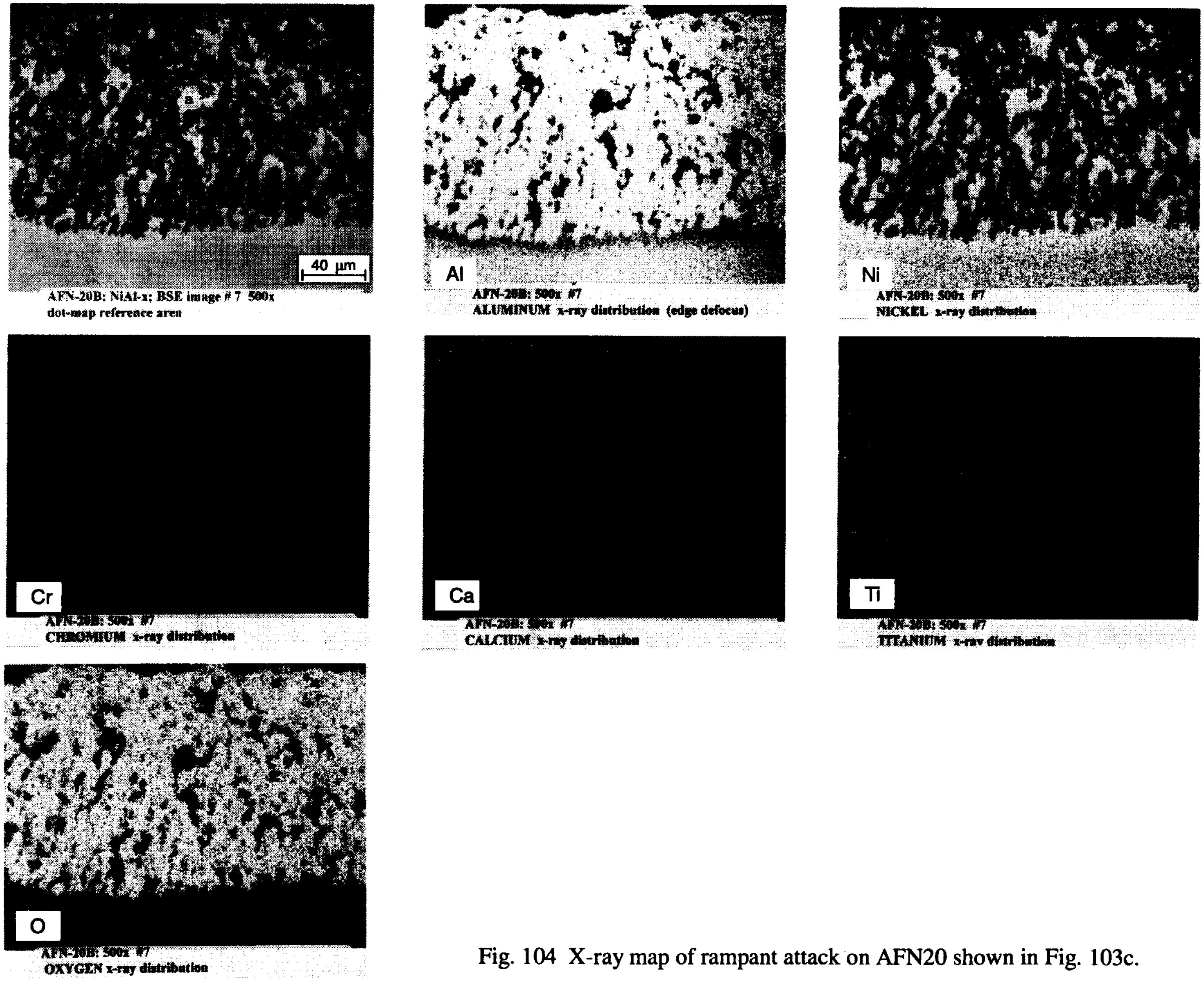

Fig. 104 X-ray map of rampant attack on AFN20 shown in Fig. 103c.

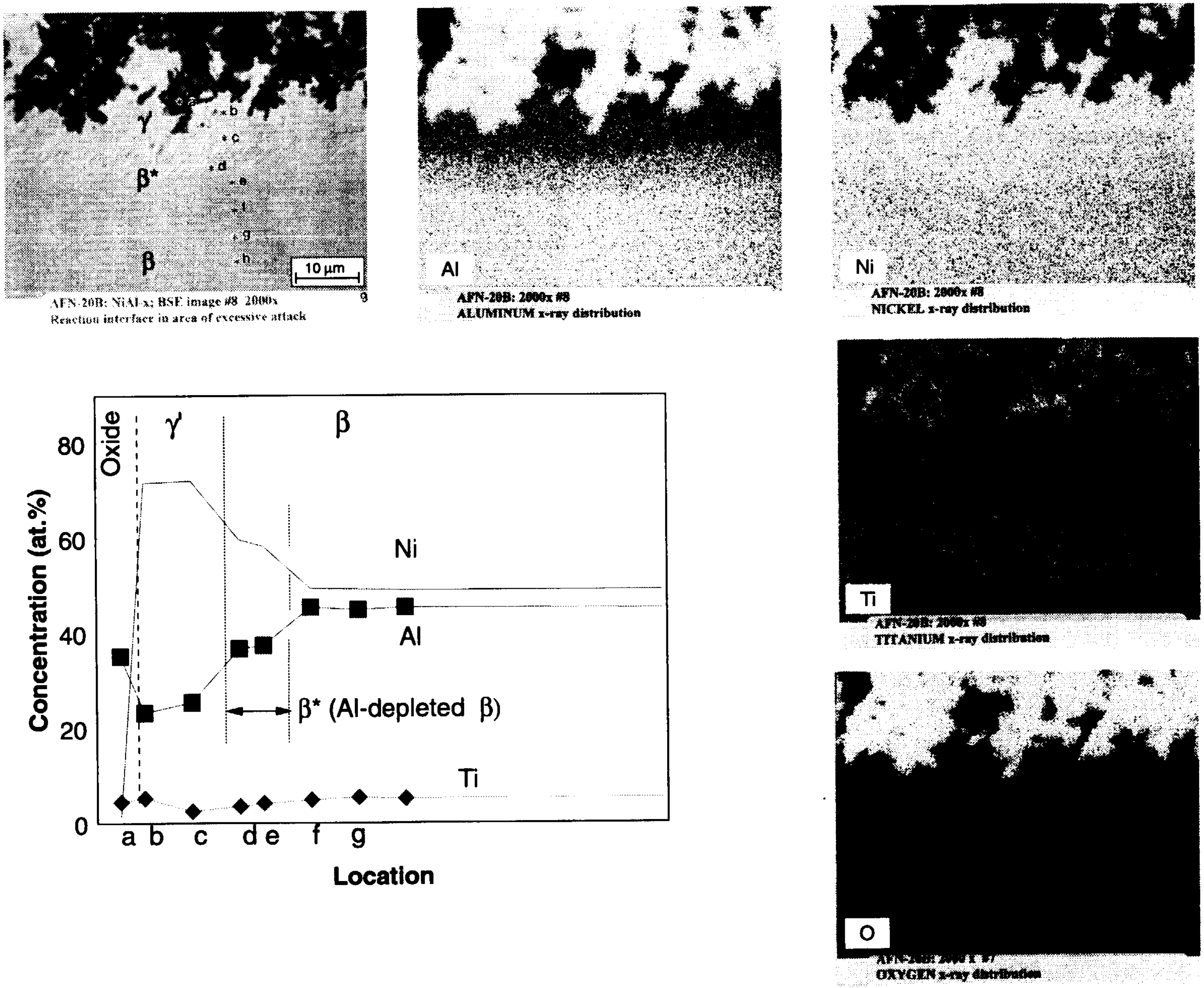

Fig. 105 X-ray map and concentration profile of the inner region of rampant attack shown in Fig. 104a (AFN20).

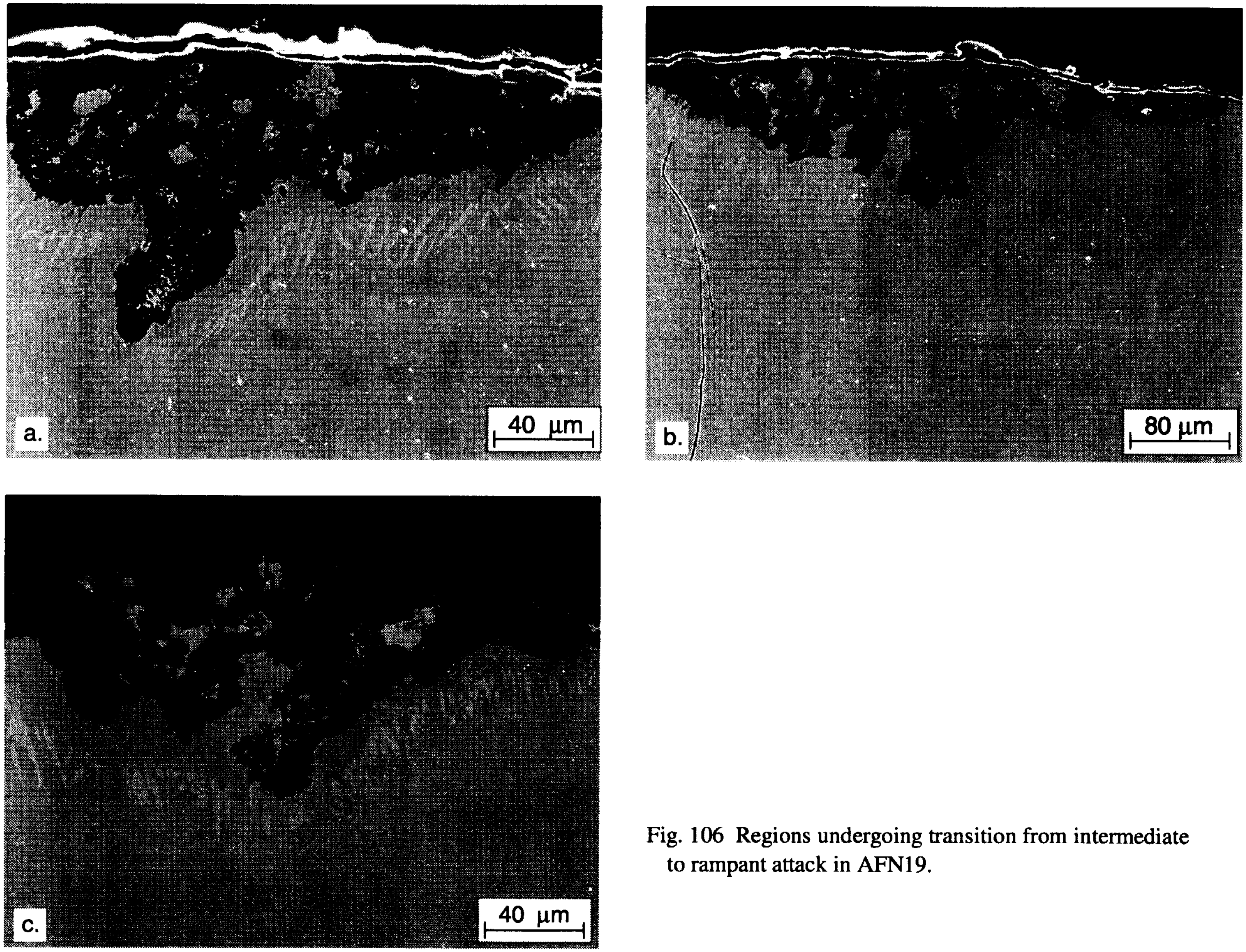

Fig. 106 Regions undergoing transition from intermediate to rampant attack in AFN19.

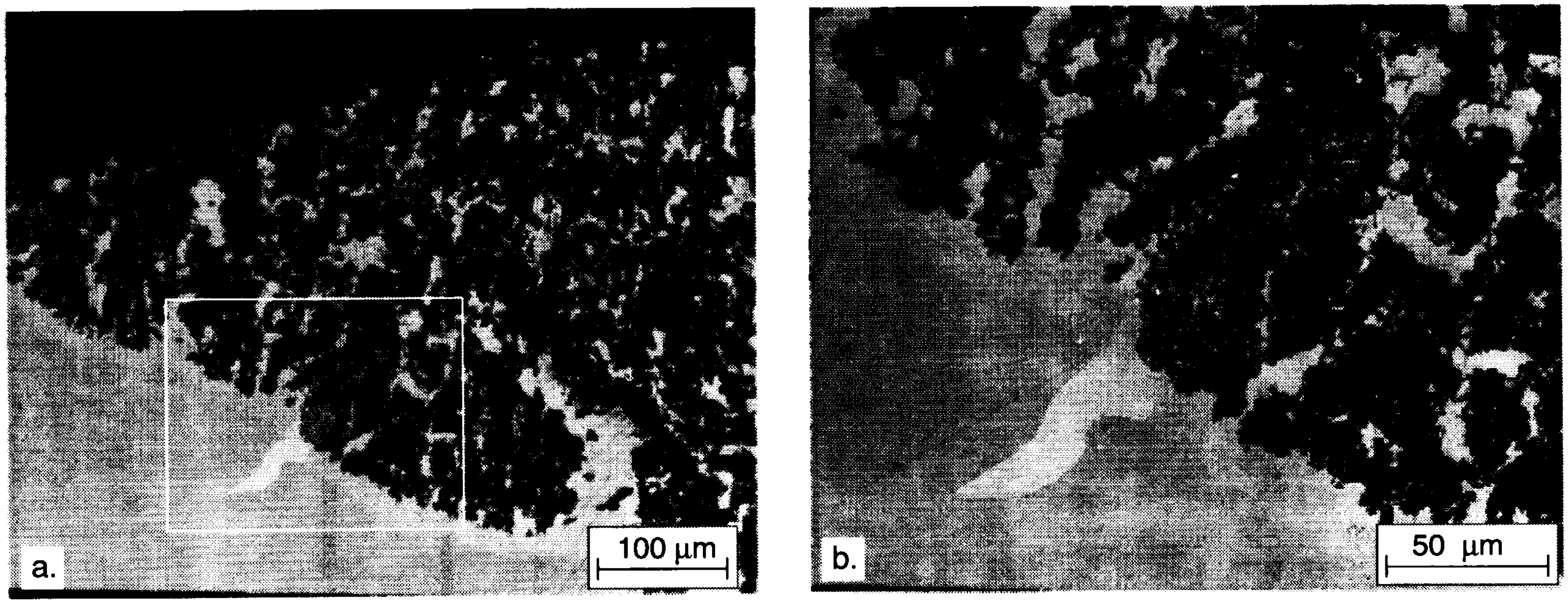

Fig. 107 Region of rampant attack on AFN20 after 300 hrs. Image (b) is a higher magnification of the box in (a).

Na_2SO_4 $CaSO_4$ $MgSO_4$

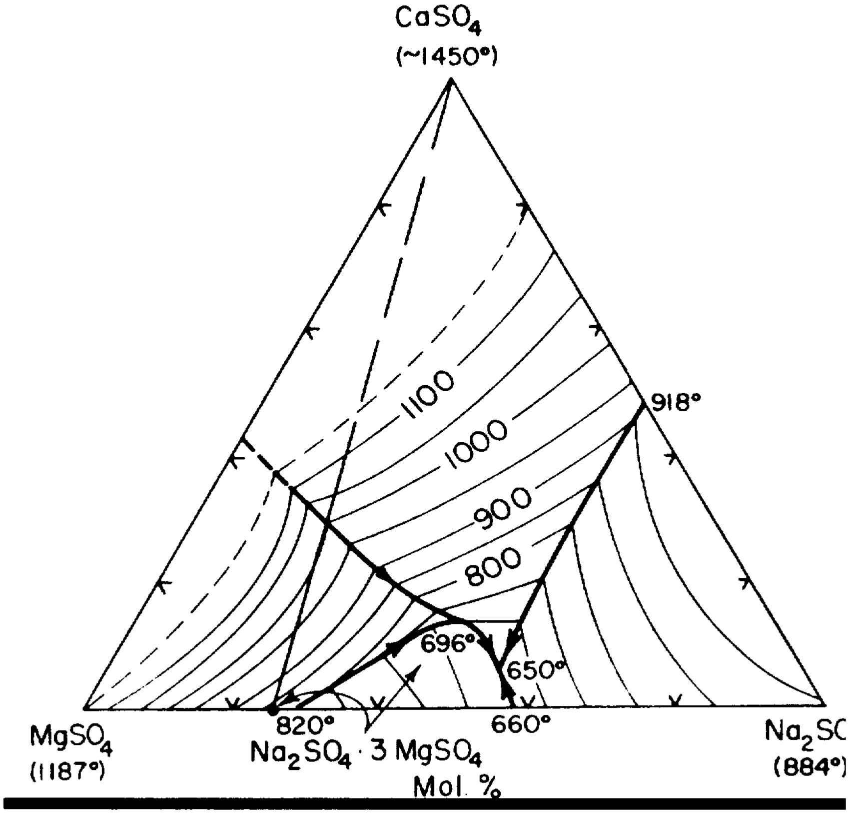

Fig. 108 Ternary phase diagram of the Na2SO4, CaSO4 and MgSO4 system (Ref 17).

APPENDIX A

Burner Rig Testing

The NiAl samples were tested in a Mach 0.3 burner rig located in the Burner Rig Test Facility at the NASA Lewis Research Center. A schematic of the burner rig is shown in Fig 1. A twelve position carousel was used to rotate the samples in the hot flame. Dimensions of the carousel are shown in Fig 2. Each sample was positioned on an individual holder which was set into the carousel. A view of one of the individual sample holders is shown with a NiAl sample in Fig 3. The design of the sample holders allowed the samples to run isothermally and be heated and cooled quickly. In addition, the holders were designed to have a minimum of contact between the sample and small alumina posts in order to reduce the trapping of condensed salts. The carousel was rotated at 250-300 RPM in the burner flame for 1 hr. After 1 hr, the burner was shifted away exposing the samples to a high velocity, ambient temperature air stream to cool the samples for a minimum of 6 minutes.

An average sample temperature was continuously monitored using a two-color and laser pyrometer aimed at the rotating samples. A feedback loop was used to make fine adjustments in the fuel to air ratio (F/A) in the combustor to maintain an average sample temperature of 900 °C (1652 °F). The F/A at the start of the testing was 0.065*. The accuracy of the pyrometer temperatures was checked with a short test run of a thermocoupled dummy sample prior to testing the NiAl samples. The thermocouple was positioned in the wall of the sample midway along the length. Temperatures were measured with the sample positioned such that the thermocouple faced both inward and outward from the center of the carousel. Heating and cooling profiles are given in Fig 4. As shown, there is very little difference in the measured temperature between the sample wall facing inward and outward from the carousel at the test temperature with only a small difference in temperature on cooling. The heating profile also shows that the sample is nearly at the test temperature (900 °C) after 3 minutes. Over the test duration of 300 hrs, differences in the two pyrometer readings occurs due to temperature changes in the test cell affecting the electronics of the pyrometers or changes in the emmisivity of the sample surfaces. As a result, an uncertainty in the test temperature of 15 °C is estimated.

Prior to testing the NiAl samples, the approximate F/A was determined with dummy samples in the carousel. NiAl samples were then placed in the carousel. The burner was then ignited with the predetermined F/A value with the carousel in the cooling position. When the burner had stabilized (a matter of minutes), the burner was shifted to impinge on the rotating carousel with the NiAl samples. The burner was operated in an automatic mode with the feedback loop from the two-color pyrometer causing small adjustments in the F/A to maintain the samples at the desired test temperature. Typically, the burner rig was programmed to perform ten 1-hr heating and 6 minute cooling cycles before shutting down so that the samples could be removed and weighed. The burner fuel was commercial grade Jet A. Air into the burner was passed through 10 micron filters.

A synthetic sea salt solution was injected into the burner to yield a concentration of 2 ppmw in the hot combustor exhaust. Past work[1] indicated the deposition of Na_2SO_4, $MgSO_4$ (or MgO) and $CaSO_4$. However, since Ca was the most prevalent alkali metal observed on either the surface or sample cross-sections, an additional deposition study was undertaken. This study used a single Pt/Rh target, approximately 1.9 cm (0.75 in) in diameter by 1.27 cm (0.5 in) high. The target was rotated on it's axis in front of the flame. Alumina supports were again used to allow the sample to operate isothermally at 900 °C. Two tests were run for times up to 15 hrs at a F/A=0.032. The deposits were dissolved in boiling deionized water. After the water dissolution, oxides were dissolved from the surface using dilute nitric acid. The ratio of deposits for both tests were very similar. Analysis of the deposits, averaged for the two targets, are given in Table I.

---

* At the end of the Series III testing, the air and fuel flowmeters used to calculate the F/A were found to require recalibration. The F/A reported above is the best estimate using indicated flows at the start of testing.

Table I

Analysis of Deposits on Pt/Rh Targets

Elements	Concentration (wt.%)
Na	22.8
Mg	6.25*
Ca	2.6
K	0.2
SO_4	49.6
Cl	nd**
Sr	0.14

* Detected after acid leach

** Not detected

The lack of Cl indicates that most of the salt is converted to sulfate in the burner. In addition to the Mg detected after the acid leach, the following elements from the corrosion of the burner and nozzle were detected: 0.37 Si, 0.14 Ni, 0.1 Fe, 0.06 Cr, 0.015 Zn and 0.006% Mn (wt %). EDS analysis of the deposit on one of the targets easily showed the presence of Na, Mg, Ca, S and O in proportions in agreement with the above results.

Different materials were used for the nozzle and burner liner in the burner rig. However, the materials were either Ni or Fe-based and typically contained Cr, Al, Si and Zr. Analysis of carbon deposits at the nozzle inside the burner showed significant concentrations of Ni (25%), Fe (5%), Al (20%), W (4%), Si (2%), Zr (0.5%) and Cr (0.4%) as well as significant Na (15%), Mg (0.5%) and Ca (0.1%). There was also an unexplained presence of Ba (5%) in the deposit within the burner. Hence, the presence of Fe, Cr, Ni, and Si on the surface of the Pt/Rh targets, as well as on the surface of the NiAl samples, can be attributed to the degradation of the burner and nozzle.

REFERENCES

1. G.C. Fryburg, F.J. Kohl, C.A. Stearns and W.L. Fielder, J. Electrochem. Soc., 129, 571, 1982.

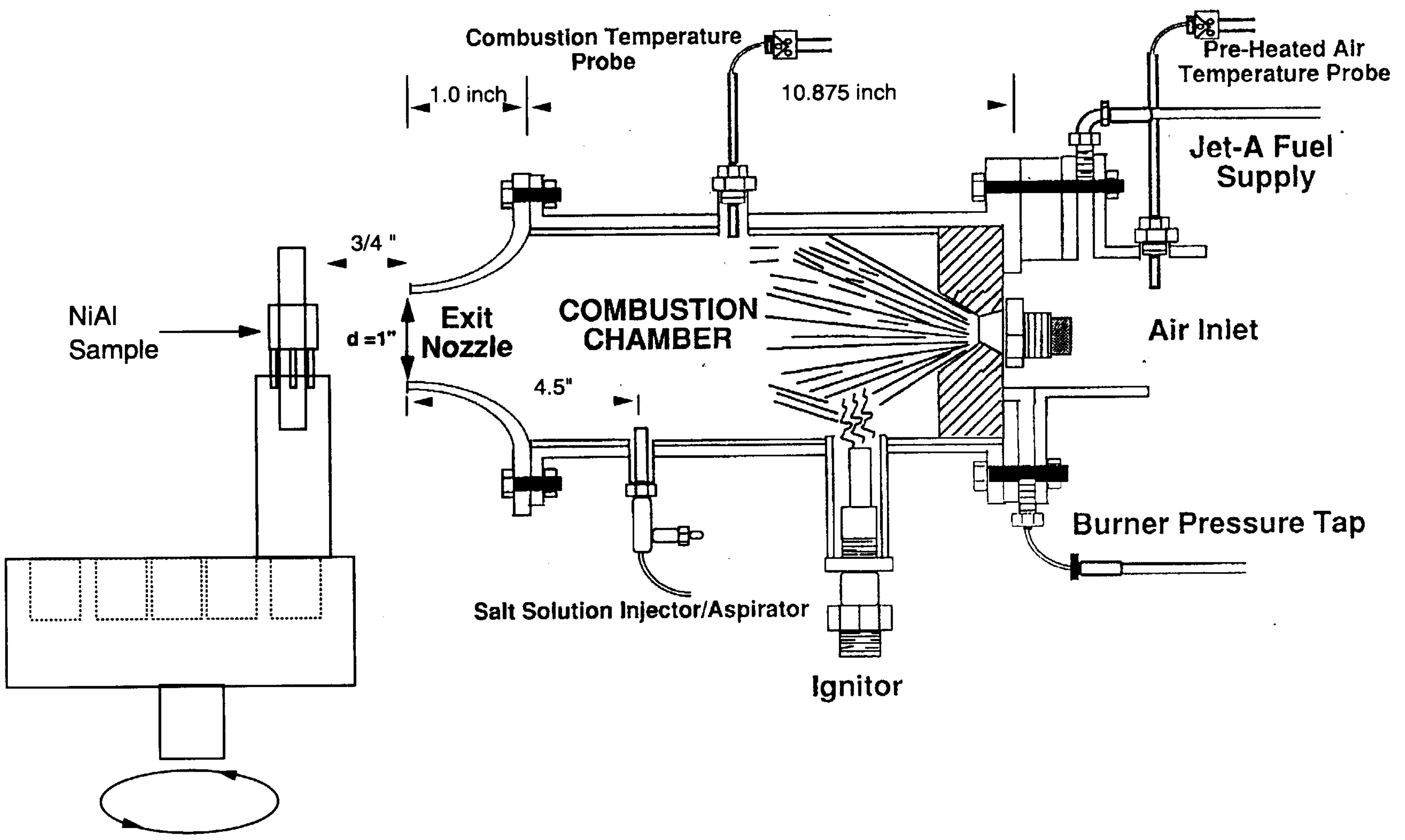

Appendix A Fig 1 Schematic of the Mach 0.3 burner rig

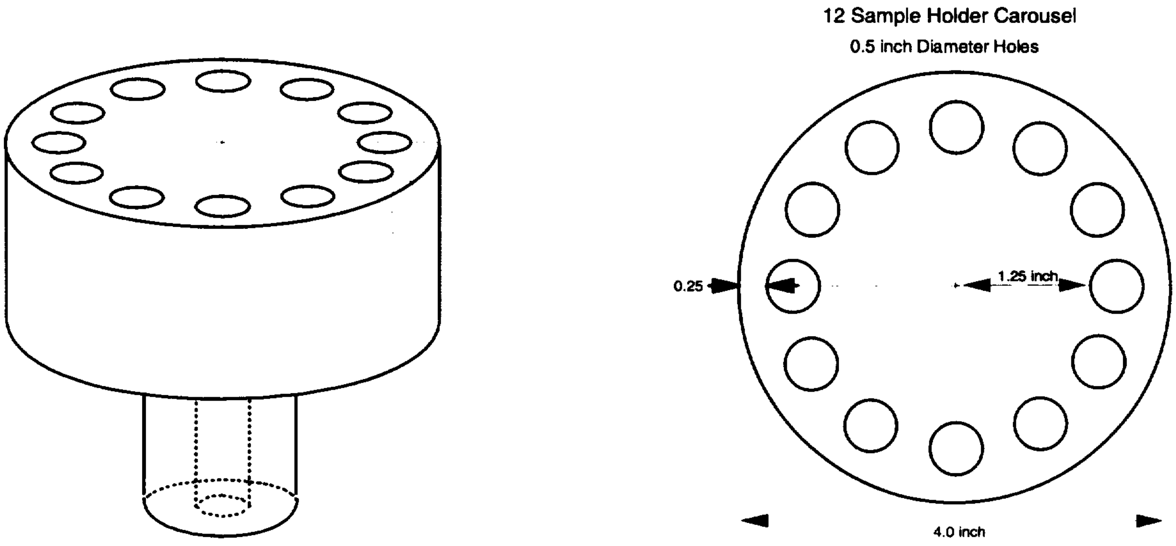

Appendix A Fig 2 Schematic of the 12 position carousel used in the burner rig testing.

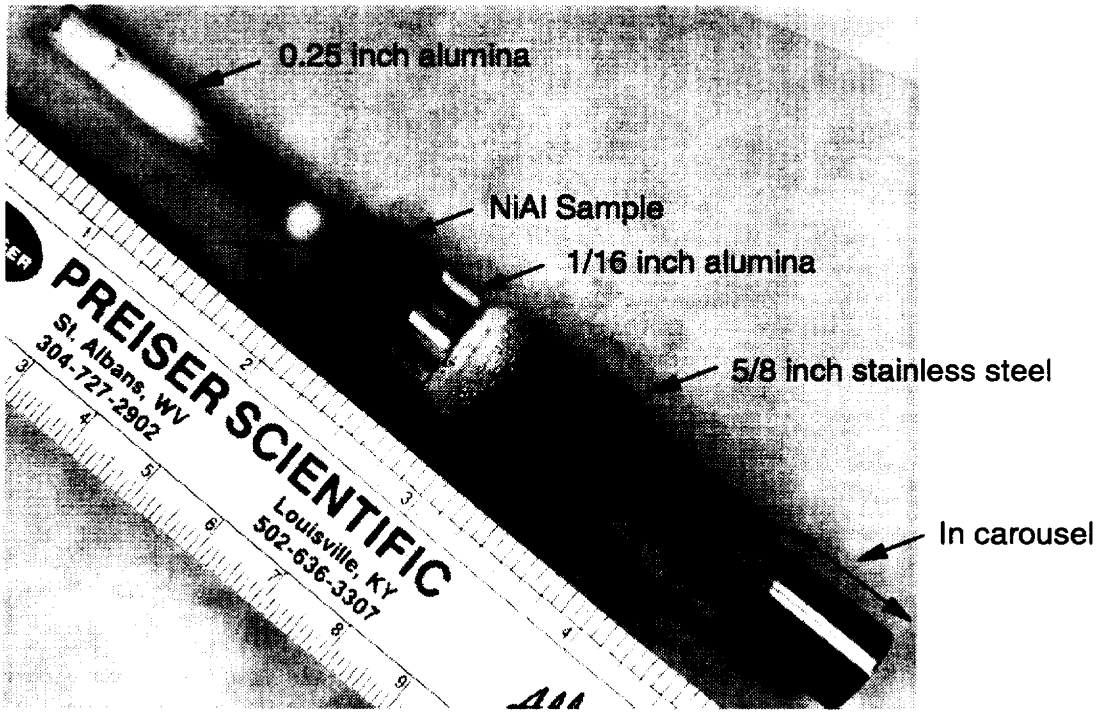

Appendix A Fig 3 View of the individual sample holders supporting the NiAl sample.

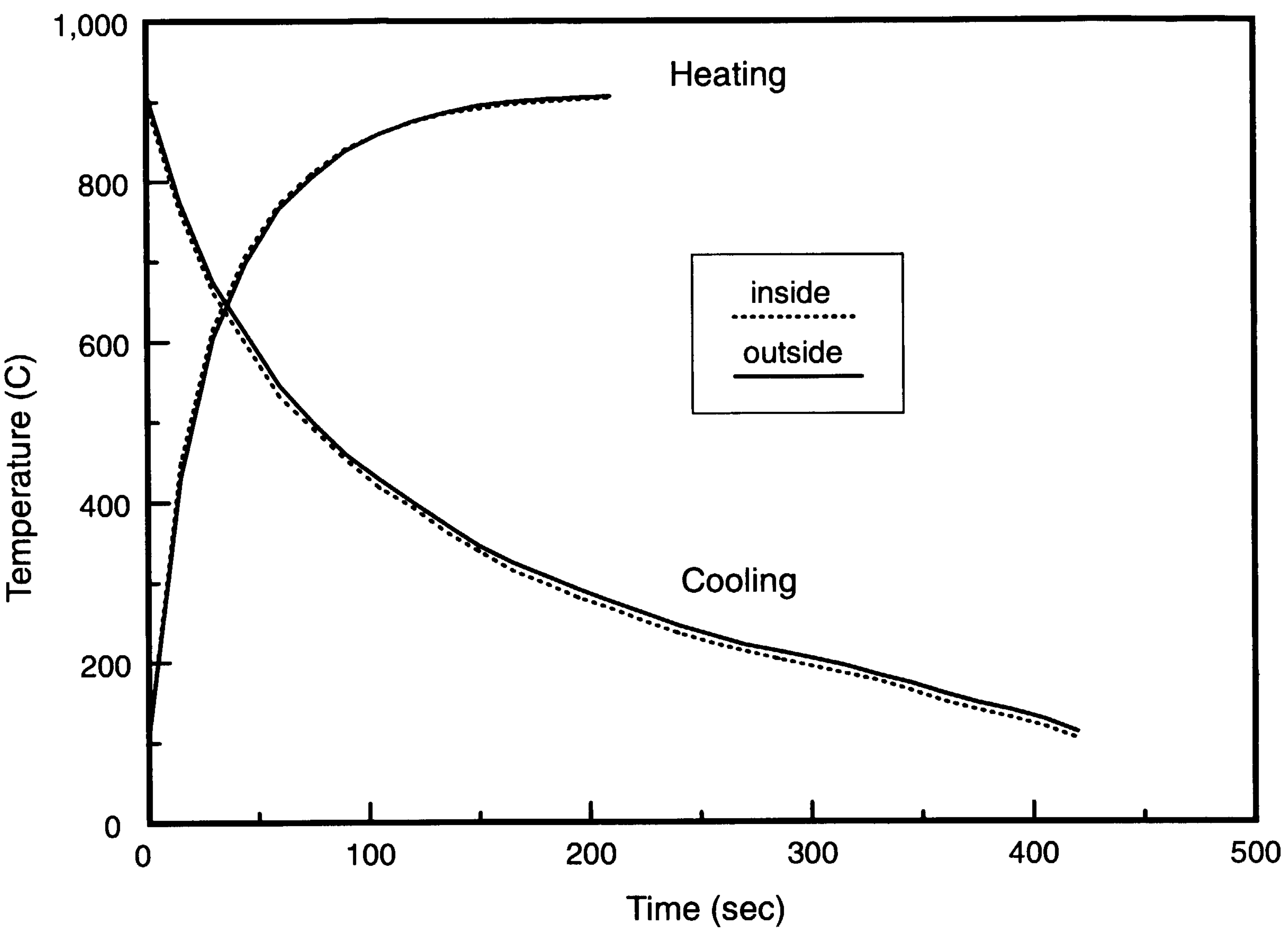

Appendix A Fig. 4 Sample temperature profiles measured by thermocouple (tc) in the sample wall. Inside and outside refer to tc position with respect to carousel (see text).

APPENDIX B

Testing Results For Electropolished Samples

The weight change for the seven NiAl samples is shown in Fig 1. As previously stated, all of the samples gained weight more rapidly due to accelerated attack on the ID of the samples. The AFN24 sample fractured longitudinally into two halves between 70 and 80 hrs and was removed from the test. The weight losses of other samples after 80 hrs are due to smaller pieces of the sample fracturing off, but allowing the sample to continue being tested.

The surface morphology of the samples after 63 hrs, the last time samples were photographed after the same test exposure, are shown in Figs 2-5. Non-uniform accelerated attack on two regions on the curved surface of AFN19 is shown in Fig 2a,b. The attacked region in Fig 2a is curved whereas the attacked region shown in Fig 2b is flat. It appears that some of the accelerated attack on the flat region follows some of the dendritic pattern discernible on the surface. The arrows in Fig 2a,b indicate the attacked curved surface shown in Fig 2c. The mounds on the end are located on the same portion of the sample with the accelerated attack on the curved surface. Typical corrosion mounds are shown on the ends and curved surfaces of AFN21 and AFN22 in Fig 3. Elongated corrosion mounds on the end of AFN21 (lower portion of Fig 3b) appear to be following small ridges remaining on the sample from the EDM cutting. Very little attack was observed on the AFN23 sample (Fig 4a,b). The AFN24 sample showed more attack on one half of the curved surface (Fig 4c). Both the AFN25 and AFN26 samples show some small mound formation on the surface. The AFN25 sample has two regions on the end where mechanical test samples were removed from the ingot. Neither region shows any indication of accelerated attack.

In general, the corrosion morphology on the electropolished samples appeared similar to that on the chemically milled samples. Typically, the corrosion morphology first appeared as small bumps, growing with time into larger mounds. In some samples, these mounds coalesced so that an entire region became raised. Several samples showed more attack near one end while other samples showed accelerated attack on irregular regions on the surface (e.g., AFN19). However, not all irregular surfaces showed accelerated attack (e.g., AFN25, Fig 5b). The flat region shown in Fig 2b may be from the edge of the ingot. Perhaps compositional inhomogeneities or impurities near the surface produced the accelerated attack on this flat region. If this flat region is from the ingot surface, it is possible that the accelerated attack on the adjacent curved surface in Fig 2a contains the same compositional inhomogeneities or impurities due to the close proximity to the surface. Further studies would be necessary to confirm whether conditions near the surface of the ingot did indeed cause the accelerated attack on some of the samples.

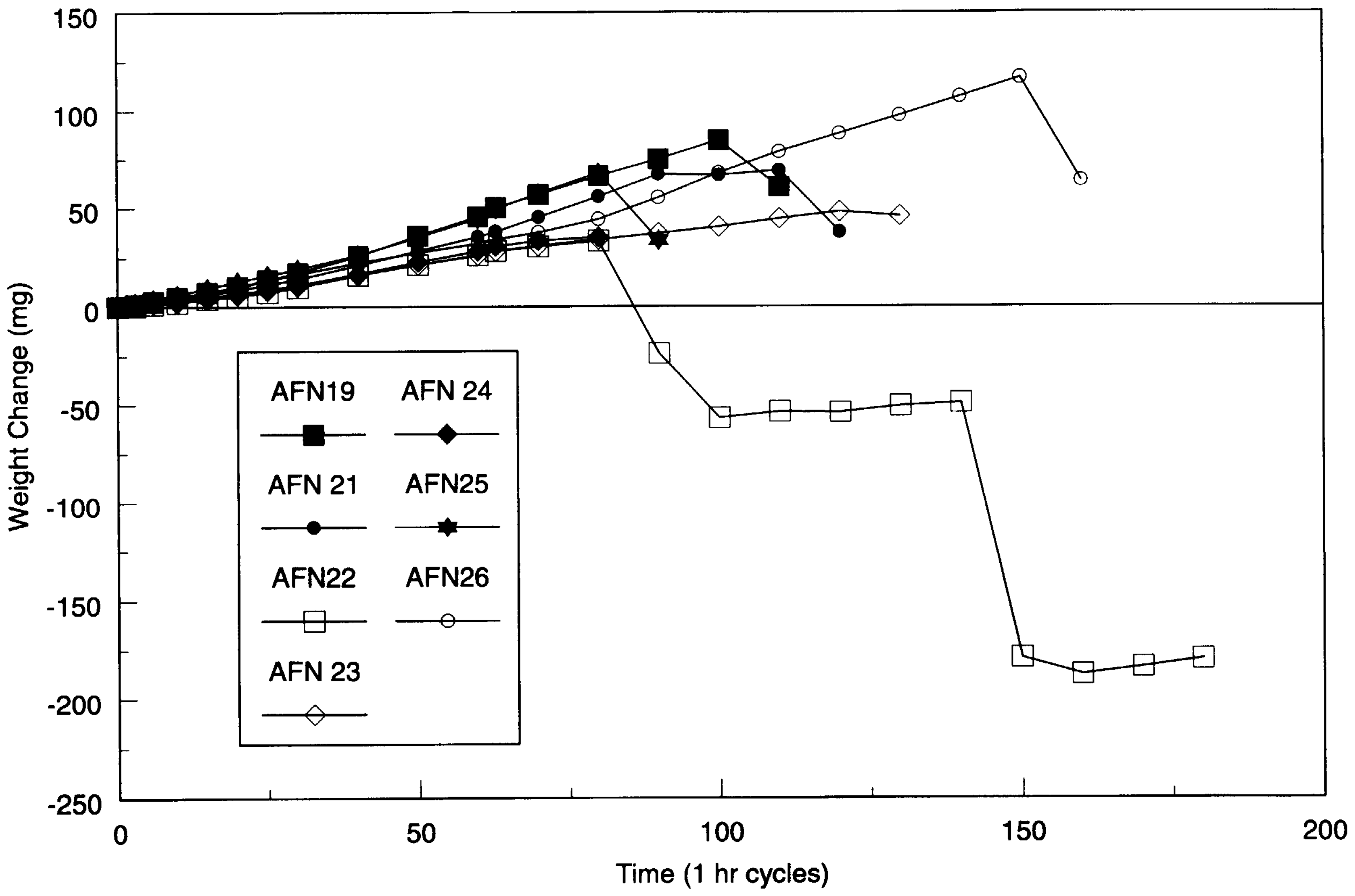

Appendix B Fig 1 Weight change during Series I, electropolished samples.

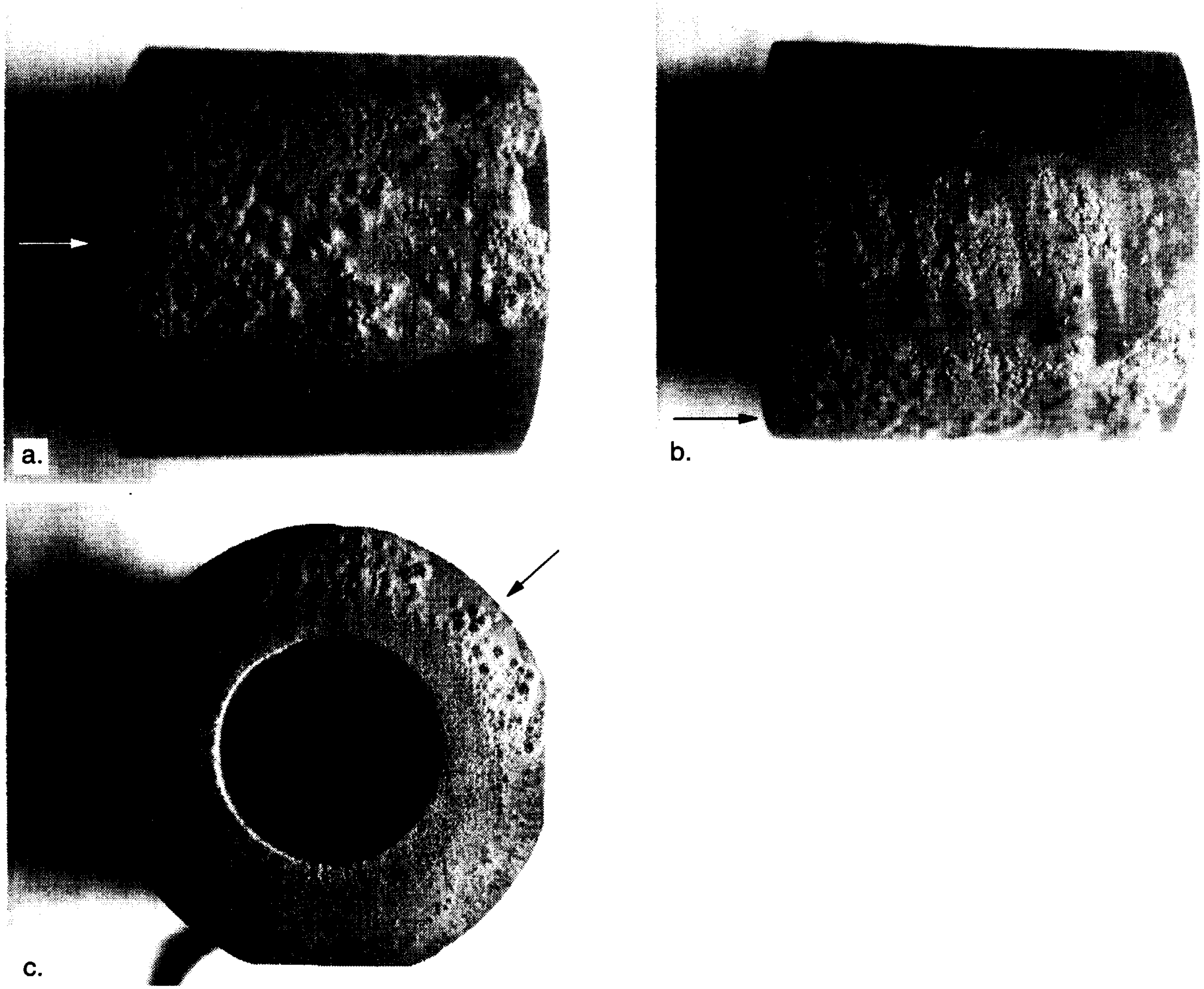

Appendix B Fig 2 Macrophotos of electropolished AFN19 after 63 hrs (a,b) two views of curved surface, (c) end to the right in (a,b). Arrow in (c) indicates the attacked curved surface shown by arrows in (a,b).

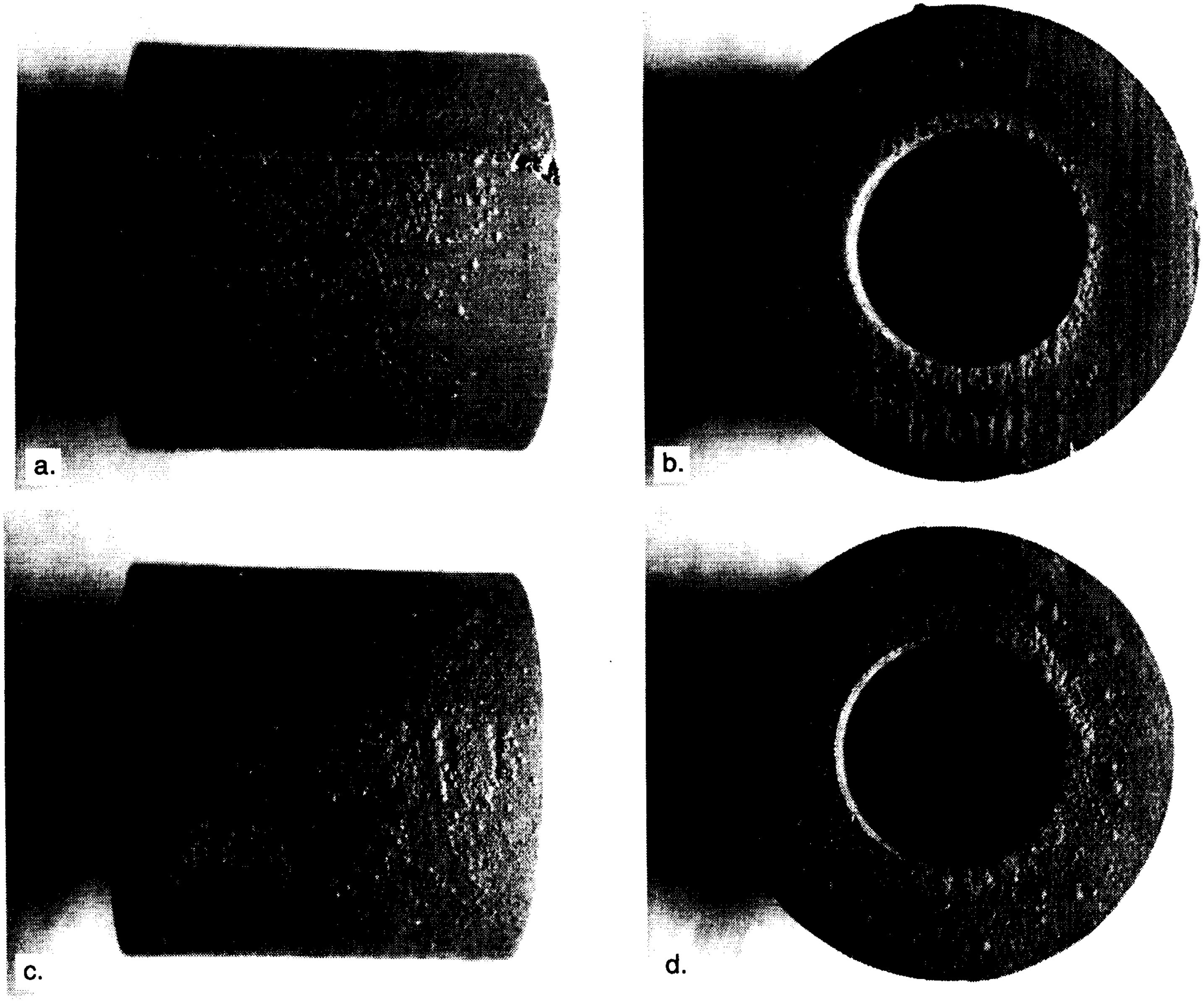

Appendix B Fig 3 Macrophotos of electropolished (a,b) AFN21, (c,d) AFN22 after 63 hrs.

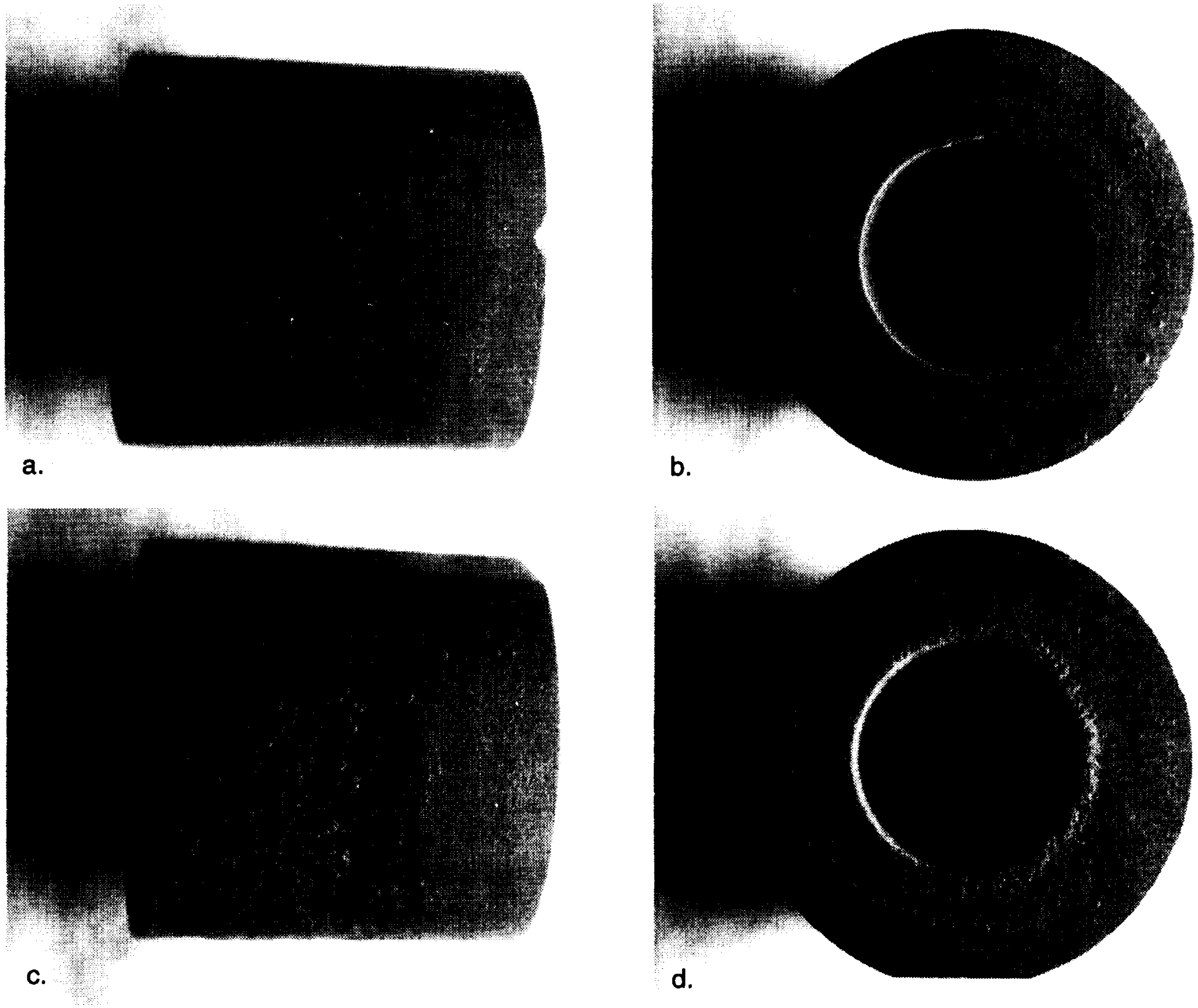

Appendix B Fig 4 Macrophotos of electropolished (a,b) AFN23, (c,d) AFN24 after 63 hrs.

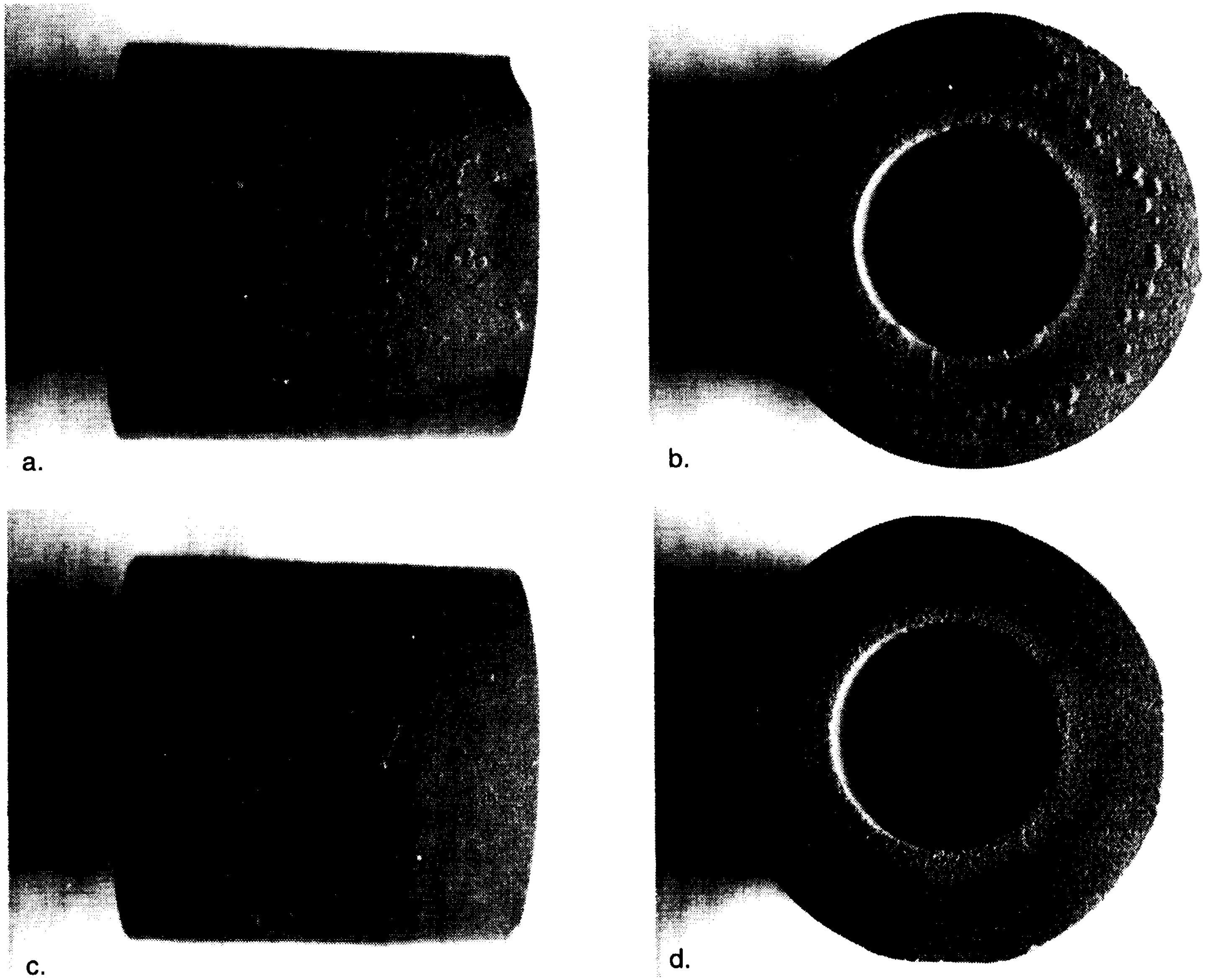

Appendix B Fig 5 Macrophotos of electropolished (a,b) AFN25, (c,d) AFN26 after 63 hrs.

REPORT DOCUMENTATION PAGE

Form Approved
OMB No. 0704-0188

1. AGENCY USE ONLY (*Leave blank*)

2. REPORT DATE
May 1998

3. REPORT TYPE AND DATES COVERED
Technical Memorandum

4. TITLE AND SUBTITLE
Hot Corrosion of Single-Crystal NiAl-X Alloys

5. FUNDING NUMBERS
WU-523-21-13-00

6. AUTHOR(S)
James A. Nesbitt

7. PERFORMING ORGANIZATION NAME(S) AND ADDRESS(ES)
National Aeronautics and Space Administration
Lewis Research Center
Cleveland, Ohio 44135-3191

8. PERFORMING ORGANIZATION REPORT NUMBER
E-10898

9. SPONSORING/MONITORING AGENCY NAME(S) AND ADDRESS(ES)
National Aeronautics and Space Administration
Washington, DC 20546-0001

10. SPONSORING/MONITORING AGENCY REPORT NUMBER
NASA TM-113128

11. SUPPLEMENTARY NOTES
Responsible person, James A. Nesbitt, organization code 5160, (216) 433-3275.

12a. DISTRIBUTION/AVAILABILITY STATEMENT
Unclassified - Unlimited
Subject Category: 26 Distribution: Nonstandard

This publication is available from the NASA Center for AeroSpace Information, (301) 621-0390.

12b. DISTRIBUTION CODE

13. ABSTRACT ***(Maximum 200 words)***

Several single-crystal NiAl-X alloys (X=Hf, Ti, Cr, Ga) underwent hot corrosion testing in a Mach 0.3 burner rig at 900°C for 300 1-hr cycles. The surface morphology after testing consisted of either mounds or an inward, uniform-type of attack which preserved surface features. It was observed that the surface morphology was affected by the surface preparation treatments. Microstructurally, the hot corrosion attack initiated as pits but evolved to a rampant attack consisting of the rapid inward growth of Al_2O_3. Electropolishing and chemical milling produced many pits and grooves on the surface. However, the presence of pits and grooves did not appear to strongly influence the hot corrosion response. Attack on many samples was strongly localized which was attributed to compositional inhomogeneity within the samples. It was found that increasing the Ti content from 1% to 5% degraded the hot corrosion response of these alloys. In contrast, the addition of 1-2% Cr reduced the susceptibility of these alloys to hot corrosion attack and negated the deleterious effect of the 4-5%Ti addition.

14. SUBJECT TERMS
Hot corrosion; NiAl; Ni aluminide

15. NUMBER OF PAGES
165

16. PRICE CODE
A08

17. SECURITY CLASSIFICATION OF REPORT	**18. SECURITY CLASSIFICATION OF THIS PAGE**	**19. SECURITY CLASSIFICATION OF ABSTRACT**	**20. LIMITATION OF ABSTRACT**
Unclassified	Unclassified	Unclassified	

NSN 7540-01-280-5500

Standard Form 298 (Rev. 2-89)
Prescribed by ANSI Std. Z39-18
298-102